UNIVERSITAT POLITÈCNICA DE CATALUNYA BARCELONATECH

Study of near field processes involved in the oxidative dissolution of the spent nuclear fuel and radionuclides release

Alexandra Espriu Gascon

UNIVERSITAT POLITÈCNICA DE CATALUNYA

Departament d'Enginyeria Química

Ph.D. Programm: Enginyeria Ambiental

STUDY OF NEAR FIELD PROCESSES INVOLVED IN THE OXIDATIVE DISSOLUTION OF THE SPENT NUCLEAR FUEL AND RADIONUCLIDES RELEASE

Author: Alexandra Espriu Gascon

Supervisors: Dr. Ignasi Casas Pons / Dr. Francisco Javier Giménez Izquierdo

Thesis presented to obtain the qualification of Doctor awarded by the Universitat Politècnica de Catalunya – Barcelona Tech

Barcelona, 31st of May of 2017

Per als meus quatre avis,

tant als que ho han pogut veure com als que no.

Resumen

Actualmente en España, las centrales nucleares están acumulando el combustible nuclear gastado (CNG) y apenas disponen de espacio suficiente para seguir almacenando el residuo generado por la actividad de la central. En consecuencia, es necesario adoptar una solución definitiva a la gestión de los residuos nucleares. La opción aceptada internacionalmente para almacenar definitivamente el CNG como la más segura y viable es el Almacenamiento Geológico Profundo (AGP) basado en el confinamiento y la protección del residuo mediante un sistema de multibarrera. Dicho sistema considera el CNG como primera barrera donde están contenidos los radionúclidos (RN) debido a las propiedades físicas y químicas del propio combustible.

Con el objetivo de evaluar la seguridad del AGP y determinar el comportamiento del CNG en condiciones relevantes para su almacenamiento definitivo, en el presente trabajo se han planteado cuatro posibles escenarios que podrían provocar la alteración del combustible. Dichos escenarios se han estudiado mediante análogos no irradiados del CNG.

En el proceso de alteración de las barreras que componen el AGP, la corrosión anaeróbica de la capsula metálica produce una elevada presión de hidrógeno que podría entrar en contacto con el CNG. A su vez, la entrada de agua en el repositorio y la temperatura a la que se encuentra el CNG podrían hacer aumentar la humedad en las proximidades del residuo. Por lo tanto, en este trabajo se ha estudiado el efecto del vapor de agua en contacto con el UO_2 en atmósfera de H_2. Los resultados obtenidos muestran que se produce la oxidación del uranio tanto en condiciones anaeróbicas como en condiciones reductoras en función de la temperatura usada. Por otro lado, en presencia de nanopartículas de paladio, análogas a las partículas épsilon del CNG, no se observó oxidación alguna del UO_2 en presencia de H_2.

En el momento en que el agua entre en contacto con el CNG, los RN segregados de la matriz más volátiles y solubles serán lixiviados de forma prácticamente instantánea (IRF) provocando un aumento significativo de radiación en las aguas subterráneas. Con el objetivo de predecir la liberación de dichos RN se ha diseñado un modelo y un algoritmo matemático que ha permitido predecir la liberación de los RN disueltos en la matriz e identificar y cuantificar los RN que forman parte de la IRF de un combustible real. Los resultados obtenidos de la aplicación del modelo concuerdan con resultados experimentales

publicados anteriormente. Por lo tanto, se puede concluir que el modelo y el algoritmo cumplen con los objetivos marcados de identificación, predicción y cuantificación de la distribución de los RN en el CNG.

Debido a que los mecanismos de alteración del UO_2 podrían variar dependiendo de la composición del agua subterránea, se ha estudiado la corrosión del CNG en contacto con aguas de cemento. Para ello se ha usado un electrodo de SIMFUEL con el que se han realizado ciclovoltamogramas, experimentos potenciostáticos y mediciones del potencial de corrosión en condiciones hiperalcalinas y en presencia de calcio y silicato como símil de aguas de cemento. Los resultados muestran una disminución de la corrosión en presencia de calcio y silicato que podría ser provocada por la precipitación de fases sólidas en la superficie del SIMFUEL o por la estabilización de las fases reducidas.

Por último, la precipitación de fases sólidas podría ayudar a reducir la concentración de los RN liberados por el CNG. En este contexto, se han estudiado y determinado las capacidades de retención de dos fases sólidas de uranio; la soddiita y la uranofana, en contacto con Cs y Sr en disolución. Se ha determinado que ambos sólidos son capaces de adsorber ambos iones en su superficie, siendo la soddiita el sólido con mayor capacidad de retener Cs y la uranofana la fase sólida con mayor capacidad de retención de Sr. Por tanto, la formación de estas fases podría disminuir la concentración de estos RN liberados a la geosfera.

Summary

Nowadays nuclear power plants (NPP) and dedicated facilities are storing the spent nuclear fuel (SNF). In the case of Spain, the NPP have enough space in their pools to keep storing the SNF produced from their activity; therefore, it is necessary to provide a final solution for the SNF management. It has been internationally accepted that the safest and most economically viable option to finally dispose the SNF is the Deep Geological Repository (DGR) which is based on the protection and confinement of the SNF by using a multibarrier system. This system considers the SNF as the first barrier where all the radionuclides (RN) are contained due to the physical and chemical properties of the fuel waste.

With the goal of assessing the safety of the DGR and determining the SNF behavior under relevant conditions for the repository, in this work, four different scenarios have been selected that might alter the nuclear waste. These scenarios were studied by using non irradiated analogues of the SNF.

During the alteration of the barriers of the DGR, the anoxic corrosion of the metallic container will produce high partial pressures of hydrogen that might get in contact with the SNF. At the same time, it is possible that vapor will be produced due to the water entry and the temperature of the SNF. In this work, the effect of water vapor and hydrogen in contact with UO_2 has been studied. It was observed that uranium is oxidized in contact with water vapor in anoxic and reducing environment and as a function of the temperature. On the other hand, when palladium nanoparticles were used as analogues of the epsilon and metallic particles of the SNF, no oxidation was observed under H_2 atmosphere.

At the time when the water gets in contact with the SNF, the RN that are segregated and are more volatile and soluble than UO_2 will be released to the water faster than the SNF matrix and will contribute to the Instant Release Fraction (IRF). With the aim of predicting the RN release, a mathematical model and a specific algorithm were designed, in order to identify and quantify the segregation of the RN that contributes to the IRF. Real leaching data was used to discuss the model and the algorithm by using the results obtained that allowed to classify the RN depending on their release source (grain boundary, oxidized phases and matrix). The dissolution rates obtained from the model agree with reported values in the bibliography.

Since the alteration mechanisms of the SNF and the UO_2 matrix depend on the ground water composition, and given the presence of concrete components in the DGR, this work studied the SNF corrosion in contact with cement waters. A SIMFUEL electrode was used to obtain cyclic voltammograms, potentiostatic and corrosion potential measurements under hyper alkaline conditions

in presence of calcium and silicate as a analogue of cementitious water. The results obtained showed that the oxidation of the SIMFUEL was partially avoided in the presence of calcium and silicate. This might be caused by the precipitation of solid phases on the electrode surface or by the stabilization of reduced phases.

Finally, saturation conditions might occur in the SNF near field and secondary solid phases might precipitate in the SNF vicinity. In this context, this work studied the influence of two uranyl silicate solid phases (soddyite and uranophane) on the Cs and Sr mobility. It was determined that both solid phases can retain the two RN on their surface and the sorption process proceeds through sorption on active sites. For the sorption of Cs, soddyite has more sorption capacity while in the case of Sr, uranophane has more sorption capacity. Therefore, the formation of these secondary phases might decrease the concentration of Cs and Sr released to the geosphere.

Acknowledgements

My dearest scientific, and not so scientific, readers,

You are about to read the acknowledgements[1] of this thesis. Let me suggest you something: if I were you, I would read everything without paying any attention to the footnotes and later on, I would stop and read the text including the notes. That way, it would be like you were first watching a movie and later on, hearing the director's comments[2].

I hope you enjoy the story.

This happened a long, long time ago[3] with an innocent girl who was helping around. All of a sudden, a man approached to her. He presented himself as a seller[4] and said that he wanted to offer her a really nice and beautiful submarine[5]. The girl though about that submarine, the offer and all what that journey might provide her and she finally decided to buy that submarine[6].

She enrolled to a trip along with some other colleges, although they worked in other areas of the device. At the beginning, our protagonist had to deal with her area on her own. Well, that is not exactly true; she had three bosses to lead her way. Of course, one of them was the seller who had become captain of the submarine. The girl discovered that he is indeed a super – perfectionist, nice, generous and funny captain. Another one of the captains is a cheerful man, quite busy but accessible at the same time. He had three different submarines to navigate: an entire university, a new and blue submarine and the one where the girl was with all of her issues[7]. Then, the third captain was like a Super Captain with his white hair and his white beard: lovely and close person. He has this kind of grave voice that doesn't matter where you are, you can hear him. He was the voice of the reason every time that she lost her nerves

[1] At least, that is what I hope. Of course you can read the whole manuscript without reading the acknowledgements.
[2] But in this case, they are the author's comments.
[3] To be precise, the story started on January 14th of 2011
[4] Well, sort of, I already knew him; he had been my Chemistry professor at the University. I remember thinking that he must have been a really handsome man when he was younger although at that moment he looked more like an uncle to me. I also remember that he was kind of strict, but really good teacher.
[5] This expression deserves a little footnote. Sometimes, in Spain, when somebody is about to make a crazy, or not so good offer, or maybe they just want to mess with somebody, we say that someone is trying to sell a submarine to somebody. I am sorry but I don't know the idiom in English, if there is one…
[6] I have to say that I could have gone to Belgium instead because I got a grant to finish my degree there but I rejected it in the end.
[7] It sounds quite complicated, right?

because of some bureaucratic issues and managed to calm her. Anybody can imagine the meetings: dealing with three different heads at the same time is not easy. Fortunately the girl managed to make it work at the end[8].

Obviously, the trip had several stops, or better said exchange of submarines. The first brought the girl to Germany where she met awesome people who supported her when her life was a complete mess. Thanks to Dani, Albert, Vane, Maria Rosa and Pelin, the life in Germany was like the eye of the storm, an oasis right in the middle of the desert. Even though the German submarine wasn't working, they all had lots of fun and learnt a lot in it, together with Thomas, Frank and Rachel.

The second submarine was Canadian, full of Canadian flags[9], peanut butter, maple syrup and corrosion everywhere. The things that the girl loved the most were the people and improving her English[10]. The colleagues from the submarine were the best, especially Nancy and Leila who helped her with the SIMFUEL and all the experiments. Then, she made some friends, Taylor, Thalia, Jeff, Joseph, Max, Balsam, and everybody in there. And it was really fun discussing with Jamie Noel about the European Union, Spanish and lots of other things while doing the samples inventory[11]. They even had a barbecue at Jamie's house with all the fellows of the lab[12]. Not to mention her roommate Shannon. She helped our protagonist a lot during the whole journey, took her to do some sightseeing in Toronto, went shopping some groceries and everything about daily life[13]. And last but not least (not even close): David W. Shoesmith, the super – captain of the Canadian submarine[14].

Back to the original submarine, the life went on. She had new national (Julio pequeño, Xanel) and international (Julio doctor, Mehrez)[15] colleges besides the people who were there from the start (Marc, Mònica and Xia) and some other who had left the lab (Edxon, Neus, Marc Travesset, Aurora, Gerard and

[8] Yeah! Right! At the end of the thesis, so annoying! I should have realized how to do it sooner but now I know how to do it without going nuts.

[9] I was really surprised. Canada is full of Canadian flags, all over the country. Not to mention, I spent the Canda day in there. By the ways, it's on July first. About the peanut butter: I ended up loving it and when Nancy and Leila asked me if I wanted anything from Canada, I told them: "just bring me some peanut butter, and I'll be the happiest girl!"

[10] Nobody spoke Spanish or Catalan. Nobody at all. The worst was the first day. I spent the first weekend with a five member family with three grown up boys, their parents and their girlfriends. They were speaking so fast, loud and with so much accent that I couldn't follow the chat. Of course, I ended up with headache.

[11] I must say that the lab is really tiny and there's only one seat. So I was sitting on the floor, and Jamie on the seat but at the end, we both ended up sitting on the floor and surrounded by SIMFUEL all over the place. We had tons of fun those days!

[12] That was really nice of all of you

[13] I treasure the memories of looking for a school bus and trying to take a picture with it. That day was awesome!

[14] Can I say that I love him? Everybody in the lab does! And even people who's not in the lab with you or not even in the same country as he does, they do too. This tells you a lot about how Dave is in person.

[15] I know in some countries you may treat them in a more formal manner but… they are lab mates and friends, so to me and everybody else, are simply Julio, Mehrez, Edxon and Xanel

Rocío are the ones that the girls remembers the most). They all shared Donuts, lots of 'Lunch Time's and 'Coffee Time's, talks and discussions[16]. They all cheered her up so many times that it will be difficult to find people like them[17]. At the end her journey, our protagonist was able to take control of the submarine and navigate on her own thanks to all the experiences she had and the people who meet her. We will see what life has prepared for her from now on.

A la meva estimada familia i amics que em pregunten "i quant et queda? Ja estàs a punt d'acabar oi?" Tot i ser les dues preguntes més odiades pels estudiants de doctorat, per sort no me les han preguntades masses vegades!

Gracias Javi, por todo. Por ser mi mejor amigo, mi apoyo y "you're my mama!". Hemos pasado por mucho en todos estos años y ahora nos toca vivir, pero esta vez de verdad. Quiero poder soñar contigo, tener nuevos proyectos y hacerlos realidad contigo, 'twice?'

Dear Captains,

It is time for me to fly away. Isn't it? Hopefully, you would have enjoyed this trip with me as much as I did. A lot of things happened; things that made me grow in more than one way.

I must say, when I read some of the acknowledgements of other thesis I always thought 'Why do they all say that they have cried, laugh… is the thesis such like a roller coaster?' I do know now the answer: It definitely is, for sure! I have some really good memories of this journey and others not so good but still, I treasure each and every one of them.

I just want you to know that I love all of you. You were there when I needed you the most and I am really thankful for that. Thanks for your patience, your support and your trust. I will always have them with me. Thanks for the memories and for helping me to grow up a little more.

This is not a farewell letter, this is a 'see you soon' and 'thanks' letter, so…

SEE YOU SOON,

THANK YOU VERY MUCH FOR EVERYTHING.

[16] And gossip! Do not forget about gossiping!
[17] I love you guys, you know that, right?

Quisiera agradecer también a ENRESA, en especial a Aurora Martínez Esparza quien me acompañó al principio de este viaje, y a Miguel Ángel Cuñado que relevó a Aurora y estuvo conmigo hasta el final.

Muchas gracias también al Ministerio de Economía y Competitividad (MINECO) por la financiación de la beca, cuya referencia es BES-2012-053098 y a los proyectos de financiación CTM2011-27680-C02-01 y ENE2014-54299-C2-1-R de origen Español. Additionally, I would like to thank the European Community for the funds associated to the FIRST-Nuclides European project.

And… Dear reader, I see you in the thesis.

Contents

Contents

General Introduction

Chapter 1:
General Introduction

Current situation of the Nuclear Waste Management in Spain

Nuclear waste is defined as a material that emits a radiation dose higher than the dose allowed by law without any use or possible profit. This type of waste needs to be managed by following a specific procedure in order to ensure its isolation ant the confinement of the waste and radioactive isotopes. There are different kinds of nuclear waste, but in this thesis dissertation only the spent nuclear fuel (SNF) obtained from the Nuclear Power Plants (NPP) will be considered for discussion.

Once the useful life of the nuclear fuel has ended, it is moved from the nuclear reactor to the pools in the NPP in order to refrigerate it. After some years, both the temperature and the activity of the nuclear waste have decreased allowing SNF to be moved to dry storage casks in the NPP. Later, the Spanish SNF will be stored in the centralized temporary dry storage (CTDS) until the final disposal facility, the deep geological repository (DGR) which is expected to be operative by 2050 (ENRESA, 2006).

Temporary Dry Storage

Dry cask storage is an emerging reality in many countries and it has to store the SNF one hundred years or more (Ewing, 2015). In the case of Spain, the CTDS is expected to be located in Villar de Cañas, Cuenca (Spain), and to be operative in 2018 (ENRESA, 2014), although, in the present year (2017), its construction is being delayed.

The main goal of the CTDS is to collect all the nuclear waste and other high radioactive waste in the country in a single facility. By doing this, the almost full pools in the NPP will be able to store more SNF from the nuclear reactor; the CTDS will also provide a specific location for the nuclear waste in case of an unexpected dismantling of a NPP.

The facility is provided with a hot cell that will allow to manage the incoming fuel to dispatch it either to the storage gallery or to the research center.

The cooling of the SNF stored in the galleries will be ensured by natural air convection from the outside.

The Deep Geological Repository

The DGR aims to store the nuclear waste and protect the natural environment from harmful radiation for thousands of years, due to the long – lived isotopes that emit radiation. Therefore, the DGR was designed by using a multi barrier system, where each barrier delays the exposition of the SNF to water. In Figure 1. 1 a scheme of the overall DGR facility is shown.

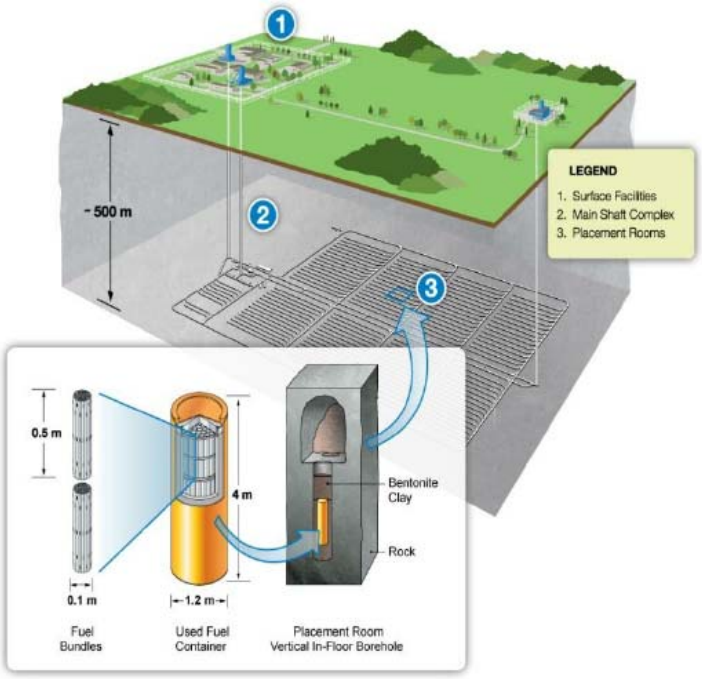

Figure 1. 1 Scheme of the DGR facilities and the general scheme of the multi barrier system expected to be used in the DGR to seal the SNF.

The first barrier is the SNF itself. It is composed of a UO_2 matrix that contains most of the inventory of the actinides and fission products from the irradiation process dissolved in it. When ground water gets in contact with the spent fuel, the UO_2 will partially control the release of the radionuclides (RN) to the ground water.

The second cladding is a one meter long metallic tube that encloses a stack of ceramic pellets of nuclear fuel (UO_2 in the Spanish case) to form a fuel pin. It is made of a zirconium alloy known as Zircaloy and has a very low corrosion rate (Poinssot et al., 2004). During the irradiation process, some neutrons are captured by metallic atoms of the cladding forming the activation products.

The third barrier consists on a metallic capsule where the SNF is introduced. Its main objective is to contain and isolate the SNF. This barrier is expected to improve the handling, to avoid physical damage to the nuclear waste and to improve the heat transfer, decreasing the temperature of the SNF. Under

long term conditions the metallic container can be corroded by water under anoxic conditions. This process will generate reducing species, such as $H_2(g)$ and solid phases such as iron hydroxides and iron oxides that are likely to precipitate (Cui et al., 2011).

The metallic capsule containing the SNF will be surrounded by a buffer clay barrier (most likely bentonite (Astudillo, 2001)) to delay the contact between water and the SNF. This material is considered to be an appropriate barrier because it has the characteristic of increasing its volume in contact with water sealing any possible crack or pore. This property will help to increase the time that water needs to pass through all the barriers before getting in contact with the SNF. The clay will also provide the groundwater with some properties that might have an effect on the SNF alteration processes, depending on the composition of the clay barrier. In addition, the clay barrier itself might adsorb part of the RN dissolved in the ground water (Cachoir et al., 2003; Forsyth et al., 1988; Mennecart et al., 2007; Molera and Eriksen, 2002).

The emplacement and the minerals of the geological location will be the final barrier of the DGR. The geological formation will modify the groundwater composition and control the water flow. Therefore, it must have specific characteristics regarding its mechanical stability, thermal conductivity, water permeability, homogeneity and enough thickness in order to protect the DGR.

Alteration of the barriers of the DGR

If all the barriers have been chosen correctly, it is expected that ground water will get in contact with the SNF after thousands of years after the DGR closure (Astudillo, 2001). The ground water composition will change after the interaction with the different barriers present in the DGR before getting in contact with the SNF.

Three main types of geological formation are identified as a function of their composition to host the repository: granitic, salt or clay bedrocks (Carbol et al., 2005). As an example of ground water composition, the granitic bedrock case is considered for discussion.

Since the bedrock will be in contact with the clay barrier, some studies have determined the ground water composition resulting from the combination of the geological formation and the clay barrier. Fernández (2005) determined the composition of the water obtained from the water saturation in contact with granitic bedrock and the bentonite barrier, which is shown in Table 1. 1.

Table 1. 1 Bentonitic granitic ground water composition

Species	Cl^-	SO_4^{2-}	HCO_3^-	Na^+	K^+	Ca^{2+}	Mg^{2+}	pH
Concentration ($mmol \cdot dm^{-3}$)	93.9 ± 9.4	45.2 ± 4.5	0.9 ± 0.1	117.9 ± 11.8	1.1 ± 0.1	15.4 ± 1.5	17.3 ± 1.7	7.6 ± 0.2

The metallic canister could be corroded in contact with water under the anoxic conditions which are expected to occur in the DGR. The stainless steel canister might be corroded to produce hydrogen and iron oxides through the following reactions (Shoesmith, 2008):

$$3Fe(s) + 4H_2O \leftrightarrow Fe_3O_4(s) + 4H_2(g)$$
$$Fe(s) + 2H_2O \leftrightarrow Fe^{2+} + H_2(g) + 2OH^-$$

Thus, reducing species Fe(II) and H_2 are expected to be produced from the metallic canister alteration being the partial pressure of H_2 approximately 10 MPa due to the slow permeability of the clay barrier after weathering (Grambow, 2010).

Some of the products obtained from the corrosion of the metallic canister might be dissolved in the aqueous phase which could provide the ground water with reducing properties. These reducing reagents might influence the alteration of the SNF in contact with ground water. For instance, the presence of Fe^{2+}(aq) was determined to inhibit the corrosion of the SNF and the radionuclide release (Amme et al., 2012, 2005; Loida et al., 1996; Shoesmith, 2008; Wu et al., 2014). The presence of dissolved hydrogen in the SNF near field also proved to decrease the dissolution of the SNF matrix (Broczkowski et al., 2007; Carbol et al., 2009; Shoesmith, 2008) which might reduce the RN release to the ground water.

Spent Nuclear Fuel (SNF)

Once the fuel has been irradiated in the NPP, it contains approximately 5% w/w of fission products, activation products and minor actinides (Astudillo, 2001) and the remaining 95% w/w is UO_2. It is obtained from the fission of the heavy atoms in the NPP. Under irradiation, the atomic nucleus is able to capture neutrons and generate new species.

Fission products are the elements produced by the fission process of heavy atoms from the fuel, such as ^{235}U. The products obtained from the radioactive decay of these elements are also considered fission products (Hedin, 1997).

The activation products are mostly obtained from the neutron activation of metallic atoms present in the cladding, the stainless steel and other structural materials. Most of them are short lived isotopes and they are β and ϒ emitters (Hedin, 1997).

The transuranic actinides are produced by the neutron capture of ^{238}U and their decay products. They are elements with atomic number higher than 90. Np, Am and Cm are also called minor actinides.

Evolution of the SNF

The SNF physical properties are different from the ones prior to the irradiation due to high pressure and temperatures in the nuclear reactor and the irradiation process itself. This process causes the formation of cracks and pores which increase the pellet volume.

After the fuel discharge from the nuclear reactor, the radiation dose will be 10^6 GBq/MT_{fuel} or higher (Bruno and Ewing, 2006). Both β and ϒ radiation will govern the radiation emitted from the SNF during the firsts 100 years after the discharge of the reactor. Due to the radioactive decay, the SNF evolves with time in composition and radiotoxicity (Astudillo, 2001; Bruno and Ewing, 2006; Ewing, 2015; Hedin, 1997; Shoesmith, 2000). As the short lived isotopes decay, the radioactivity of the waste also decreases as it can be observed in Figure 1. 2. Afterwards, the radiation dose will be provided by the α-radiation emitted from the fuel by isotopes of Pu, Am, Np and U mainly. Finally, the radiation emitted from the fuel will reach the same value as natural uranium minerals millions of years after the discharge (Astudillo, 2001).

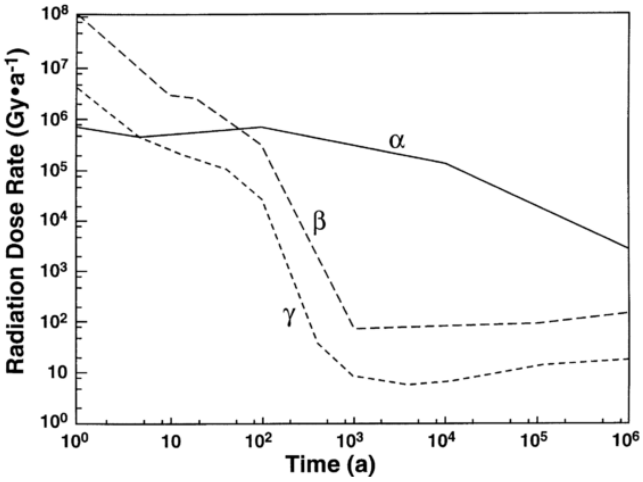

Figure 1. 2 Evolution of the α, β and ϒ dose rates in the water layer in contact with Canadian SNF with high burn – up from Shoesmith (2000).

Only the most stable isotopes (such as ^{99}Tc (210,000 years), ^{79}Se (1.1 million years), ^{135}Cs (2.3 million years) or ^{129}I (16 million years)) will remain in the SNF after long periods of time. Each long-lived radionuclide has its relative importance for the performance assessment depending on their mobility under the DGR conditions. For instance, those elements with high solubility and high mobility are likely to be released rapidly when the SNF gets in contact with groundwater.

At the time when the ground water will get in contact with the SNF which is thousands of years after the DGR closure depending on the life time of the barriers (Astudillo, 2001), the radiation emitted is expected to be mainly due to the α-radiation, as it can be observed in Figure 1. 2.

Characteristics of the SNF

Due to the fission and the radioactive decay, the SNF contains most of the elements in the periodic table forming different compounds and/or being different physical states. As it can be observed in Figure 1. 3, some elements can be segregated as metallic particles (alloys) such as Mo, Tc, Ru, Rh, Pd, Ag, Cd, In, Sn, Sb and Te. There are other elements that are also segregated forming oxides precipitates like Rb, Cs, Ba, Zr, Nd, Mo and Te. Most of the volatile and/or mobile elements can be found in bubbles, pores, cracks and in the gap between the cladding and the SNF pellet such as Kr, Xe, Br, I and Cs. Finally, some elements such as actinides and lanthanides are completely dissolved in the UO_2 matrix (Kleykamp, 1985).

Distribution of the radionuclides

The RN distribution in the SNF on the pellet radial axis depends on the irradiation history of the fuel, the type of fuel, the linear power density (LPD), the fuel burn-up (Grambow, 2000) and thermal gradient (Rondinella and Wiss, 2010).

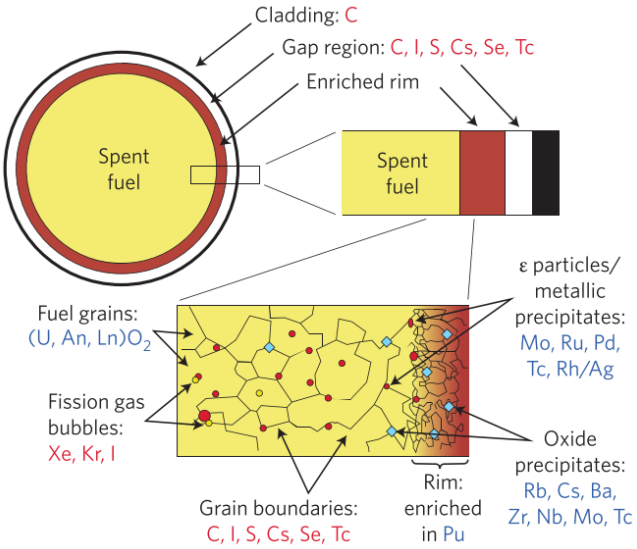

Figure 1. 3 Scheme of the SNF composition and the location of the different RNs and the parts of the fuel (Bruno and Ewing, 2006; Ewing, 2015)

The SNF pellet can be divided into three different parts that are identified by their location and the RN contained in them: the gap, the rim and the core of the pellet. They can be observed in Figure 1. 3.

Gap

The gap region is located between the cladding and the fuel pellet. This region is where the fission gas (FG) is accumulated: between the core of the nuclear fuel pellet and the periphery. As a result, the gap region is rich in FG and other volatile elements like ^{129}I, ^{137}Cs, ^{135}Cs, ^{36}Cl, ^{79}Se and possibly ^{126}Sn. It also might contain non volatile and partially segregated RN like ^{14}C (Kleykamp, 1985; Poinssot et al., 2005).

Rim and High Burn-up Structure

The rim of the SNF is located in the periphery of the pellet, close to the gap region and the cladding.

This region presents higher concentration of Pu than in the central part of the fuel pellet. It focuses in SNF with burn-ups higher than 40 MWd/kgU (Matzke et al., 1989; Rondinella and Wiss, 2010; Walker et al., 2006) and at irradiation temperatures 1100 ± 100 ^{0}C approximately (Sonoda et al., 2002). This fact is caused by the epithermal neutron absorption of the ^{238}U (Sonoda et al., 2002). The higher Pu

concentration at the radial outer edge of the pellet leads to the increase of the local burn – up in this region which could be twice or three times the average BU of the fuel rod.

As a consequence, the porosity increases and grain subdivision occurs in this region: this results in the formation of the high burn – up structure (HBS) (Matzke et al., 1989; Rondinella and Wiss, 2010; Serrano-Purroy et al., 2012). It was observed that the width of the HBS increased with the increase of the average BU. The pores in the rim are rich in FG and volatile elements like ^{129}I, ^{137}Cs, ^{135}Cs, ^{36}Cl, ^{79}Se. At the same time, the grains in the rim are rich in actinides and fission products due to the higher local BU (Kleykamp, 1985; Poinssot et al., 2005).

Core

The core of the SNF is the center part of the pellet. Most of the RNs inventory retained in the fuel is dissolved in the UO_2 matrix and, as a consequence, the matrix will govern their release to the environment.

The RN that are expected to be fully dissolved in the matrix are mainly lanthanides (La, Ce, Nd, Gd, etc.) and actinides (Ac, Th, Np, Pu, Am, Cm, etc.) due to their similarities with uranium and their solubility in the UO_2 (Kleykamp, 1985).

Spent Fuel Analogues

In order to develop a model for the SNF assessment under relevant conditions for the DGR, studies have been performed using different types of analogues of SNF under repository conditions. Since the ground water is expected to get in contact with the SNF after thousands of years, in order to properly study the system of the SNF under DGR conditions, the fuel samples should have similar characteristics to a hundreds or thousands of years old nuclear waste. Since nowadays it is not possible to work with SNF old enough, analogues of the SNF are being used. These studies allowed to characterize different processes involved in SNF alteration under relevant conditions for the CTDS and DGR.

Some studies (Fors et al., 2009; Johnson et al., 2012; Roth et al., 2013; Serrano-Purroy et al., 2012) worked with fresh SNF samples which have slightly different physical and chemical characteristics due to the radionuclide inventory location and the α, β and/or γ decay of the RNs (Grambow, 2010).

There is another type of analogues known as SIMFUEL that consist on doped UO_2. These samples have stable isotopes in their structure with similar properties to the RN in the SNF. The dopants used and their concentrations depend on the SNF studied.

Due to the fact that approximately 95% of the SNF is UO_2, some authors worked with unirradiated UO_2 (Bae et al., 1994; Martínez-Torrents et al., 2013; Pierce et al., 2005; Rey et al., 2008; Taylor et al., 1992). These samples have the advantage that they are handled easily and the results obtained with these samples provide information about the SNF matrix behavior.

There are UO_2 samples doped with radiation – emitter isotopes (mainly alpha – emitters) such as Pu (Jégou et al., 2005b; Mennecart et al., 2014; Walker et al., 2006). There are other studies (Corbel et al., 2001; Traboulsi et al., 2015) where alpha radiation was provided by an external radiation source. These samples allow to study the effect of the radiation and the alteration of UO_2 depending on the dose rate emitted.

Many other studies, instead of using radiation emitters, have doped UO_2 pellets with different elements known to be present in the SNF. For example, UO_2 can be doped with noble nanosized metallic particles (such as palladium, platinum etc.) that are known for having a catalytic effect and for enhancing the catalytic activity under dry conditions (Campelo et al., 2009). According to Cui et al. (2012) who studied the metallic alloys in the SNF and characterized them, the size of these particles is in submicro and nanometric scale which leads to particles with very specific properties.

SNF alteration processes

When groundwater gets in contact with the SNF, first there will be a fast release of volatile (mainly fission gases (FG) in the gap) and soluble RNs such as Xe, Kr, I, Cs and Cl. These RNs will be present in large inventories at the gap. These RN will be available to water contact and so, they will be rapidly and easily leached. The fraction of the inventory of these RNs that are released to water and provide a high peak of radiation to groundwater is called Instant Release Fraction (IRF). In addition, any previously oxidized layers will be easily dissolved due to the increase of solubility of the UO_2 matrix when U(IV) is oxidized to U(VI).

Other processes might occur afterwards which could govern the leaching of the SNF. Some of these processes are summarized in Figure 1. 4.

The presence of the oxidizing radiolitic products of the alpha-radiolysis of water and other oxidant reagents present in the ground water are expected to modify the redox conditions in the near field of the SNF causing the uranium oxidation at the contact surface with water (Shoesmith, 2000). The UO_2 matrix will be leached at lower rate than the oxidized layers due to its low solubility (Segall et al., 1988).

This process will govern the release of the RN to groundwater at long contact times (Bruno and Ewing, 2006). Lastly, segregated oxides and metallic alloys with lower solubility than the UO_2 matrix will be leached.

Under DGR conditions and during the SNF leaching, saturation conditions might be reached and the formation of solid phases containing RN might happen. Their composition depends on the groundwater and the chemical reactions in the SNF near field. These solid phases would precipitate at the same time that the RN are being leached, hence these solids might control the release of RN to groundwater.

To summarize, the alteration of the SNF by ground water is most simply described as six sequential processes as reported by Ewing (2015).

1. The volatile elements and FG at the free surface will be released in the first instant.
2. Once the water gets in contact with the SNF surface, the IRF and the oxidized layers will be leached to the ground water.
3. The radiolysis of water by the radiation emitted by the SNF will produce both reducing and oxidizing agents.

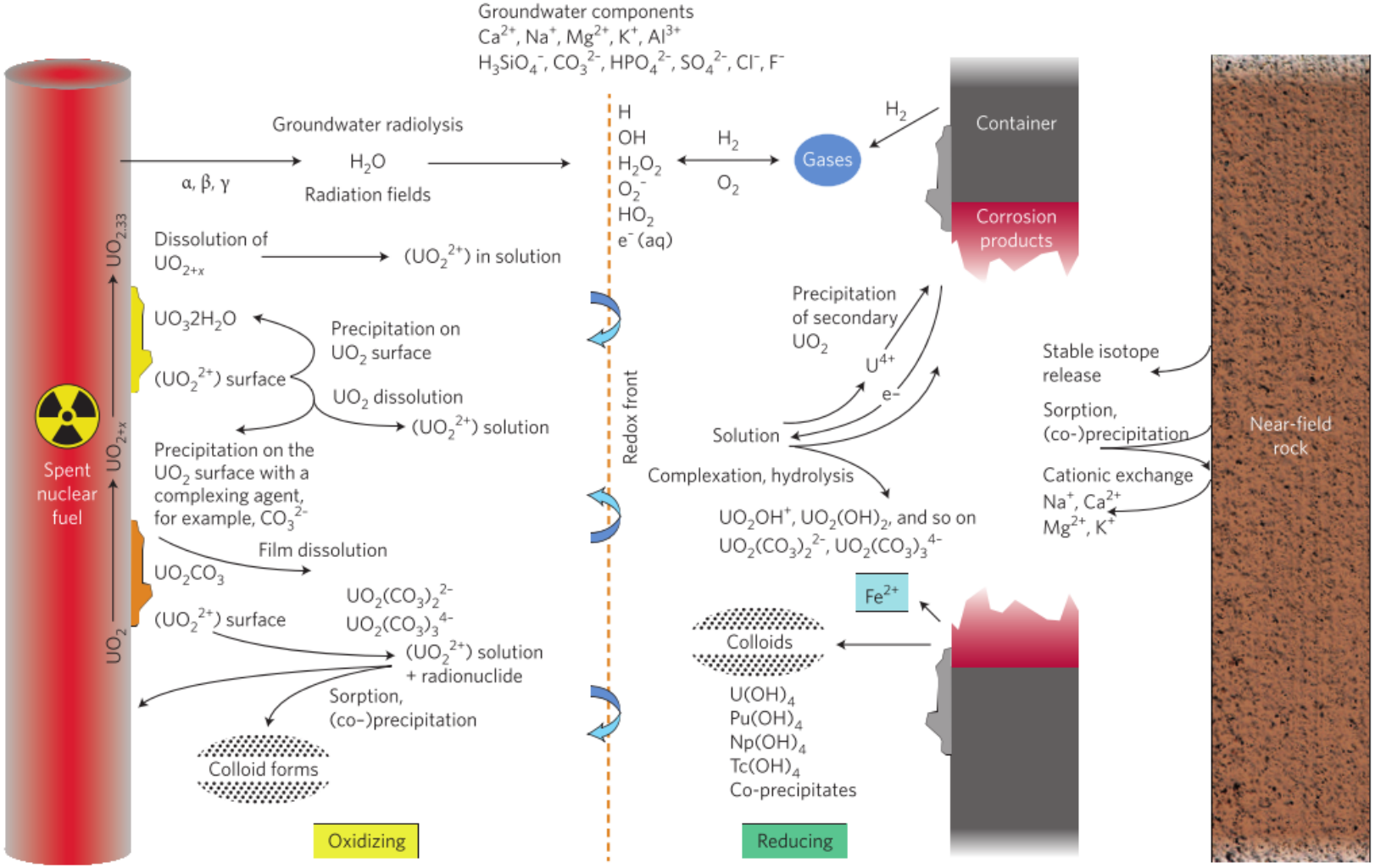

Figure 1. 4 Scheme of the chemical processes that can be involved in the long-term alteration of the SNF and long term behavior of the DGR provided by Ewing (2015)

4. The oxidizing products will oxidize the outer UO_2 and hence, the surface will be rich in U(VI). However, reducing species such as H_2 and Fe^{2+}(aq) from the corrosion of the canister at anoxic conditions could inhibit the oxidation process of UO_2.
5. The highly soluble U(VI) outer layer will be dissolved in the ground water. This process can be enhanced by the presence of complex ligands in the water such as carbonates.
6. The dissolution of the SNF continues and the concentration of RN increases until the saturation is reached and solid phases precipitate. They might contain uranyl in their structure, forming the uranyl secondary phases.

Alpha-radiolysis of water

The radiation expected to be emitted from the SNF after hundreds or thousands of years after the discharge is the α – radiation from the long – lived isotopes. This type of radiation breaks the water molecule to produce molecular species (H_2, H_2O_2, O_2) and radical species ($^{\cdot}OH$, $O_2^{\cdot-}$, $HO_2^{\cdot}$, e^-_{aq}, $H^{\cdot}$) (see reaction (1.1)). A summary of the reactions involved in the radiolysis of neutral water was provided by Pastina et al. (1999).

$$H_2O + \alpha_{radiation} \rightarrow H_2;\ O_2; H_2O_2; OH;\ H;\ e^-_{aq}; HO_2;\ H_3O^+ \quad (1.1)$$

From all the species produced during the radiolysis of the water molecule, molecular hydrogen, oxygen and hydrogen peroxide are the most stable products.

Oxidative dissolution

Due to the increase of the solubility of U(VI) phases, the oxidation of the UO_2 is one of the main mechanisms for the matrix dissolution. Roth and Jonsson (2008) described the oxidative dissolution mechanism by using the reactions in Eq. (1.2) and Eq. (1.3) where the second step can be enhanced by the presence of complexing agents such as carbonate in the dissolution (de Pablo et al., 1999; Giménez et al., 2005).

$$UO_2 + OX \rightarrow UO_2^{2+} + RED \quad (1.2)$$

$$UO_2^{2+}(s) \rightarrow UO_2^{2+}(aq) \quad (1.3)$$

The reaction in Eq. (1.2) has been studied by using either H_2O_2 as a product of the water radiolysis or by using O_2 or air at different pH values.

Effect of the oxygen

Under accident conditions, oxygen could get in contact with the SNF during its dry storage in the CTDS due to the cooling system of the SNF storage gallery (natural air convenction). Also, molecular oxygen might be dissolved in water due to the water radiolysis produced from the water radiolysis at concentrations approximately 10^{-7} mol · dm^{-3} (Cera et al., 2000; Quiñones et al., 2000).

The effect of oxygen on UO_2 under dry conditions and moist environment, corresponding to the CTDS conditions and repository conditions respectively, will be discussed in Chapter 3 of this manuscript.

Some studies regarding the effect of the oxygen partial pressure (P_{O2}) on the oxidative dissolution of SNF analogues have been performed under aqueous conditions (Broczkowski et al., 2005; Casas et al., 1994b; de Pablo et al., 2004; Gray and Wilson, 1995; Shoesmith, 2007; Shoesmith et al., 1989; Torrero et al., 1997). It was observed an increase of the dissolution rate with the increase of the P_{O2} (Torrero et al., 1997) and the kinetic constant was determined to be 0.0013 $M^{-1}{\cdot}s^{-1}$ for the adsorption of oxygen on the surface active sites (Merino et al., 2005). It is accepted that the oxidation step is caused by electron transfer with the oxygen molecule on the UO_2 surface (Roth and Jonsson, 2008) following the reaction mechanism in reactions (1.4) and (1.5). These reactions were determined to be a function of the P_{O2}.

$$> UO_2 + O_2 \leftrightarrow > UO_2 - O_2 \quad (1.4)$$

$$> UO_2 - O_2 + > UO_2 \leftrightarrow 2 > UO_3 \quad (1.5)$$

Where '*>UO_2*' are the active surface sites, '*>$UO_2 - O_2$*' are the occupied surface sites and '*>UO_3*' are the fully oxidized sites.

It was reported in Clarens (2004) that at low values of oxygen partial pressures, the limiting step might be the adsorption of the oxygen molecule to the active sites (reaction (1.4)) and the dissolution rate is proportional to the P_{O2}. At high values of oxygen partial pressures, the limiting step is likely to be the oxidation reaction (reaction (1.5)) since all the active sites are occupied by oxygen molecules. Therefore, the dissolution rate does not depend on the P_{O2} (Shoesmith, 2000).

Effect of hydrogen peroxide

As it is mentioned previously, hydrogen peroxide is one of the products of the alpha – radiolysis and the most important molecular oxidant specie in the SNF near field (Ekeroth et al., 2006). Regarding the UO_2 matrix, oxidizing products such as H_2O_2 prevail over the reducing species and the matrix is oxidized (Eriksen et al., 2012; Jégou et al., 2005b; Mennecart et al., 2014; Sattonnay et al., 2001; Stroes-Gascoyne

et al., 2005; Wren et al., 2005). This fact might lead to the oxidation and later dissolution of the UO_2 as $UO_2^{2+}{}_{aq}$ at low pH values (Torrero et al., 1997) which will cause the release of all the RN contained in the SNF matrix. On the other hand, uranyl peroxide phases such as studtite will precipitate under alkaline conditions (Clarens et al., 2005, 2004; Kubatko et al., 2003; Meca et al., 2011). Therefore, the interaction between the UO_2 matrix and H_2O_2 has been widely studied (Clarens et al., 2004; Corbel et al., 2006; Eary and Cathles, 1983; Goldik et al., 2006; Martínez-Torrents et al., 2013; Sunder et al., 2004) and reported (Shoesmith, 2000). In this last report, the different alteration processes of UO_2 were detailed as a function of the hydrogen peroxide concentration at pH = 9.5.

- At concentrations below 10^{-4} mol·dm^{-3}, the corrosion potential of the system is proportional to the hydrogen peroxide concentration.
- At concentrations between 10^{-4} to 10^{-2} mol·dm^{-3}, the surface of the UO_2 is buffered by the hydrogen peroxide decomposition into oxygen and water
- At concentrations higher than 10^{-2} mol·dm^{-3}, U(VI) phases precipitate on the surface and block the further oxidation of uranium as well as the hydrogen peroxide decomposition.

Corbel et al. (2006) provided with information about the effect of the hydrogen peroxide as a radiolitic product. The authors compared the behavior of the system using an alpha – radiation source and the system using hydrogen peroxide as a reactant added to the solution. They observed the precipitation of studtite ($UO_2(O)_2{\cdot}4H_2O$) in both cases, but the evolution of the system was different depending on the H_2O_2 source. The uranium release obtained by using the radiation source increased until the maximum value reached was $2.75{\cdot}10^4$ μgU/L after 4 hours of experimental time. When H_2O_2 was added to the solution, the uranium release was much lower with a maximum value of 170 μgU/L after 100 hours of experimental time. The authors explained this observation by means of pH because they observed a decrease of the pH in the vicinity of the UO_2 surface when the radiation source was used.

Effect of pH

Acidic conditions

The concentration of H^+ and OH^- also influences the matrix dissolution. In the case of acidic conditions, de Pablo et al. (2004) proposed the following mechanism taking into account the formation of protonated surface complexes on the oxidized layers:

$$> UO_3 + H^+ \leftrightarrow > UO_3 - H^+ \rightarrow UO_2(OH)^+(aq) \quad (1.6)$$

Recent studies confirmed that under acidic conditions, the UO_2 is oxidized by electron transfer mechanism (Gaulard-Balandret et al., 2012). The uranium dissolution occurs via an intermediate species with U(V) on the surface of UO_2. The proposed mechanisms under non-complexing media are:

$$UO_{2+x} + H_2O \leftrightarrow (UO_{2+x}(OH))_{ads} + H^+ + e^- \quad (1.7)$$

$$(UO_{2+x}(OH))_{ads} + H^+ \leftrightarrow UO_2^{2+}(aq) + H_2O + e^- \quad (1.8)$$

Where 'UO_{2+x}' is an oxide mixture of U(IV) and U(V) surface layer and '$(UO_{2+x}(OH))_{ads}$' is an intermediate surface species. Therefore, acidic condition will lead to the extraction of UO_2^{2+} from the surface causing the increase of uranium concentration in the dissolution and, at the same time, a barely oxidized sample surface (Santos et al., 2006a; Torrero et al., 1997).

Torrero et al. (1997) observed that the UO_2 sample surface obtained after performing experiments under acidic conditions was mainly U(IV) due to the leaching of the oxidized uranium as UO_2^{2+}(aq).

Alkaline conditions

Under basic conditions (pH values higher than 6.7), the solid surface obtained by Torrero et al. (1997) presented an oxidized layer ($UO_{2.25}$). The proposed mechanisms for the oxidation of UO_2 under neutral and alkaline conditions are based on electron transfer reactions involving an intermediate oxidation step prior to the dissolution (de Pablo et al., 2004):

$$> UO_3 + H_2O \leftrightarrow > UO_3 - H_2O \rightarrow UO_2(OH)_2(aq) \quad (1.9)$$

Santos et al. (2006a) performed electrochemical studies on a SIMFUEL electrode in order to determine the effect of the pH on the corrosion of UO_2. They suggested the following dissolution mechanism under alkaline conditions:

$$UO_2 + xH_2O \leftrightarrow U^{IV}_{1-2x}U^{V}_{2x}O_{2+x} + 2xH^+ + 2xe^- \quad (1.10)$$

$$U^{IV}_{1-2x}U^{V}_{2x}O_{2+x} + 3OH^- \leftrightarrow U^{VI}O_{2+x}(OH)_3^-(aq) + 2e^- \quad (1.11)$$

Additionally, the uranyl cation is easily complexed by hydroxyl ions in the solution (Casas et al., 1998) which enhances the uranyl release (Pierce et al., 2005) and stabilizes the cation in the dissolution. The general reaction proposed by Santos et al. (2006a) is:

$$UO_2^{2+} + xOH^- \leftrightarrow UO_2(OH)_x^{(2-x)+} \quad (1.12)$$

Despite the alkaline conditions, some works have reported the possibility of local acidification at high oxidizing conditions (Santos et al., 2006b, 2004). This phenomenon was observed on the grain boundaries (GBs), missing grains sites and surface defects of the fuel surface. There is a first oxidation step where the UO_2 is oxidized forming a surface layer of UO_{2+x} as protons are produced (Figure 1. 5 (A)).

An oxidized outer layer (UO_{2+x} – $UO_2OH(ads)$) grows on the UO_2 surface as the oxygen is incorporated in the UO_2 (Figure 1. 5 (B)). This layer is further oxidized to UO_2^{2+} and hence, released from the solid phase. Under low solubility conditions such as the ones used by Santos et al. (2004), a U(VI) phase precipitates on the sample surface (Figure 1. 5 (C)). The authors suggested the formation of $UO_3 \cdot yH_2O$ based on the XPS results obtained and the experimental conditions used. At high oxidizing conditions, the oxidation of uranium to uranyl ion occurs in the pores of the solid phase (Figure 1. 5 (D)) which creates local acidity due to the proton production from the hydrolysis. Then, the local acidity causes the dissolution of the UO_{2+x} layer and the release of $UO_2^{2+}(aq)$ to the dissolution (Figure 1. 5 (E)).

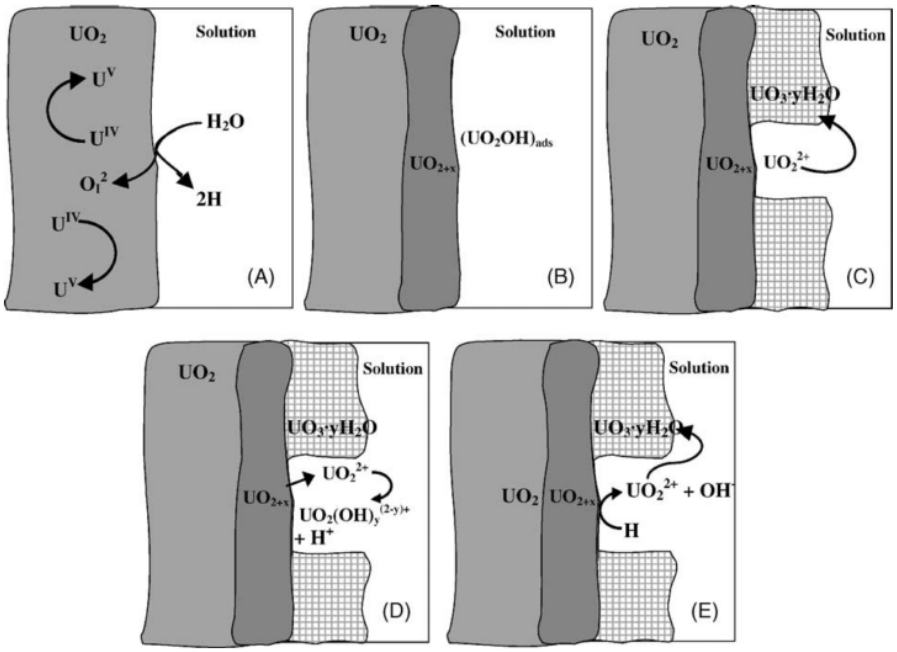

Figure 1. 5 Scheme of the different stages of local acidity development under oxidizing pe values from Santos et al. (2004)**.**

It was determined that the extension of this phenomenon depends on the pe of the dissolution and hence, more oxidizing conditions will lead to the formation of local acidity on the surface defects of the sample surface.

Effect of ligand agents

Carbonates

Carbonate anion is expected to be present in granitic ground water (see Table 1. 1) and hence, it is necessary to know the influence of carbonate and hydrogen carbonate in contact with the UO_2. It is known that carbonate is likely to form complexes and enhance the dissolution of certain species, but not the oxidation. Therefore, the effect of carbonate is usually studied together with another oxidizing reactant.

In the study performed by de Pablo et al. (1999), the authors observed an influence of the hydrogen carbonate concentration on the dissolution of the UO_2 and proposed the following mechanisms. As it can be observed, the first step is expected to be caused by other oxidizing species, such as oxygen or hydrogen peroxide while the presence of HCO_3^- is expected to enhance the dissolution.

$$> UO_2 + \frac{1}{2} O_2 \leftrightarrow > UO_3 \quad (1.13)$$

$$> UO_3 + HCO_3^- \rightarrow > UO_3 - HCO_3^- \quad (1.14)$$

$$> UO_3 - HCO_3^- \rightarrow "U(VI)(aq)" \quad (1.15)$$

Giménez et al. (2005) studied the two parameters of the system (the oxygen and the carbonate) on the oxidative dissolution of the UO_2. The results obtained agreed with the proposed mechanisms and observed that at bicarbonate concentrations lower than 10^{-2} mol·dm^{-3}, the reaction (1.15) cannot be assumed to be fast reaction. The results also suggested that there was a surface layer oxidized but not released to the solution.

The effect of the carbonate concentration was reviewed in Shoesmith (2000) who proposed different UO_2 alteration mechanisms as a function of the ligand concentration:

- Under alkaline conditions and without carbonate in the dissolution, the formation of uranyl secondary phases will suppress the oxidative dissolution process.
- At carbonate concentrations lower than 10^{-3} mol·dm^{-3}, the secondary phase precipitation is avoided due to the formation of uranyl carbonate complexes in the aqueous phase.
- At carbonate concentrations between 10^{-3} and 0.1 mol·dm^{-3}, the formation of an intermediate specie on the surface influences the kinetics of the process and hence, the dissolution rate is function of the carbonate concentration.

- At carbonate concentrations higher than 0.1 mol·dm^{-3}, the precipitation of uranyl solid phases such as UO_2CO_3 might decrease the UO_2 dissolution.

Secondary phase precipitation

The water saturation in the SNF near field could lead to the precipitation of different uranyl secondary phases which may introduce variations to the RN release mechanisms. Therefore, it is necessary to determine these solid phases that are likely to precipitate, their characteristics and their retention properties (these last properties will be discussed in Chapter 5 of this thesis).

In order to determine the solid phases that are most likely to precipitate, Wronkiewicz et al. (1996, 1992) performed precipitation studies using silica-bicarbonate simulated ground water in contact with UO_2 under unsaturated conditions. The phases identified are shown in Table 1. 2. However, the corrosion of the metallic canister causes the precipitation of Fe – phases which also retain RN (Cui et al., 2009; Rovira et al., 2008, 2004)

Table 1. 2 Secondary phase containing uranyl ion identified by Wronkiewicz et al. (1992)

Name	Formula
Becquerelite	$CaU_6O_{19}\cdot 10H_2O$
Boltwoodite	$K(H_3O)UO_2(SiO_4)\cdot nH_2O$
Compreignacite	$K_2U_6O_{19}\cdot 11H_2O$
Schoepite	$UO_3\cdot 2H_2O$
Dehydrated schoepite	$UO_3\cdot 0.8H_2O$
Sklodowskite	$Mg(UO_2)_2(SiO_3OH)_2\cdot 5H_2O$
Soddyite	$U_5Si_2O_{19}\cdot 6H_2O$
Uranophane	$Ca(UO_2)_2(SiO_3OH)_2\cdot 5H_2O$

In addition, the products of the alpha radiolysis have an effect on the secondary phase formation. Especially the presence of H_2O_2 causes the precipitation of uranyl peroxide phases (such as studtite ($UO_4\cdot 4H_2O$)) (Hanson et al., 2005; McNamara et al., 2002) that have been observed by using UO_2 doped with radiation emitter dopants (Corbel et al., 2006; Jégou et al., 2005a).

In order to determine the influence of the secondary phases under repository conditions, kinetic and thermodynamic data of these solid phases have been determined. This information allows to establish the long-term stability of each solid phase.

Thermodynamic and Kinetic data

Due to the fact that this manuscript presents data regarding soddyite and uranophane, only these two solid phases are considered for discussion in this section even though there are other uranyl secondary phases that are also relevant under the DGR conditions as commented above.

Soddyite

This solid phase is likely to precipitate in the presence of silicate in the solution (Finch and Murakami, 1999; Finn et al., 1997; Wilson, 1990). Due to the uranium speciation at pH higher than 6 and the products of the uranyl hydrolysis at pH lower than 4, it has been complicated to relate the activity of UO_2^{2+} to the measured U concentration (Giammar and Hering, 2002). As a consequence, several solubility constants have been reported for soddyite (reaction (1.16)).

Table 1. 3 Solubility constants corrected by Giammar and Hering (2002) and dissolution rates of soddyite

Constant	Value	Experimental Conditions	Citation
Solubility constant ($\log K^{o}_{s0}$)	5.35*	pH = 3 Anoxic conditions (Ar) Batch experiment	(Nguyen et al., 1992)
	5.39*	pH = 3 $[NaClO_4]$ = 0.1 mol·dm^{-3} Anoxic conditions (N_2) Batch experiment	(Moll et al., 1996)
	5.50*	pH = 3 Oxic conditions (air) Batch experiment	
	2.76 – 6.99*	pH from 8.54 to 9.11 $[HCO_3^-]$ from 1 to 20 mmol·dm^{-3} $[NaClO_4]$ = 7 mmol·dm^{-3} Oxic conditions (air) Batch experiment	(Pérez et al., 1997)
	5.98	Calculated	(Liu et al., 2004)
	6.43 (+0.20/-0.37)	Synthetic sample pH lower than 3.9 Initial concentration of U and Si Static regime	(Gorman-Lewis et al., 2007)
Dissolution rate (r)	$(1.9 \pm 0.3) \cdot 10^{-10}$ mol·m^{-2}·s^{-1}	pH = 6 $[NaNO_3]$ = 0.01 mol·dm^{-3} Flow-through experiments	(Giammar and Hering, 2002)
	$1.39 \cdot 10^{-10}$ mol·m^{-2}·s^{-1}	pH from 8.54 to 9.11 $[HCO_3^-]$ = 1 mmol·dm^{-3} $[NaClO_4]$ = 7 mmol·dm^{-3} Oxic conditions (air) Batch experiment	(Pérez et al., 1997)

**Corrected value from Giammar and Hering (2002) by using the database provided by Grenthe et al. (1992)*

$$(UO_2)_2SiO_4 \cdot 2H_2O(cr) + 4H^+ \leftrightarrow 2UO_2^{2+} + SiO_2(aq) + 4H_2O(l) \quad (1.16)$$

Giammar and Hering (2002) recalculated some of those constants in order to adjust the results and suppress some experimental artifacts related to the ionic strength and speciation. Their results are presented in Table 1. 3 together with the original experimental conditions and references.

The standard molar Gibbs free energy of formation for soddyite was experimentally determined by Nguyen et al. (1992) and the value obtained was -3658.0 ± 4.8 kJ·mol^{-1}.

The dissolution rate of soddyite was studied by Pérez et al. (1997) in presence of carbonate using the experimental conditions detailed in Table 1. 3. The results showed higher dissolution rate as the carbonate concentration was increased. In that case, the authors suggested the following dissolution reaction:

$$(UO_2)_2SiO_4 \cdot 2H_2O(cr) + 6HCO_3^- \leftrightarrow 2UO_2(CO_3)_3^{4-} + H_4SiO_4 + 2H^+ + 2H_2O(l) \quad (1.17)$$

Uranophane

This solid phase is expected to precipitate in presence of silicate, as soddyite, but it also requires the presence of Ca^{2+} ions in the solution. This uranyl silicate was observed in previous studies (Wilson, 1988) as possible solid phase in the SNF near field.

Its standard molar Gibbs free energy was determined experimentally also by Nguyen et al. (1992) who provided its value: -6210.6 ± 7.6 kJ·mol^{-1}.

As in the previous case, solubility constant value is complicated to determine due to the complexity of the system and all the possible speciation of the ions in the solution. For this reason, Guillaumont et al. (2003) do not recommend an specific solubility value for the reaction (1.18).

$$\begin{aligned} Ca(H_3O)_2(UO_2)_2(SiO_4)_2 \cdot 3H_2O(cr) + 6H^+ \leftrightarrow \\ \leftrightarrow Ca^{2+} + 2UO_2^{2+}(aq) + 2Si(OH)_4(aq) + 5H_2O(l) \end{aligned} \quad (1.18)$$

Despite the statement of Guillaumont et al., an attempt to deduce the log K^o_s value can be made from the data published by Nguyen et al. (1992) and the value obtained is 9.42 ± 0.48. However, some authors disagree with the experimental methodology used by Nguyen et al. and hence, they performed more experiments that are shown in Table 1. 4.

It can be observed that the dissolution rates values provided by Pérez et al. (2000) are one order of magnitude higher than the one provided by Casas et al. (1994a). This fact might be caused by the higher crystallinity degree of the natural sample compared with the synthetic samples used by Pérez et al.

In addition, the presence of ligand reactants such as bicarbonate anions increases the dissolution rate, as it can be observed by the results obtained by Pérez et al.

Table 1. 4 Solubility constants of uranophane determined under different experimental conditions

Constant	Value	Experimental Conditions	Citation
Solubility constant ($\log K^{o}_{s0}$)	9.42 ± 0.48	pH = 3.5 Anoxic conditions Batch experiment	(Nguyen et al., 1992)
	7.8 ± 0.8	Natural sample Reducing, anoxic and oxidizing conditions Synthetic groundwater $[HCO_3^-] = 3\cdot10^{-3}$ mol·dm^{-3} and double distilled water Batch experiment	(Casas et al., 1994a)
	8.26	Calculated	(Chen et al., 1999)
	11.7 ± 0.6	$[HCO_3^-]$ from 10^{-3} to $2\cdot10^{-2}$ mol·dm^{-3} Dynamic and static regime	(Liu et al., 2004; Pérez et al., 2000)
	10.82 (+0.29/-0.62)	pH between 3.0 and 8.5 $[KNO_3]$ = 50 mmol·dm^{-3} Oxic conditions Batch experiment	(Shvareva et al., 2011)
Dissolution rate (r) (mol·m^{-2}·s^{-1})	$2.35\cdot10^{-12}$	Natural sample Reducing, anoxic and oxidizing conditions Synthetic groundwater $[HCO_3^-] = 3\cdot10^{-3}$ mol·dm^{-3} and double distilled water Batch experiment	(Casas et al., 1994a)
	Log (r) = -8.3(±0.6) + 0.7(±0.3) log $[HCO_3^-]$	$[HCO_3^-]$ from 10^{-3} to $2\cdot10^{-2}$ mol·dm^{-3} Static regime	(Pérez et al., 2000)
	Log (r) = -9.2(±0.4) + 0.7(±0.2) log $[HCO_3^-]$	$[HCO_3^-]$ from 10^{-3} to $2\cdot10^{-2}$ mol·dm^{-3} Batch experiment	

Relevant effects of secondary phase precipitation for the performance assessment

Since the secondary phases mentioned in Table 1. 2 are expected to precipitate in presence of other RN, the solid phases might retain some of these RN which will help to control the release of some radioactive isotopes.

The incorporation of certain ions into the some solid structure has been studied by Burns et al. (1997). The work was focused on the possible incorporation of long-lived actinides like U, Np or Pu into uranyl phases. These RNs were assumed to be fully incorporated in the solid phase, without forming any segregate phase due to their low concentration.

On the other hand, the RN can be bounded to the surface of the solid phase by either physical and / or chemical bonds. Since the last chapter of this manuscript studies the sorption process between two ions and two solid phases, the retention mechanisms and the state of the art regarding retention properties of the uranyl solid phases will be discussed there.

Bibliography

Amme, M., Bors, W., Michel, C., Stettmaier, K., Rasmussen, G., Betti, M., 2005. Effects of Fe(II) and hydrogen peroxide interaction upon dissolving UO_2 under geologic repository conditions. Environ. Sci. Technol. 39, 221–229. doi:10.1021/es040034x

Amme, M., Pehrman, R., Deutsch, R., Roth, O., Jonsson, M., 2012. Combined effects of Fe(II) and oxidizing radiolysis products on UO_2 and PuO_2 dissolution in a system containing solid UO_2 and PuO_2. J. Nucl. Mater. 430, 1–5. doi:10.1016/j.jnucmat.2012.06.036

Astudillo, J., 2001. El almacenamiento geológico profundo de los residuos readioactivos de alta actividad. Principios básicos y tecnología, Online. ed. Grafistaff, Madrid (Spain).

Bae, K.K., Kim, B.G., Lee, Y.W., Yang, M.S., Park, H.S., 1994. Oxidation behavior of unirradiated UO_2 pellets. J. Nucl. Mater. 209, 274–279. doi:10.1016/0022-3115(94)90263-1

Broczkowski, M.E., Noël, J.J., Shoesmith, D.W., 2007. The influence of dissolved hydrogen on the surface composition of doped uranium dioxide under aqueous corrosion conditions. J. Electroanal. Chem. 602, 8–16. doi:10.1016/j.jelechem.2006.11.021

Broczkowski, M.E., Noël, J.J., Shoesmith, D.W., 2005. The inhibiting effects of hydrogen on the corrosion of uranium dioxide under nuclear waste disposal conditions. J. Nucl. Mater. 346, 16–23. doi:10.1016/j.jnucmat.2005.04.070

Bruno, J., Ewing, R.C., 2006. Spent nuclear fuel. Elements 2, 343–349. doi:10.2113/gselements.2.6.343

Burns, P.C., Ewing, R.C., Miller, M.L., 1997. Incorporation mechanisms of actinide elements into the structures of U6+ phases formed during the oxidation of spent nuclear fuel. J. Nucl. Mater. 245, 1–9. doi:10.1016/S0022-3115(97)00006-8

Cachoir, C., Lemmens, K., Van den Berghe, S., Van Iseghem, P., 2003. UO_2 dissolution in Boom Clay conditions. J. Nucl. Mater. 321, 49–59. doi:10.1016/S0022-3115(03)00199-5

Campelo, J.M., Luna, D., Luque, R., Marinas, J.M., Romero, A. a, 2009. Sustainable preparation of supported metal nanoparticles and their applications in catalysis. ChemSusChem 2, 18–45. doi:10.1002/cssc.200800227

Carbol, P., Cobos-Sabate, J., Glatz, J.-P., Ronchi, C.., Rondinella, V., Loida, A., Metz, V., Kienzler, B., Spahiu, K., Grambow, B., Quiñones, J., Martínez-Esparza, A., 2005. TR-05-09 on the dissolution of ^{233}U doped UO_2(s), high burn-up spent fuel and MOX fuel. Stockholm, Sweden.

Carbol, P., Fors, P., Gouder, T., Spahiu, K., 2009. Hydrogen suppresses UO_2 corrosion. Geochim. Cosmochim. Acta 73, 4366–4375.

Casas, I., Bruno, J., Cera, E., Finch, R.J., Ewing, R.C., 1994a. Kinetic and thermodynamic studies of uranium minerals. Assessment of the long-term evolution of spent nuclear fuel. TR 94-16. Stockholm, Sweden.

Casas, I., de Pablo, J., Giménez, J., Torrero, M.E., Bruno, J., Cera, E., Finch, R.J., Ewing, R.C., 1998. The role of pe , pH , and carbonate on the solubility of UO_2 and uraninite under nominally reducing conditions. Geochim. Cosmochim. Acta 62, 2223–2231.

Casas, I., Giménez, J., Marti, V., Torrero, M.E., Pablo, J. de, 1994b. Kinetic Studies of Unirradiated UO_2 Dissolution under Oxidizing Conditions in Batch and Flow Experiments. Radiochim. Acta 66–67, 23–28. doi:10.1524/ract.1994.6667.special-issue.23

Cera, E., Merino, J., Bruno, J., 2000. Liberación de los radionucleidos e isótopos estables contenidos en la matriz del combustible. Modelo conceptual y modelo matemático del comportamiento del residuo, TransEdit. ed. ENDESA, Madrid.

Chen, F., Ewing, R.C., Clark, S.B., 1999. The Gibbs free energies and enthalpies of formation of U6+ phases: An empirical method of prediction. Am. Mineral. 84, 650–664. doi:10.2138/am-1999-0418

Clarens, F., 2004. Efecto de la radiólisis y de los productos radiolíticos en la disolución del UO_2: Aplicación al modelo de alteración de la matriz del combustible nuclear gastado. Ph.D. Dissertation. Universitat Politècnica de Catalunya.

Clarens, F., De Pablo, J., Casas, I., Giménez, J., Rovira, M., Merino, J., Cera, E., Bruno, J., Quiñones, J., Martínez-Esparza, A., 2005. The oxidative dissolution of unirradiated UO_2 by hydrogen peroxide as a function of pH. J. Nucl. Mater. 345, 225–231. doi:10.1016/j.jnucmat.2005.06.002

Clarens, F., De Pablo, J., Díez-Perez, I., Casas, I., Gimenez, J., Rovira, M., 2004. Formation of studtite during the oxidative dissolution of UO_2 by hydrogen peroxide: A SFM study. Environ. Sci. Technol. 38, 6656–6661. doi:10.1021/es0492891

Corbel, C., Sattonnay, G., Guilbert, S., Garrido, F., Barthe, M.-F., Jegou, C., 2006. Addition versus radiolytic production effects of hydrogen peroxide on aqueous corrosion of UO_2. J. Nucl. Mater. 348, 1–17. doi:10.1016/j.jnucmat.2005.05.009

Corbel, C., Sattonnay, G., Lucchini, J.F., Ardois, C., Barthe, M.-F., Huet, F., Dehaudt, P., Hickel, B., Jegou, C., 2001. Increase of the uranium release at an UO_2/H_2O interface under He^{2+} ion beam irradiation. Nucl. Instruments Methods Phys. Res. Sect. B Beam Interact. with Mater. Atoms 179, 225–229. doi:10.1016/S0168-583X(01)00519-5

Cui, D., Low, J., Spahiu, K., 2011. Environmental behaviors of spent nuclear fuel and canister materials. Energy Environ. Sci. 4, 2537. doi:10.1039/c0ee00582g

Cui, D., Ranebo, Y., Lee, J., Rondinella, V., Pan, J., Spahiu, K., 2009. Immobilization of Radionuclides on Iron Canister Material at Simulated Near-field Conditions, in: Materials Research Society Symposium Proceedings. Materials Research Society, Boston, USA, pp. 111–116. doi:10.1557/PROC-1124-Q02-04

Cui, D., Rondinella, V.V., Fortner, J. a., Kropf, a. J., Eriksson, L., Wronkiewicz, D.J., Spahiu, K., 2012. Characterization of alloy particles extracted from spent nuclear fuel. J. Nucl. Mater. 420, 328–333. doi:10.1016/j.jnucmat.2011.10.015

de Pablo, J., Casas, I., Giménez, J., Clarens, F., Duro, L., Bruno, J., 2004. The oxidative dissolution mechanism of uranium dioxide. The effect of pH and oxygen partial pressure, in: Materials Research Society Symposium Proceedings. pp. 83–88. doi:10.1557/PROC-807-83

de Pablo, J., Casas, I., Giménez, J., Molera, M., Rovira, M., Duro, L., Bruno, J., 1999. The oxidative dissolution mechanism of uranium dioxide . I . The effect of temperature in hydrogen carbonate medium. Geochim. Cosmochim. Acta 63, 3097–3103. doi:10.1016/S0016-7037(99)00237-9

Eary, L.E., Cathles, L.M., 1983. A kinetic model of UO_2 dissolution in acid, H_2O_2 solutions that includes uranium peroxide hydrate precipitation. Metall. Trans. B 14, 325–334. doi:10.1007/BF02654350

Ekeroth, E., Roth, O., Jonsson, M., 2006. The relative impact of radiolysis products in radiation induced oxidative dissolution of UO_2. J. Nucl. Mater. 355, 38–46. doi:10.1016/j.jnucmat.2006.04.001

ENRESA, 2014. 7º Plan Nacional De I + D. 2014-2018, First edit. ed. TransEdit, Madrid (Spain).

ENRESA, 2006. Sexto Plan General de Residuos Radiactivos.

Eriksen, T.E., Shoesmith, D.W., Jonsson, M., 2012. Radiation induced dissolution of UO_2 based nuclear fuel – A critical review of predictive modelling approaches. J. Nucl. Mater. 420, 409–423. doi:10.1016/j.jnucmat.2011.10.027

Ewing, R.C., 2015. Long-term storage of spent nuclear fuel. Nat. Mater. 14, 252–257. doi:10.1038/nmat4226

Fernández, A.M., 2005. Preparación de una agua intersticial sintética bentonítica a diferentes salinidades (Preparation of a synthetic bentonitic interstitial water at different salinities). Informe DMA/M214213/05. Madrid (Spain).

Finch, R., Murakami, T., 1999. Systematics and paragenesis of uranium minerals. Rev. Mineral. Geochemistry 38, 91–179.

Finn, P.A., Finch, R., Buck, E., Bates, J., 1997. Corrosion mechanisms of spent fuel under oxidizing conditions, in: Materials Research Society Symposium - Proceedings. MRS. doi:10.1557/PROC-506-123

Fors, P., Carbol, P., Van Winckel, S., Spahiu, K., 2009. Corrosion of high burn-up structured UO_2 fuel in presence of dissolved H_2. J. Nucl. Mater. 394, 1–8. doi:10.1016/j.jnucmat.2009.07.004

Forsyth, R.S., Werme, L.O., Bruno, J., 1988. Preliminary study of spent UO2 fuel corrosion in the presence of bentonite. J. Nucl. Mater. 160, 218–223. doi:10.1016/0022-3115(88)90050-5

Gaulard-Balandret, C., Larabi-Gruet, N., Miserque, F., Radwan, J., Ferry, C., Chaussé, A., 2012. Kinetics of oxidation and dissolution of uranium dioxide in aqueous acid solutions. Electrochim. Acta 83, 471–477. doi:10.1016/j.electacta.2012.04.022

Giammar, D.E., Hering, J.G., 2002. Equilibrium and kinetic aspects of soddyite dissolution and secondary phase precipitation in aqueous suspension. Geochim. Cosmochim. Acta 66, 3235–3245. doi:10.1016/S0016-7037(02)00927-4

Giménez, J., Clarens, F., Casas, I., Rovira, M., De Pablo, J., Bruno, J., 2005. Oxidation and dissolution of UO_2 in bicarbonate media: Implications for the spent nuclear fuel oxidative dissolution mechanism. J. Nucl. Mater. 345, 232–238. doi:10.1016/j.jnucmat.2005.06.003

Goldik, J.S., Noël, J.J., Shoesmith, D.W., 2006. Surface electrochemistry of UO_2 in dilute alkaline hydrogen peroxide solutions. Electrochim. Acta 51, 3278–3286. doi:10.1016/j.electacta.2005.09.019

Gorman-Lewis, D., Mazeina, L., Fein, J.B., Szymanowski, J.E.S., Burns, P.C., Navrotsky, A., 2007. Thermodynamic properties of soddyite from solubility and calorimetry measurements. J. Chem.

Thermodyn. 39, 568–575. doi:10.1016/j.jct.2006.09.005

Grambow, B., 2010. Model Uncertainty for the Mechanism of Dissolution of Spent Fuel in Nuclear Waste Repository. Final MICADO Project report. European Commission. doi:10.2777/25846

Grambow, B., 2000. Opinions on SKB's Safety Assessments SR 97 and SFL 3-5. A Review by SKI Consultants.

Gray, W.J., Wilson, C.N., 1995. Spent fuel dissolution studies FY 1991 to 1994. Richland, Washington, USA.

Grenthe-Chairman, I., Fuger, J., Lemire, R.J., Canada, M., Muller, A.B., Wanner, H., Forest, I., 1992. Chemical Thermodynamics of Uranium, Digital. ed. Nuclear Energy Agency, Paris.

Guillaumont, R., Fanghänel, T., Fuger, J., Grenthe, I., Neck, V., Palmer, D.A., Rand, M.H., 2003. Update on the Chemical Thermodynamics of Uranium, Neptunium, Plutonium, Americium and Technetium, Vol. 5. ed. OECD Nuclear Energy Agency, Data Bank, Issy-les-Moulineaux, France.

Hanson, B.B., Mcnamara, B., Buck, E., Friese, J., Jenson, E., Krupka, K., Arey, B., 2005. Corrosion of commercial spent nuclear fuel. 1. Formation of studtite and metastudtite. Radiochim. Acta 93, 159–168. doi:10.1524/ract.93.3.159.61613

Hedin, A., 1997. Spent nuclear fuel - how dangerous is it?, IAEA Technical Report 97-13. Stockholm, Sweden.

Jégou, C., Muzeau, B., Broudic, V., Peuget, S., Poulesquen, A., Roudil, D., Corbel, C., 2005a. Effect of external gamma irradiation on dissolution of the spent UO_2 fuel matrix. J. Nucl. Mater. 341, 62–82. doi:10.1016/j.jnucmat.2005.01.008

Jégou, C., Muzeau, B., Broudic, V., Poulesquen, A., Roudil, D., Jorion, F., Corbel, C., 2005b. Effect of alpha irradiation on UO_2 surface reactivity in aqueous media. Radiochim. Acta 93, 35–42. doi:10.1524/ract.93.1.35.58294

Johnson, L., Günther-Leopold, I., Kobler Waldis, J., Linder, H.P., Low, J., Cui, D., Ekeroth, E., Spahiu, K., Evins, L.Z., 2012. Rapid aqueous release of fission products from high burn-up LWR fuel: Experimental results and correlations with fission gas release. J. Nucl. Mater. 420, 54–62. doi:10.1016/j.jnucmat.2011.09.007

Kleykamp, H., 1985. The chemical state of the fission products in oxide fuels. J. Nucl. Mater. 131, 221–246. doi:10.1016/0022-3115(85)90460-X

Kubatko, K.A.H., Helean, K.B., Navrotsky, A., Burns, P.C., 2003. Stability of Peroxide-Containing Uranyl Minerals. Science (80-.). 302, 1191–1193. doi:10.1126/science.1090259

Liu, C., Zachara, J.M., Qafoku, O., McKinley, J.P., Heald, S.M., Wang, Z., 2004. Dissolution of uranyl microprecipitates in subsurface sediments at Hanford Site, USA. Geochim. Cosmochim. Acta 68, 4519–4537. doi:10.1016/j.gca.2004.04.017

Loida, a., Grambow, B., Geckeis, H., 1996. Anoxic corrosion of various high burnup spent fuel samples. J. Nucl. Mater. 238, 11–22. doi:10.1016/S0022-3115(96)00338-8

Martínez-Torrents, A., Meca, S., Baumann, N., Martí, V., Giménez, J., De Pablo, J., Casas, I., 2013.

Uranium speciation studies at alkaline pH and in the presence of hydrogen peroxide using time-resolved laser-induced fluorescence spectroscopy. Polyhedron 55, 92–101. doi:10.1016/j.poly.2013.02.075

Matzke, H., Blank, H., Coquerelle, M., Lassmann, K., Ray, I.L.F., Ronchi, C., Walker, C.T., 1989. Oxide fuel transients. J. Nucl. Mater. 166, 165–178. doi:10.1016/0022-3115(89)90187-6

McNamara, B., Buck, E., Hanson, B., Sattonnay, G., Ardois, C., Corbel, C., Lucchini, J.F., Barthe, M.-F., Garrido, F., Gosset, D., Parks, G.A., Shoesmith, D.W., 2002. Observation of Studtite and Metastudtite on Spent Fuel. MRS Proc. 757, II9.7. doi:10.1557/PROC-757-II9.7

Meca, S., Martínez-Torrents, A., Martí, V., Giménez, J., Casas, I., De Pablo, J., 2011. Determination of the equilibrium formation constants of two U(vi)-peroxide complexes at alkaline pH. Dalt. Trans. 40, 7976–7982. doi:10.1039/c0dt01672a

Mennecart, T., Cachoir, C., Lemmens, K., 2014. Influence of the alpha radiation on the UO_2 dissolution in high pH cementitious waters. J. Radioanal. Nucl. Chem. 304, 61–66. doi:10.1007/s10967-014-3667-z

Mennecart, T., Cachoir, C., Lemmens, K., 2007. Dissolution behaviour of UO_2 in anoxic conditions: Comparison of Ca-bentonite and Boom Clay, in: MRS Proceedings. pp. 41–46.

Merino, J., Cera, E., Bruno, J., Quiñones, J., Casas, I., Clarens, F., Giménez, J., De Pablo, J., Rovira, M., Martínez-Esparza, A., 2005. Radiolytic modelling of spent fuel oxidative dissolution mechanism. Calibration against UO_2 dynamic leaching experiments. J. Nucl. Mater. 346, 40–47. doi:10.1016/j.jnucmat.2005.05.019

Molera, M., Eriksen, T., 2002. Diffusion of $^{22}Na^{+}$, $^{85}Sr^{2+}$, $^{134}Cs^{+}$ and $^{57}Co^{2+}$ in bentonite clay compacted to different densities: experiments and modeling. Radiochim. Acta 90, 753–760. doi:10.1524/ract.2002.90.9-11_2002.753

Moll, H., Geipel, G., Matz, W., Bernhard, G., Nitsche, H., 1996. Solubility and Speciation of $(UO_2)_2SiO_4 \cdot 2H_2O$ in Aqueous Systems. Radiochim. Acta 74, 3–7. doi:10.1524/ract.1996.74.special-issue.3

Nguyen, S.N., Silva, R.J., Weed, H.C., Andrews, J.E., 1992. Standard Gibbs free energies of formation at the temperature 303.15 K of four uranyl silicates: soddyite, uranophane, sodium boltwoodite, and sodium weeksite. J. Chem. Thermodyn. 24, 359–376. doi:10.1016/S0021-9614(05)80155-7

Pastina, B., Isabey, J., Hickel, B., 1999. The influence of water chemistry on the radiolysis of the primary coolant water in pressurized water reactors. J. Nucl. Mater. 264, 309–318.

Pérez, I., Casas, I., Martín, M., Bruno, J., 2000. The thermodynamics and kinetics of uranophane dissolution in bicarbonate test solutions. Geochim. Cosmochim. Acta 64, 603–608. doi:10.1016/S0016-7037(99)00337-3

Pérez, I., Casas, I., Torrero, M.E., Cera, E., Duro, L., Bruno, J., 1997. Dissolution studies of soddyite as a long-term analogue of the oxidative alteration of the spent nuclear fuel matrix, in: Materials Research Society Symposium - Proceedings. Materials Research Society, pp. 565–572. doi:10.1557/PROC-465-565

Pierce, E.M., Icenhower, J.P., Serne, R.J., Catalano, J.G., 2005. Experimental determination of UO_2(cr)

dissolution kinetics: Effects of solution saturation state and pH. J. Nucl. Mater. 345, 206–218. doi:10.1016/j.jnucmat.2005.05.012

Poinssot, C., Ferry, C., Kelm, M., Grambow, B., Martinez-Esparza, A., Johnson, L., ...&, Christensen, H., 2005. Final Report of the European Project Spent Fuel Stability under Repository Conditions. European Commission Report CEA: France.

Poinssot, C., Ferry, C., Kelm, M., Grambow, B., Martínez, A., Johnson, L., Andriambololona, Z., Bruno, J., Cachoir, C., Cavedon, J.M., Christensen, H., Corbel, C., Jegou, C., Lemmens, K., Loida, A., Lovera, P., Miserque, F., de Pablo, J., A., P., Quiñones, J., Rondinella, V., Spahiu, K., Wegen, D.H., 2004. SPENT FUEL STABILITY UNDER REPOSITORY CONDITIONS – FINAL REPORT OF THE EUROPEAN PROJECT.

Quiñones, J., Serrano, J., Díaz Arocas, P., Rodríguez Almazán, J.L., Bruno, J., Cera, E., Merino, J., Esteban, J.A., Martínez-Esparza, A., 2000. Cálculo de la generación de productos radiolíticos en agua por radiación alfa: determinación de la velocidad de alteración de la matriz del combustible nuclear gastado. ENRESA Publicación Técnica 2/2000.

Rey, a., Giménez, J., Casas, I., Clarens, F., de Pablo, J., 2008. Secondary phase formation on UO_2 in phosphate media. Appl. Geochemistry 23, 2249–2255. doi:10.1016/j.apgeochem.2008.03.008

Rondinella, V. V., Wiss, T., 2010. The high burn-up structure in nuclear fuel. Mater. Today 13, 24–32. doi:10.1016/S1369-7021(10)70221-2

Roth, O., Jonsson, M., 2008. Oxidation of UO_2(s) in aqueous solution. Cent. Eur. J. Chem. 6, 1–14. doi:10.2478/s11532-007-0067-z

Roth, O., Low, J., Granfors, M., Spahiu, K., 2013. Effects of matrix composition on instant release fractions from high burn-up nuclear fuel, in: Materials Research Society Symposium Proceedings. Cambridge University Press, Boston, USA, pp. 145–150.

Rovira, M., De Pablo, J., Casas, I., Giménez, J., Clarens, F., 2004. Sorption of caesium on commercial magnetite with low silica content: Experimental and modelling, in: Materials Research Society Symposium Proceedings. pp. 677–682.

Rovira, M., Giménez, J., Martínez, M., Martínez-Lladó, X., de Pablo, J., Martí, V., Duro, L., 2008. Sorption of selenium(IV) and selenium(VI) onto natural iron oxides: goethite and hematite. J. Hazard. Mater. 150, 279–84. doi:10.1016/j.jhazmat.2007.04.098

Santos, B.G., Nesbitt, H.W., Noël, J.J., Shoesmith, D.W., 2004. X-ray photoelectron spectroscopy study of anodically oxidized SIMFUEL surfaces. Electrochim. Acta 49, 1863–1873. doi:10.1016/j.electacta.2003.12.016

Santos, B.G., Noël, J.J., Shoesmith, D.W., 2006a. The effect of pH on the anodic dissolution of SIMFUEL (UO_2). J. Electroanal. Chem. 586, 1–11. doi:10.1016/j.jelechem.2005.09.021

Santos, B.G., Noël, J.J., Shoesmith, D.W., 2006b. The influence of potential on the anodic dissolution of SIMFUEL (UO_2). Electrochim. Acta 51, 4157–4166. doi:10.1016/j.electacta.2005.11.038

Sattonnay, G., Ardois, C., Corbel, C., Lucchini, J.F., Barthe, M.-F., Garrido, F., Gosset, D., 2001. Alpha-radiolysis effects on UO_2 alteration in water. J. Nucl. Mater. 288, 11–19. doi:10.1016/S0022-3115(00)00714-5

Segall, R.L., Smart, R.S.C., Turner, P.S., 1988. Surface and Near-Surface Chemistry of Oxide Materials, Vol. 47. Elsevier Science Publishers B.V., Amsterdam.

Serrano-Purroy, D., Clarens, F., González-Robles, E., Glatz, J.P., Wegen, D.H., de Pablo, J., Casas, I., Giménez, J., Martínez-Esparza, A., 2012. Instant release fraction and matrix release of high burn-up UO_2 spent nuclear fuel: Effect of high burn-up structure and leaching solution composition. J. Nucl. Mater. 427, 249–258. doi:10.1016/j.jnucmat.2012.04.036

Shoesmith, D.W., 2008. The Role of Dissolved Hydrogen on the Corrosion / Dissolution of Spent Nuclear Fuel. NWMO TR-2008-19. Ontario, Canada.

Shoesmith, D.W., 2007. Used Fuel and Uranium Dioxide Dissolution Studies – A Review. MWMO TR-2007-03. Ontario, Canada.

Shoesmith, D.W., 2000. Fuel corrosion processes under waste disposal conditions. J. Nucl. Mater. 282, 1–31. doi:10.1016/S0022-3115(00)00392-5

Shoesmith, D.W., Sunder, S., Bailey, M.G., Wallace, G.J., 1989. The corrosion of nuclear fuel (UO2) in oxygenated solutions. Corros. Sci. 29, 1115–1128. doi:10.1016/0010-938X(89)90048-6

Shvareva, T.Y., Mazeina, L., Gorman-Lewis, D., Burns, P.C., Szymanowski, J.E.S., Fein, J.B., Navrotsky, A., 2011. Thermodynamic characterization of boltwoodite and uranophane: Enthalpy of formation and aqueous solubility. Geochim. Cosmochim. Acta 75, 5269–5282. doi:10.1016/j.gca.2011.06.041

Sonoda, T., Kinoshita, M., Ray, I.L.F., Wiss, T., Thiele, H., Pellottiero, D., Rondinella, V. V, Matzke, H., 2002. Transmission electron microscopy observation on irradiation-induced microstructural evolution in high burn-up UO_2 disk fuel. Nucl. Instruments Methods Phys. Res. Sect. B Beam Interact. with Mater. Atoms 191, 622–628. doi:10.1016/S0168-583X(02)00622-5

Stroes-Gascoyne, S., Garisto, F., Betteridge, J.S., 2005. The effects of alpha-radiolysis on UO_2 dissolution determined from batch experiments with ^{238}Pu-doped UO_2. J. Nucl. Mater. 346, 5–15. doi:10.1016/j.jnucmat.2005.04.069

Sunder, S., Miller, N.H., Shoesmith, D.W., 2004. Corrosion of uranium dioxide in hydrogen peroxide solutions. Corros. Sci. 46, 1095–1111. doi:10.1016/j.corsci.2003.09.005

Taylor, P., Wood, D.D., Duclos, A.M., 1992. The early stages of U_3O_8 formation on unirradiated CANDU UO_2 fuel oxidized in air at 200-300°C. J. Nucl. Mater. 189, 116–123. doi:10.1016/0022-3115(92)90425-K

Torrero, M.E., Baraj, E., De Pablo, J., Giménez, J., Casas, I., 1997. Kinetics of corrosion and dissolution of uranium dioxide as a function of pH. Int. J. Chem. Kinet. 29, 261–267.

Traboulsi, A., Vandenborre, J., Blain, G., Humbert, B., Haddad, F., Fattahi, M., 2015. Radiolytic corrosion of uranium dioxide induced by He^{2+} localized irradiation of water: Role of the produced H_2O_2 distance. J. Nucl. Mater. 467, 832–839. doi:10.1016/j.jnucmat.2015.10.061

Walker, C.T., Staicu, D., Sheindlin, M., Papaioannou, D., Goll, W., Sontheimer, F., 2006. On the thermal conductivity of UO_2 nuclear fuel at a high burn-up of around 100MWd/kgHM. J. Nucl. Mater. 350, 19–39. doi:10.1016/j.jnucmat.2005.11.007

Wilson, C.N., 1990. Results from NNWSI Series 3: Spent Fuel Dissolution Tests. Richland, Washington, USA.

Wilson, C.N., 1988. Summary of results from the series 2 and 3 MMSWI bare fuel dissolution tests. Mater. Res. Soc. Symp. Proc. 112, 473–483.

Wren, J.C., Shoesmith, D.W., Sunder, S., 2005. Corrosion Behavior of Uranium Dioxide in Alpha Radiolytically Decomposed Water. J. Electrochem. Soc. 152, B470. doi:10.1149/1.2047349

Wronkiewicz, D.J., Bates, J.K., Gerding, T.J., Veleckis, E., Tani, B.S., 1992. Uranium release and secondary phase formation during unsaturated testing of UO_2 at 90°C. J. Nucl. Mater. 190, 107–127. doi:10.1016/0022-3115(92)90081-U

Wronkiewicz, D.J., Bates, J.K., Wolf, S.F., Buck, E.C., 1996. Ten-year results from unsaturated drip tests with UO_2 at 90 ° C : implications for the corrosion of spent nuclear fuel. J. Nucl. Mater. 238, 78–95. doi:10.1016/S0022-3115(96)00383-2

Wu, L., Qin, Z., Shoesmith, D.W., 2014. An improved model for the corrosion of used nuclear fuel inside a failed waste container under permanent disposal conditions. Corros. Sci. 84, 85–95. doi:10.1016/j.corsci.2014.03.019

Chapter 2:
General Objective

This thesis dissertation aims to assist to the SNF alteration model used to predict the behavior of the nuclear waste under relevant conditions for its final disposal. To achieve this goal, this work studies different analogues of the SNF under four possible scenarios that might happen during the nuclear waste cycle. These scenarios might influence the dissolution mechanisms of the nuclear waste and the radionuclides release to the groundwater.

The scenarios proposed are as follows:

1. The possible contact of the SNF with moist under reducing environment. This scenario might cause the oxidation of the UO_2 matrix which could increase the oxidized layer prior to the water contact.
2. Once the water gets in contact with the SNF, a part of the inventory of some RN will be released faster than the matrix which will lead to the increase of the radiotoxicity of the ground water. In this context, a mathematical model regarding the RN release will be designed with the corresponding algorithm to predict the RN release.
3. The possible interaction between the SNF and cementitious waters due to cementitious materials present in the repository. These conditions might have an influence on the corrosion of the SNF.
4. The probable retention of RN by uranyl silicate secondary phases that might precipitate in contact with cementitious water under repository conditions.

Chapter 3:
XPS study of UO_2 surface evolution in water vapor/hydrogen atmosphere. Influence of temperature and palladium particles.

Introduction

The behavior of uranium dioxide under dry and humid conditions has been studied for more than 50 years due to its relevance for the final disposal assessment. Here the results obtained in previous studies are briefly presented.

Dry oxidation of the fuel

The oxidation of UO_2 under oxidizing atmosphere (in contact of either air or oxygen) is accepted to be a two steps reaction mechanism involving the reaction shown in reaction (3.1) at temperatures between 180 to 350 ^{0}C (Aronson et al., 1957; Belle, 1961; McEachern and Taylor, 1998):

$$UO_2 \rightarrow U_4O_9 / U_3O_7 \rightarrow U_3O_8 \quad (3.1)$$

Aronson et al. (1957) suggested that when UO_2 gets in contact with oxygen the uranium on the surface is oxidized to a mixture of two phases, U_4O_9 and U_3O_7, almost instantaneously.

First oxidation step

This first step of the oxidation reaction is observed as a pseudo parabolic curve when the weight gain is plotted against time (see Figure 3. 1). This fact is assumed to correspond to a diffusion controlled reaction mechanism and its activation energy is 95.7 kJ/mol for powder samples and 99.0 kJ/mol for sintered pellets (McEachern, 1997; Rousseau et al., 2006). McEachern (1997) proposed the Eq. (3.2) to calculate the parabolic rate constant of the oxidizing reaction:

$$Ln(k) = \left(\frac{-95700}{RT}\right) - 17.33 \quad (3.2)$$

Being 'k' the rate constant, 'R' the gas constant as 8.314 $J \cdot K \cdot mol^{-1}$ and 'T' the temperature in Kelvin. This expression has been used in later studies in order to develop mathematical approaches to the UO_2 oxidation process (Quémard et al., 2009; Taylor, 2005).

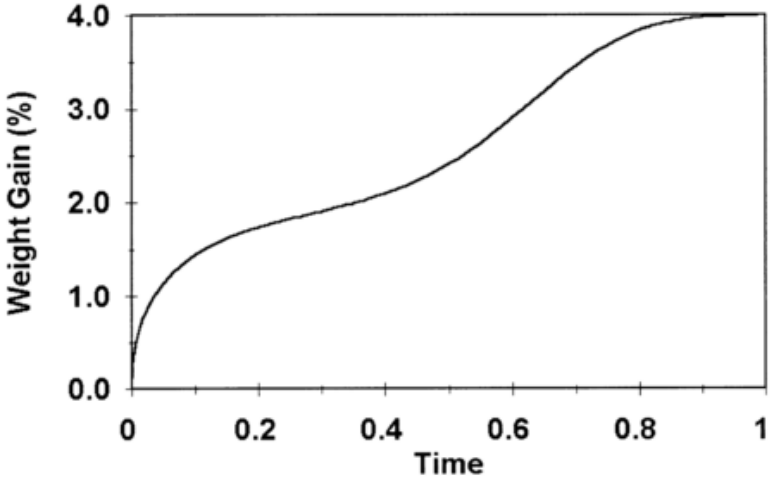

Figure 3. 1 Diffusion - controlled kinetics for the formation of U_4O_9/U_3O_7 and sigmoidal nucleation and growth kinetics for the formation of U_3O_8 commonly observed for UO_2 powder samples from McEachern and Taylor (1998)

The value of the parabolic rate constant in Eq. (3.2) refers to two compounds at the same time: U_4O_9 and U_3O_7 and some studies disagreed with this combination. For instance, Poulesquen et al. (2007) presented a mathematical approach for the oxidation of powder and fines of uranium dioxide under air or oxygen atmosphere at low temperatures. In this model, Poulesquen et al. considered the hypo and hyper – stoichiometric phases of U_4O_9 and U_3O_7 and the final oxidation state was U_3O_7 (see Figure 3. 2).

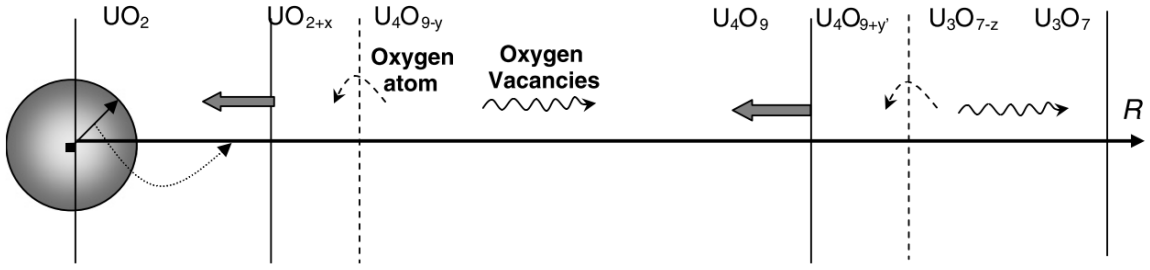

Figure 3. 2 Scheme of the oxidation of UO_2 powder particle assumed in the model proposed by Poulesquen et al. (2007)

By using this model, the activation energies for U_4O_9 and U_3O_7 were determined to be 57 $kJ \cdot mol^{-1}$ and 123 $kJ \cdot mol^{-1}$, respectively.

It has been observed by McEachern and Taylor (1998, 1994) that this first reaction step has a significant impact on the weight gain of the UO_2 sample and hence, the authors considered it an important parameter to take into account when performing experiments with real SNF.

The physical damage induced by the oxidation was studied by Quémard et al. (2009) who analyzed the sample cracking by using XRD and microscopic analysis *in situ* under an oxidizing atmosphere with 20% of O_2. Besides obtaining images of clear cracking evolution of the samples used (see Figure 3. 3 as an example with the characteristic popcorn morphology described by McEachern and Taylor (1998), the XRD results showed that the macro – fractures are linked to the U_3O_7 formation. These cracks were mainly observed in the first part of the oxidation process and provided with fresh UO_2 to the atmosphere. The first oxidizing step occurred on the fresh UO_2 and so, it started oxidizing to U_4O_9 and U_3O_7.

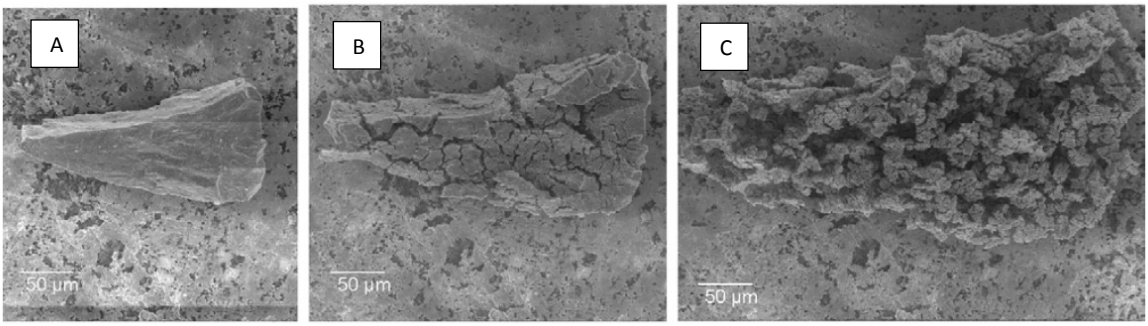

Figure 3. 3 A piece of UO_2 pellet oxidized at 603 K and 265 Pa of oxygen partial pressure from Quémard et al. (2009)**: A) Initial state, B) after 30 minutes of exposure and C) after 5 hours and 30 minutes of exposure.**

At low oxygen partial pressures, the study performed by Nakamura et al. (1993) determined that U_3O_7 is a stable oxide phase and it is located at grain boundaries. This fact was observed by Wasywich et al. (1993) when they studied the Canada Deuterium Uranium (CANDU) in contact with dry air at 423 K. They also characterized the oxidized phase as α-U_3O_7.

Second oxidation step

The second step of the reaction was achieved at temperatures higher than 250 ^{0}C (523 K) where nuclei of U_3O_8 start to form on the surface and grow towards the sample bulk. In order to proceed with the oxidation process, the previously oxidized phase must be β – U_3O_7 otherwise the oxidation to U_3O_8 will not occur on powder samples (McEachern and Taylor, 1998; Rousseau et al., 2006; Westrum and Grønvold, 1962).

Aronson et al. (1957) noticed a change in the surface area during the second step of the oxidation reaction and suggested the differences between their densities as the cause for this change (U_3O_7 had 11.4 $g \cdot cm^{-3}$ and U_3O_8 had 8.35 $g \cdot cm^{-3}$). According with the previous results, Nakamura et al. (1993) observed the presence of traces of U_3O_8 at high temperatures. At the same time, the oxidation rate observed changed and by the time the authors finished the experiments, the sample presented severe damage such as black fine powder and volume expansion. A few years later Sunder and Miller (1996) performed a study on CANDU samples at 423 K using gamma field (with a dose rate of 15 Gy/h) for two years and they found U_3O_8 for the first time at such low temperatures. In this work, the authors claimed that the formation rate of U_3O_8 was very slow, which could explain the results obtained.

Overall oxidation reaction and its mechanisms

Taylor (2005) reviewed the data for the oxidation of UO_2 in contact with air over a wide range of temperature: from 400 to 2000 K, even though there were only few data available at high temperatures. Figure 3. 4 shows the phase diagram for the uranium – oxygen system from UO_2 to UO_3 based on the thermodynamic data published by Guéneau et al. (2002).

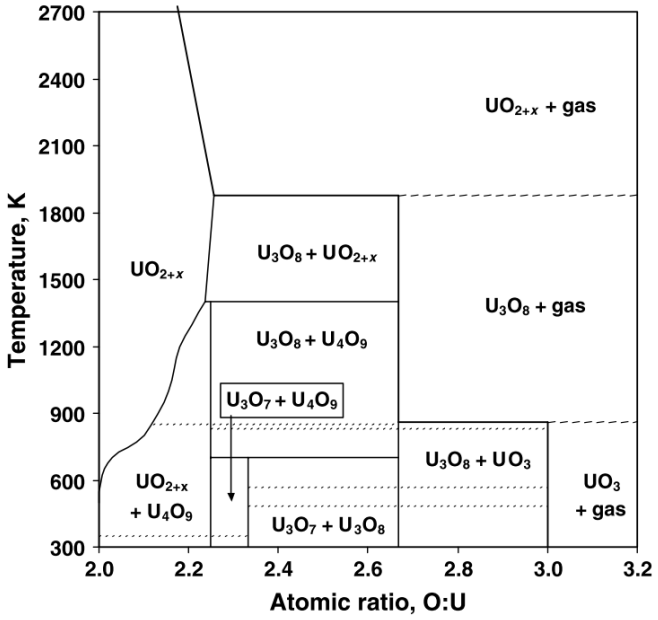

Figure 3. 4 Portion of the U – O phase diagram obtained from Taylor (2005) **with emphasis on solid phases with compositions between UO_2 and UO_3. The dotted lines represent solid phase transition in U_4O_9 at 349 K and 850 K, and in U_3O_8 at 483, 568 and 830 K. The two dashed lines represent the decomposition of UO_3 at 861 K and the decomposition of U_3O_8 at 1878 K.**

Further studies were performed aiming to a better understanding of the mechanisms of the oxidation of UO_2 taking into account the two-step reaction mentioned. Rousseau et al. (2006) studied the

mechanisms of the oxidation and limiting steps at 250 ^{0}C. To study that, they performed an oxidation experiment under 20% of O_2 and analyzed the sample surface *in situ*. Taking into account the hypothesis that the limiting step does not depend on the temperature, they increased the experimental temperature suddenly from 250 to 280 ^{0}C and evaluated the oxidation rate right before and after that change. The evolution of the ratio between both rates allowed them to differentiate 4 regions (see Figure 3. 5).

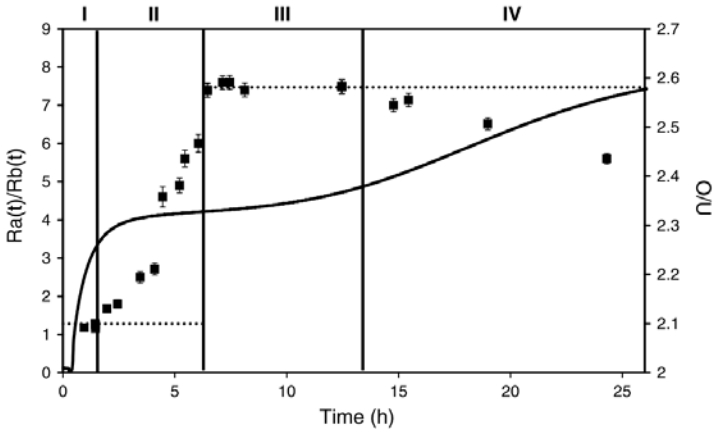

Figure 3. 5 Typical oxidation curve of a UO_2 powder sample to U_3O_8 at 250^{0}C under air (21% of O_2) along with the rate ratio between the rate after and before increasing the temperature from Rousseau et al. (2006)

- REGION I: This region corresponds to the first 2 hours of their experiment. It presented the same oxidation rate before and after increasing the temperature. Hence, the process involved corresponds to a limiting rate step. Since the product obtained by the authors was U_4O_9, they suggested that the reaction mechanism corresponded to a diffusion controlled mechanism.
- REGION II: This region is located between 2 hours and 6 hours of experimental time. Here the ratio between rates increased with the time and therefore there seems to be no limiting rate step mechanism. Here the authors suggested that two reactions might take place at the same time: firstly the oxidation of fresh UO_2 into U_4O_9 and secondly the oxidation of the already formed U_4O_9 into U_3O_7. Also, they observed the formation of cracks on the surface that provide fresh UO_2 available to the oxidizing environment.
- REGION III: It is located between 6 and 14 hours of experimental time. In this region the rate ratio was constant and hence, a limiting rate step mechanism was occurring. The authors suggested that nuclei of U_3O_8 might start to form.
- REGION IV: This region is located from 14 hours of experimental time until the end of the curve. Here the rate ratio decreased which means that there was no limiting rate step

mechanism in this region. In this last domain, the authors suggested the growth of the U_3O_8 oxidized layer towards the bulk of the sample and the formation of more nuclei in this region.

Once the cracks are formed, the authors suggested that the oxidized layer grows towards the bulk of the sample by following a succession of elementary steps. First the oxygen is adsorbed on the surface and so an external interface reaction occurs between the oxygen and the uranium. Then this oxygen is diffused through the oxidized phase and it reacts with the internal interphase.

Effect of water vapor, steam and/or moist environment

Uranium dioxide oxidation has been studied in contact with water vapor – steam or under moist environment. In this section studies performed with heavy water (D_2O and $D_2{}^{18}O$) are also contemplated since they were used as molecular and atomic markers. The results obtained were considered to be comparable to the studies performed with H_2O.

After being irradiated, the nuclear fuel can get in contact with moist within two phases of the SNF cycle. First, in case of an accident during fuel discharge or during fuel transfer operations and breaking of the cladding occurs; moist air can get in contact with the fuel. Then, during the long – term storage of defective canisters, water vapor also can reach the SNF (Higgs et al., 2007).

Reactions and mechanisms on UO_2 and SNF

The behavior of uranium dioxide in contact with water vapor is of relevance in order to know its state before entering in contact with ground water. In this case, the water molecule is dissociated and it oxidizes the UO_2 surface additionally to the hydrogen production at low temperatures (from 85 to 373K) (MacCrone et al., 1986; Winer et al., 1987) by the possible electron tunneling in UO_2.

MacCrone et al. (1986) observed the oxidation of the UO_2 surface in contact with water vapor with nitrogen gas and water vapor with air at temperatures from 85 to 298K. The authors proposed the chemisorption of water hydrolysis products O^- and O_2^- as shown in reaction (3.3) as possible mechanism for the UO_2 surface oxidation in contact with water.

$$O^{2-}_{(lattice\ or\ interstitial)} + H_2O(v) \rightarrow HO^-_{(lattice\ or\ interstitial)} + HO^-_{(surface)} \quad (3.3)$$

This fact was also observed by other authors (Hedhili et al., 2000; Winer et al., 1987) who also observed that OH^- is easily adsorbed on the oxide surface depending on the experimental temperature. Their results indicate that H_2O is completely dissociated and oxygens are incorporated in the outer layers of the crystal and diffused into the UO_2 bulk (reaction (3.4)). They also observed an effect of the surface

defects but it was Stulz et al. (2004) who studied the oxidation caused by water on uranium dioxide as a function of the surface defects. They created the surface defects by sputtering the sample with Ar^+ beam. In addition, they performed annealing treatments in order to reduce the defects. The main conclusion was that water provided the oxygen to heal the surface defects by water hydrolysis (see reaction (3.5)).

$$UO_2 + xH_2O \rightarrow UO_{2+x}(surface) + xH_2(g) \quad (3.4)$$

$$UO_{2-x} + xH_2O(v) \rightarrow UO_2 + xH_2 \quad (3.5)$$

Stultz et al. (2004) suggested that these defects have oxygen vacancies which enhance the water dissociation. This statement was confirmed by other authors (Idriss, 2010; Senanayake et al., 2007b; Senanayake and Idriss, 2004) who found a proportionality between the oxygen defects and the amount of dissociative adsorption of water. Furthermore, Cohen et al. (2014) observed an orientation of the hydroxyl group on the sample surface as a function of the surface defects at temperatures from 300 to 400 K.

Moist environment might also lead the UO_2 to precipitate different hydrated phases collected in the Table 3. 1 reported by Ferry et al. (2005) Most of the phases reported were produced at relative humidity between 30% and 70%.

Table 3. 1 Hydrated phases obtained from uranium oxide under moist environment (Ferry et al., 2005)

Hydrated Phase	Crystalline System	Formation
$U_3O_8(OH)_2$	Triclinic	It is produced at temperatures between 600 and 700 K
$UO_3 \cdot 0.8H_2O$	Orthorhombic	
$\alpha - UO_2(OH)_2$	Orthorhombic	It is produced from the dehydration of schoepite at temperatures of 600 K.
$\beta - UO_2(OH)_2$	Orthorhombic	UO_3 hydration at temperatures between 473 and 563 K
$\Upsilon - UO_2(OH)_2$	Monoclinic	Secondary phase obtained during the formation of the β form
$UO_2(UO_3)_5 \cdot 10H_2O$	Orthorhombic	
$UO_3 \cdot 2H_2O$	Orthorhombic	Natural compound obtained from the hydration of UO_3 at room temperature

The effect of water vapor and moist environment has been also studied on the SNF by Wasywich et al. (1993) who observed the oxidation of the CANDU samples. Their results showed a homogeneous oxidized surface. Leenaers et al. (2003) also observed production of hydrogen which was attributed to the oxidation of UO_2 to UO_{2+x} caused by water. The authors also considered the production of H_2O_2 as a possible source for the H_2 production and the uranium oxidation. They saw that the grain boundaries were weakened first which increased the sensitivity to the chemical attack to the fuel.

In addition to the water vapor, the SNF might also get in contact with high amounts of hydrogen, up to 10 MPa (Grambow, 2010) from the stainless steel corrosion under anoxic conditions. Since each one of the species has different redox properties, it is necessary to determine which of these species will prevail in the SNF near field under relevant conditions for the DGR.

Specific Objectives

This chapter will be focused on the study of UO_2 under moist environment at relevant conditions for the SNF disposal. More precisely, the goal of this study is to determine the effect of the water vapor under hydrogen atmosphere on UO_2 and UO_2 doped with palladium nanoparticles as a analogue of the SNF.

Additionally, the effect of the experimental temperature inside the reactor will be also studied under relevant conditions for the temporary and definitive storage of the SNF in the CTDS and the DGR.

Experimental Methodology

Sample preparation

UO_2 Samples

ENUSA (Empresa Nacional del Uranio S.A., Spain) provided the synthetic UO_2 used in the study. Uranium dioxide was ground and sieved to obtain powder with less than 0.75 μm of particle size. Then, the powder was pressed to make a pellet with 10 mm diameter and 3 mm of thickness. The pellet was placed into a sample holder and introduced into the ultra-high vacuum (UHV) SPECS platform without using any adhesive (see Figure 3. 6).

Figure 3. 6 UO_2 sample into the XPS sample holder before being introduced into the SPECS platform

UO_2 Doped Samples

The amount of noble metals were obtained from the experimental inventory results of a SNF with 60 GWd/t_U of burn up (Serrano-Purroy et al., 2012). It was calculated that in the SNF approximately 0.5% wt. was from ε-particles and 1.5% wt. comes from metallic alloy particles. ε-particles are here defined as precipitates containing noble metals (such as Au, Ag, Pd, Pt, Ru and Rh) and metallic particles are considered to contain other metallic elements (such as Mo, Tc, Cd, In, Sn, Sb and Te) (Ferry et al., 2005).

In order to dope the samples, the corresponding amount of $PdCl_2$ from Sigma Aldrich was dissolved and added to 2 g of UO_2 powder. The $PdCl_2$ was dissolved into an acidic solution HCl/H_2O using 1.4/100 volumetric proportion per each gram of $PdCl_2$. Once the palladium powder was dissolved, the resulting dissolution was placed on the UO_2 powder drop by drop until the solid was saturated with liquid. After, it was dried at room temperature and, in case of having reminding palladium dissolution, these last two steps were repeated until all the Pd had been added. Afterwards, the solid was dried by using an oven at 350^0C to remove the water molecules under air atmosphere. This procedure and the sample characterization have been published in Espriu-Gascon et al. (2016).

The powder obtained was pressed and placed into a sample holder without using any adhesive. Then, it was introduced into the UHV SPECS platform to perform the experiments like it was done for the non-doped sample.

Electron Microscopy

After doping the UO_2 powder with Pd, the samples needed to be analyzed by electron microscopy to characterize the palladium particles, both their size and their location.

First, a suspension of 5 ml of acetone containing 1 mg of doped sample was placed in the ultrasound for 1 hour to obtain a homogeneous suspension. Then, one drop of it was placed on a grid and it was dried before introducing the sample in the High Resolution Transmission Electron Microscopy (HR-TEM).

HR-TEM platform allows to perform Energy Dispersive X-Ray (EDS) measurements and Scanning Transmission Electron Microscopy (S/TEM) images all with the same device. The HR-TEM equipment is a JEM-2011 unit that uses a voltage of 200 kV to accelerate the electron. A FEI Tecnai F20 S/TEM microscope was used to obtain the S/TEM images and the EDS analysis with the same acceleration voltage (200 kV).

X-Ray Photoelectron Spectroscopy (XPS) technique

This technique consists of irradiating a sample with monoenergetic soft X-rays and analyzing the electrons emitted. There are two different types of X-Ray sources: MgKα X-rays (1253.6 eV) or AlKα X-rays (1486.8 eV). The photons emitted by the source have limited penetrating power in the sample, of the order of 1-10 micrometers (Wagner et al., 1979).

The photons excite the electrons and these last ones are emitted due to the excess of energy. They have such kinetic energy that follows the Eq. (3.6):

$$KE = h\upsilon - BE - \Phi_S \tag{3.6}$$

Where Kinetic Energy is expressed as KE, hυ is the energy of the photon, the Binding Energy is expressed as BE and Φ_S is the spectrometer work function.

BE may be regarded as the ionization energy of the atom for a particular configuration. Since each atom has different ions, each ion has its own BE and hence, the emitted electrons will have different kinetic energies.

Other phenomena can also take place during the XPS analysis related to the electron emission such as Auger electrons. They are emitted because of the relaxation of the energetic ions left after the photoemission. When a photoelectron is emitted from a low energetic level, it leaves an orbital vacancy. This vacancy is then occupied by an electron located at higher energy levels and a second electron from this same high energetic level is emitted due to the excess of energy.

When the electron leaves the atom, there are probabilities of interaction with matter that may cause the loss of energy. So, even though photons can reach micrometers of depth, the electrons measured are originated within tens Angstroms below the sample surface. For this reason, the measurements have to be performed under vacuum to avoid electrons to hit other atoms present in the analysis chamber. The electrons are detected by an electron spectrometer according to their kinetic energy. The figure obtained from the spectrometer measures the electrons emitted a function of the KE and the graph is known as XPS spectrum.

Data Interpretation

The spectrum can be shown as function of the electron kinetic energy or as a function of its binding energy (Eq. (3.6)). In order to be able to compare the results with the bibliographic ones, the results will be expressed as a function of the BE. Moreover, the results are usually shown with the BE scale increasing to the left.

The electrons that have not lost any energy produce well-defined peaks. Several types of peaks can be observed in any XPS spectra. Some of them are always observed and others depend on the sample, its physical and chemical nature.

The photoelectron lines are the most intense lines, usually symmetrical and narrow. These are the lines usually used to perform the data treatment for the XPS results. Auger lines are groups of signals in complex patterns. There are four main Auger series named as the initial and final vacancies in the Auger transitions: KLL, LMM, MNN and NOO. The X-ray satellites are a family of minor peaks at lower BE than the photoelectron lines. Their intensity and spacing from the main XPS peaks is characteristic of the X-ray anode material. The pattern can be observed in Table 3. 2.

The shake-up lines are caused by an ion left in an excited state which leads to a reduction of the kinetic energy of the emitted electrons. The result is a formation of a satellite peak at lower energy, kinetic energy (or higher binding energy), than the main peak. As an example, UO_2 has one shake-up peak at 6.7

eV from each of the main peaks in the U 4f band. Their displacement and relative intensities is useful to identify the chemical state of an element in most of the cases.

Table 3. 2 X-ray satellite energies and relative intensity caused by the X-ray source

Anode		$\alpha_{1,2}$	α_3	α_4	α_5	α_6
Mg	Displacement (eV)	0	8.4	10.2	17.5	20.0
	Relative height	100	8.0	4.1	0.55	0.45
Al	Displacement (eV)	0	9.8	11.8	20.1	23.4
	Relative height	100	6.4	3.2	0.4	0.3

The valence lines and bands are located at low BE and have low intensity. These lines are caused by the electrons in the molecular orbitals and solid state energy bands. This region is useful to differentiate the insulators from the conductors due to the presence or absence of a band in the conduction area (Fermi level located at 0 eV of BE).

Data Treatment

The data treatment was done with the CasaXPS® software from Casa Software Ltd., UK. All the spectra were previously centered by using the O^{2-} band at 529.7 eV and the de-convolutions were performed using a Shirley background. Also, the curves used had a 30% of Lorenzian curve and 70% of Gaussian curve(Santos et al., 2004).

$U4f_{7/2}$ band has been de-convoluted using three different bands: U(IV), U(V) and U(VI). To obtain the oxidation state of the uranium, the distances among U(IV), U(V) and U(VI) bands were fixed to the ones reported in Table 3. 3 (Allen et al., 1987; Idriss, 2010; Ilton et al., 2007; McEachern and Taylor, 1998; Stumpf et al., 2009; Van den Berghe et al., 2000)

Table 3. 3 Reported values of Binding Energies (BE) of U(VI), U(V) and U(VI) bands as well as the corresponding satellite locations for each oxidation state as a function of the $U4f_{5/2}$ band position

Band	BE $U4f_{7/2}$ (eV)	ΔBE satellite (eV)
U(IV)	379.5 – 380.0	6.7
U(V)	380.0 – 380.6	8.0 – 9.0
U(VI)	380.8 – 381.4	4 ; 10

The Platform

Both the experiments and the analysis were performed inside the UHV SPECS platform at the Center for Research in nanoEngineering (CRnE) (see Figure 3. 7). The XPS analysis chamber is equipped with an Al anode XR50 source operating at 150 W and a Phoibos MCD-9 detector. The spectra were recorded at a pressure below 10^{-8} mbar and the accuracy of the binding energies was ± 0.1 eV. The analysis chamber was connected via a closed line to a high pressure chamber (HPC) where the experiments were performed at atmospheric pressure.

A gas stream of 15 ml/min passed through a saturator filled with ultrapure water (Milli-Q) at room temperature. Then, the saturated gas was introduced to the HPC and entered in contact with the sample. Into the reactor, the temperature was set at a specific value by an infrared light and a termo-couple in contact with the sample holder. That temperature was kept constant until the end of the experiment. Once the experiment finished, the sample was transferred to the XPS analysis chamber without being exposed to the external atmosphere.

Figure 3. 7 XPS platform at the CRnE (UPC)

The two gases used were argon and hydrogen with 99.999% of purity from Messer (Germany). The amount of water introduced in the HPC at room temperature has been estimated to be approximately $3.4 \cdot 10^{-4}$ ml/min (Hyun and Kim, 2004; Perry et al., 1997).

Experiments Performed

The experiments were divided into three different series depending on the reactants used:

The first series of experiments were performed under a hydrogen atmosphere. The main purpose of them was to reduce the sample surface and obtain stoichiometric UO_2. Depending on the type of

sample, the temperatures used were different in order to reduce the surface and avoid major changes to the samples. In the case of UO_2 sample, the temperature was set at 500^0C to get U(IV) on the surface and it was called T-H_2 (500) (see Table 3. 4). In the case of doped samples, the temperature used was 350^0C for 20 minutes to keep the palladium nanoparticles (Pd-NPs) size constant and hence, their properties. This experiment was called T-H_2 (350) (see Table 3. 4). This type of treatment was performed every time before each experiment to ensure that the initial sample surface was always UO_2.

The second series of experiments were performed using an argon stream saturated with ultrapure water at room temperature. Afterwards, the gas mixture was introduced in the HPC where the solid sample was placed. Inside the HPC, the temperature was increased until the experimental temperature was reached. Each experiment was performed at different temperature: one at 100, another one at 200 and another one at 350 ^{0}C. This experimental temperature remained constant for 10 minutes and then it was decreased until room temperature. The experimental conditions are reported in Table 3. 4 for the experiments named T-Ar-H_2O (T). Afterwards, the sample was transferred to the analysis chamber.

Table 3. 4 Experimental conditions for each treatment performed to the three samples used in this chapter.

Treatment	Gas	Flow rate (ml/min)	H_2O vapor	Temperature (^{0}C)	Time (minutes)
T-H_2 (350)	H_2	15		350	20
T-H_2 (500)	H_2	15		500	20
T-Ar H_2O (100)	Ar	15	Yes	100	10
T-Ar H_2O (200)	Ar	15	Yes	200	10
T-Ar H_2O (350)	Ar	15	Yes	350	10
T-H_2 H_2O (60)	H_2	15	Yes	60	10
T-H_2 H_2O (100)	H_2	15	Yes	100	10
T-H_2 H_2O (200)	H_2	15	Yes	200	10
T-H_2 H_2O (350)	H_2	15	Yes	350	10

The third type of experiments was performed using a hydrogen stream saturated with ultrapure water at room temperature. As in the previous case, gas mixture was introduced to the HPC where the temperature was increased until the experimental temperature. Each treatment was performed at a certain temperature values: one at 60, another one at 100, another one at 200 and another one at 350 ^{0}C. The temperature was kept constant for 10 minutes and then it was decreased until room temperature. A summary of the main experimental conditions can be observed for each one of the

experiments named T-H_2-H_2O (T) in Table 3. 4. Afterwards, the sample was transferred to the XPS analysis chamber under vacuum conditions and without entering in contact with the atmosphere.

In the following sections, the experiments will be named as it is shown in Table 3. 4.

Results and Discussion

In this section, the results are shown as figures. The numerical results obtained from the U4f$_{7/2}$ band deconvolution are shown as tables in the Annex A. The main spectrum characteristics of each spectrum obtained are also shown in Annex B.

UO_2 Sample

The sample as prepared

Before performing any experiment, the sample was analyzed by XPS to determine its initial oxidized state. The result obtained showed that the sample surface was oxidized as it can be deduced by the double satellite of U 4f$_{5/2}$ XPS band and the U 4f$_{7/2}$ Binding Energy (380.0 eV) in Figure 3. 8. The presence of the double satellite at 400 and 397 eV clearly proved the presence of oxidized uranium states (Allen et al., 1987; Idriss, 2010; Ilton et al., 2007; McEachern and Taylor, 1998; Stumpf et al., 2009); therefore, the U4f$_{7/2}$ band was de-convoluted into three different bands representative of U(IV), U(V) and U(VI) contributions, respectively.

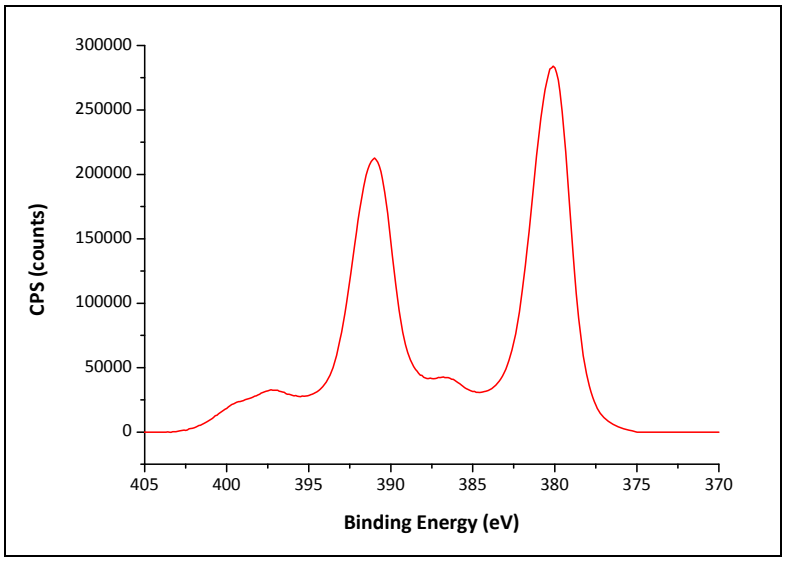

Figure 3. 8 U4f XPS band obtained before performing any experiment on the sample

The results showed that the initial oxidized state of the sample surface corresponded to a mixture with the following amounts of each oxidized states: 50.0% (±5%) of U(IV), 26.2% (±5%) of U(V) and 23.8% (±5%) of U(VI). The resulting oxide can be expressed as $(U^{IV}_{0.5}U^{V}_{0.262}U^{VI}_{0.238})O_{2.37}$. This initial oxidized state might be caused by the sample pre-treatment or by the contact with the atmosphere prior to the experiments (Poulesquen et al., 2007), or both. Accordingly with Taylor (2005) and the phase uranium – oxygen phase diagram (see Figure 3. 4) there is a mixture of two oxide phases on the sample surface:

U_3O_7 and U_3O_8. In order to reach the $(U^{IV}_{0.5}U^{V}_{0.262}U^{VI}_{0.238})O_{2.37}$ composition, the amount of U_3O_7 is calculated to be 89% while the amount of U_3O_8 is 11%.

As a consequence, the first step was to reduce the solid surface in order to obtain stoichiometric UO_2.

Reduction of the sample surface

Since the objective of the work performed in this chapter was following the evolution of the UO_2 oxidation, prior to perform any experiment, the sample surface needed to be as U(IV). To reach this state, the treatment T-H2 (500) was performed (see Table 3. 4). After the treatment, the sample surface was analyzed and the spectra obtained can be observed in Figure 3. 9.

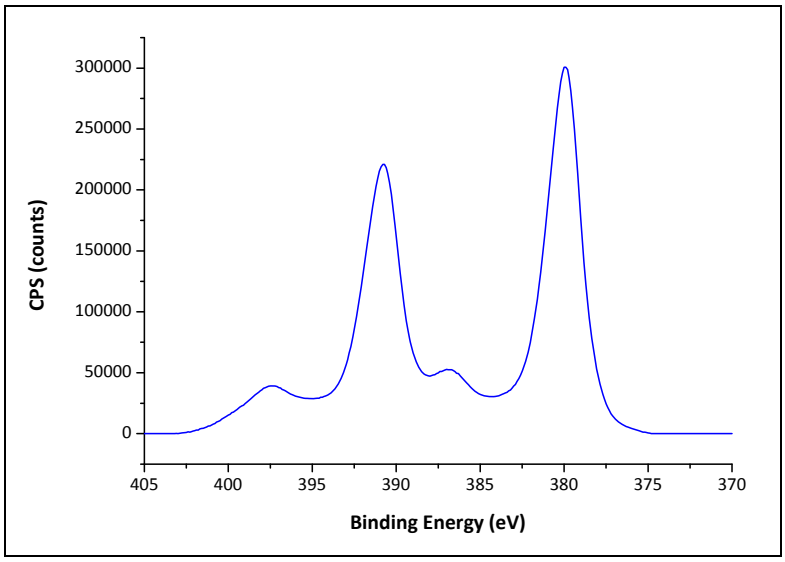

Figure 3. 9 U4f XPS band obtained after performing a treatment with 15ml/min of H_2 at 500^{0}C for 20 minutes.

The main characteristics of the spectrum obtained were that the BE of $U4f_{7/2}$ band was located at 379.6 eV and its full width at half maximum (FWHM) was 2.0 eV. There was also only one single satellite identified at 6.7 eV from the $U4f_{5/2}$ peak position. Regarding the reported values in Table 3. 3, it can be concluded that this treatment allowed to obtain U(IV) on the sample surface.

Hence, this treatment has always been performed between two successive experiments with water vapor to ensure that in all cases the initial surface corresponded to a stoichiometric UO_2.

Experiments under Argon and Water Vapor

The UO_2 sample was put in contact with an argon stream saturated with water vapor as it is detailed in Table 3. 4 for the treatments T-Ar-H_2O (T). These experiments aimed to determine the effect of water vapor on the U(IV) at different temperatures: 100, 200 and 350 ^{0}C.

The results showed that water vapor oxidized the uranium under the experimental conditions in all cases. The oxidation was observed to be enhanced as the temperature was increased (see Figure 3. 10). At 100^{0}C, the UO_2 started to oxidize, but U(IV) remained as the most important contribution to the U4$f_{7/2}$ band reaching 56.9% (see Table A. 1). When the experimental temperature was set at 200^{0}C, the amount of U(IV) decreased drastically. At the same time, the U(VI) contribution increased and it reached a value similar to that of U(IV). When the experiment was performed at 350^{0}C the surface obtained showed even higher oxidation state. The amount of U(V) increased and reached 57% of the analyzed volume. U(VI) was the second oxidized state with a 35% of contribution and U(IV) was the lowest of the three of them (7%).

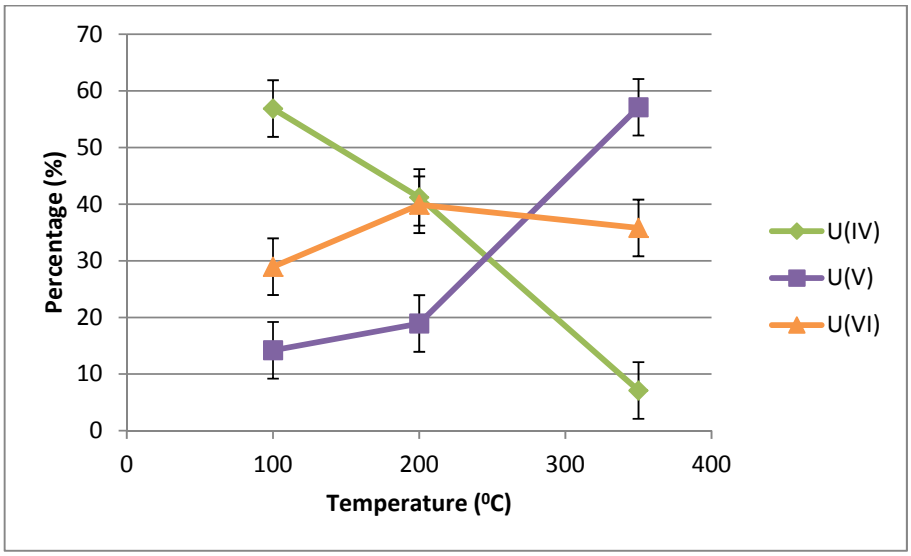

Figure 3. 10 Evolution of the sample surface in contact with 15 ml/min of Ar stream saturated with water vapor as a function of the experimental temperature. Green dots are due to U(IV) percentage; purple dots are due to U(V) percentage and orange dots are due to U(VI) percentage

These results are in good agreement with the ones reported in previous works (Haschke, 1998; McEachern and Taylor, 1998; Senanayake et al., 2007a) that reported that the water enhances the UO_2 oxidation. Two possible paths were proposed in those studies: either through the oxygen diffusion in the outer layers or by forming hydrated uranyl phases on the surface. The temperature increases the oxygen

diffusivity into the UO_2 matrix as it can be observed in Eq. (3.2). As a consequence, the oxidation is enhanced.

Considering the mechanisms mentioned in the introduction of the chapter, the results suggest that the water molecule is dissociated on the UO_2 surface (Hedhili et al., 2000). The increase of U(V) observed between 200 to 350 ^{0}C might be due to the fact that oxygen diffusion into the bulk is faster than the second oxidation step of the oxidation process caused by water vapor. Another possibility was suggested by (Cohen et al., 2014; Senanayake et al., 2007b; Senanayake and Idriss, 2004) who explained the increase of oxygen content on the sample surface as a healing process of the surface defects favored by the increasing temperature. The authors proposed that oxygen accumulates on the surface defects of UO_2 and heals the defect sites such as oxygen vacancies. However, the oxygen diffusion from the core to the shell of the powder cannot be completely ruled out either.

These results showed that the presence of water vapor oxidized the UO_2 under an anoxic atmosphere such as argon or nitrogen. The temperature is also an important factor to take into account, regarding the results obtained in this section. If the temperature is below 100^{0}C, most of the uranium will be U(IV). The opposite will happen if the temperature is higher.

Experiments under Hydrogen and Water Vapor

Once the effect of the water vapor for the system has been determined, a hydrogen stream saturated with water vapor was put in contact with the UO_2 as it is detained in Table 3. 4 for the experiments T-H2-H2O (T). After performing the experiment, the sample surface was analyzed and U4f$_{7/2}$ band was de-convoluted into U(IV), U(V) and U(VI). The results obtained can be observed in Figure 3. 11 as a function of the experimental temperature; the numerical results are reported in Table A. 2.

The oxidizing effect of the water vapor can be observed on the UO_2 surface despite the presence of hydrogen in the atmosphere.

At low temperature, the oxidizing effect of the water vapor prevails over the reducing effect of the hydrogen and hence, the oxidation of UO_2 occurred. At 60^{0}C, the U(IV) band was the main contribution to the U4f$_{7/2}$ while U(V) and U(VI) had similar contributions. The oxidation increased with the increase of temperature from 60 to 120^{0}C. At 120^{0}C the oxidation process was enhanced and the three oxidized states reached similar percentages in the U4f band: U(IV) decreased and both U(V) and U(VI) increased compared with the results obtained at lower temperature.

When the T-H_2-H_2O (200) treatment was performed on UO_2 sample, the results obtained were close to the results obtained at 120^{0}C. Since the surface compositions obtained were within the error tolerance considered, it can be concluded that the UO_2 oxidation may be the same at both temperatures.

Finally, when the T-H_2-H_2O (350) experiment was performed, the oxidation state of the surface decreased, compared with the surface composition obtained at 200 ^{0}C as it can be observed in Figure 3. 11. The UO_2 surface was oxidized but U(IV) was the main contribution observed to the U4$f_{7/2}$ band.

Therefore, the surface of UO_2 has been oxidized in all the cases to different extent as it was observed by the BE position of the U4$f_{7/2}$ band and the double satellite appearance (see Table B. 2).

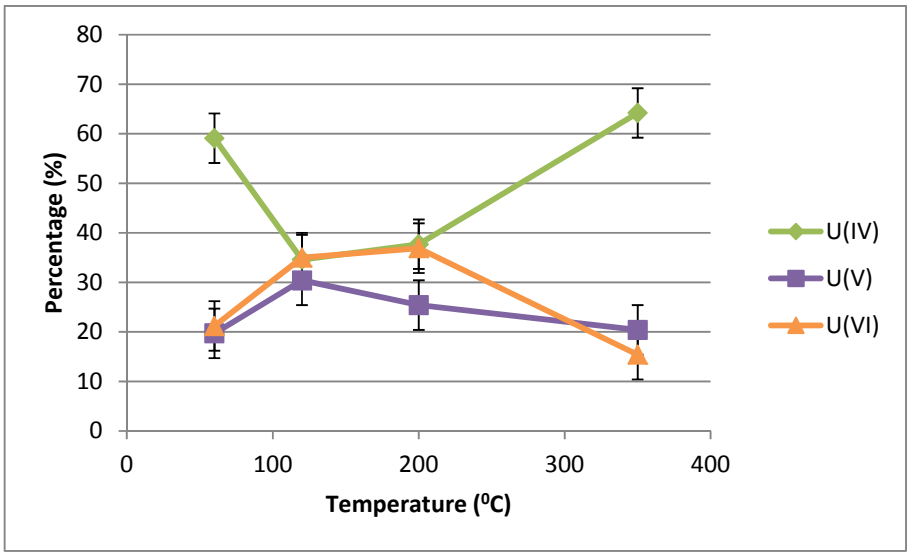

Figure 3. 11 Evolution of U(IV), U(V) and U(VI) with the temperature when the UO_2 sample was put in contact with hydrogen and water vapor for 10 minutes. The green ♦ marker for U(IV), the purple ■ marker for U(V) and the orange ▲marker for U(VI).

The increase of the oxidation state observed from 60 to 100ºC might be due to the enhancement of the oxidation reaction by the increase of the oxygen diffusion into the UO_2 (Eq. (3.2)). The oxygen diffusion has been observed to be the limiting step of the oxidation reaction in the first oxidation stages (Rousseau et al., 2006). This same tendency should be observed when the temperature was increased from 100 to 200 ^{0}C but the obtained uranium oxidized state showed otherwise. This fact might be caused by the presence of hydrogen which might be starting to avoid the UO_2 oxidation at some temperature between 100 ^{0}C and 200 ^{0}C. Another hypothesis might be a possible limiting step mechanism of the oxidation reaction that is independent of the temperature within the range of 100 and 200 ^{0}C. The possible crystalline rearrangement under water vapor conditions (Ferry et al., 2005)

caused by the oxidation of UO_2 might be the limiting step of the oxidation reaction. As a consequence, the sample surface composition might be the same for both cases. From 200 to 350 ^{0}C the oxidized state of the sample surface decreased. Since the increase of the temperature should enhance the oxidation of UO_2, the possible cause might be the increase and/or the activation of the hydrogen reducing effect. These results have been published by Espriu-Gascon et al. (2015).

Effect of a reducing environment

As it has been explained in the General Introduction of this thesis, the conditions of the CTS and the DGR might be different: the first one will be under natural air convection and the second one under reducing conditions due to the metallic canister corrosion. The two environments showed to have different effects on the UO_2 surface especially at high temperatures.

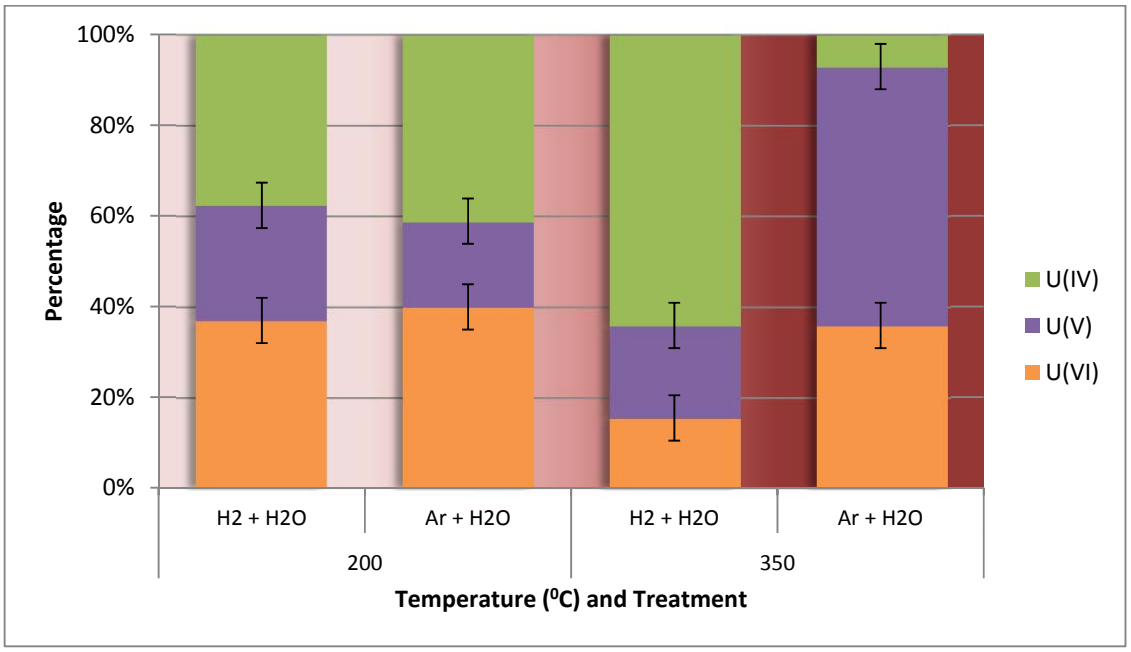

Figure 3. 12 Evolution of the uranium oxidized state as a function of the treatment and the experimental temperature on the UO_2 sample

In Figure 3. 12 the effect of the H_2 can be observed compared with the results obtained under anoxic and reducing atmosphere.

The results obtained at 200^{0}C are considered to be the same oxidized state regarding the intrinsic measurement errors of the XPS and the fitting routine used. This can be observed in the U4$f_{7/2}$ band positions that were 380.0 eV for the T-H_2 -H_2O (200) and 380.1 eV for the T-Ar-H_2O (200) which are

within the XPS measurement error (± 0.1 eV) (see Table B. 1 and Table B. 2). Hence, both systems are assumed to show the same behavior at 200^0C.

At 350^0C, the uranium oxidized state was more oxidized under argon atmosphere than under hydrogen atmosphere. In Figure 3. 12, it can be observed that the U(IV) contribution obtained under argon atmosphere was the lowest (7.1%) while the U(IV) contribution obtained under hydrogen atmosphere was the highest (64.2%). At the same time, the amount of U(VI) obtained after performing the T-Ar-H_2O (350) treatment was (35.8%) equals to the sum of the U(V) and the U(VI) contributions after the T-H_2-H_2O (350) (20.4 and 15.4% respectively). Therefore, the presence of hydrogen avoided further oxidation of the U(V) to U(VI) and the oxidation of U(IV) to U(V). This fact might be due to the attenuating effect of the hydrogen on the oxidation at high temperatures.

Pd doped Samples

Samples characterization

The palladium doped samples were analyzed by electron microscopy in order to characterize the palladium particles. A small amount of each sample was also dissolved in acidic dissolution and analyzed by Inductively Coupled Plasma Mass Spectrometry (ICP-MS) in order to determine the exact ratio between Pd and U.

Electron Microscopy Images

TEM and S/TEM were used to observe the synthesized palladium particles in nanometric scale. These techniques allow to determine the location, shape and size of the Pd particles.

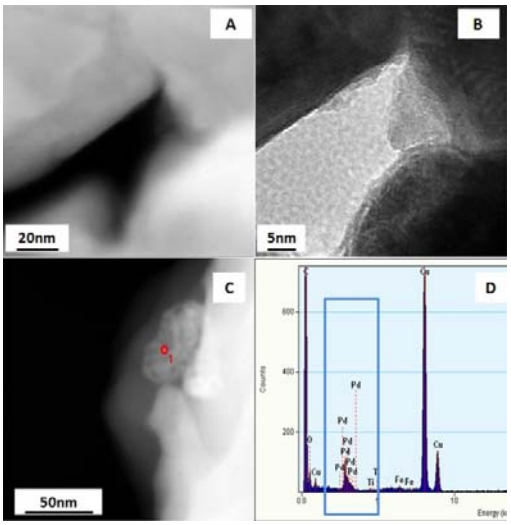

Figure 3. 13 S/TEM image (A); HR-TEM image of the same in A (B); S/TEM image of a particle observed in the edge (C); EDS of the red dot in the C verifying the presence of Pd at nanometric scale(D).

The same sample region can be observed in Figure 3. 13 (A) and (B) using different techniques and scales. In Figure 3. 13 (A), where the S/TEM was used, the heavier compound is shown in white. Since UO_2 is heavier than Pd, and palladium is expected to be forming nanoparticles (NPs) while the UO_2 particle size is larger, such white zones could be hiding the Pd-NPs. In Figure 3. 13 (B) (HR-TEM image) the same image in Figure 3. 13 (A) is shown with the darker regions for the heavier compounds and the white regions for light compounds. Two compounds can be observed in the center of this image. EDS was performed in the grey region and it determined that the precipitate was Pd. It can also be observed in the same image that the Pd size was in the nanometric scale order.

Another sample region is shown in order to check for other Pd-NPs on the sample. In Figure 3. 13 (C) obtained by S/TEM, another region is shown with a clear grey zone. To determine the composition of

this precipitate, EDS was performed on the red dot and the results showed that the particle observed was Pd (see Figure 3. 13 (D)).

In order to obtain more results and to corroborate the presence of palladium on the UO_2 surface, a linear profile was performed on another doped particle (see Figure 3. 14(A)). It can be observed that there is a precipitate on the surface of a macro-particle in the analyzed region. EDS performed on the line showed that the macro – particle contained U, as expected from UO_2 particles, and the precipitate contained Pd, as expected from the Pd-NPS (see Figure 3. 14(C) and (B) respectively). It can be observed a slight decrease of the U signal right in the region where the Pd signal was detected. This fact is caused by the Pd-NPs covering the UO_2 which shadowed the EDS signal of uranium.

Moreover, the size of the palladium particle is proved to be in the nanometric scale as it can be seen in Figure 3. 14.

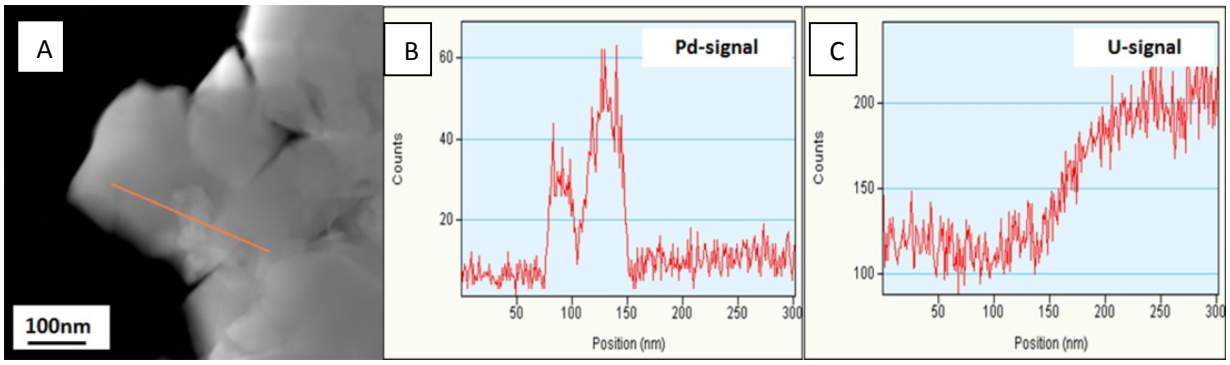

Figure 3. 14 S/TEM image; the line indicates the mapping region obtained by EDS (A); EDS signal of Pd (B); EDS signal of U (C).

Another region of the sample was analyzed. In this region, another line mapping and EDS measurements confirmed the previous observations regarding the particle size and distribution on the sample. In Figure 3. 15, the TEM image obtained of the sample is shown. It can be observed that there is a particle with the atoms arranged in columns that are parallel to the electron beam. Therefore, in Figure 3. 15 (A) and (B), white dots of the particle are the atoms forming the particle. The distance between the atoms was measured using the software *ImageJ* and the distance obtained was 335 pm. Compared with 338 pm of atomic distance of Pd^0 from the bibliographic value and considering the error of the measurement, it can be concluded that the Pd-NPs contained metallic Pd. The crystallographic structure of the particle can be identified in the electron diffractogramm in Figure 3. 15 (C). Hence, it can be conclude that the UO_2 powder was doped with Pd^0-NPs on surface. It can also be concluded that the synthesis

methodology provided Pd nanoparticles reproducing those which are expected to be precipitated in the SNF (Cui et al., 2012).

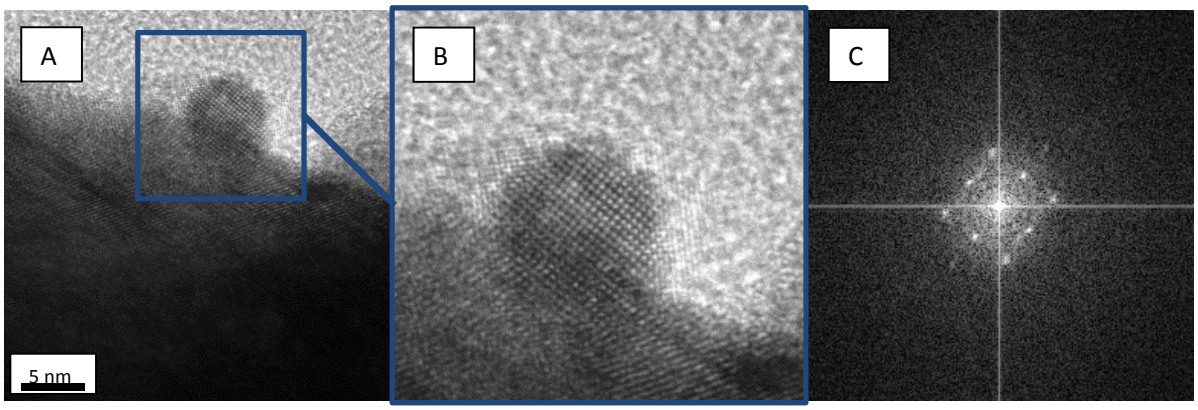

Figure 3. 15 HR-TEM image of a Pd particle at the edge of one UO_2 powder particle (A); Zoom in of A where the Pd atoms columns can be clearly observed (B); Electron diffraction of the particle (C)

Chemical Composition

From the two Pd-NPs doped samples, three samples were taken from each one of them and dissolved with HNO_3 concentrated. The concentration of the dissolution was then analyzed by ICP-MS and the results are shown in Table 3. 5.

Table 3. 5 Chemical composition of the Pd-NPs UO_2 samples obtained by ICP-MS

$\%_t$ wt. of Pd	Sample weight (g)	Pd (mg/l)	U (mg/l)	ratio Pd/U (%)
0.50%	0.013	5.4	1030	0.52%
	0.014	6.0	1130	0.53%
	0.012	5.0	950	0.53%
1.50%	0.018	7.9	1480	0.53%
	0.017	26	1350	1.93%
	0.021	31	1620	1.91%

According to the results obtained, one of the samples composition was 0.53% ± 0.01% of Pd. The other measured sample composition was 1.45% ± 0.50%. These differences between results obtained for the 1.50% doped sample might be caused by palladium precipitates, although they were not observed in the microscopic analysis their presence cannot be completely ruled out. Another possibility might be due to the synthesis methodology. During the procedure, the UO_2 powder sample is spread on a flat surface and then the palladium solution is added drop by drop. It could be that the sample was not properly spread and hence, some UO_2 powder particles might have higher content of Pd than others.

Reduction of the sample surface

Once the two samples were prepared and characterized by electron microscopy, they were analyzed by XPS in order to determine the oxidized state of uranium. The spectra showed that the uranium was clearly oxidized which might be due to preparation methodology used to obtain the doped samples.

As a consequence, the T-H_2 (350) experiment was performed on the sample. In this case the chosen temperature was lower than the reducing experiment performed on the UO_2 sample in order to preserve the characteristics of the Pd-NPs. At higher temperatures, the nanoparticles could melt and form bigger particles which might cause the loss of some important properties of the metallic nanoparticles.

The spectrum obtained showed that the surface was completely reduced. The U4f band showed the U(IV) satellite at 6.7 eV from the $U4f_{5/2}$ band, the peak position of the $U4f_{7/2}$ band was located at 379.5 eV and its FWHM was 2.0 eV for both samples.

Argon and Water Vapor Experiment

The effect of the water vapor on the samples doped with Pd has been studied at different temperatures under anoxic conditions. The experimental conditions were the same explained before for the UO_2 sample for the T-Ar-H_2O (T) experiment (see Table 3. 4). The surface was analyzed by XPS and the results of the spectra treatment can be observed in Figure 3. 16 for both samples. The de-convolution results are shown in Table A. 3 and Table A. 4 for the 0.5% and the 1.5% doped samples, respectively.

A decrease of the U(IV) band with the increase of the temperature can be observed for both samples. At the same time, the contributions of the oxidized phases increased. Both samples started with the UO_2 surface completely stoichiometric at 100^0C that was oxidized after performing the experiment at 200^0C. At this temperature the two samples are slightly different, being the one doped with 0.5% wt. of Pd more oxidized. The opposite can be observed at 350^0C where the amount of U(VI) for the 1.5% Pd sample (56.1%) was higher than the amount of U(VI) for the 0.5% Pd sample(31.4%). These results are congruent with the $U4f_{7/2}$ peak position which was higher for the 1.5% Pd sample than for the 0.5% Pd sample.

The results suggest that the water is dissociated on the samples surface at temperatures higher than 100 ^{0}C. As it happened for the non – doped sample, the content of oxygen on the sample surface might be due to the increase of the oxidation rate with the increase of temperature from Eq. (3.2).

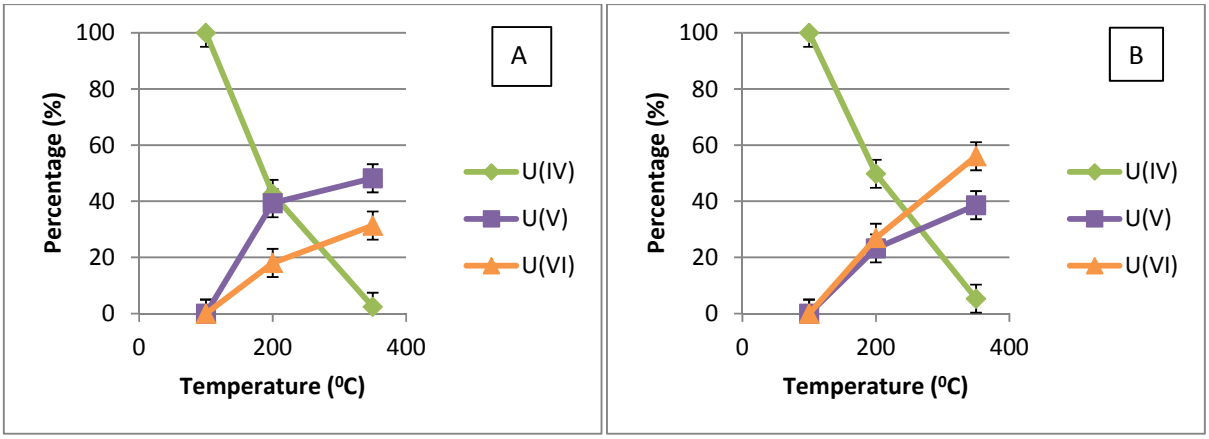

Figure 3. 16 Evolution of the uranium oxidized state contribution to the $U4f_{7/2}$ band for the 0.5% wt. Pd doped sample (A) and for the 1.5% wt. Pd doped sample (B)

The different amount of palladium in each sample showed no effect on the oxidation. If hydrogen is formed and adsorbed on the sample surface, it could have been activated by the Pd-NPs and the oxidation would have been avoided, but the results showed the opposite situation. Since the oxidation proceeded, a possible hypothesis could be that hydrogen is released before being activated and hence, the oxidation continues.

Hydrogen and Water Vapor Experiment

Regarding the possible environment in the DGR, experiments with hydrogen and water vapor were performed on the doped samples. In this case the results were exactly the same for both type of samples and so only one graphic is shown in Figure 3. 17.

In the case of the Pd-doped samples, the samples remained reduced when the T-H2-H2O (T) experiments were performed. The U4f spectrum obtained had one single satellite at 6.7 eV from the $U4f_{5/2}$ band. Regarding the $U4f_{7/2}$ band, its BE was located at 379.5 eV and the FWHM was 2.0 eV (see Table B. 5 and Table B. 6), values that have been attributed to U(IV) in Table 3. 3.

In addition, the increasing temperature had no effect on the sample surface composition as it can be seen in Figure 3. 17. The numerical results are shown in Table A. 5 for the 0.5% doped sample and in Table A. 6 for the 1.5% doped sample.

Under the conditions used in this section, it is likely that the Pd-NPs on the surface have enhanced the hydrogen reducing effect since Pd is a catalyst for hydrogen processes. As a consequence, the oxidizing effect of water vapor was completely suppressed.

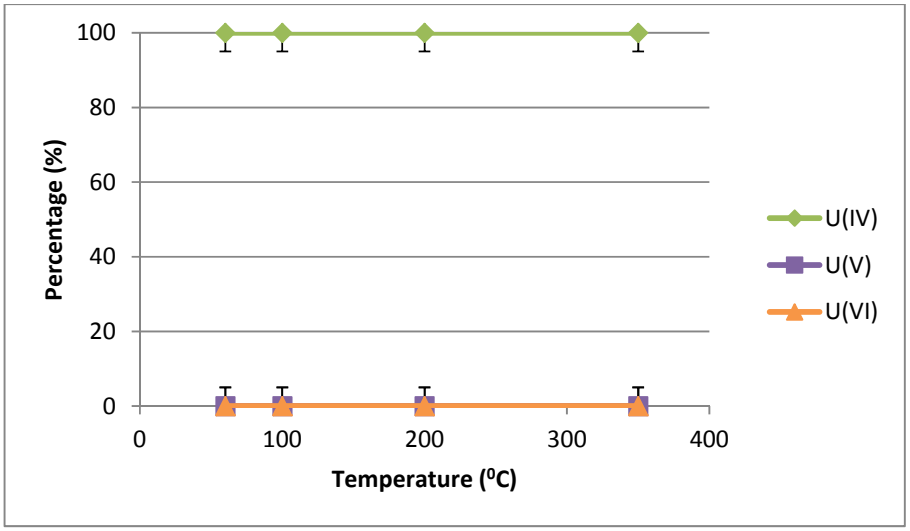

Figure 3. 17 Evolution of U(IV), U(V) and U(VI) with the temperature when the Pd-doped samples were put in contact with hydrogen and water vapor for 10 minutes

Effect of a reducing environment

In order to determine the effect of the gas used on doped samples, the experiments performed under argon atmosphere and under hydrogen atmosphere were compared as a function of the temperature. The results obtained of the uranium oxidized state are shown in Figure 3. 18 as a function of the gas stream.

The main difference observed was that under reducing atmosphere and water vapor, the surface was always U(IV) and no effect of the temperature was observed. Meanwhile, in contact with argon and water vapor, the surface was oxidized at 200 and 350^{0}C.

Regarding the results obtained in this section, it can be said that anoxic conditions may lead to an oxidation of the SNF at temperatures higher than 100^{0}C, since the oxidation has been observed for all kinds of samples under non – reactive environment.

Under reducing conditions, the oxidation of the SNF caused by the water vapor was completely suppressed as the results show (Figure 3. 18). Therefore the UO_2 is protected by the presence of both hydrogen and Pd-NPs on the sample.

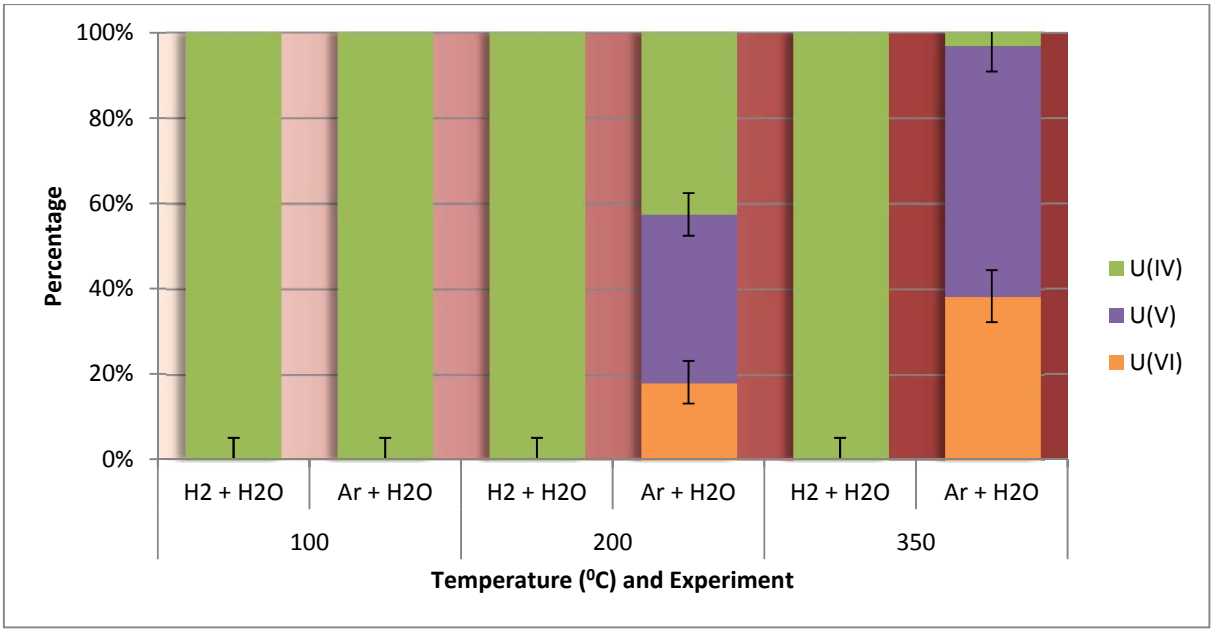

Figure 3. 18 Evolution of the uranium oxidized state as a function of the temperature and the treatment for the Pd-doped UO_2 samples

Effect of the ε-particles and metallic particles

It has been previously studied the effect of the water vapor under anoxic or reducing atmosphere on the surface of UO_2 and UO_2 doped with Pd-NPs separately. In this section a comparison among samples is presented in order to determine the effect of the palladium particles on the system.

Figure 3. 19 (A, B and C) show the evolution of each uranium oxidized state and Figure 3. 19 (D) shows the BE of $U4f_{7/2}$ band as a function of temperature for the experiments performed under argon atmosphere. The numerical results are shown in the Annex A, Table A. 7, Table A. 8, Table A. 9 and Table A. 10. U(IV) contribution (Figure 3. 19 (A)) decreased with the increase of the temperature for all the samples following a decreasing linear tendency. On the other hand, U(V) and U(IV) increased with the temperature (Figure 3. 19 (B) and (C)). It can be observed that all the samples presented similar behaviors except for the results obtained at 100^0C. At this temperature, the UO_2 sample was oxidized while the Pd doped samples showed no oxidation on their surfaces. Hence, the palladium particles avoid the oxidation process at 100^0C and showed no significant effect at higher temperatures.

A possible explanation could be that at 100 ^{0}C, the oxygen might be reacting with the hydrogen before being diffused into the UO_2 sample bulk. This process could be additionally enhanced by the presence of Pd-NPs.

This fact is not observed at higher temperatures probably due to the oxygen diffusion into the sample bulk. Since the oxygen diffusion rate depends on the temperature, at 200 and 350 ^{0}C the oxygen diffusion could be kinetically favored over the reduction effect of the hydrogen produced from water hydrolysis observed previously (Cohen et al., 2014; Ferry et al., 2005; Hedhili et al., 2000; Higgs et al., 2007; Senanayake et al., 2007b, 2005; Stultz et al., 2004).

On the other hand under hydrogen atmosphere, samples doped with palladium had a different behavior from the non-doped sample (Figure 3. 20). It can be observed that the UO_2 sample was oxidized in contact with hydrogen saturated with water vapor while the Pd doped samples showed no oxidation on the surface (see Table A. 11, Table A. 12 and Table A. 13). These results in Figure 3. 20 (A, B and C) are congruent with the U $4f_{7/2}$ band position in Figure 3. 20 (D). In Table A. 14, it can be seen that the BE of the UO_2 sample varied while the BE of Pd doped samples was constant.

It can be concluded that Pd-NPs protected the UO_2 from oxidation under hydrogen atmosphere. Under anoxic conditions, this protective effect was only observed at temperatures lower than 100^{0}C.

Both samples had the same oxidation state after performing the T-H_2-H_2O (T) experiments and hence, no significant effect of the amount of Pd was observed. This fact might happen because 0.5% w/w of Pd-NPs is enough to completely avoid any oxidation caused by the water molecule dissociation.

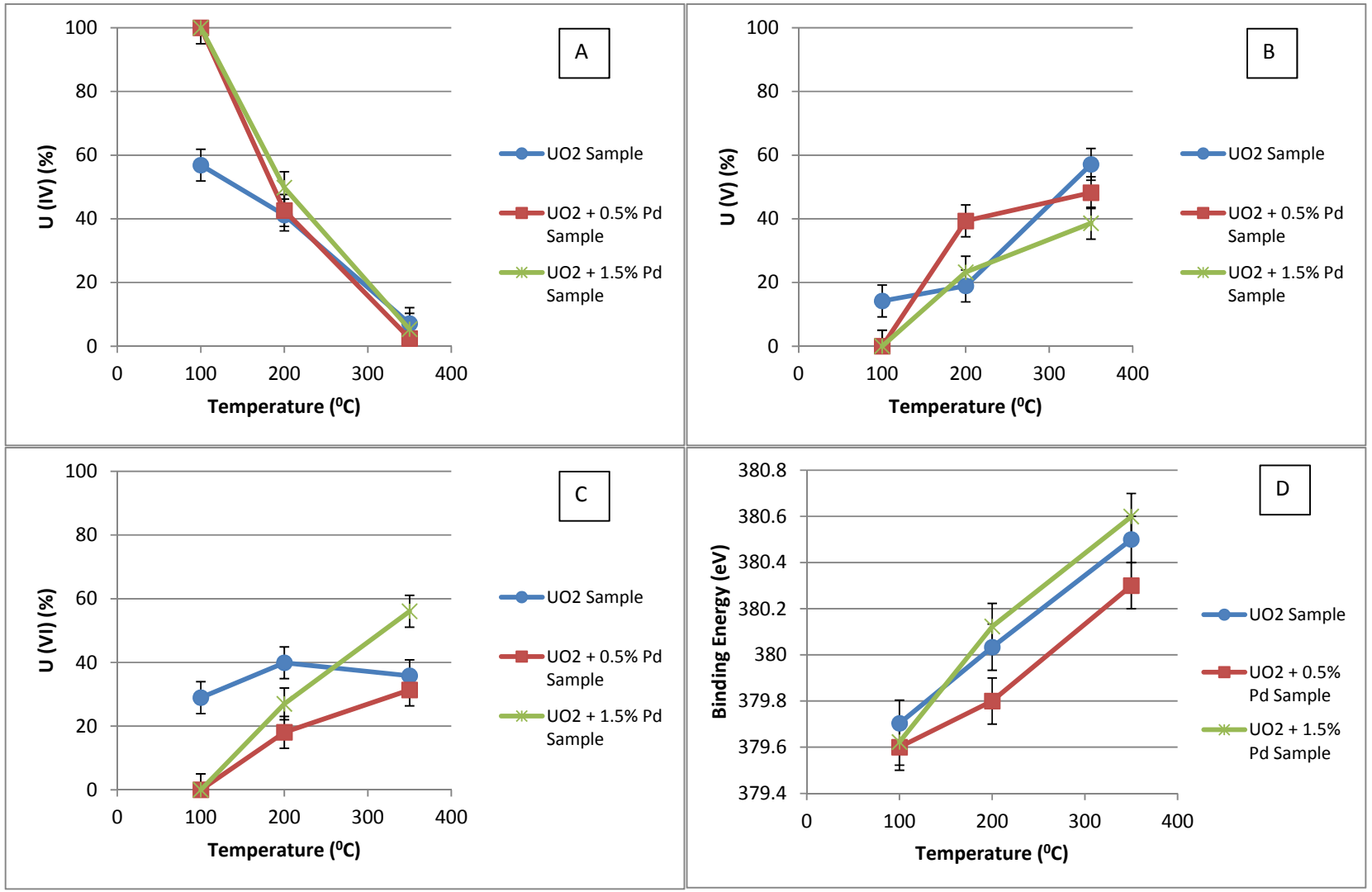

Figure 3. 19 Evolution of the amount of U(IV) (A), U(V) (B) and U(VI) (C) as a function of the temperature and the type of sample; Evolution of the $U4f_{7/2}$ band position with the temperature (D) when the samples were put in contact with Ar and with water vapor at a constant temperature for 10 minutes.

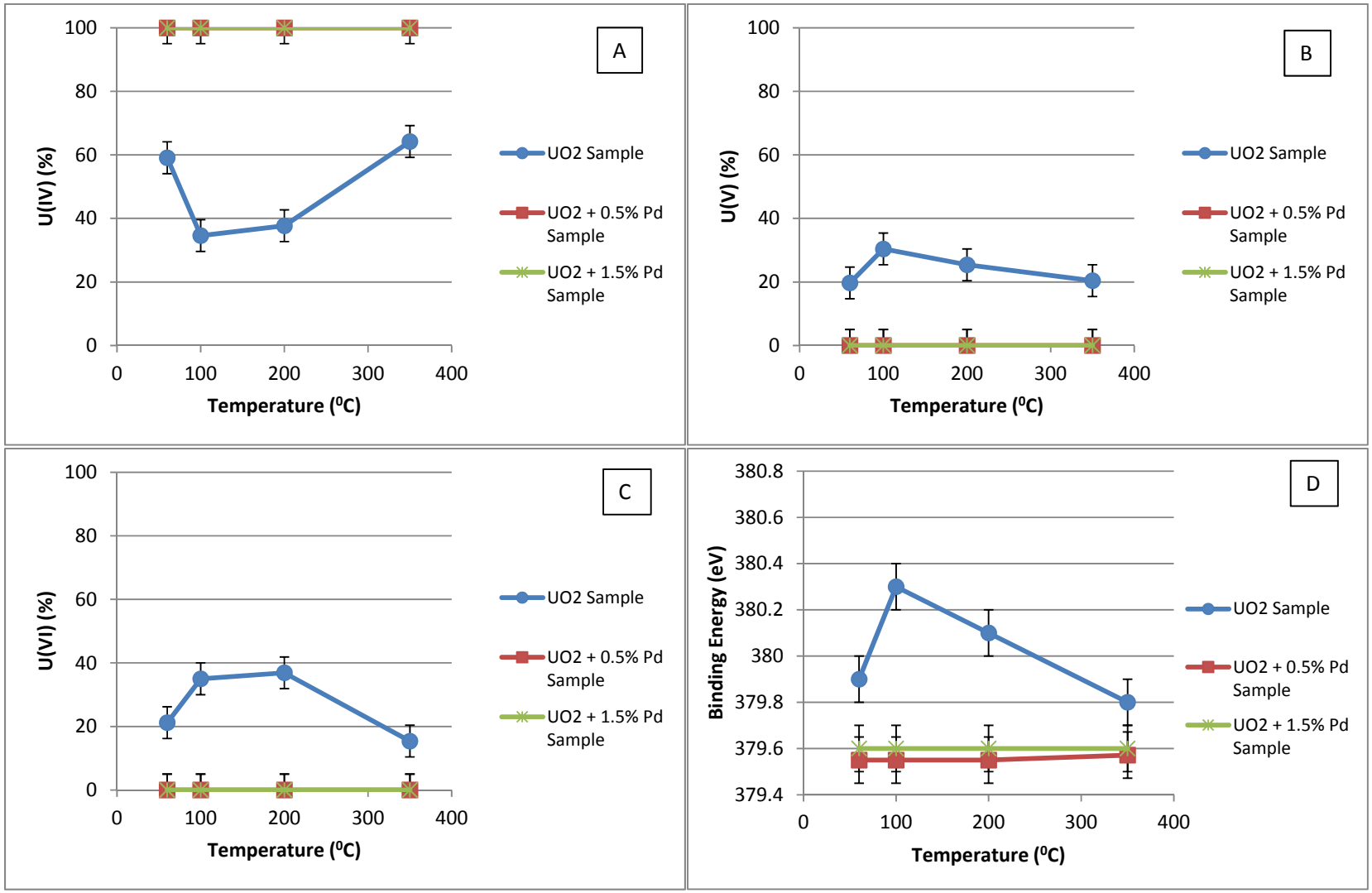

Figure 3. 20 Evolution of the amount of U(IV) (A), U(V) (B) and U(VI) (C) as a function of the temperature and the type of sample; Evolution of the $U4f_{7/2}$ band position with the temperature (D) when the samples were put in contact with H_2 and with water vapor at a constant temperature for 10 minutes.

Conclusions

In this chapter, the effect of water vapor under anoxic and reducing conditions on the UO_2 surface has been studied. The effect of Pd-NPs on the process mentioned has been also studied with the objective of getting a better approach to the SNF. The oxidation state was determined by using the $U4f_{7/2}$ XPS bans which has been de-convoluted into U(IV), U(V) and U(VI) bands to obtain the surface oxidized state.

UO_2 sample under argon saturated with water vapor showed that the uranium oxidized state increased with the increase of temperature. Therefore, water had an oxidizing effect on the sample surface enhanced with the increase of the temperature. A maximum of the oxidized state was reached at 350^0C when the amount of U(V) and U(VI) were 57.1 % and 35.8 %, respectively. These results are in good agreement with the ones reported for water vapor (Cohen et al., 2014; Ferry et al., 2005; Hedhili et al., 2000; Higgs et al., 2007; Senanayake et al., 2007b, 2005; Stultz et al., 2004).

When the UO_2 sample was put in contact with a hydrogen stream saturated with water vapor the oxidation of U(IV) was also observed. In this case, the tendency of the oxidized state of uranium was different from the tendency observed under argon atmosphere: the highest oxidation was observed from 120 to 200 ^{0}C when the amount of U(IV) was between 34.6 and 37.7 %. At 350^0C, the oxidation was limited by the presence of hydrogen which partially avoided oxidation and the amount of U(IV) increased to 64% compared with the results at 100 and 200 ^{0}C.

Two different types of palladium doped samples were prepared using the doping immersion methodology. They were characterized by using electron microscopic techniques and the results showed that metallic Pd-NPs were deposited on the UO_2 powder particles. The chemical composition of the synthetized samples was 0.5% wt. of Pd (±0.05) and 1.5% wt. of Pd (±0.5).

When the experiments under an argon stream saturated with water vapor were performed on the Pd-doped samples, the results showed similar behaviors for both samples. They both were oxidized at temperatures higher than 100^0C and the oxidation process was enhanced with the increase of the temperature. The minimum amount of U(IV) was reached at 350^0C with 2.4% and 5.2% for 0.5% and 1.5 % wt. doped samples, respectively.

On the other hand, when the experiments were performed in contact with a hydrogen stream saturated with water vapor, no oxidation was observed at any temperature.

Comparing the results obtained among samples under argon and water vapor conditions, it seems evident that the presence of Pd-NPs avoided any significant oxidation at 100 ^{0}C. When the temperature was increased, the presence of Pd-NPs showed no significant effect on the UO_2 oxidation. Moreover, the increase of the temperature from 200 to 350 ^{0}C caused an increase of the uranium oxidation under argon atmosphere despite the presence of palladium. This fact might be caused by the enhancement of oxygen diffusion into the sample bulk with the increase of the temperature.

When the experiments were performed under hydrogen saturated with water, a clear effect of the Pd-NPs was observed. While the UO_2 sample was oxidized due to the water vapor effect, the Pd doped sample surface remained reduced. This happened for all the temperatures used in this study and hence, the surface oxidation was completely avoided in presence of the Pd-NPs and the reducing atmosphere probably due to the catalytic effect of the Pd-NPs.

Bibliography

Allen, G.C., Tempest, P.A., Tyler, J.W., 1987. Oxidation of Crystalline UO_2 , studied using X-Ray Photoelectron Spectroscopy and X-Ray Diffraction. J. Chem. Soc. Faraday Trans. 1 83, 925–935. doi:10.1039/F19878300925

Aronson, S., Roof, R.B., Belle, J., 1957. Kinetic study of the oxidation of uranium dioxide. J. Chem. Phys. 27, 137–144. doi:10.1063/1.1743653

Belle, J., 1961. Uranium dioxide: properties and nuclear applications. Naval Reactors, Division of Reactor Development, US Atomic Energy Commission.

Cohen, S., Mintz, M.H., Zalkind, S., Seibert, A., Gouder, T., Shamir, N., 2014. Water chemisorption on a sputter deposited uranium dioxide film - Effect of defects. Solid State Ionics 263, 39–45. doi:10.1016/j.ssi.2014.05.003

Cui, D., Rondinella, V.V., Fortner, J. a., Kropf, a. J., Eriksson, L., Wronkiewicz, D.J., Spahiu, K., 2012. Characterization of alloy particles extracted from spent nuclear fuel. J. Nucl. Mater. 420, 328–333. doi:10.1016/j.jnucmat.2011.10.015

Espriu-Gascon, A., Bastos-Arrieta, J., Gimenez, J., Casas, I., de Pablo, J., 2016. Preparation and characterisation of Pd nanoparticles doped UO2 samples. Int. J. Nanotechnol. 13, 627–633. doi:10.1504/IJNT.2016.079665

Espriu-Gascon, A., Llorca, J., Domínguez, M., Giménez, J., Casas, I., de Pablo, J., 2015. UO_2 surface oxidation by mixtures of water vapor and hydrogen as a function of temperature. J. Nucl. Mater. 467, 240–243. doi:10.1016/j.jnucmat.2015.09.047

Ferry, C., Poinssot, C., Broudic, V., Cappelaere, C., Desgranges, L., Garcia, P., Jegou, C., Lovera, P., Marimbeau, P., Corbel, C., Miserque, F., Piron, J.P., Poulesquen, A., Roudil, D., Gras, J.M., Bouffioux, P., 2005. Referentiel scientifique sur l'evolution a long terme des combustibles uses. Technical Report.

Grambow, B., 2010. Model Uncertainty for the Mechanism of Dissolution of Spent Fuel in Nuclear Waste Repository. Final MICADO Project report. European Commission. doi:10.2777/25846

Guéneau, C., Chartier, A., Brutzel, L. V., 2002. Thermodynamic and thermophysical properties of the actinides oxides, in: Konings, R. (Ed.), Comprehensive Nuclear Materials. Elsevier, Amsterdam, 2012.

Haschke, J.M., 1998. Corrosion of uranium in air and water vapor: Consequences for environmental dispersal. J. Alloys Compd. 278, 149–160. doi:10.1016/S0925-8388(98)00639-2

Hedhili, M.N., Yakshinskiy, B. V, Madey, T.E., 2000. Interaction of water vapor with UO_2 (0 0 1). Surf. Sci. 445, 512–525. doi:10.1016/S0039-6028(99)01117-6

Higgs, J.D., Lewis, B.J., Thompson, W.T., He, Z., 2007. A conceptual model for the fuel oxidation of defective fuel. J. Nucl. Mater. 366, 99–128. doi:10.1016/j.jnucmat.2006.12.050

Hyun, D., Kim, J., 2004. Study of external humidification method in proton exchange membrane fuel cell. J. Power Sources 126, 98–103. doi:10.1016/j.jpowsour.2003.08.041

Idriss, H., 2010. Surface reactions of uranium oxide powder, thin films and single crystals. Surf. Sci. Rep. 65, 67–109. doi:10.1016/j.surfrep.2010.01.001

Ilton, E.S., Boily, J.-F., Bagus, P.S., 2007. Beam induced reduction of U(VI) during X-ray photoelectron spectroscopy: The utility of the U4f satellite structure for identifying uranium oxidation states in mixed valence uranium oxides. Surf. Sci. 601, 908–916. doi:10.1016/j.susc.2006.11.067

Leenaers, A., Sannen, L., Van den Berghe, S., Verwerft, M., 2003. Oxidation of spent UO_2 fuel stored in moist environment. J. Nucl. Mater. 317, 226–233. doi:10.1016/S0022-3115(03)00104-1

MacCrone, R.K., Sankaran, S., Shatynski, S.R., Colmenares, C.A., 1986. Complex defects in the oxidation of uranium. Metall. Trans. A 17, 911–914. doi:10.1007/BF02661256

McEachern, R.J., 1997. A review of kinetic data on the rate of U_3O_7 formation on UO_2. J. Nucl. Mater. doi:10.1016/S0022-3115(96)00733-7

McEachern, R.J., Taylor, P., 1998. A review of the oxidation of uranium dioxide at temperatures below 400°C. J. Nucl. Mater. 254, 87–121. doi:10.1016/S0022-3115(97)00343-7

McEachern, R.J., Taylor, P., 1994. On the reported anisotropic rate of formation of U_4O_9 on UO_2. J. Nucl. Mater. 217, 322–324.

Nakamura, J., Otomo, T., Kawasaki, S., 1993. Oxidation of UO_2 under dry storage condition. J. Nucl. Sci. Technol. 30, 181–184. doi:10.1080/18811248.1993.9734466

Perry, R.H., Green, D.W., Maloney, J.O., 1997. Chemical Engineer Handbook, McGraw-Hil. ed.

Poulesquen, A., Desgranges, L., Ferry, C., 2007. An improved model to evaluate the oxidation kinetics of uranium dioxide during dry storage. J. Nucl. Mater. 362, 402–410. doi:10.1016/j.jnucmat.2007.01.084

Quémard, L., Desgranges, L., Bouineau, V., Pijolat, M., Baldinozzi, G., Millot, N., Nièpce, J.C., Poulesquen, A., 2009. On the origin of the sigmoid shape in the UO_2 oxidation weight gain curves. J. Eur. Ceram. Soc. 29, 2791–2798. doi:10.1016/j.jeurceramsoc.2009.04.010

Rousseau, G., Desgranges, L., Charlot, F., Millot, N., Nièpce, J.C., Pijolat, M., Valdivieso, F., Baldinozzi, G., Bérar, J.F., 2006. A detailed study of UO_2 to U_3O_8 oxidation phases and the associated rate-limiting steps. J. Nucl. Mater. 355, 10–20. doi:10.1016/j.jnucmat.2006.03.015

Santos, B.G., Nesbitt, H.W., Noël, J.J., Shoesmith, D.W., 2004. X-ray photoelectron spectroscopy study of anodically oxidized SIMFUEL surfaces. Electrochim. Acta 49, 1863–1873. doi:10.1016/j.electacta.2003.12.016

Senanayake, S.D., Idriss, H., 2004. Water reactions over stoichiometric and reduced UO_2(111) single crystal surfaces. Surf. Sci. 563, 135–144. doi:10.1016/j.susc.2004.06.169

Senanayake, S.D., Rousseau, R., Colegrave, D., Idriss, H., 2005. The reaction of water on polycrystalline UO_2: Pathways to surface and bulk oxidation. J. Nucl. Mater. 342, 179–187. doi:10.1016/j.jnucmat.2005.04.060

Senanayake, S.D., Waterhouse, G.I.N., Chan, A.S.Y., Madey, T.E., Mullins, D.R., Idriss, H., 2007a. Probing Surface Oxidation of Reduced Uranium Dioxide Thin Film Using Synchrotron Radiation. J. Phys.

Chem. C 111, 7963–7970. doi:10.1021/jp068828g

Senanayake, S.D., Waterhouse, G.I.N., Chan, a. S.Y., Madey, T.E., Mullins, D.R., Idriss, H., 2007b. The reactions of water vapour on the surfaces of stoichiometric and reduced uranium dioxide: A high resolution XPS study. Catal. Today 120, 151–157. doi:10.1016/j.cattod.2006.07.040

Serrano-Purroy, D., Clarens, F., González-Robles, E., Glatz, J.P., Wegen, D.H., de Pablo, J., Casas, I., Giménez, J., Martínez-Esparza, A., 2012. Instant release fraction and matrix release of high burn-up UO_2 spent nuclear fuel: Effect of high burn-up structure and leaching solution composition. J. Nucl. Mater. 427, 249–258. doi:10.1016/j.jnucmat.2012.04.036

Stultz, J., Paffett, M.T., Joyce, S.A., 2004. Thermal Evolution of Hydrogen Following Water Adsorption on Defective UO_2 (100). J. Phys. Chem. 2, 2362–2364. doi:10.1021/jp031066u

Stumpf, S., Seibert, A., Gouder, T., Huber, F., Wiss, T., Römer, J., 2009. Development of fuel-model interfaces: Investigations by XPS, TEM, SEM and AFM. J. Nucl. Mater. 385, 208–211. doi:10.1016/j.jnucmat.2008.08.061

Sunder, S., Miller, N.H., 1996. Oxidation of CANDU uranium oxide fuel by air in gamma radiation at 150°C. J. Nucl. Mater. 231, 121–131. doi:10.1016/0022-3115(96)00347-9

Taylor, P., 2005. Thermodynamic and kinetic aspects of UO_2 fuel oxidation in air at 400–2000K. J. Nucl. Mater. 344, 206–212. doi:10.1016/j.jnucmat.2005.04.043

Van den Berghe, S., Laval, J.-P., Gaudreau, B., Terryn, H., Verwerft, M., 2000. XPS investigations on cesium uranates: mixed valency behaviour of uranium. J. Nucl. Mater. 277, 28–36. doi:10.1016/S0022-3115(99)00146-4

Wagner, C.D., Riggs, W.M., Davis, L.E., Moulder, J.F., Muilenber, G.E., 1979. Handbook of X-Ray Photoelectron Spectroscopy.pdf. Perkin-Elmer Corporation, Minesota, USA.

Wasywich, K.M., Hocking, W.H., Shoesmith, D.W., Taylor, P., 1993. Differences in oxidation behavior of used CANDU fuel during prolonged storage in moisture-saturated air and dry at 150°C. Nucl. Technol. 104, 309–329.

Westrum, E.F., Grønvold, F., 1962. Triuranium heptaoxides: Heat capacities and thermodynamic properties of α- and β-U_3O_7 from 5 to 350°K. J. Phys. Chem. Solids 23, 39–53. doi:10.1016/0022-3697(62)90055-0

Winer, K., Colmenares, C.A., Smith, R.L., Wooten, F., 1987. Interaction of water vapor with clean and oxygen-covered uranium surfaces. Surf. Sci. 183, 67–99. doi:10.1016/S0039-6028(87)80336-9

Chapter 4:
Design of a mathematical model to predict the radionuclides release and the contribution to the IRF in leaching experiments

Introduction

Once the groundwater will get in contact with the spent fuel, the oxidized uranium layer will dissolve with the RNs contained in it. The rest of the matrix of the SNF will dissolve more slowly due to its low solubility.

The release of the FP can be classified within three different groups by comparing their release with that of the matrix. There is one group of RNs that are completely dissolved in the matrix, hence their release is controlled by the matrix dissolution. Other RN will be partially segregated forming insoluble solid phases, hence their release will be lower than the matrix. The last group includes RNs that are partially segregated from the matrix, and show a faster release than the SNF matrix. The release of this last group of RN is expected to govern the initial radiation dose that could arise from the SNF to the environment (González-Robles et al., 2015; Johnson et al., 2012, 2005; Werme et al., 2004)

Instant Release Fraction (IRF)

The fraction of the inventory of safety-relevant RN that will be released from the SNF and the fuel assembly at a faster dissolution rate than the matrix is considered as the Instant Release Fraction (IRF) (Johnson et al., 2005, 2004; Kienzler and González-Robles, 2013; Serrano-Purroy et al., 2012, 2011) (see Figure 4. 1). Its composition and value depends on the location of the RNs in the fuel after the irradiation and the evolution of the SNF before the contact between SNF and groundwater takes place (Johnson et al., 2005). Depending on the RN physical state and its location, two types of IRF can be distinguished (Johnson et al., 2012; Roth et al., 2013; Werme et al., 2004).

The rapid release fraction (RRF) is referred as the release from the fuel / cladding gap. Some authors consider the RRF to lasts for the first weeks or months of leaching time (Johnson et al., 2012).

Another part of the IRF will be released slower than the RRF and separately from the UO_2 matrix. This release is also considered as IRF and it takes into account the RNs segregated to the grain boundaries (GB) of the fuel. It is expected to lasts for a longer time than the RRF.

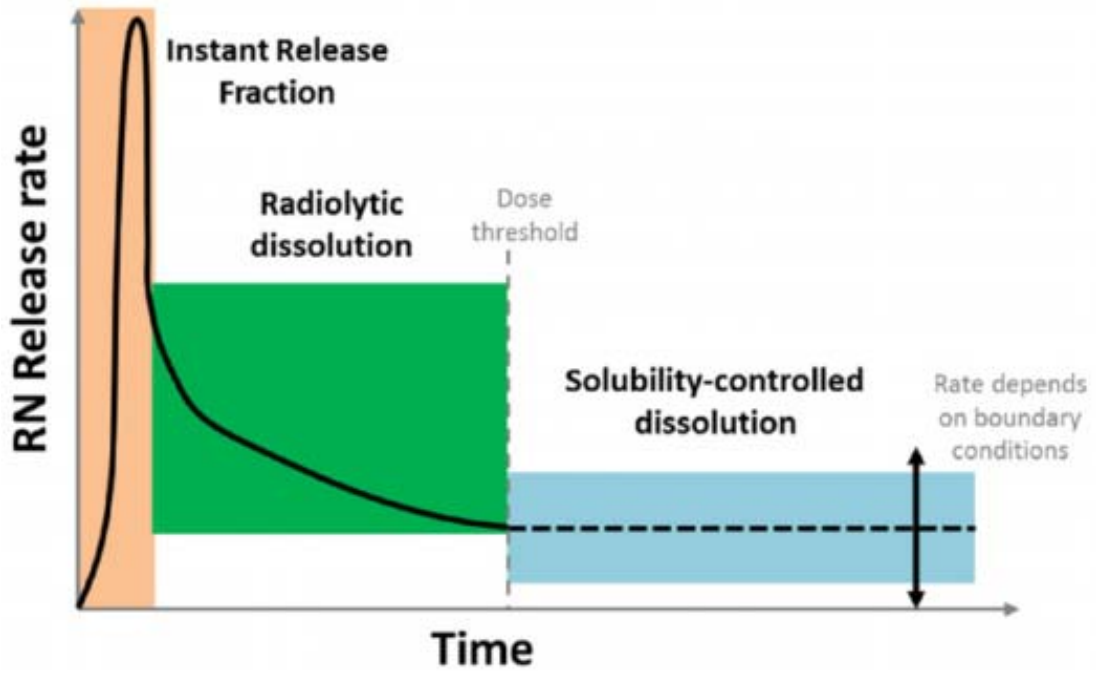

Figure 4. 1 Schematic representation of the main kinetic regimes of the spent fuel provided by Poinssot and Gin (2012)

Location of radionuclides

Even though the location of the radionuclides has been explained in Chapter 1, here a brief description is done concerning the IRF and the RN expected to contribute to it. The RNs expected to be dissolved in the matrix and to dissolve congruently with the matrix will not be considered in this section.

During the irradiation, the RNs migrate through the SNF due to the thermal gradient between the center of the fuel and its outer region. This migration is influenced by the RNs boiling and melting temperature. Hence, volatile and mobile RN will be partially segregated from the matrix to the gap region and surfaces such as cracks, fractures and GB and plenum of the fuel rod.

Gap and empty volumes

Here the most volatile RNs are expected to be located as fission gases and/or also segregated. Some examples of key RN located in the gap region are ^{129}I, ^{137}Cs, ^{135}Cs, ^{36}Cl and ^{79}Se. There are some doubts about the possibility of finding ^{126}Sn and ^{14}C (Johnson et al., 2005, 2004). The elements contained in this part of the SNF are considered to contribute to the IRF.

Empty volumes are filled with fission gasses (FG) (Krypton and Xenon) which can also be found dissolved in the SNF forming bubbles. The FG release was studied by González-Robles and Fuβ (2015) who observed an evolution of the FG with time.

On the other hand, the release of FP on the sheath walls, SNF outer surface and macro –cracks were studied by using segmented samples of spent fuel including the cladding (Ekeroth et al., 2012; González-Robles et al., 2015; Roudil et al., 2007).

Rim structure

In this part of the SNF there are bubbles and pores that contain part of the inventory of fission gases and volatiles such as ^{129}I, ^{137}Cs, ^{135}Cs, ^{36}Cl, ^{79}Se and ^{126}Sn. Additionally, these RN are also found inside the UO_2 grains of the rim zone. The most pessimistic estimations[1] consider these elements as part of the IRF (Johnson et al., 2005, 2004).

Due to its proximity to the gap, this region of the fuel is of interest for the performance assessment , hence leaching experiments were performed on rim samples (Roudil et al., 2009). In the study performed by Roudil et al. (2009) it was observed that the inventory of $^{134/137}Cs$ and ^{90}Sr in the rim was higher than the gap and GB for samples with high burn – up (BU) (60 MWd/kgU). Nevertheless, regarding the results obtained, the authors suggested that the contribution of the rim to the IRF might be less than expected due to the small dimensions of this region (volume and weight) compared with the full pellet.

Grain boundaries

Volatile RNs with high diffusion coefficient are located at the grain boundaries, such as ^{129}I, ^{137}Cs, ^{135}Cs, ^{36}Cl, ^{79}Se and probably ^{126}Sn. Also, segregated metallic alloys can be found in there suc as ^{99}Tc or ^{107}Pd (Johnson et al., 2005).

The contribution of the GB to the IRF is considered in the most pessimistic scenarios due to the difficulty of determining their leachability and long – term stability (Johnson et al., 2004, 1985). Some hypotheses consider that during the IRF-relevant time scale, a selective dissolution of the GB might occur while the core of the grain might remain undissolved. In that case, the soluble FPs and FG enclosed as bubbles in the GB might be leached out gradually; this process will cause the increase of the surface area exposed to ground water.

[1] Such over predictions of average IRF values are mostly made in cases where data is limited or unavailable, and analogues are used to derive estimates.

Mathematical models of the RN release

During the 'Spent Fuel Stability' (SFS) European Project (Poinssot et al., 2005), a general IRF model was developed in order to predict the instant release as a function of time. This model first assumed that the grains shape was spherical with 8 μm of diameter. The second assumption was that the diffusion along GB was higher than in the grain core (through UO_2 grains). The third hypothesis was that the RN redistribution after the fuel discharge was controlled by α self – irradiation enhanced diffusion. Assuming that water penetrates the GB and pores rapidly and considering pessimistic values of gap, GB and pore inventories, the model predicted the values of IRF observed in Table 4. 1. In this table, the values indicated are bounding values of the IRF.

Table 4. 1 Estimated IRF values (%) of some mobile FP for a PWR UO_2 fuel with 55 of BU. Estimations at different breaching times (Poinssot et al., 2005).

Nuclide	After Irradiation	Container failure time (years)		
		1,000	10,000	100,000
^{14}C	10	13	14	16
^{36}Cl	11	14	15	17
^{79}Se	11	14	15	17
^{129}I	11	14	15	17
^{135}Cs	11	14	15	17

In the study performed by Pekala et al. (2014) in the European project 'Fast / Instant Release of Safety Relevant Radionuclides from Spent Nuclear Fuel' (FIRST – Nuclides Project), the authors provided a model based on the water saturation of the SNF. The model quantifies the filling of the cracks, all the interconnected smaller cracks and available fuel surfaces by water gradually in a segmented sample. The authors considered that water controls the release of some RN at the SNF pellet by wetting of available surfaces such as lateral faces of the pellet and cracks. Comparing their results with experimental leaching data of some RNs, the authors observed that release rate are radionuclide – specific and suggested the RN different chemical properties as a possible cause for this behavior (see Figure 4. 2).

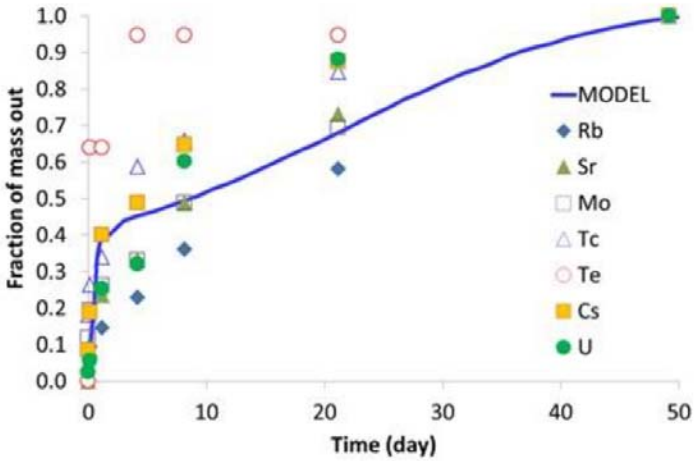

Figure 4. 2 Prediction of the RN mass accumulated in the leachant as a function of time compared with experimental leaching data from a SNF pellet (González-Robles, 2011) (normalized to unity) taking into account that 40% of the total release is initially located in macro – cracks

Estimations of IRF

Since Iodine and Cesium have long – lived isotopes, they have been of interest in previous works (Ekeroth et al., 2012; González-Robles et al., 2016; Johnson et al., 2004). Werme et al. (2004) and Johnson et al. (2004) determined a correlation between the FGR and the ^{129}I and ^{137}Cs release during leaching experiments. This correlation allows to estimate their contribution to the IRF.

During the experiments performed by Wilson (1990) the authors observed that gap and GB release data of ^{137}Cs and ^{129}I were correlated with the FGR (see Figure 4. 3 and Figure 4. 4). Later, more data were provided and gap and GB inventories of some RNs where reported by Johnson et al. (2004) as shown in Table 4. 2.

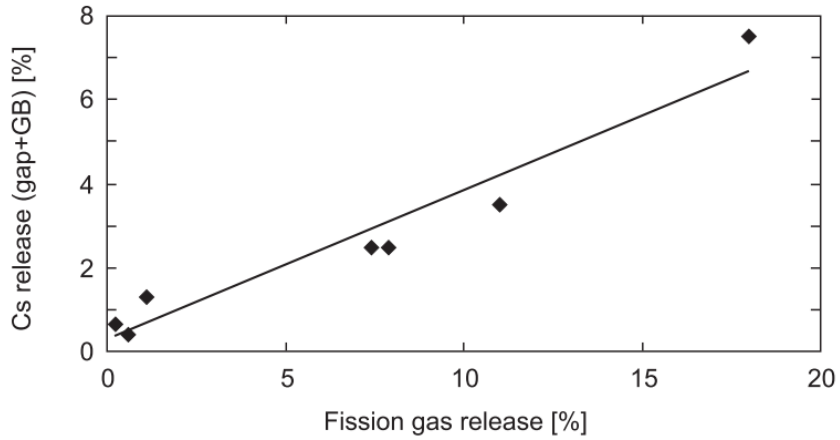

Figure 4. 3 Release of ^{137}Cs from the gap and GB as a function of the FGR from Johnson et al. (2004)

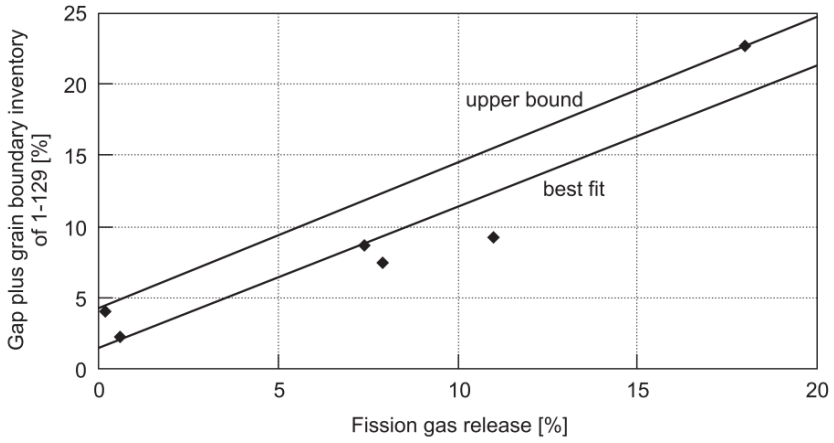

Figure 4. 4 Release data of ^{129}I from the gap and GB as a function of the FGR from Johnson et al. (2004)

It can be observed that a correlation ^{137}Cs : FGR can be stablished at 1 : 3 approximately. This fact is consistent with the different diffusion coefficients of Cs and the fission gases. However, Johnson and Tait (1997) observed that the correlation between Cs and FGR is not always 1 : 3. In fact, when the IRF was lower than 1% the release of ^{137}Cs is similar to the FGR.

In the case of Iodine, Gray (1999) suggested that there is a 1 : 1 correlation between the FGR and iodine in the gap and GB which is in good agreement with the similarity between both diffusion coefficients. As a consequence, the majority of the ^{129}I from the matrix might be located at the GB (Johnson et al., 2004).

It was accepted that estimating the RN release by FGR might be a good option to provide with a good bounding estimate of the IRF. The final maximum estimation of the IRF corresponding to pessimistic assumption was determined to be the iodine release (Johnson et al., 2004; Poinssot et al., 2005). This value provides the maximum value of IRF which follows the sequence (Johnson et al., 2005):

$$FGR \approx I > Cs > \text{other RN}$$

The objective of some European Projects such as SFS (Poinssot et al., 2005), Near Field Processes (NF-PRO) (Grambow et al., 2008) and FIRST-Nuclides (Kienzler et al., 2014) was to obtain a better understanding of the IRF. Therefore, more data on the RN release was obtained in the framework of these projects. Some of them are reported in Table 4. 2 by Johnson et al. (2004), other ones were obtained by Roudil et al. (2007) and summarized by González-Robles, E. (2011). Also, data from Johnson et al. (2012) has been added to the reported IRF values in Table 4. 2.

Table 4. 2 Gap and GB leaching data (%) for different types of fuels with their characteristic BU (MWd/kg_U) and FGR (%)

Fuel ID	BU	FGR	Cs Gap	Cs GB	Sr Gap	Sr GB	Tc Gap	Tc GB	I Gap	I GB	C Gap
BWR (Oskarsham)[a]	42	0.7	≈ 1								
BWR (Ringhals)[a]	20 – 49	1.1	0.4 – 0.8		0.07		0.1 to 0.7				
PWR (Ringhals)[a]	43	1.05	≈ 1								
ATM-103 (PWR)[a]	30	0.25	0.2	0.48	0.01	0.11					
ATM-104 (PWR)[a]	44	1.1	1.2	0.1							
ATM-105 (BWR)[a]	31	0.59	0.3	0.1					0.1	2.2	
ATM-105 (BWR)[a]	34	7.9	1.5	1.0					2.5	5	
ATM-106 (PWR)[a]	43	7.4	2	0.5	0.11	0.03	0.13		0.1	8.5	
ATM-106 (PWR)[a]	46	11.0	2.5	1.0	0.02	0.13	0.01	0.01	1.2	8.0	
ATM-106 (PWR)[a]	50	18.0	6.5	1.0	0.1	0.07	0.05	0.12	15	7.6	
UOX (PWR)[b]	22	0.14	0.27		0.025						
UOX (PWR)[b]	37	0.23	0.6		0.04						
UOX (PWR)[b]	47	0.41	2.3		0.15						
UOX (PWR)[b]	60	2.8	1.0	0.38	0.03	0.18					
PWR-HBR[a]	31	0.2	0.8		0.024		0.03		0.008		0.001
PWR-TP[a]	27	0.3	0.32		0.012		0.04		0.002		
PWR-HBR[a]	31	0.2							0.284		0.33
PWR-TP[a]	27	0.3	0.4				< 0.01		0.076		3.0
ATM-101[a]	28	0.2	2						4		2 to 7
PWR[a]	30	0.36	0.6						0.07		
Leibstadt UO_2(BWR)[c]	65.3	3.69 ± 0.1	1.38								
Gösgen UO_2(PWR)[c]	64	20.6 ± 0.5	3.20						5.90		
Gösgen MOX(PWR)[c]	63	26.7 ± 0.6	3.54						4.98		
Ringhals 3 UO_2(PWR)[c]	58.2	0.94 ± 0.1	1.78						2.29		
Ringhals 4 UO_2(PWR)[c]	61.4	2.3 ± 0.2	1.30						2.16		
Ringhals 3 UO_2(PWR)[c]	66.5	2.6 ± 0.2	1.40						2.28		
North Anna UO_2(PWR)[c]	75.4	5.0 ± 0.3	2.41						5.23		

[a] (Johnson et al., 2004) plotted in Figure 4. 3 and Figure 4. 4; [b] (Roudil et al., 2007); [c] (Johnson et al., 2012) after 90 days of contact time

Experimental Data

Due to the relevance of the IRF for the performance assessment, data has been obtained from leaching experiments on SNF either in dynamic regime (Serrano-Purroy et al., 2011) or in static regime (González-Robles et al., 2015; Martínez-Torrents et al., 2014). RN release data was also collected under the FIRST – Nuclides Project (Kienzler et al., 2014).

SNF samples were put in contact with leachant dissolutions and the RN concentration was measured after a determined contact time. The results showed that both leachant composition and irradiation history of the fuel samples are key parameters of the system (Carbol et al., 2005; González-Robles et al., 2015; Johnson et al., 2005; Serrano-Purroy et al., 2012; Windt et al., 2006). The sample preparation procedure proved to be an important factor to study the RN release (Roth et al., 2014, 2013). In particular, some studies (De Pablo et al., 2009; González-Robles et al., 2016, 2015; Serrano-Purroy et al., 2012) used samples coming from different parts of the SNF pellet in order to study the different contributions to the IRF.

Cladded Samples

This type of samples can be a full pellet sample or only part of it such as a disk from the middle part of a pellet. In Figure 4. 5 from González-Robles et al. (2015), two examples of pellet sample can be observed.

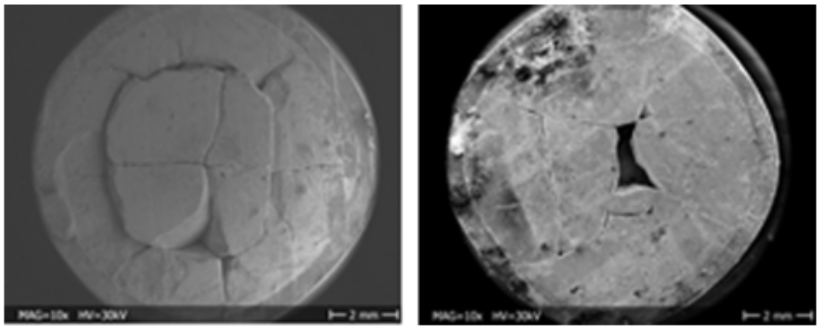

Figure 4. 5 Cross section of two pellet samples obtained from González-Robles et al. (2015). The image on the left is from a BWR sample with 53 MWd/kg$_U$ and the image on the right is from a PWR sample with 52 MWd/kg$_U$

The IRF obtained by using these samples is mainly due to the FP from the gap and fractures. In addition, there are other contributions that come from the rim and the GB exposed to the leachant. In this case, the release of the RNs is due to all the contributions (gap, GB and matrix) at the sample time.

Powder samples

Some studies were performed using powder samples that came from the same SNF segment. The segment was drilled and two types of samples could be obtained (De Pablo et al., 2009; Serrano-Purroy et al., 2012, 2011). One was obtained from the central part of the pellet (CORE) and the other from the outer part of the pellet (OUT) (see Figure 4. 6).

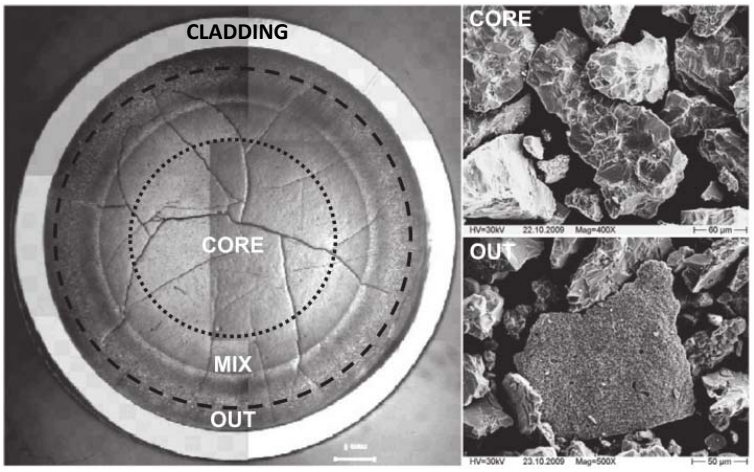

Figure 4. 6 Image of SNF samples. On the left side of the image a cross section of a segmented sample can be observed as well as the original locations for CORE and OUT powder samples from Serrano-Purroy et al. (2012).

The leaching experiments performed on CORE samples are expected to show the contribution of the GB to the IRF. Also, the matrix dissolution is expected for long experimental contact times.

On the other hand, experiments carried on OUT samples allow to observe the contribution of the high burn – up structure (if present) and the outer pellet regions.

By using a powder sample, grains that were previously in the bulk of the segment sample are exposed to the leachant, the so called internal grain boundaries (GBi). This fact will cause an increase of the RN release that come from the GBi.

Leaching data interpretation

Data from leaching experiments is influenced by the RN location, its reactivity and the surface oxidation state. These factors influence the dissolution rate of the RN compared with the UO_2 dissolution rate (matrix dissolution rate).

The release of some RN is controlled by the uranium dissolution , hence they dissolve congruently with the matrix. Other RNs dissolve incongruently from the matrix with different dissolution rates.

In order to identify the elements released different from the matrix, new variables were defined (Hanson and Stout, 2004; Roudil et al., 2007; Serrano-Purroy et al., 2012) (see Eq. (4.1)):

$$FIAP_i(\%) = \frac{m_{RN,aq}}{m_{RN,SNF}} \cdot 100 = \frac{[RN] \cdot V_{aq}}{m_{SNF} \cdot H_{RN}} \cdot 100 \quad (4.1)$$

Where $FIAP_i$ is the relative amount of the RN in the aqueous phase as percentage of the total inventory in the sample; '$m_{RN,aq}$' is the amount of radionuclide in the aqueous phase in grams; '$m_{RN,SNF}$' is the initial amount of radionuclide in the fuel sample in grams; '*[RN]*' is the radionuclide concentration in mol·dm^{-3}, 'V' is the volume of the leachant in dm^3; 'm_{SNF}' is the sample weight in grams and 'H_{RN}' is the radionuclide inventory in grams of RN per gram of fuel sample.

Another variable used is known as Fractional Radionuclide Release Normalized to Uranium (FNU_{RN} see Eq. (4.2)); it aims to compare the FIAP of any radionuclide with the FIAP of uranium.

$$FNU_{RN} = \frac{FIAP_i}{FIAP_U} \quad (4.2)$$

Where '$FIAP_U$' is the fraction of inventory in aqueous phase of uranium. This parameter allows to determine the elements that have higher release than the uranium, hence than the matrix. Those RNs with FNU higher than 1 have higher dissolution rate than the matrix. As a consequence, they are contributing to the IRF. The RNs that are dissolved congruent with the matrix have FNU values close to 1. They are not considered as part of the IRF. Finally, the RNs with FNU values lower than 1 are dissolved slower than the matrix.

Since the IRF is considered to be caused by the RN segregated from the matrix, the instant release fraction value could be calculated as Serrano-Purroy et al (2012) suggested in Eq. (4.3).

$$IRF = FIAP_i - FIAP_U \quad (4.3)$$

Unfortunately, these values depend on the experimental time and so an arbitrary release time should be used in order to compare all the results from all the RNs. Until now there is still no clear way to distinguish when each contribution finishes. This fact makes difficult the accurate determination of the amount of RN released segregated from the uranium matrix, as it was noticed by some authors (González-Robles et al., 2015; Johnson et al., 2012, 1985).

Specific Objectives

This work aims to identify the RNs that are dissolved segregated from the matrix by using a semi – empirical mathematical model and a specific algorithm.

This model will be fitted to the uranium experimental leaching data in order to determine the main parameters of the model. These parameters will allow to predict the release of RN dissolved by the UO_2 matrix. All the other elements that are segregated and dissolve differently than the matrix will not be properly predicted by using the matrix dissolution parameters. The elements with higher release than the matrix will be modelled in order to quantify them as part of the IRF.

Description of the model

As it has been described in the introduction section, there are several contributions to the IRF depending on the locations of the radionuclides released. These contributions can be studied by using different type of samples: e.g. pellet and powder samples.

During the leaching experiments, three processes might happen at the same time: the RN release from the gap, the RN release from the GB and the RN release from exposed surface grains. Figure 4. 7 describes the process considered schematically. When the experiments are performed with pellet samples, only the surface of the pellet (with gap region, cracks, cavity surfaces, available GB and available grains) is the RN leaching source. When the experiments are performed with powder samples, the contribution of GB, micro fissures and bubbles increases compared with the pellet samples. This happens because in pellet samples, there are a lot of GB inside the pellet which are not accessible to water. A similar situation occurs for the UO_2 grains, which are the least available to water contact in the SNF pellet samples.

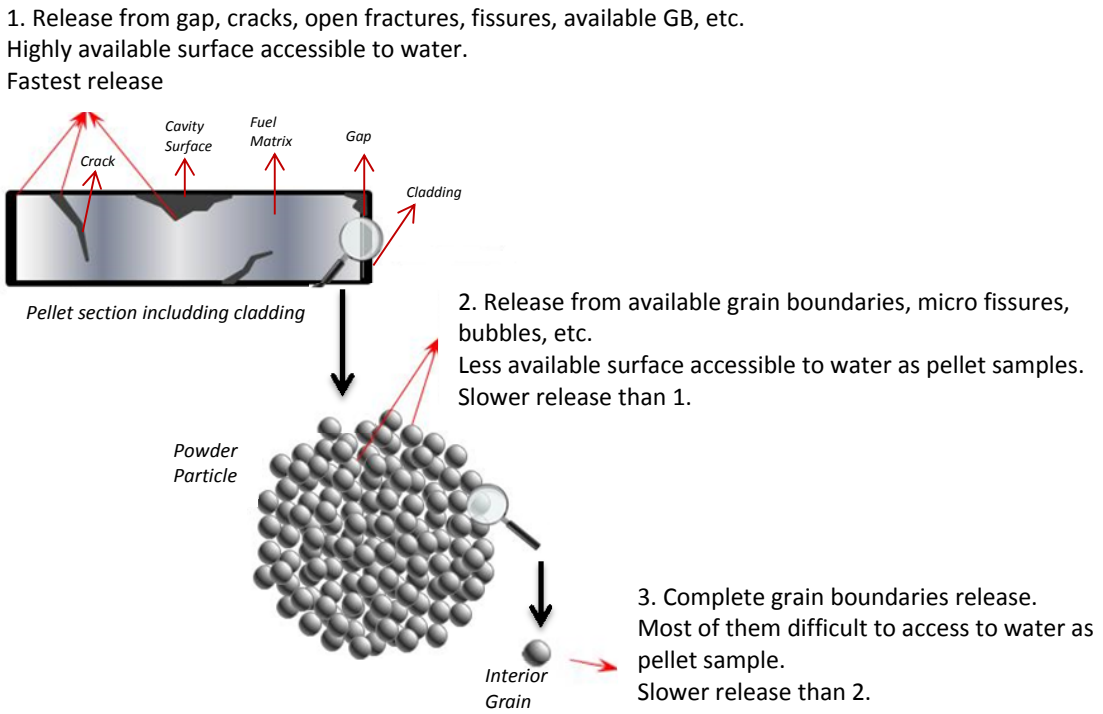

Figure 4. 7 Scheme of the conceptual release of RN from the SNF segregated from the UO_2 matrix based on the radionuclides location, their availability to water and sample preparation from Casas et al. (2014)

Taking into account the different dissolution rates, these three contributions might be identified by using a kinetic dissolution model. This model is named "Segregated Radionuclide Identification

Model" called SERNIM hereafter. Considering a first order kinetic dissolution of each contribution, the general equation is shown in Eq. (4.4).

$$m_{RN}(t) = \sum_{c=1}^{N} m(c)_{RN,\infty} \cdot \left(1 - e^{-k_c t}\right) \quad (4.4)$$

Where '$m_{RN}(t)$' is the amount of radionuclide leached in the dissolution; '*c*' is the ranking of the contribution (being the first one the fastest release); '*N*' is the total of contributions to the RN release that are considered; '$m(c)_{RN,\infty}$' is the total amount of radionuclide released from '*c*' contribution; 'k_c' is the kinetic dissolution constant of the '*c*' contribution and '*t*' is the experimental time (in this chapter the unit used is 'days').

Algorithm

In order to determine the different parameters shown in the SERNIM (Eq. (4.4)) for each radionuclide, a specific algorithm should be followed. Additionally, this routine allows to differentiate the RNs that are segregated from the matrix from those RNs that dissolve congruent with the matrix. A scheme of this algorithm is shown in Figure 4. 8.

The algorithm starts by fitting SERNIM to the experimental leaching data of uranium. In this first step, two contributions are considered to be released as it is shown in Eq. (4.5). The fastest is assumed to correspond to uranium oxidized phases or fines. The other contribution has a lower dissolution rate and it is attributed to the SNF matrix dissolution.

$$m_U(t) = m(ox)_{U,\infty} \cdot \left(1 - e^{-k_{ox} t}\right) + m(ma)_{U,\infty} \cdot \left(1 - e^{-k_{ma} t}\right) \quad (4.5)$$

Where '$m_U(t)$' is the amount of uranium leached; '$m(ox)_{U,\infty}$' and '$m(ma)_{U,\infty}$' are the total amount of uranium released from the oxidized layers and the matrix, respectively, and 'k_{ox}' and 'k_{ma}' are the kinetic dissolution constant of each contribution.

If results from powder samples are fitted using SERNIM, the mass balance should be accomplished , hence '$m(ma)_{U,\infty}$' is calculated as a function of the radionuclide inventory which in this case is determined as in Eq. (4.6):

$$m(ma)_{U,\infty} = m_{U,TOTAL} - m(ox)_{U,\infty} = \frac{M_{sample} \cdot H_U}{MW} - m(ox)_{U,\infty} \quad (4.6)$$

Being '$m_{U,TOTAL}$' the total amount of uranium in the sample, 'M_{sample}' the sample weight, the 'H_U' is the uranium inventory in grams of uranium / grams of sample and '*MW*' the molecular weight of uranium (in this case). As a result, SERNIM has only three parameters to fit in the case of uranium: '$m(ox)_{U,\infty}$', 'k_{ox}' and 'k_{ma}'. Once these parameters are known, the relative amount of uranium released from the total amount of uranium in the sample is calculated and so, the first step of the algorithm in Figure 4. 8 is completed.

The relative percentages of '$m(ox)_{U,\infty}$' and '$m(ma)_{U,\infty}$' to the total of the RN in the sample are determined '$m(ox)_{U,\infty(\%)}$', '$m(ma)_{U,\infty(\%)}$'. The next step is to try to predict the release of the other RNs as if they were released with the SNF matrix. In order to do it, the dissolution constant k_{ox} and k_{ma} can be applied directly, but the other two parameters need to be adapted to the modeled radionuclide by Eq. (4.7), showing the example of technetium.

$$m(ox,U)_{Tc,\infty} = m_{Tc,TOTAL} \cdot \frac{m(ox)_{U,\infty}(\%)}{100} = \frac{M_{sample} \cdot Inventory}{MW} \cdot \frac{m(ox)_{U,\infty}(\%)}{100} \qquad (4.7)$$

Where '$m(ox,U)_{Tc,\infty}$' is the amount of technetium released by the second contribution and predicted by uranium release and '$m_{Tc,TOTAL}$' is the total amount of Tc in the sample calculated with its inventory. An analogue expression can be used to determine the amount of Tc released by the slowest contribution ($m(ma,U)_{Tc}$). In other words, $m(ox)_{U,\infty}(\%)$ and $m(ma)_{U,\infty}(\%)$ are applied to the total amount of Tc of the sample to obtain $m(ox,U)_{Tc,\infty}$ and $m(ma,U)_{Tc,\infty}$.

Once all the parameters for the new RN are determined, in this case Tc, its release is calculated and compared with the experimental leaching data. From this prediction, there are two different possible results:

One possible result is that the experimental leaching data is well predicted by the parameters obtained for uranium. This means that the RN is dissolving congruently with the SNF matrix, hence it is not segregated. As a consequence, this RN is not considered to contribute to the IRF.

The other possibility is that the release does not match the predicted release data. Then, again there are two possible scenarios: data can be under – estimated or over – estimated.

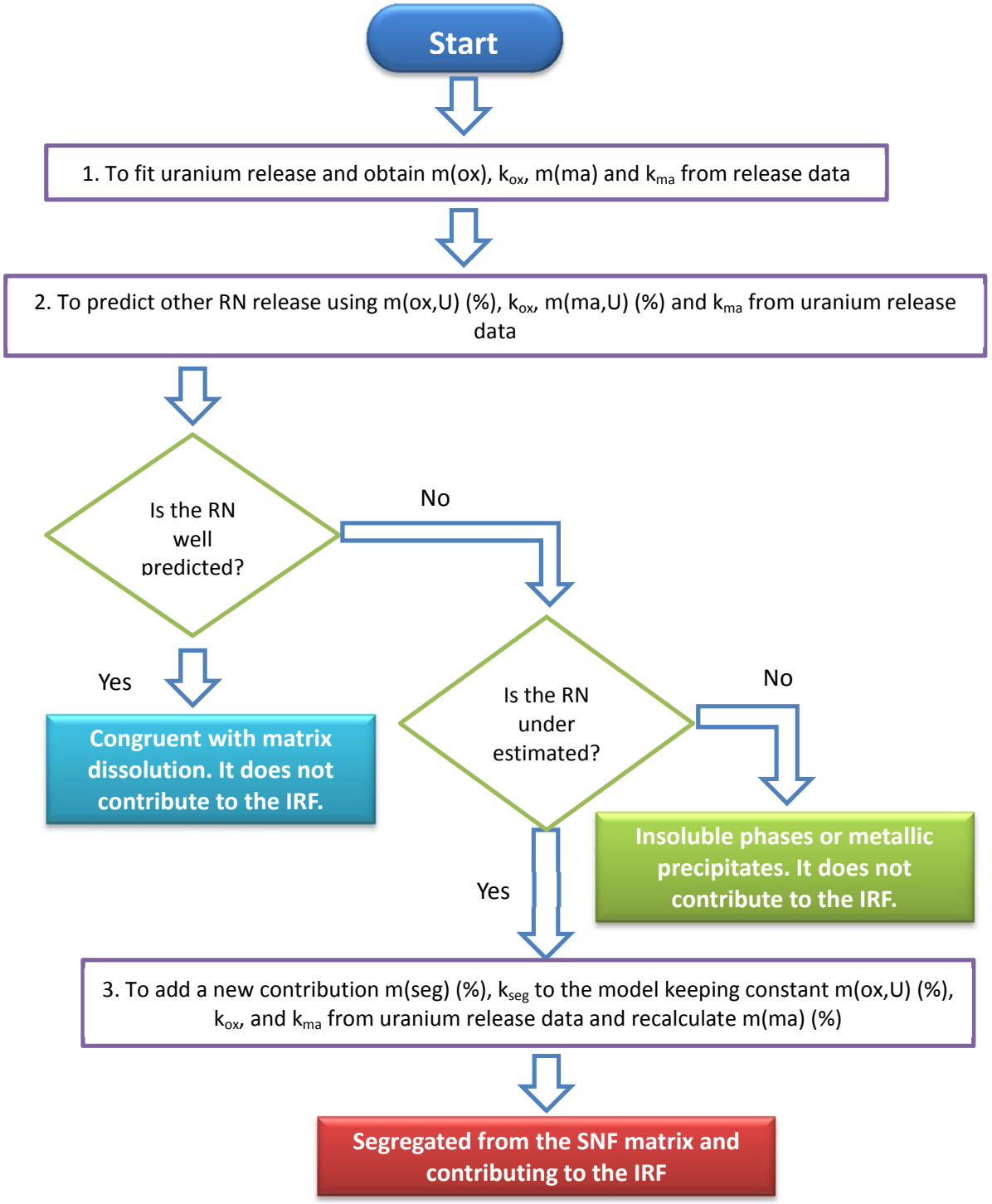

Figure 4. 8 Scheme of the algorithm developed in this chapter

If SERNIM has over – estimated the release of the RN, the leaching data is lower than the leaching predicted by SERNIM. This case is expected for RNs that are segregated forming more insoluble phases than the matrix. Since their release is lower than the matrix, these RNs are not considered to contribute to the IRF.

If SERNIM has under – estimated the experimental release, leaching data are higher than the data predicted by SERNIM. In this case the RN is assumed to be segregated from the uranium with higher dissolution rate than the matrix. Hence, the element is considered to contribute to the IRF and SERNIM needs to be re – adjusted (Figure 4. 8).

To quantify the amount of RN segregated, a new contribution must be introduced in the SERNIM so it can be expressed as Eq. (4.8). This new contribution introduces two more parameters '$m(seg)_{Tc,\infty}$' and 'k_{seg}'.

$$m_{Tc}(t) = m(seg)_{Tc,\infty} \cdot \left(1 - e^{-k_{seg}t}\right) + m(ox,U)_{Tc,\infty} \cdot (1 - e^{-k_{ox}t}) + m(ma)_{Tc,\infty} \cdot (1 - e^{-k_{ma}t}) \quad (4.8)$$

The parameter '$m(ma)_{Tc,\infty}$' is adjusted to comply with the mass balance as it is shown in Eq. (4.9).

$$m(ma)_{Tc,\infty} = m_{Tc,TOTAL} - m(seg)_{Tc,\infty} - m(ox,U)_{Tc,\infty} = \frac{M_{sample} \cdot H_{Tc}}{MW} - m(seg)_{Tc,\infty} - m(ox,U)_{Tc,\infty} \quad (4.9)$$

As a consequence, the second contribution is determined by uranium release and the other two contributions are modified in order to determine the contribution to the IRF and achieve the mass balance.

The fitting was performed using the Matlab® software. The specific mathematical tool was the "Curve Fitting Tool" which is based on the least square routine.

Limitations of the model

SERNIM was designed under the following assumptions:

- Homogeneous composition of the aqueous phase
- Constant inventories during the experimental and analytical time
- No precipitation

In this approach, the release of the RN into the solution is modelled considering that the leachant composition is homogeneous. Therefore, the heterogeneity among particles of the SNF powder

sample has no effect on the resulting leachant composition. However, the availability of the RN to water contact and the solubility properties of each segregated RN-compound will determine the RN release evolution as a function of time.

As a first mathematical approach to the identification of the RN segregated from the matrix, the inventory was considered to be constant during the experimental time. This means that no RN production or decay was introduced in SERNIM, which would require a new inventory value at each experimental time. In this case, the inventory values were obtained experimentally.

SERNIM is applied to leaching data obtained by following a procedure that it is supposed to avoid precipitation phenomena (González-Robles et al., 2015) in order to study only the leaching phenomena and avoid any modification of the concentration. Therefore, no precipitation has been considered in the SERNIM expression.

Sensitivity analysis of SERNIM

SERNIM is designed to obtain information from the leaching data, hence any uncertainty in the experimental data could influence the results. Some parameters might be more sensible than others to errors or variations in the experimental data. Therefore, it is necessary to perform a sensitivity analysis of SERNIM in order to determine these key parameters. Due to the fact that SERNIM is a semi – empirical model based on experimental data, the analysis is performed using the uranium release data obtained from a SNF powder sample. This sample coming from the center of a SNF pellet is fitted in this section. The SNF used was provided from a BWR nuclear power plant and its BU was 42 MWd · kgU^{-1}. The average linear power density was 217 W · cm^{-1} and its FGR was 2.3 %. The irradiation time used with this SNF was 1475 days and the grain size was 15.0 ± 0.1 μm. The sample weight of the powder sample was 0.1089 ± 0.0001 grams and the mean particle size obtained from the SEM images was 50 ± 20 μm. The experimental conditions used to obtain the leaching data are detailed elsewhere (Martínez-Torrents et al., 2014).

The Matlab® software used provides a confidence range of values for each parameter. This fact allows the quantification of the uncertainty in the results. The results obtained are shown in Figure 4. 9 and Table 4. 3. As it can be observed in Table 4. 3, the error range obtained for the total amount of uranium released by the oxidized phase is lower than the nominal value determined by the fitting. This fact suggests that the value of m(ox) is one of the key parameters in the model.

Table 4. 3 Fitting parameters and 95% confidence bounds obtained by the fitting software

Parameter	Nominal Value	Upper Boundary	Lower Boundary	Range
$m(ox)_{U,\infty}$	$1.1 \cdot 10^{-5}$	$2.0 \cdot 10^{-5}$	$0.2 \cdot 10^{-5}$	$\pm 0.9 \cdot 10^{-5}$
k_{ox}	$6.0 \cdot 10^{-2}$	$12.3 \cdot 10^{-2}$	$-0.3 \cdot 10^{-2}$	$\pm 6.3 \cdot 10^{-2}$
k_{ma}	$0.3 \cdot 10^{-4}$	$2.7 \cdot 10^{-4}$	$-2.1 \cdot 10^{-4}$	$\pm 2.4 \cdot 10^{-4}$
R^2	**0.9535**			

On the other hand, the error range obtained for the two dissolution constants is higher than the nominal value of k_{ox} and k_{ma}. This fact causes negative values of the lower boundaries. These wide uncertainties of the dissolution constants suggest that k_{ox} and k_{ma} have less influence on the model results than m(ox).

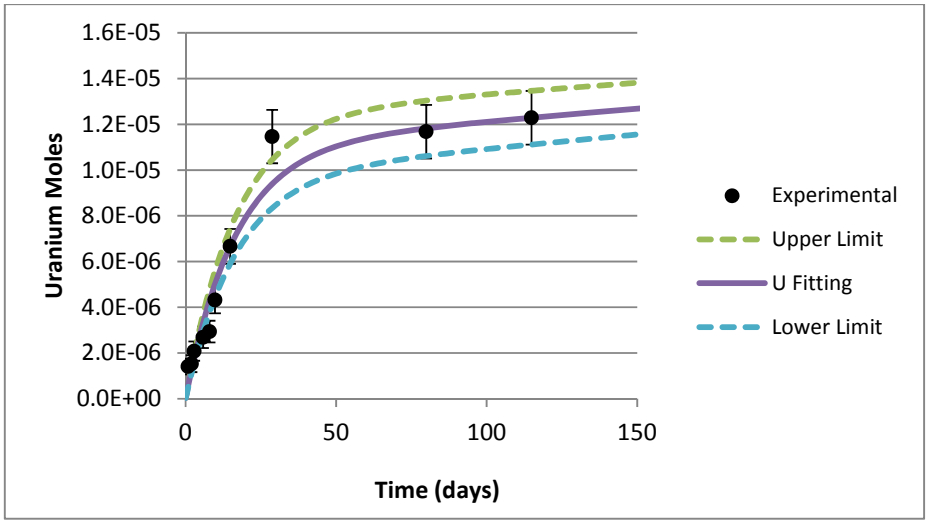

Figure 4. 9 Fitting result of the SERNIM for uranium release

When the experimental error was introduced in the leaching data, the results showed higher variation for the $m(ox)_{U,\infty}$ value than for the k_{ox} and k_{ma} parameters (see Table 4. 4). Hence, it can be concluded that the $m(ox)_{RN,\infty}$ is strongly influenced by the experimental uncertainty of the concentration or inventory measurements.

Table 4. 4 Fitting results of uranium release taking into account the experimental error.

Parameter	Value		Units	Relative value (%)
$m(ox)_{U,\infty}$	$1.10 \cdot 10^{-5}$	$\pm 0.13 \cdot 10^{-6}$	moles	2.87
k_{ox}	0.06	$\pm 10^{-5}$	$days^{-1}$	
$m(ma)_{U,\infty}$	$3.73 \cdot 10^{-4}$	$\pm 1.35 \cdot 10^{-6}$	moles	97.13
k_{ma}	$2.96 \cdot 10^{-5}$	$\pm 3.40 \cdot 10^{-6}$	$days^{-1}$	

Also, proportional variations to the parameters were introduced in Table 4. 5. Only one parameter was changed at each graph in order to determine its influence on the SERNIM results. The resulting curves were compared to the curve obtained with the nominal values in Figures 4. 10 - 4. 12.

Table 4. 5 Induced parameter variation to the SERNIM and Figures list where the results of each parameter variation are shown

Parameter	Nominal Value	+ 10%	-10 %	Figure
$m(ox)_{U,\infty}$	$1.1 \cdot 10^{-5}$	$1.2 \cdot 10^{-5}$	$1.0 \cdot 10^{-5}$	4. 10
k_{ox}	$6.0 \cdot 10^{-2}$	$6.6 \cdot 10^{-2}$	$5.4 \cdot 10^{-2}$	4. 11
k_{ma}	$3.0 \cdot 10^{-5}$	$3.3 \cdot 10^{-5}$	$2.7 \cdot 10^{-5}$	4. 12

As it was suggested by the confidence bounds, small variations of the $m(ox)_{U,\infty}$ produced large oscillations of the SERNIM results (see Figure 4. 10). Due to the non – linearity of the system, only the maximum data deviation was calculated: 10^{-6}. As it can be observed in Table 4. 5, 10^{-6} was also the variation induced to the $m(ox)_{U,\infty}$ parameter. Regarding the SERNIM design, this variations is expected due to the $m(ox)_{U,\infty}$ parameter multiplying the exponential factor. Since this parameter depends on the cumulative moles and the RN inventory determined experimentally, errors in any of these two measurements will significantly influence the value of $m(c)_{RN,\infty}$.

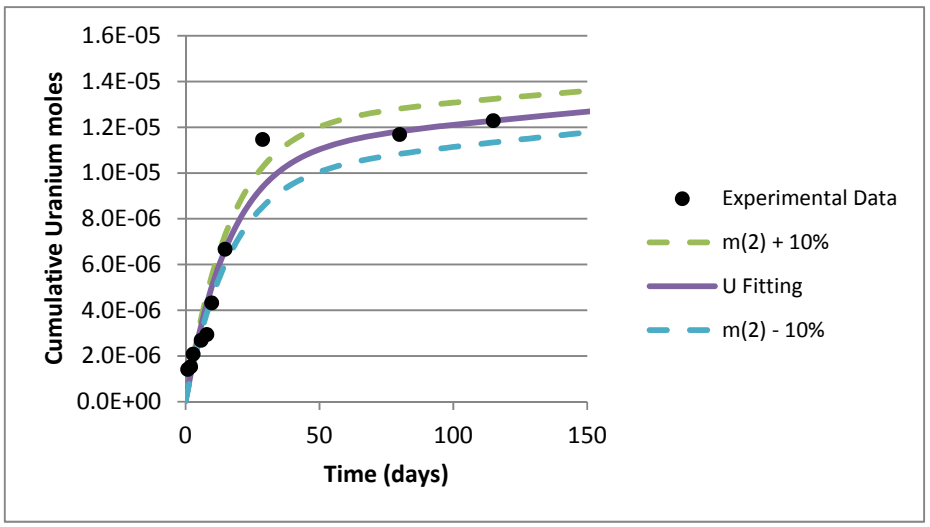

Figure 4. 10 Influence of the m(ox) introduced variation of the 10% to the SERNIM model

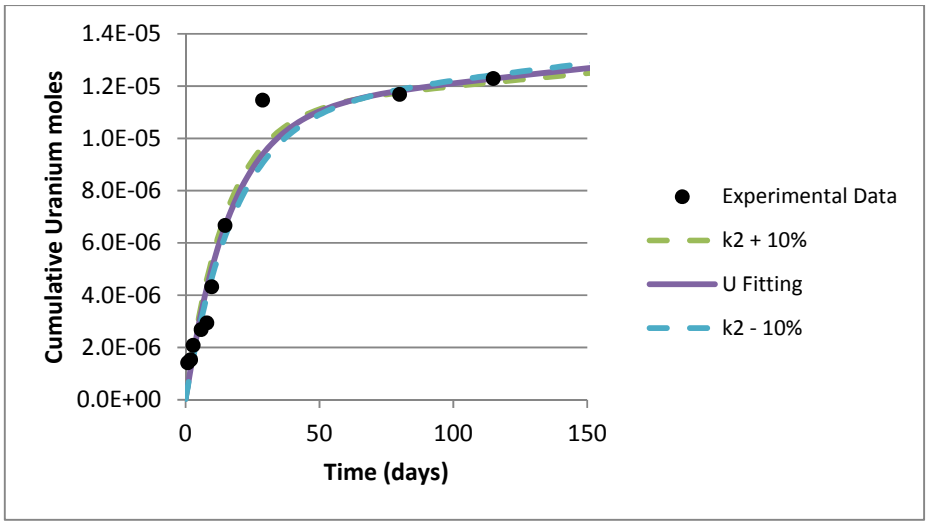

Figure 4. 11 Influence of the k_{ox} introduced variation of the 10% to the SERNIM model

Variations in the dissolution constant values k_{ox} and k_{ma} barely modified the result of SERNIM obtained by using the nominal parameter values as it can be observed in Figure 4. 11 for k_{ox} and in Figure 4. 12 for k_{ma}.

This low influence of k_{ox} and k_{ma} can be expected regarding the SERNIM Eq. (4.5). They appear inside the model as negative exponent.

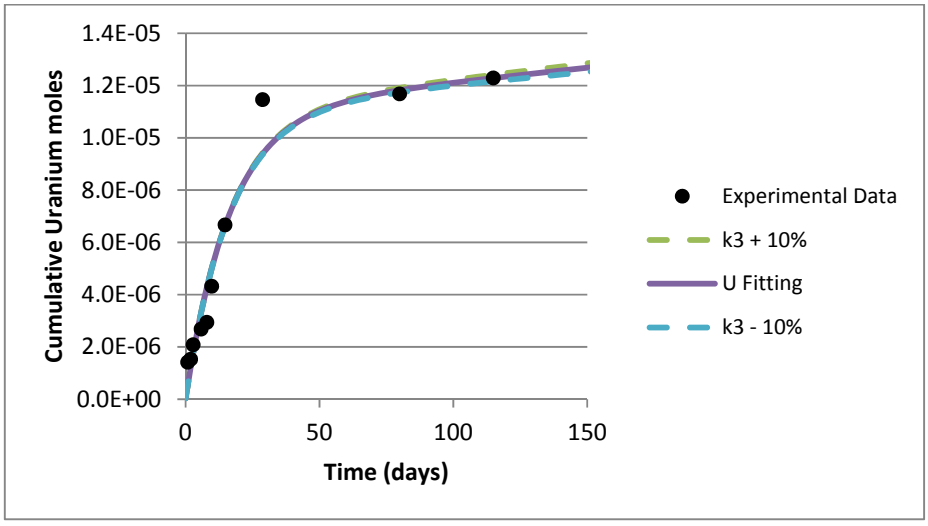

Figure 4. 12 Influence of the k_{ma} introduced variation of the 10% to the SERNIM model

Experimental data fitting and prediction

Uranium release

As it was explained in previous sections, the first element to be fitted is uranium. In Figure 4. 13 the result of the SERNIM (Eq. (4.5)) is shown. The fitting results are shown taking into account the experimental error.

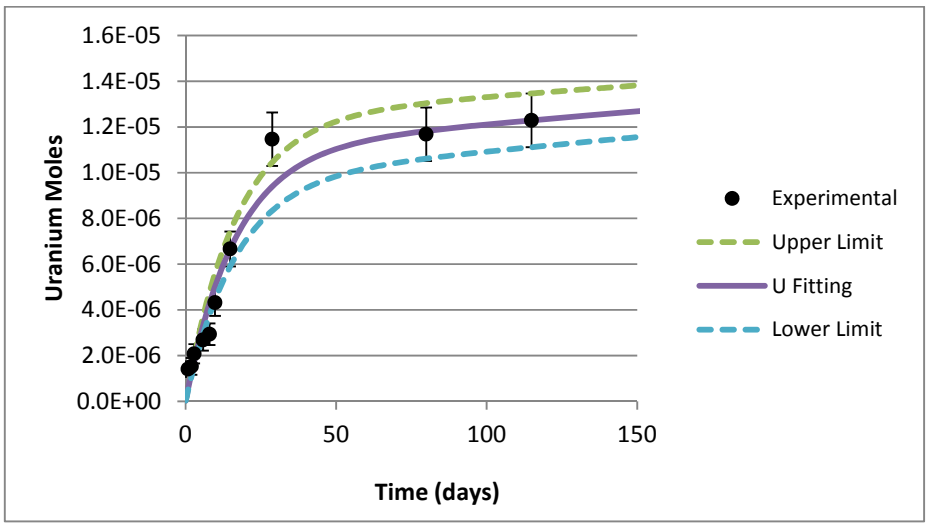

Figure 4. 13 Fitting of Uranium by SERNIM shown in Eq. (4.5) and experimental error

Both the Upper and the Lower limit were calculated by adding the experimental error in order to fit again the SERNIM in Eq. (4.5) to the new data.

The fitting results obtained with the Matlab® software can be observed in Table 4. 6. The relative amount of uranium released by the second contribution and assumed to correspond to the oxidized phases and fines is 2.87%. The error range is determined by using the experimental error reported i. e. SERNIM parameters in Eq. (4.5) were adjusted for the upper release values and lower release values. The error range was obtained from these results.

Table 4. 6 Fitting results of the two contributions of the SERNIM of the uranium release from a BWR sample with 42 MWd/kgU (CORE sample)

Parameter	Value		Units	Relative value (%)
$m(ox)_{U,\infty}$	$1.10 \cdot 10^{-5}$	$\pm 1.35 \cdot 10^{-6}$	moles	2.87
k_{ox}	0.06	$\pm 10^{-5}$	$days^{-1}$	
$m(ma)_{U,\infty}$	$3.73 \cdot 10^{-4}$	$\pm 1.35 \cdot 10^{-6}$	moles	97.13
k_{ma}	$2.96 \cdot 10^{-5}$	$\pm 3.40 \cdot 10^{-6}$	$days^{-1}$	
R^2	**0.9535**			

Cerium release

Once all the parameters of the uranium release are obtained, the rest of the RNs are predicted using these values and Eq. (4.7). For instance, cerium is predicted by using the parameters where the last column in Table 4. 7 was used to determine the numeric values of '$m(ox)_{Ce,\infty}$' and '$m(ma)_{Ce,\infty}$'. The values of the release constant were also kept constant.

Table 4. 7 Fitting parameters obtained from the uranium fitting to predict cerium release

Parameter	Value		Units	Relative value (%)
$m(ox,U)_{Ce,\infty}$	$5.99 \cdot 10^{-8}$	$\pm 7.20 \cdot 10^{-9}$	moles	2.87
k_{ox}	0.06	$\pm 10^{-5}$	$days^{-1}$	
$m(ma,U)_{Ce,\infty}$	$2.03 \cdot 10^{-6}$	$\pm 7.20 \cdot 10^{-9}$	moles	97.13
k_{ma}	$2.96 \cdot 10^{-5}$	$\pm 3.40 \cdot 10^{-6}$	$days^{-1}$	
R^2	**0.9535**			

Figure 4. 14 shows the prediction made by the uranium release. As it can be observed, Ce release data is well estimated. This is assumed to correspond to RNs that are completely dissolved in the SNF. Hence, its release is governed by the matrix dissolution. In this case, Ce will not contribute to the IRF.

Since Ce release is well predicted, no additional changes were made to SERNIM and leaching data is assumed to follow the SERNIM predicted by uranium release.

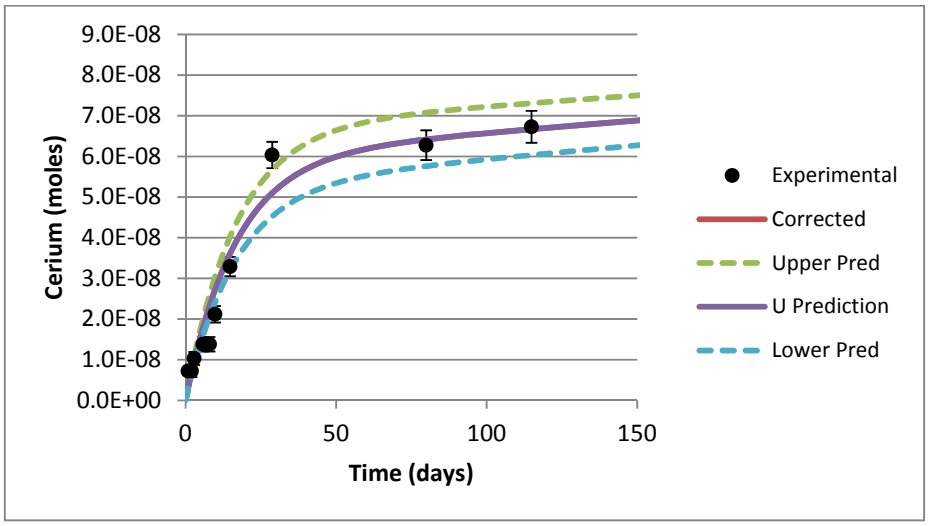

Figure 4. 14 Prediction of the release of Ce obtained by using the parameters from uranium release

Cesium release

As for the Ce release, cesium was predicted by using the parameters obtained with the uranium fitting by determining the '$m(ox)_{Cs,\infty}$' and '$m(ma)_{Cs,\infty}$' values from the last column in (see Table 4. 8).

Table 4. 8 Parameters for the Cs release prediction obtained by using the parameters from uranium release

Parameter	Value		Units	Relative value (%)
$m(ox,U)_{Cs,\infty}$	$6.46 \cdot 10^{-8}$	$\pm 7.75 \cdot 10^{-9}$	moles	2.87
k_{ox}	0.06	$\pm 10^{-5}$	$days^{-1}$	
$m(ma,U)_{Cs,\infty}$	$2.19 \cdot 10^{-6}$	$\pm 7.75 \cdot 10^{-9}$	moles	97.13
k_{ma}	$2.96 \cdot 10^{-5}$	$\pm 3.40 \cdot 10^{-6}$	$days^{-1}$	
R^2	**0.2958**			

As it can be observed in Figure 4. 15, the leaching data is not well predicted. Actually, they are under predicted, which means that the RN is segregated from the uranium matrix exhibiting release. In order to determine the amount of cesium segregated, a new contribution is introduced in SERNIM as in Eq. (4.8). The values of $m(ox)_{Cs,\infty}$, k_{ox} and k_{ma} were fixed at the values in Table 4. 8 and $m(seg)_{Cs,\infty}$, k_{ox} and $m(ma)_{Cs,\infty}$ were adjusted, being $m(ma)_{Cs,\infty}$ function of $m(seg)_{Cs,\infty}$ and $m(ox)_{Cs,\infty}$ as shown in Eq (4.9) with regard to the mass balance.

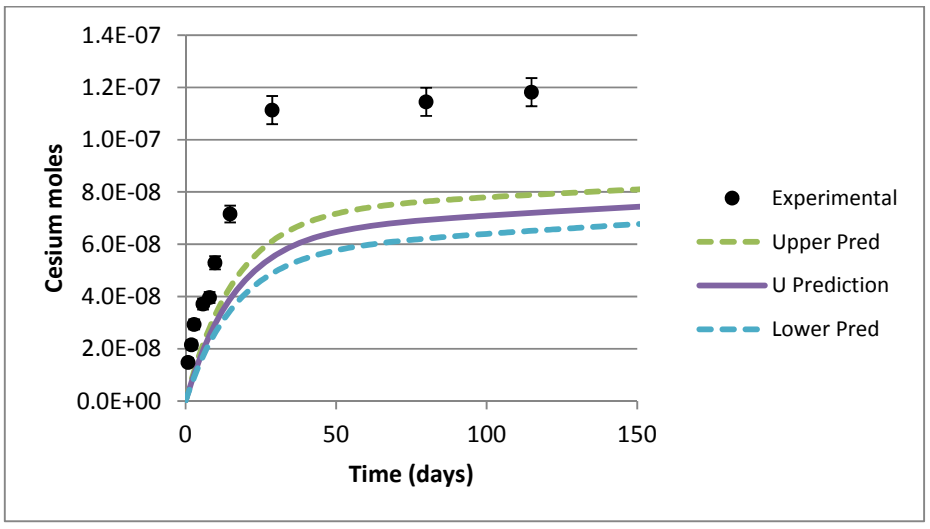

Figure 4. 15 Prediction of the release of cesium obtained by using the parameters from uranium release

The resulting model is shown in Figure 4. 16 and the numerical results of the parameters can be observed in Table 4. 9. It was needed to add a slightly faster contribution to the cesium release that represented 2.06% of the Cs. This amount of Cs is assumed to come from the GB where the RN is segregated. Therefore, Cs is expected to contribute to the IRF.

Table 4. 9 Values of the parameters for the three contribution model used to fit the Cs release of a CORE sample from a 42 MWd/kg$_U$ BWR SNF

Parameter	Value		Units	Relative value (%)
$m(seg)_{Cs,\infty}$	$4.63 \cdot 10^{-8}$		moles	2.06
k_{seg}	0.08		$days^{-1}$	
$m(ox,U)_{Cs,\infty}$	$6.46 \cdot 10^{-8}$	$\pm 7.75 \cdot 10^{-9}$	moles	2.87
k_{ox}	0.06	$\pm 10^{-5}$	$days^{-1}$	
$m(ma)_{Cs,\infty}$	$2.14 \cdot 10^{-6}$		moles	95.07
k_{ma}	$2.96 \cdot 10^{-5}$	$\pm 3.40 \cdot 10^{-6}$	$days^{-1}$	
R^2	**0.9647**			

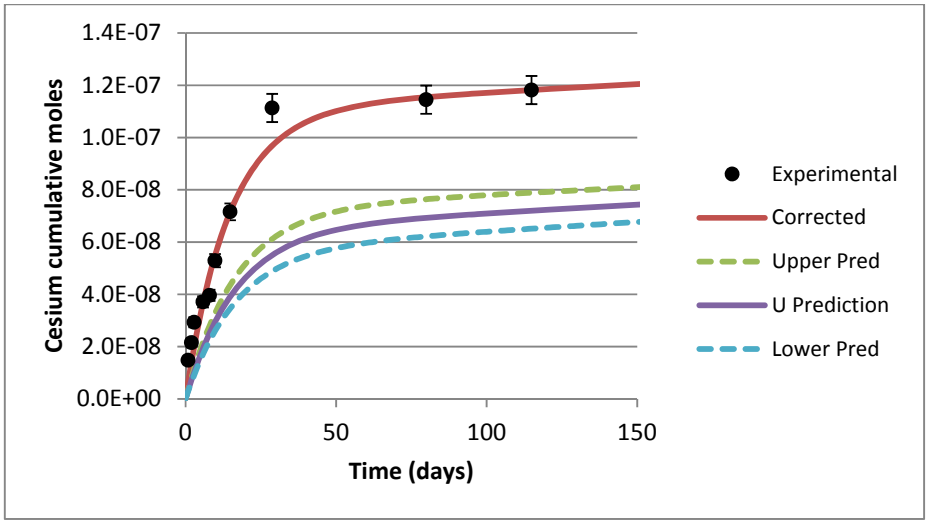

Figure 4. 16 Fitting result of the Cs release data of the CORE sample from a 42 MWd/kg$_U$ BWR SNF

Rhodium release

Rh release is also predicted by using the values obtained from uranium release following the same methodology explained before. The values obtained are shown in Table 4. 10.

Table 4. 10 Fitting parameters obtained from the uranium fitting to predict rhodium release

Parameter	Value		Units	Relative value (%)
$m(ox,U)_{Rh,\infty}$	$6.46 \cdot 10^{-8}$	$\pm 7.75 \cdot 10^{-9}$	moles	2.87
k_{ox}	0.06	$\pm 10^{-5}$	$days^{-1}$	
$m(ma,U)_{Rh,\infty}$	$2.19 \cdot 10^{-6}$	$\pm 7.75 \cdot 10^{-9}$	moles	97.13
k_{ma}	$2.96 \cdot 10^{-5}$	$\pm 3.40 \cdot 10^{-6}$	$days^{-1}$	
R^2	**0.0**			

SERNIM predicted a higher release than the one observed during the experiment. This fact is assumed to be due to the segregation from the matrix. Since Rh is dissolving less than uranium, it

is possible to think that their solubilities are different, being uranium more soluble than rhodium. Actually, Rh is found as metallic precipitates in the SNF (Bramman et al., 1968; Cui et al., 2004; González-Robles et al., 2015; Kleykamp, 1985), which would explain these differences of solubilities.

Therefore, Rh is not expected to contribute to the IRF because of its low solubility even though it is segregated from the matrix.

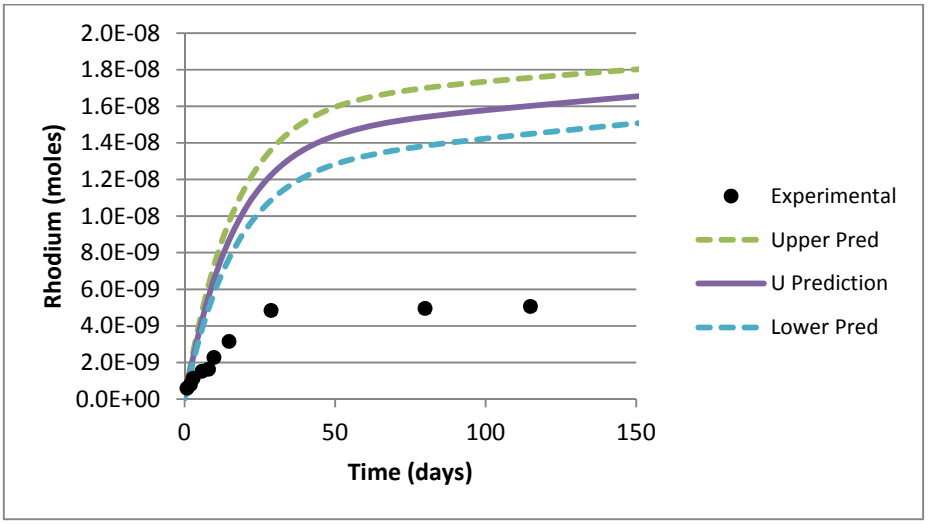

Figure 4. 17 Prediction of the release of Rh obtained by using the parameters from uranium release

Fitting results

SERNIM has been fitted to a total amount of 13 RN from the same SNF powder sample: U, Cs, Sr, Rb, Nd, Tc, Mo, Am, Pu, Rh, Ru, Ce and La. The results obtained for the '$m(c)_{RN,\infty}$' parameters are shown in Table 4. 11. The graphs obtained for each RN are shown in the Annex C of the chapter as well as the parameters and boundary values provided by the Matlab® software.

It can be observed that four elements were identified as segregated from the matrix: Cs, Sr, Rb and Nd. From all of them, Cs is found as the most segregated RN and Sr the least. The order obtained from the most segregated to the least.

$$Cs > Nd \sim Rb > Sr$$

On the other hand, the kinetic constants obtained are shown in Table 4. 12.

Table 4. 11 Values of the m^i (moles) and (%) parameter obtain by the algorithm for 13 radionuclides from leaching data of a 42 MWd/kg_U BWR CORE sample

Element	m(seg)	m(ox,U)	m(ma)	m(seg)(%)	m(ox,U)(%)	m(ma)(%)
U		$1.10\cdot10^{-5}$	$3.73\cdot10^{-4}$		2.87%	97.13%
Cs	$4.63\cdot10^{-8}$	$6.46\cdot10^{-8}$	$2.14\cdot10^{-6}$	2.06%	2.87%	95.07%
Sr	$8.71\cdot10^{-9}$	$3.84\cdot10^{-8}$	$1.29\cdot10^{-6}$	0.65%	2.87%	96.48%
Tc		$2.66\cdot10^{-8}$	$9.02\cdot10^{-7}$		2.87%	97.13%
Mo		$1.21\cdot10^{-7}$	$4.10\cdot10^{-6}$		2.87%	97.13%
Rb	$5.05\cdot10^{-9}$	$1.59\cdot10^{-8}$	$5.35\cdot10^{-7}$	0.91%	2.87%	96.22%
Am		$2.79\cdot10^{-9}$	$9.45\cdot10^{-8}$		2.87%	97.13%
Rh*		$1.44\cdot10^{-8}$	$4.87\cdot10^{-7}$		2.87%	97.13%
Ru*		$7.50\cdot10^{-8}$	$2.54\cdot10^{-6}$		2.87%	97.13%
Pu		$1.33\cdot10^{-7}$	$4.51\cdot10^{-6}$		2.87%	97.13%
Ce		$5.99\cdot10^{-8}$	$2.03\cdot10^{-6}$		2.87%	97.13%
La		$3.34\cdot10^{-8}$	$1.13\cdot10^{-6}$		2.87%	97.13%

**Elements that were over estimated by SERNIM by using the parameters values shown in the table*

Table 4. 12 Values of the kinetic constant parameter of SERNIM (k_i in $days^{-1}$) obtain by the algorithm for 13 radionuclides from leaching data of a 42 MWd/kg_U BWR CORE sample

Element	k_{seg}	k_{ox}	k_{ma}
U		0.06 ± 10^{-5}	$2.96\cdot10^{-5} \pm 3.40 \cdot 10^{-6}$
Cs	0.08	0.06 ± 10^{-5}	$2.96\cdot10^{-5} \pm 3.40 \cdot 10^{-6}$
Sr	0.13	0.06 ± 10^{-5}	$2.96\cdot10^{-5} \pm 3.40 \cdot 10^{-6}$
Tc		0.06 ± 10^{-5}	$2.96\cdot10^{-5} \pm 3.40 \cdot 10^{-6}$
Mo		0.06 ± 10^{-5}	$2.96\cdot10^{-5} \pm 3.40 \cdot 10^{-6}$
Rb	0.06	0.06 ± 10^{-5}	$2.96\cdot10^{-5} \pm 3.40 \cdot 10^{-6}$
Am		0.06 ± 10^{-5}	$2.96\cdot10^{-5} \pm 3.40 \cdot 10^{-6}$
Rh		0.06 ± 10^{-5}	$2.96\cdot10^{-5} \pm 3.40 \cdot 10^{-6}$
Ru		0.06 ± 10^{-5}	$2.96\cdot10^{-5} \pm 3.40 \cdot 10^{-6}$
Pu		0.06 ± 10^{-5}	$2.96\cdot10^{-5} \pm 3.40 \cdot 10^{-6}$
Ce		0.06 ± 10^{-5}	$2.96\cdot10^{-5} \pm 3.40 \cdot 10^{-6}$
La		0.06 ± 10^{-5}	$2.96\cdot10^{-5} \pm 3.40 \cdot 10^{-6}$

Discussion

The dissolution rate calculated from SERNIM is expressed in Eq. (4.10). Since each addend is associated to a specific IRF contribution, individual contribution dissolution rates can be determined.

$$\frac{dm_{RN}(t)}{dt} = \sum_{c}^{N} m(c)_{RN,\infty} \cdot k_c \cdot \left(e^{-k_c \cdot t}\right) \quad (4.10)$$

Taking into account the surface area of the sample (4652 ± 2000 mm^2), the dissolution rate obtained for the matrix contribution from uranium fitted parameters in Table 4. 6 is (2.75 ± 0.30)·10^{-11} mol·m^{-2}·s^{-1}. This value is close to the matrix dissolution rate determined by the Conceptual Model of the Matrix Alteration Model (MAM) in the SFS project (Poinssot et al., 2005) (4.60 ± 1.80) · 10^{-11} mol·m^{-2}·s^{-1}. It is also close to the dissolution rate value determined experimentally within the SFS project (3.20 ± 0.2) · 10^{-11} mol·m^{-2}·s^{-1} in contact with the same leachant composition. This fact gives confidence to the hypothesis of the matrix dissolution under these conditions and helps identifing its contribution to the leaching data.

Congruent dissolution with the matrix

The elements that were well predicted using the parameters obtained from the uranium fitting were: Mo, Am, Pu, Ce and La. This happens with the RNs that are dissolved into the uranium matrix (Kleykamp, 1985) and their release is controlled by the uranium dissolution. These results are in good agreement with previous works (González-Robles et al., 2015; Metz et al., 2012; Serrano-Purroy et al., 2012), where some actinides, such as Pu and Am, and some lanthanides, such as Ce and La, were also observed to be released congruently with the matrix. In these previous works, the elements were identified by using the FIAP values in Eq. (4.2) and calculated the IRF with the Eq. (4.3).

The prediction obtained for the molybdenum release fitted well the experimental data, which indicates that Mo is dissolved congruently with the matrix in the studied case. These results are in disagreement with the expected location of Tc and Mo which are expected to be forming metallic precipitates as epsilon particles (Kleykamp, 1985) and/or oxide precipitates at the GB (Serrano et al., 2001).

In the case of the Tc, the leaching data was well estimated for the initial leaching time (less than 30 days of leaching time). Afterwards, the leaching data were over estimated. This may be caused by different distribution of the Tc within the SNF. The first and rapid release might be due to Tc in the oxidized phases (such as TcO_4^-) that is released with the oxidized matrix. After 30 days, Tc release rate decreased to lower values than the ones predicted for the matrix. This may be caused by the metallic precipitates containing Tc (Johnson et al., 2005; Werme et al., 2004) which will dissolve less than the matrix.

Over – estimated dissolution: Rh and Ru

In the case of Rhodium and Ruthenium, the prediction obtained by the matrix release over – estimated the concentration of these RNs in the leachant. This fact is assumed to happen for phases with lower solubility than the SNF matrix such as metallic precipitates.

These results are in good agreement with the ones obtained in the literature. Mennecart et al. (2014) observed a metallic alloy precipitate formed by Mo, Ru, Tc, Rh and Pd in a SNF sample with an average BU of 50.5 MWd/kg_U. These metallic alloys have been studied by Kleykamp (1989, 1985) and reported in more recent works (Ewing, 2015; Metz et al., 2012).

Under – estimated dissolution: Cs, Sr and Rb

When the release prediction for Cs, Sr and Rb was compared with the experimental release data, SERNIM under – estimated their release. This fact is assumed to be caused by the segregation of these RNs to the GB. Hence, they are considered to be segregated from the matrix and contributing to the IRF.

A possible way to compare the results obtained with SERNIM with the experimental data is by using the IRF in Eq. (4.3) and the FIAPs values. In order to verify the suitability of this data treatment, the same expression has been used to calculate the IRF values of the 42 MWd/kg_U BWR CORE sample. The results obtained for Cs, Sr and Rb are shown in Table 4. 13.

Taking into account a 10% of error range based on the results in Table 4. 6 – 4. 10, it can be observed that the values after 100 days of contact time correspond to the segregated amount of RN determined by the SERNIM as unit fraction.

It is important to consider that all the bibliographic data of IRF was determined by using FIAP values which are time dependent. As a consequence, the results obtained after 68 days of leaching

might differ from the IRF results obtained after 350 days. This fact might produce under – estimations of the segregation of RNs.

Table 4. 13 IRF values of Cs, Sr and Rb determined by Eq. (4.3) for the leaching data obtained from 42 MWd/kg$_U$ BWR CORE sample used in this study

Time (days)	Cs	Sr	Rb
1	$2.90 \cdot 10^{-3}$	$1.19 \cdot 10^{-3}$	$8.33 \cdot 10^{-4}$
2	$5.56 \cdot 10^{-3}$	$2.52 \cdot 10^{-3}$	$1.86 \cdot 10^{-3}$
3	$7.61 \cdot 10^{-3}$	$3.83 \cdot 10^{-3}$	$2.52 \cdot 10^{-3}$
6	$9.51 \cdot 10^{-3}$	$5.12 \cdot 10^{-3}$	$3.14 \cdot 10^{-3}$
8	$9.96 \cdot 10^{-3}$	$5.36 \cdot 10^{-3}$	$3.74 \cdot 10^{-3}$
10	$1.23 \cdot 10^{-2}$	$6.29 \cdot 10^{-3}$	$4.38 \cdot 10^{-3}$
15	$1.44 \cdot 10^{-2}$	$6.55 \cdot 10^{-3}$	$5.04 \cdot 10^{-3}$
29	$1.96 \cdot 10^{-2}$	$6.48 \cdot 10^{-3}$	$7.65 \cdot 10^{-3}$
80	$2.04 \cdot 10^{-2}$	$6.84 \cdot 10^{-3}$	$8.20 \cdot 10^{-3}$
115	$(2.0 \pm 0.6) \cdot 10^{-2}$	$(6.5 \pm 5.0) \cdot 10^{-3}$	$(8.1 \pm 7.0) \cdot 10^{-3}$

Since a powder sample from the core of a SNF pellet is considered to have no contribution from the gap or rim region, the comparison between powder and pellet samples will not provide with more information regarding SERNIM suitability. Therefore, the discussion will take into account powder samples from the core of the pellet when possible.

Cesium

Cs showed the highest segregation of all the RNs studied determined by the model in this work: 2.06% of the total of Cs for the powder sample. The fact that SERNIM was able to identify Cs as a segregated RN from the matrix is in good agreement with the results obtained previously and with the cesium contribution expected to the IRF (Ewing, 2015; Johnson et al., 2004; Kienzler et al., 2014; Kienzler and González-Robles, 2013; Roudil et al., 2007; Werme et al., 2004). This fact gives confidence in SERNIM, but the resulting value needs to be compared with the published data.

Previous experimental data of the different RNs release have been reported by Valls et al. (2014). The IRF (%) of Cs for different SNF samples was calculated by using the Eq. (4.3) and the results are shown in Annex D, Figure D. 1 as a function of the fuel BU, in Figure D. 2 as function of the LPD and in Figure D. 3 as function of the FGR.

It can be observed that the amount of Cs segregated obtained using SERNIM is in the higher range of the values reported in the bibliography in all three figures. It should be taken into account that for fragment samples, there are still some GB in the bulk of the fragments that cannot be dissolved

until the water penetrates the sample bulk. On the other hand, in powder samples more GB are available to water. This fact would cause an increase of the Cs released from that location. Therefore, the values obtained with fragments might under – estimate the amount of Cs segregated in the GB.

In order to remove the effect of the sample size and available surface, a new variable has been proposed: the IRF normalized to the specific surface area (IRFS), as defined in Eq. (4.11). The IRF in percentage is determined by the '*FIAP*'s using the Eq. (4.3) and the '*SA*' is the specific surface area of the sample. The resulting parameter is expressed in (%) · g_{sample} · m^{-2}.

$$IRFS = \frac{IRF}{SA} \tag{4.11}$$

The results show no clear influence of the BU, the LPD or the FGR on the Cs segregated (see Figure 4. 18 - 4. 20). As in the previous graphs, the value obtained with SERNIM is one of the highest values reported.

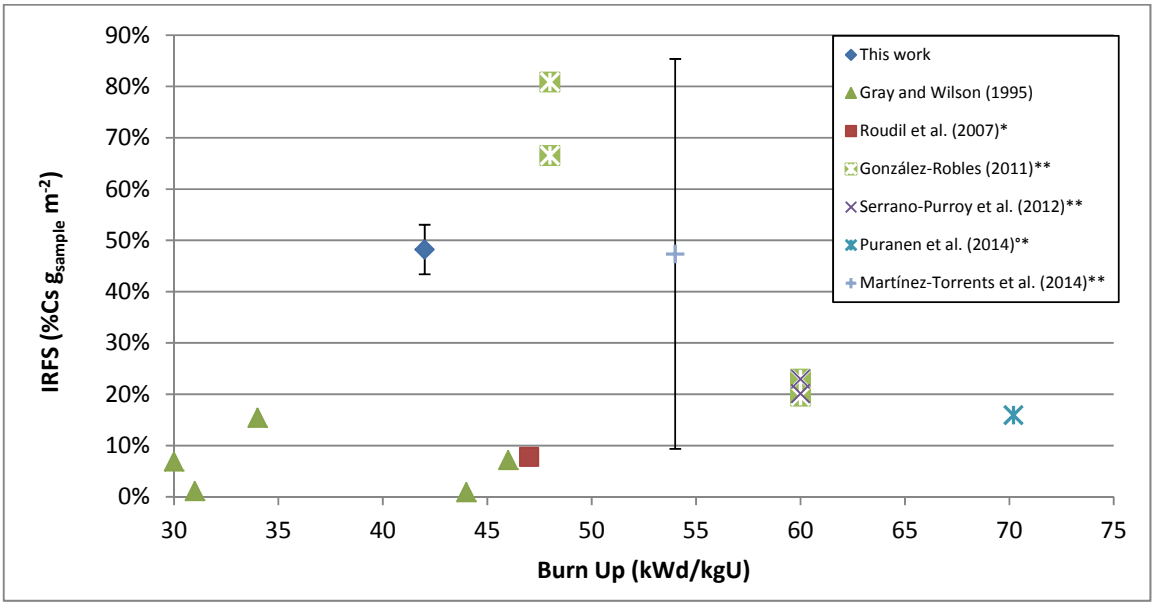

Figure 4. 18 Influence of the BU on the Cs segregated at the grain boundaries normalized by the specific surface area of the sample

[0] Fragment samples
** FIAP data*
*** IRF determined by using the Eq. (4.3)*

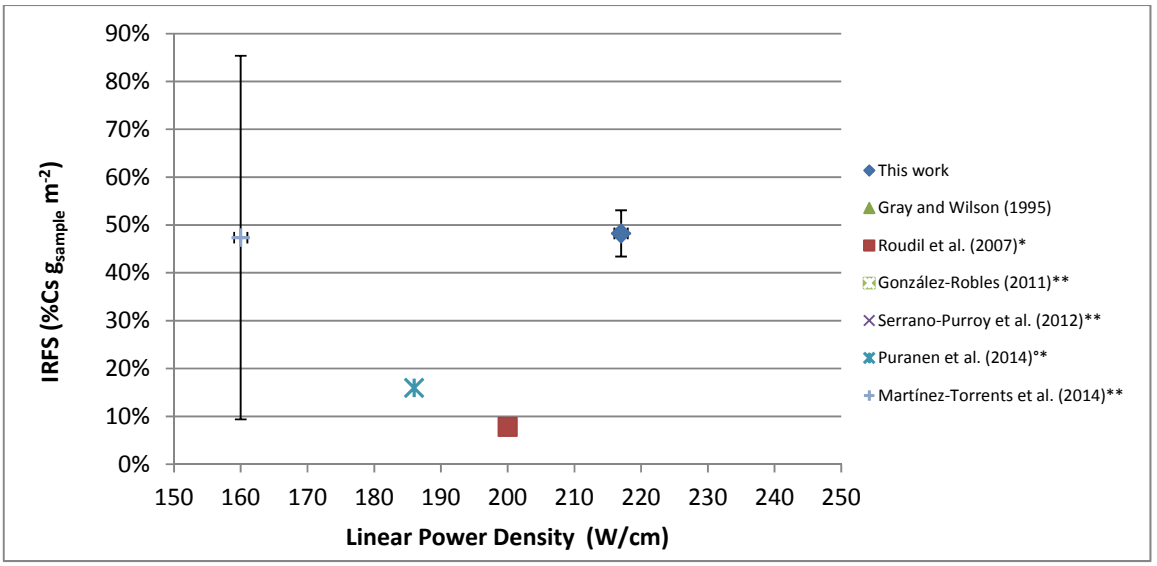

Figure 4. 19 Influence of the LPD on the % of Cs segregated from the matrix and normalized by the specific surface area of the sample

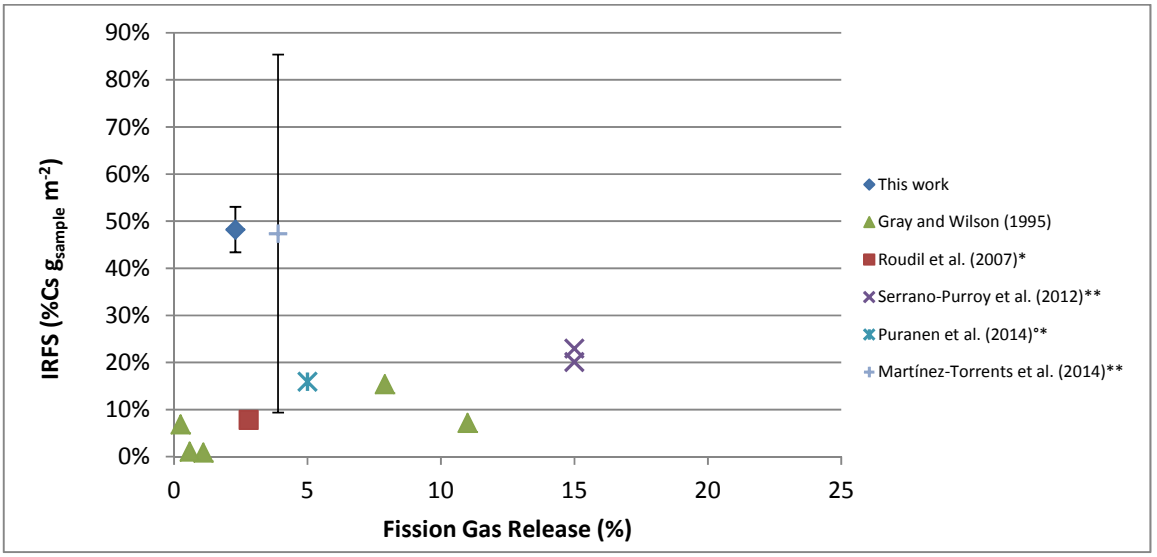

Figure 4. 20 Percentage of Cs segregated from the matrix and normalized by the specific surface area of the sample as a function of the FGR

It should be noticed that the correlation between Cs release and FGR observed by previous works (Johnson et al., 2005; Werme et al., 2004) takes into account the Cs from gap and grain boundaries, but in this work only GB inventories are considered for the discussion. This fact is due to the sample characteristics. As a result, data reported by Johnson et al. (2004) that has been considered for discussion shows no correlation with the FGR in Figure D. 3 or Figure 4. 20.

Regarding the figures obtained, there might be other parameters that influence the Cs segregation to the GB, such as the irradiation temperature or the grain size of the fuel. On one hand, the temperature affects the RN diffusion coefficient , hence its migration to the GB (Bagger et al., 1994). Also, the grain size might have an effect on the diffusion path to the GB.

The different sample pre – treatments constitute another important factor to be taken into account. The drilling process used to obtain powder from SNF pellets could produce changes in the sample. It might influence the RN location and might oxidize the SNF due to the air atmosphere and the high temperatures during the process. Also, the washing procedures performed to remove fines from the powder samples might have dissolved some of the Cs at the external GB, too.

Even though no clear tendency was observed in the graphs, the results obtained with SERNIM can be compared with the reported values. The result of $m(seg)_{Cs,\infty}$ assumed to correspond to the IRF of Cs from the GB is in the range of the experimental values of IRF of Cs reported for GB. This gives confidence in the result obtained with the model designed in this work.

By using the parameters obtained from SERNIM and Eq. (4.10), the dissolution rate of the segregated Cs is $9.22 \cdot 10^{-12}$ $mol_{Cs} \cdot m^{-2} \cdot s^{-1}$. In addition, the time necessary to dissolve 95% of the Cs segregated can be determined by using Eq. (4.12). The result showed that after 36.7 days, 95% of the Cs in the GB that contributes to the IRF will be already released to the dissolution. This result depends on the dissolution constant determined for the segregated phase.

$$t\ (days) = \frac{-Ln(1 - 0.95)}{k_1} \tag{4.12}$$

Strontium

SERNIM determined that 0.67% of the Sr in the powder sample was leached faster, being segregated from the matrix. Taking into account the hypothesis of the algorithm, this is the amount of Sr segregated to the GB that will contribute to the IRF.

Having identified Sr as a segregated RN and located at GB is in good agreement with previous works where it was found in the gap and at GB (Johnson et al., 2004; Roudil et al., 2009, 2007; Serrano-Purroy et al., 2012). Assuming that the Sr observed by SERNIM is segregated from the matrix and located at GB, the result can be compared with the published data of IRF of Sr coming from GB. The methodology used to compare the data is the same as it was explained in the case of

Cs. As in the previous case, leaching experiments that used powder or fragmented samples from the center part of the SNF pellet are considered for comparison.

The amount of Sr segregated to the GB and considered to participate in the IRF can be observed in Annex D as a function of the BU in Figure D. 4, as a function of the LPD in Figure D. 5 and as a function of the FGR in Figure D. 6.

It can be observed that the value obtained with SERNIM is within the experimental range of data determined as the IRF of Sr from GB. However, the effect of the sample surface and GB exposed to water might under – estimate some of the results. Thus, normalization of the results by specific surface area of the sample has been done. In order to obtain the IRFS, Eq. (4.11) was applied to the results in Annex D (Valls et al., 2014).

It can be observed in Figures 4. 21 - 4. 23 that the value of $m(seg)_{Sr,\infty}$ corresponding to the segregated Sr to the GB and assumed to contribute to the IRF, is inside the IRFS Sr determined by the bibliographic values. This fact proves suitability of SERMIN to identify and quantify the Sr in GB.

On the other hand, no correlation is observed between the IRFS of Sr from GB and the parameters studied in this section and observed in Figures 4. 21 - 4. 23. The value obtained with SERNIM, as well as the values provided by Serrano-Purroy et al. (2012) and Martínez-Torrents et al (2014), are the highest values observed. On the other hand, the values reported by Johnson et al. (2004), Roudil et al. (2007) and Puranen et al. (2014) are the lowest values in all the graphs (Figures 4. 21 - 4. 23). This fact might be explained by the different pre –treatment used to remove fines from the samples. As it was mentioned before, also the drilling process might have influenced the RN location. Moreover, the washing procedures might have leached some RN from the GB before performing the leaching experiments.

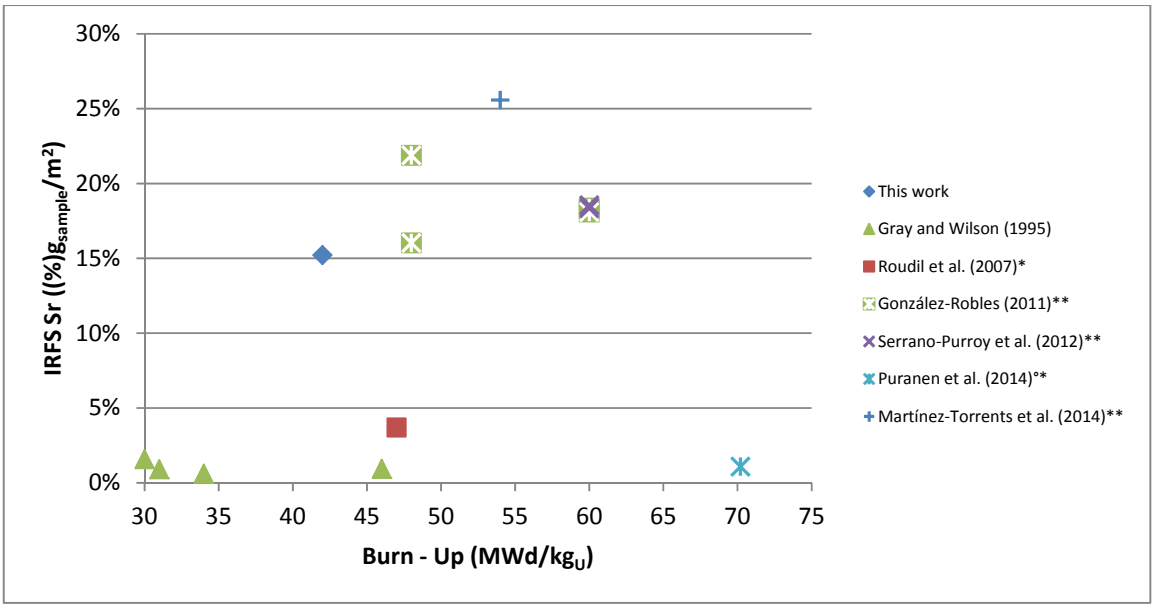

Figure 4. 21 IRFS of Sr from GB as a function of the BU

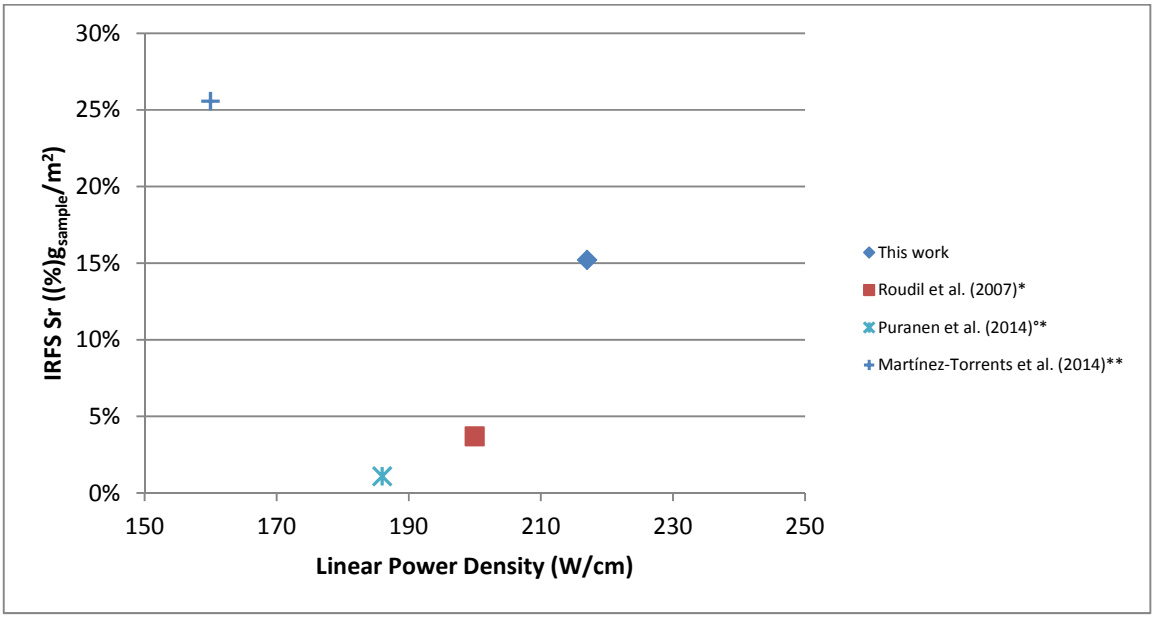

Figure 4. 22 IRFS of Sr in GB as a function of the LPD

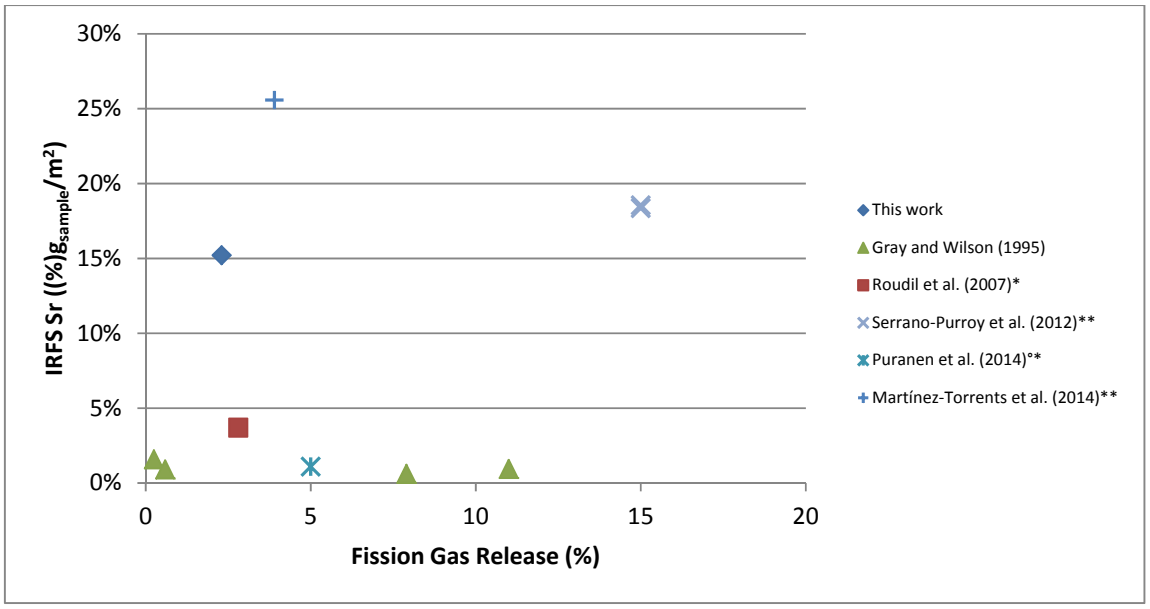

Figure 4. 23 IRFS of Sr in the GB as a function of the FGR

The dissolution rate of the segregated Sr is $2.82 \cdot 10^{-12}$ $mol_{Sr} \cdot m^{-2} \cdot s^{-1}$, as determined by using the Eq. (4.10). In order to determine the leaching time necessary to dissolve 95% of the Sr segregated, the parameters obtained using SERNIM in the Sr case were applied in Eq. (4.12). 23.6 days of leaching time are necessary to dissolve 95% of the Sr segregated at the GB. This is shorter than the 36.7 days necessary to dissolve 95% Cs at the GB because the dissolution constant of Sr is higher than dissolution constant of Cs (see Table 4. 12).

Rubidium

Rb is also determined by SERNIM as a segregated RN located at the GB and assumed to contribute to the IRF. Its segregation is 0.91% of the total Rb in the powder sample. It has been previously observed that Rb has an initial release faster than the matrix in some leaching studies (González-Robles et al., 2015; Martínez-Torrents et al., 2014; Serrano-Purroy et al., 2012).

Valls et al. (2014) collected the IRF of Rb obtained from the FIAP values and by using Eq. (4.3). The results are shown in the Annex D section as a function of BU (Figure D. 7), as a function of the LPD (Figure D. 8) and as a function of FGR (Figure D. 9).

To compare the samples among them and suppress the effect of the surface area, the results in Annex D section were normalized to obtain the IRFS. The IRFS results are shown as a function of BU in Figure 4. 24 and FGR in Figure 4. 25. The effect of the LPD is not shown because the resulting graph has only two experimental points.

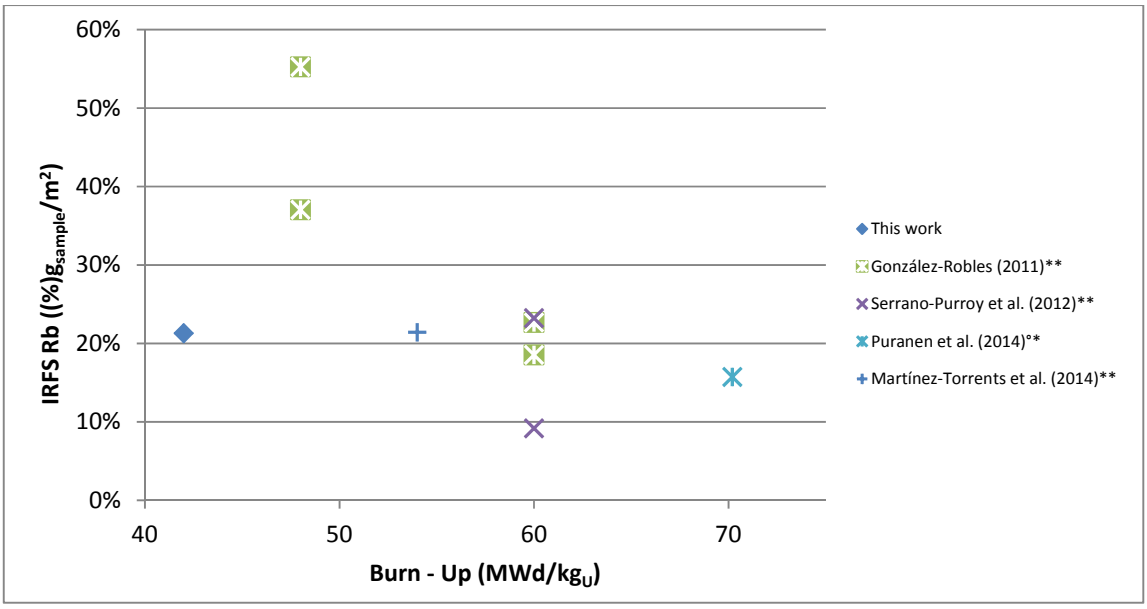

Figure 4. 24 IRFS of Rb as a function of the sample BU

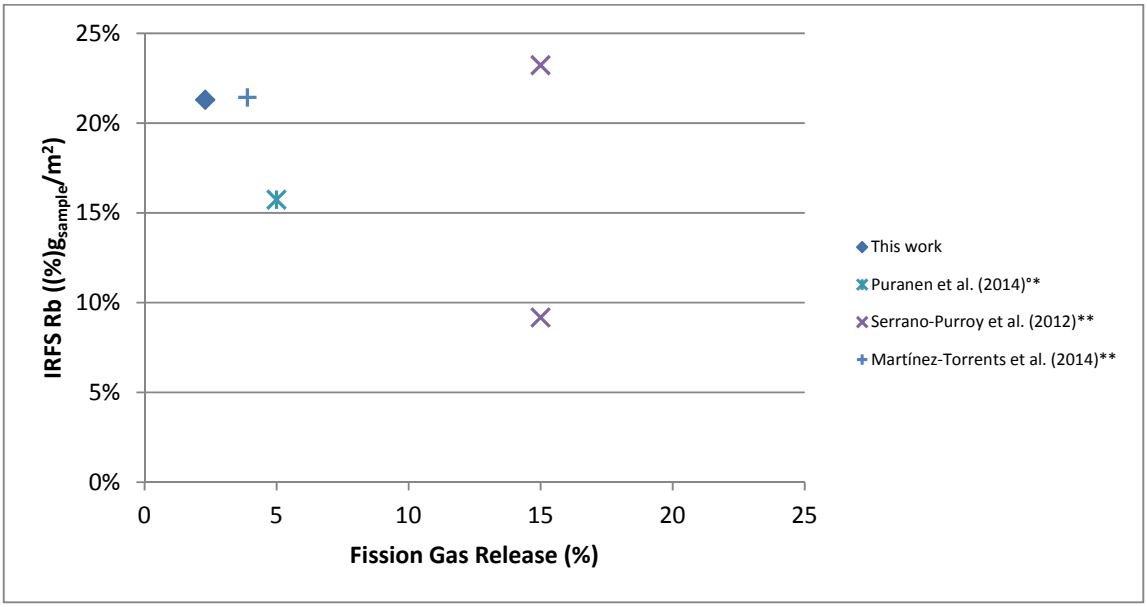

Figure 4. 25 IRFS of Rb as a function of the FGR measured

The fact that the value of $m(seg)_{Rb,\infty}$ is in the range of the experimental data obtained for the IRFS of Rb gives confidence to the results obtained with SERNIM. It can be observed that the value obtained with SERNIM is also located in the lower range of the IRF values in Annex D section. It is similar to the values obtained by Martínez – Torrents (2014) and Puranen et al. (2014). This gives confidence in SERNIM and to the values obtained from it. However, no clear tendency can be observed.

It can be observed in Figure 4. 24 and Figure 4. 25 that there is no influence of the BU or the FGR on the IRFS values. This can be caused by other parameters that might have an effect on the migration of Rb to the GB, such as the thermal gradient or the grain size discussed previously. Also the sample pre – treatment might cause variations in the results.

The SERNIM results still allow to determine the dissolution rate of the segregated Rb: $7.54 \cdot 10^{-12}$ $mol_{Rb} \cdot m^{-2} \cdot s^{-1}$. Also, SERNIM results allow to determine the necessary time to dissolve 95% of the Rb segregated at GB, which is 52.3 days of leaching time.

Conclusions

SERNIM proved to be suitable to identify the RNs that dissolve congruently or segregated from the matrix in the leaching experiments. Also, the result obtained for the matrix dissolution rate ((2.75 ± 0.30)·10^{-11} $mol_U \cdot m^{-2} \cdot s^{-1}$) is in good agreement with the matrix dissolution rate reported in Poinssot et al. (2005) ((4.60 ± 1.80) · 10^{-11} $mol \cdot m^{-2} \cdot s^{-1}$) and in the SFS project (3.20 ± 0.2) · 10^{-11} $mol \cdot m^{-2} \cdot s^{-1}$ in contact with the same leachant composition. This gives confidence in the results and the assumptions made.

The results obtained showed that Mo, Tc Pu, Am, Ce and La were dissolved congruently with the matrix. All of them were well predicted by using SERNIM and matrix parameters. Hence, it can be concluded that their release is controlled by the SNF matrix dissolution.

Regarding the RNs that were identified as segregated from the matrix, Ru and Rh were identified as segregated but with lower release than the matrix. This corresponds to segregated and less soluble phases than the matrix. The results obtained are in good agreement with the literature. Therefore, it can be concluded that SERNIM identified these RNs correctly.

The model determined that Cs, Sr and Rb released faster than the matrix as it was also determined by using the IRF obtained from FIAP values.

By using the parameters from SERNIM, it has been determined that 2.06% of Cs is located at GB and its dissolution rate is 9.22 · 10^{-12} $mol_{Cs} \cdot m^{-2} \cdot s^{-1}$. Cesium is expected to contribute to the IRF, hence it is expected to be segregated from the matrix in the gap and GB. In this case, since the gap contribution was eliminated by the sample pre – treatment, the Cs segregated is assumed to be located at the GB. Therefore, SERNIM identified correctly Cs as segregated RN. Also, the percentage of Cs segregated is within the reported range of Cs in the GB experimentally determined. The time to dissolve 95% of Cs segregated is 36.7 days.

The fraction of Rb segregated was 0.91% as it has been previously observed. It was determined that its dissolution rate is 7.54 ·10^{-12} $mol_{Rb} \cdot m^{-2} \cdot s^{-1}$. It can be observed that the predicted amount of segregated Rb is in the range of the experimental values, which gives confidence in the results obtained with SERNIM. The time necessary to dissolve 95% of the Rb in the GB is 52.3 days.

Finally, 0.67% of Sr was also determined to be segregated at GB by SERNIM. This result is in good agreement with previous results regarding Sr release in leaching experiments. By using the values

obtained by the model, it was determined that the dissolution rate of Sr at GB is $2.82 \cdot 10^{-12}$ $mol_{Sr} \cdot m^{-2} \cdot s^{-1}$. It was also determined that the leaching time necessary to release 95% of the Sr segregated that is 23.6 days.

Therefore, SERNIM proved to provide a good approach to the description of leaching data, and to be suitable to identify the elements segregated from the matrix. In addition, the model provides information about the release rate and the leaching time necessary to dissolve each one of the contributions.

Further Research

SERNIM is expected to be applied to more experimental data sets in order to determine the effect of the rim, the HBS, the LPD and/or the BU of the fuel pellet.

Experimental release data from powder samples from the outer part of the pellet can be used to predict the RN release with SERNIM in order to observe the effect of the rim. In the case that the average BU of the pellet is higher than 40 $MWd \cdot kg_U^{-1}$, the effect of the HBS on the RN segregation and contribution to the IRF might also be observed.

To observe the effect of the BU, LPD or grain size with SERNIM, the experimental release data from a powder sample from the center of the pellet can be used. The results obtained will be compared with those obtained in this study.

Bibliography

Bagger, C., Mogensen, M., Walker, C.T., 1994. Temperature measurements in high burnup UO_2, nuclear fuel: Implications for thermal conductivity , grain growth and gas release. J. Nucl. Mater. 211, 11–29. doi:http://dx.doi.org/10.1016/0022-3115(94)90276-3

Bramman, J.I., Sharpe, R.M., Thom, D., Yates, G., 1968. Metallic fission-product inclusions in irradiated oxide fuels. J. Nucl. Mater. 25, 201–215.

Carbol, P., Cobos-Sabate, J., Glatz, J.-P., Ronchi, C.., Rondinella, V., Loida, A., Metz, V., Kienzler, B., Spahiu, K., Grambow, B., Quiñones, J., Martínez-Esparza, A., 2005. TR-05-09 on the dissolution of ^{233}U doped UO_2(s), high burn-up spent fuel and MOX fuel. Stockholm, Sweden.

Casas, I., Espriu-Gascon, A., Serrano-Purroy, D., Martínez-Torrents, A., Martinez-Esparza, A., de Pablo, J., 2014. IRF modelling from spent fuel leaching experiments, in: Kienzler, B., Metz, V., Valls, A. (Eds.), Final Workshop Proceedings of the Collaborative Project “Fast / Instant Release of Safety Relevant Radionuclides from Spent Nuclear Fuel” (7th EC FP CP FIRST-Nuclides). KIT Scientific Publishing, Karlsruhe, Germany, pp. 227–236.

Cui, D., Low, J., Sjöstedt, C.J., Spahiu, K., 2004. On Mo-Ru-Tc-Pd-Rh-Te alloy particles extracted from spent fuel and their leaching behavior under Ar and H2 atmospheres. Radiochim. Acta 92, 551–555. doi:10.1524/ract.92.9.551.55001

De Pablo, J., Serrano-Purroy, D., Gonzalez-Robles, E., Clarens, F., Martinez-Esparza, A., Wegen, D.H., Casas, I., Christiansen, B., Glatz, J.P., Gimenez, J., 2009. Effect of HBS structure in fast release fraction of 48 GWd/tU PWR fuel, in: Materials Research Society Symposium Proceedings. pp. 613–620.

Ekeroth, E., Cui, D., Low, J., Granfors, M., Zwicky, H.U., Spahiu, K., Evins, L.Z., 2012. Instant release fractions from corrosion studies with high burnup LWR fuel, in: Materials Research Society Symposium Proceedings. Cambridge University Press, San Francisco, CA, pp. 125–130. doi:10.1557/opl.2012.565

Ewing, R.C., 2015. Long-term storage of spent nuclear fuel. Nat. Mater. 14, 252–257. doi:10.1038/nmat4226

González-Robles, E., 2011. Study of Radionuclide Release in commercials UO_2 Spent Nuclear Fuels. Universitat Politècnica de Catalunya (UPC).

González-Robles, E., Fuß, M., 2015. Study of the release of the fission gases (Xe and Kr) and the fission products (Cs and I) under anoxic conditions In bicarbonate water, in: Gin, S., Jubin, R., Matyáš, J., Vance, E. (Eds.), Materials Research Society Symposium Proceedings, Vol. 1744. MRS, Boston, USA, pp. 35–41.

González-Robles, E., Metz, V., Wegen, D.H., Herm, M., Papaioannou, D., Bohnert, E., Gretter, R., Müller, N., Nasyrow, R., de Weerd, W., Wiss, T., Kienzler, B., 2016. Determination of fission gas release of spent nuclear fuel in puncturing test and in leaching experiments under anoxic conditions. J. Nucl. Mater. 479, 67–75. doi:10.1016/j.jnucmat.2016.06.035

González-Robles, E., Serrano-Purroy, D., Sureda, R., Casas, I., de Pablo, J., 2015. Dissolution experiments of commercial PWR (52 MWd/kgU) and BWR (53 MWd/kgU) spent nuclear fuel

cladded segments in bicarbonate water under oxidizing conditions. Experimental determination of matrix and instant release fraction. J. Nucl. Mater. 465, 63–70. doi:10.1016/j.jnucmat.2015.05.012

Grambow, B., Lemmens, K., Minet, Y., Poinssot, C., Spahiu, K., Bosbach, D., Cachoir, C., Casas, I., Clarens, F., Christiansen, B., De Pablo, J., Ferry, C., Giménez, J., Gin, S., Glatz, J.P., Gago, J.A., Gonzalez-Robles, E., Hyatt, N.C., Iglesias, E., Kienzler, B., Luckscheiter, B., Martinez-Esparza, A., Metz, V., Ödegaard-Jensen, A., Ollila, K., Quiñones, J., Rey, A., Ribet, S., Rondinella, V. V., Skarnemark, G., Wegen, D.H., Serrano-Purroy, D., Wiss, T., 2008. RTD Component 1: Dissolution and release from the waste matrix: Final Synthesis Report. F16W-CT-2003-02389. Brussels, Belgium.

Gray, W.J., 1999. Inventories of iodine-129 and cesium-137 in the gaps and grain boundaries of LWR spent fuels, in: Materials Research Society Symposium - Proceedings. Materials Research Society, Boston, USA, pp. 487–494.

Hanson, B.D., Stout, R.B., 2004. Reexamining the dissolution of spent fuel: A comparison of different methods for calculating rates, in: Hanchar, J.M., Stroes-Gascoyne, S., Browning, L. (Eds.), Materials Research Society Symposium Proceedings. Cambridge University Press, San Francisco, CA, pp. 89–94.

Johnson, L., Ferry, C., Poinssot, C., Lovera, P., 2005. Spent fuel radionuclide source-term model for assessing spent fuel performance in geological disposal. Part I: Assessment of the instant release fraction. J. Nucl. Mater. 346, 56–65. doi:10.1016/j.jnucmat.2005.04.071

Johnson, L., Günther-Leopold, I., Kobler Waldis, J., Linder, H.P., Low, J., Cui, D., Ekeroth, E., Spahiu, K., Evins, L.Z., 2012. Rapid aqueous release of fission products from high burn-up LWR fuel: Experimental results and correlations with fission gas release. J. Nucl. Mater. 420, 54–62. doi:10.1016/j.jnucmat.2011.09.007

Johnson, L., Poinssot, C., Ferry, C., Lovera, P., 2004. Technical Report 04-08. Estimates of the Instant Release Fraction for UO2 and MOX Fuel at t=0. NAGRA: Wettingen, Switzerland.

Johnson, L.H., Garisto, N.C., Stroes-Gascoyne, S., 1985. Used fuel dissolution studies in Canada, in: Post, R.G., Wacks, M.E. (Eds.), Proc. Waste Management. Atomic Energy of Canada, Pinawa, Manitoba, Canada, p. 479.

Johnson, L.H., Tait, J.C., 1997. Release of segregated radionuclides from spent fuel.

Kienzler, B., González-Robles, E., 2013. State-of-the-art on instant release of fission products from spent nuclear fuel, in: ASME 2013 15th International Conference on Environmental Remediation and Radioactive Waste Management. American Society of Mechanical Engineers, Brussels, Belgium, p. 9. doi:10.1115/ICEM2013-96044

Kienzler, B., Metz, V., Duro, L., Valls, A., 2014. Final Workshop Proceedings of the Collaborative Project “Fast / Instant Release of Safety Relevant Radionuclides from Spent Nuclear Fuel” (7th EC FP CP FIRST-Nuclides), KIT Scient. ed. KIT Scientific Publishing, Karlsruhe, Germany.

Kleykamp, H., 1989. Constitution and thermodynamics of the Mo-Ru, Mo-Pd, Ru-Pd and Mo-Ru-Pd systems. J. Nucl. Mater. 167, 49–63. doi:10.1016/0022-3115(89)90424-8

Kleykamp, H., 1985. The chemical state of the fission products in oxide fuels. J. Nucl. Mater. 131, 221–246. doi:10.1016/0022-3115(85)90460-X

Martínez-Torrents, A., Sureda, R., de Pablo, J., Clarens, F., Serrano-Purroy, D., Aldave de las Heras, L., Casas, I., 2014. Corrosion test of commercial UO_2 BWR spent fuel for fast/instance release studies, in: Kienzler, B., Metz, V., Valls, A. (Eds.), Final Workshop Proceedings of the Collaborative Project "Fast / Instant Release of Safety Relevant Radionuclides from Spent Nuclear Fuel" (7th EC FP CP FIRST-Nuclides). KIT Scientific Publishing, Karlsruhe, Germany, pp. 157–168.

Mennecart, T., Lemmens, K., Cachoir, C., 2014. Charcterisation and leaching test for the experimental determination of IRF radionuclides from belgian high-burnup spent nuclear fuel, in: Kienzler, B., Metz, V., Valls, A. (Eds.), Final Workshop Proceedings of the Collaborative Project "Fast / Instant Release of Safety Relevant Radionuclides from Spent Nuclear Fuel" (7th EC FP CP FIRST-Nuclides). KIT Scientific Publishing, Karlsruhe, Germany, pp. 147–156.

Metz, V., Geckeis, H., González-Robles, E., Loida, A., Bube, C., Kienzler, B., 2012. Radionuclide behaviour in the near-field of a geological repository for spent nuclear fuel. Radiochim. Acta 100, 699–713. doi:10.1524/ract.2012.1967

Pekala, M., Idiart, A., Duro, L., 2014. Modelling of spent fuel saturation with water - implications for the instant release fraction (IRF), in: Kienzler, B., Metz, V., Valls, A. (Eds.), Final Workshop Proceedings of the Collaborative Project "Fast / Instant Release of Safety Relevant Radionuclides from Spent Nuclear Fuel" (7th EC FP CP FIRST-Nuclides). KIT Scientific Publishing, Karlsruhe, Germany, pp. 211–221.

Poinssot, C., Ferry, C., Kelm, M., Grambow, B., Martinez-Esparza, A., Johnson, L., ...&, Christensen, H., 2005. Final Report of the European Project Spent Fuel Stability under Repository Conditions. European Commission Report CEA: France.

Poinssot, C., Gin, S., 2012. Long-term Behavior Science: The cornerstone approach for reliably assessing the long-term performance of nuclear waste. J. Nucl. Mater. 420, 182–192. doi:10.1016/j.jnucmat.2011.09.012

Puranen, A., Granfors, M., Roth, O., 2014. Laser ablation study of irradiated standard UO_2 fuel and AL/CR doped UO_2 fuel, in: Kienzler, B., Metz, V., Valls, A. (Eds.), Final Workshop Proceedings of the Collaborative Project "Fast / Instant Release of Safety Relevant Radionuclides from Spent Nuclear Fuel" (7th EC FP CP FIRST-Nuclides). KIT Scientific Publishing, Karlsruhe, Germany, pp. 81–90.

Roth, O., Low, J., Granfors, M., Spahiu, K., 2013. Effects of matrix composition on instant release fractions from high burn-up nuclear fuel, in: Materials Research Society Symposium Proceedings. Cambridge University Press, Boston, USA, pp. 145–150.

Roth, O., Low, J., Spahiu, K., 2014. Effects of matrix composition and sample preparation on instant release fractions from high burnup nuclear fuel, in: MRS Proceedings. Materials Research Society, pp. 261–266. doi:10.1557/opl.2014.653

Roudil, D., Jégou, C., Broudic, V., Muzeau, B., Peuget, S., Deschanels, X., 2007. Gap and grain

boundaries inventories from pressurized water reactor spent fuels. J. Nucl. Mater. 362, 411–415. doi:10.1016/j.jnucmat.2007.01.086

Roudil, D., Jegou, C., Broudic, V., Tribet, M., 2009. Rim Instant Release Radionuclide Inventory From French High Burnup Spent UOX Fuel, in: MRS Proceedings. Cambridge University Press, p. 627. doi:10.1557/PROC-1193-627

Serrano-Purroy, D., Casas, I., González-Robles, E., Glatz, J.P., Wegen, D.H., Clarens, F., Giménez, J., de Pablo, J., Martínez-Esparza, A., 2011. Dynamic leaching studies of 48 MWd/kgU UO_2 commercial spent nuclear fuel under oxic conditions. J. Nucl. Mater.

Serrano-Purroy, D., Clarens, F., González-Robles, E., Glatz, J.P., Wegen, D.H., de Pablo, J., Casas, I., Giménez, J., Martínez-Esparza, A., 2012. Instant release fraction and matrix release of high burn-up UO_2 spent nuclear fuel: Effect of high burn-up structure and leaching solution composition. J. Nucl. Mater. 427, 249–258. doi:10.1016/j.jnucmat.2012.04.036

Serrano, J.A., Glatz, J.P., Toscano, E.H., Barrero, J., Papaioannou, D., 2001. Influence of low-temperature air oxidation on the dissolution behaviour of high burn-up LWR spent fuel. J. Nucl. Mater. 294, 339–343.

Valls, A., Duro, L., González-Robles, E., 2014. IRF Database. In: State of the Art report. Deliverable D5.1, 3rd update. Available at FIRST-Nuclides project webpage: http://www.firstnuclides.eu/deliberables.aspx.

Werme, L.O., Johnson, L.H., Oversby, V.M., King, F., Spahiu, K., Grambow, B., Shoesmith, D.W., 2004. Technical Report TR-04-19. Spent fuel performance under repository conditions: A model for use in SR-Can. SKB: Stockholm, Sweden.

Wilson, C.N., 1990. Results from NNWSI Series 3: Spent Fuel Dissolution Tests. Richland, Washington, USA.

Windt, B.L. De, Schneider, H., Ferry, C., Catalette, H., Lagneau, V., Poinssot, C., Poulesquen, A., Jegou, C., 2006. Modeling spent nuclear fuel alteration and radionuclide migration. Radiochim. Acta 94, 787–794. doi:10.1524/ract.2006.94.9.787

Chapter 5:
Study of SIMFUEL electrode corrosion at hyper-alkaline conditions in contact with silicate and calcium

Introduction

In the previous chapter the oxidation of UO_2 has been studied under water vapor conditions. But when ground water gets in contact with the nuclear waste many processes between the water and the SNF can occur depending on the solution concentration, redox conditions, pH, etc. In order to assess the SNF performance most studies have been carried out by using spent fuel analogues such as SIMFUEL (Chung et al., 2010; Shoesmith, 2008; Wu and Shoesmith, 2014).

As it has been explained in Chapter 1, groundwater properties depend on minerals, engineered barriers and elements with which water gets in contact. As a consequence, three types of waters can be differentiated as a function of the geological media relevant for SNF disposal: granitic waters, clay waters and brines. Besides the characteristics obtained from the erosion of the natural soil and minerals, additional species introduced due to the DGR structures will come from the canister corrosion (such as iron ions or hydrogen) and other engineered structures (such as bentonite, concrete or cement).

Since cement is expected to be used, and has been recently proposed to be used in the deep geological disposal to seal possible cracks of the different structures, this chapter is focused on the effect of cement waters in contact with the spent fuel.

Cementitious waters in the SNF near field

Waters in contact with most of the cementitious materials have high pH values and contain silicate and calcium ions (Berner, 1992; Rojo et al., 2014). Therefore, the study of UO_2 corrosion at these conditions is necessary; some studies have already been carried out on the influence of very alkaline pH values on UO_2 dissolution (de Pablo et al., 2004).(Santos et al., 2006a) studied the influence of pH on the corrosion of SIMFUEL, a chemical analogue of the SNF. The proposed oxidation mechanism at high pH was as follows:

$$UO_2 + xH_2O \rightarrow U^{IV}_{1-2x}U^{V}_{2x}O_{2+x} + 2xH^+ + 2xe^-$$

$$U^{IV}_{1-2x}U^{V}_{2x}O_{2+x} + 3OH^- \rightarrow U^{VI}O_{2+x}(OH)^-_3 + 2e^-$$

The effect of Silicate

The effect of silicate on the SIMFUEL corrosion has been previously studied using a 1.5% at. simulated BU SIMFUEL at pH 9.5 by Santos et al. (2006b). The authors found that silicate could not avoid the first step of the oxidation of the UO_2 to $U^{V}_{2x}U^{IV}_{1-2x}O_{2+x}$. However, at the specified pH value the subsequent reaction, from $U^{V}_{2x}U^{IV}_{1-2x}O_{2+x}$ to $UO_3 \cdot xH_2O$ was suppressed. This fact was suggested to be caused by the adsorption of silicate on the fuel surface since the precipitation of a uranium-silicate hydrated phase at high corrosion potentials was observed (Shoesmith, 2007).

The SIMFUEL was electrochemically oxidized by applying 20 nA for 600 hours and the resulting surface presented a precipitate phase rich in silicium and oxygen and lower uranium which was attributed to a U(VI) silicate deposit.

The effect of Calcium

The effect of the presence of calcium has been also studied by Santos et al. (2006c) by using 1.5% at. SIMFUEL at pH 9.5. The main result was that calcium had a similar effect than silicate on the SIMFUEL corrosion: it could not avoid the first oxidation step but it inhibited the further oxidation of the $U^{V}_{2x}U^{IV}_{1-2x}O_{2+x}$ layer. The authors proposed two different explanations: the destabilization of the $UO_2(OH)_{2ads}$ precursor layer of the uranium dissolution on the UO_2 surface, and the inhibition of O^{2-} anions transfer reaction to the fuel surface.

Cerrato et al. (2012) studied the effect of the presence of divalent ions (Ca^{2+} and Zn^{2+}) on the uranium dissolution under anoxic conditions. The authors observed that the uranium dissolution rate decreased in presence of any of the cations, compared with the leachant free of divalent cations at pH 7.8 (Figure 5. 1).

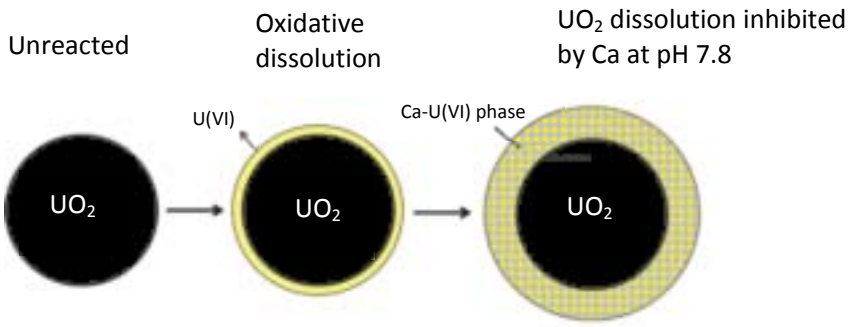

Figure 5. 1 Scheme of the effect of calcium on a UO_2 particle provided by Cerrato et al. (2012)

This fact was suggested to be caused by solid phase precipitation that was considered to passivate the surface of the UO_2. In the case of calcium, the authors did not suggest a specific solid phase, but they observed that the precipitate on the UO_2 surface contained calcium and U(VI) (see Figure 5. 1) similar to bequerelite. Under oxic conditions, Cerrato et al. observed the inhibition of the uranium dissolution and suggested that the solid phase precipitated might be controlling the oxidative dissolution of UO_2.

The effect of Calcium and Silicate

Both Ca and Si were suggested by Shoesmith (2000) to be relevant for the corrosion of UO_2 in contact with ground water because they enhance the precipitation of insoluble phases. These solid phases might rapidly suppress uranium dissolution.

The effect of Ca-Si hydrates on the U(VI) concentration was studied by Harfouche et al. (2006) who observed the formation of Ca-Si-U(VI) phase similar to uranophane at the end of the experiment. Kienzler et al. (2010) studied the long term effect of cementitious waters on doped UO_2 and observed the precipitation of a solid phase. The authors analyzed the precipitates and determined that approximately 95% was uranophane. The remaining 5% contained a mixture of other solid phases such as soddyite, autunite, bequerelite, meta-schoepite, etc.

Corrosion Studies

Corrosion studies are performed in order to understand the chemical interaction between UO_2 and the environment and to prevent – or at least minimize – any potential harm caused. Since the processes involved in the corrosion mechanism are mostly electrochemical, electrochemical analysis is widely used to perform these studies.

There are two key parameters to be considered when performing the corrosion studies: thermodynamics and kinetics.

Thermodynamics

Due to the contact with the environment, a dynamic equilibrium is established between the material and the corrosion products.

$$M \leftrightarrow M^{+} + e^{-}$$

If the reaction above is considered, where 'M' is a non-oxidized metal and 'M^{+}' is the oxidized metal, the free energy change at the dynamic equilibrium can be expressed by Eq. (5.1).

$$\Delta\overline{G} = \Delta G_{M/M^{+}} + nFE_{M/M^{+}} = 0 \quad (5.1)$$

Where '$\Delta\overline{G}$' is the free energy of the dynamic equilibrium, 'ΔG' is the free energy of the chemical reaction, 'n' is the number of electrons involved in the reaction, 'F' is the Faraday number and 'E' is the potential associated to this particular dynamic equilibrium. Under these circumstances, Eq. (5.1) can be rewritten as Eq. (5.2).

$$\Delta G_{M/M^{+}} = -nFE_{M/M^{+}} \quad (5.2)$$

Nernst Equation Derivation

The free energy of each reaction is known for standard conditions (ΔG^{o}). Under non-standard conditions, the free energy of the system changes. As a consequence, the potential of the system needs to be recalculated.

Taking into account the following reaction:

$$aA + mH^{+} + ne^{-} \leftrightarrow bB + dH_2O$$

And using Eq. (5.3) and Eq. (5.2), the potential under dynamic equilibrium and non-standard conditions can be determined as Eq. (5.4). It should be noticed that in Eq. (5.3) and (5.4) the activities of all the reactants in aqueous phase are approximated to their concentrations. In the case that there is a gas dissolved, its activity is approximated by its partial pressure in Eq. (5.3) and (5.4).

$$\Delta G = \Delta G^{o} + RTLn\left(\frac{[B]^{b}[H_2O]^{d}}{[A]^{a}[H^{+}]^{m}}\right) \quad (5.3)$$

$$E = E^{o} + \frac{RT}{nF}Ln\left(\frac{[A]^{a}[H^{+}]^{m}}{[B]^{b}[H_2O]^{d}}\right) \quad (5.4)$$

Where 'E^{o}' is the standard potential of the reaction, 'R' is the gas constant (8.314 $C{\cdot}V{\cdot}mol^{-1}{\cdot}K^{-1}$), 'T' is the temperature in Kelvin.

Pourbaix Diagram

Pourbaix diagrams are one of the most important tools used in electrochemistry. They relate the electrochemical and corrosion behavior of any material that can be corroded with the pH and the

electrochemical potential of the aqueous media. They show the specific conditions of potential and pH under which the material does not react or can react and form oxides, complexes, or even dissolve.

The lines in the diagram represent the conditions of thermodynamic equilibrium for a given reaction by using Eq. (5.4). Three types of lines can be identified:

- Horizontal lines: they represent processes that are independent of the pH.
- Vertical lines: they represent processes that do not involve any electron transfer
- Sloping lines: they represent processes that involve both pH and electron transfer.

A clear example of Pourbaix diagram of uranium is shown in Figure 5. 2 with 10^{-5} mol·dm^{-3} of uranium (example obtained with the software Medusa (Puigdomènech, 2004)).

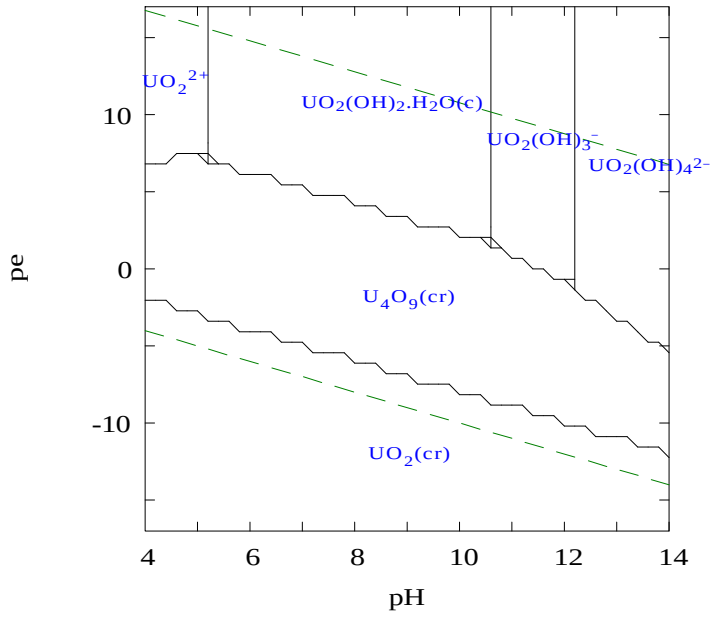

Figure 5. 2 Pourbaix diagram of 10^{-5} mol·dm^{-3} of uranium and 0.1 mol·dm^{-3} of ionic strength at 25^{0}C (Grenthe-Chairman et al., 1992)

Since this type of diagram is based on thermodynamic data, it provides no information about reaction rates (kinetics of the process). For this same reason, no information about the intermediate states is shown either. Only the equilibrium of the system is shown.

Corrosion Potential and Corrosion Current

At the precise moment that the SNF gets in contact with a solution (or electrolyte), the equilibrium of the system is modified due to the difference in potentials, as it can be observed in Figure 5. 3. As a consequence, a driving force for the corrosion appears which can be defined as the potential

difference $E_{Ox/Red}$ – $E_{UO2/UO22+}$ (Shoesmith, 2007). Therefore, the system needs to evolve in order to reach the equilibrium where the anodic and cathodic reactions are balanced:

Anodic	$UO_2 \leftrightarrow UO_2^{2+} + 2e^-$	$E_{UO2/UO22+}$
Cathodic	$Ox + 2e^- \leftrightarrow Red$	$E_{Ox/Red}$

Where "*Ox*" is the oxidized specie and "*Red*" is the reduced specie.

The SNF increases its potential to the corrosion potential (E_{CORR}) depending on the environmental potential. In this equilibrium state, the anodic and the cathodic current are equal and of opposite sign and their value corresponds to the corrosion current (i_{CORR}).

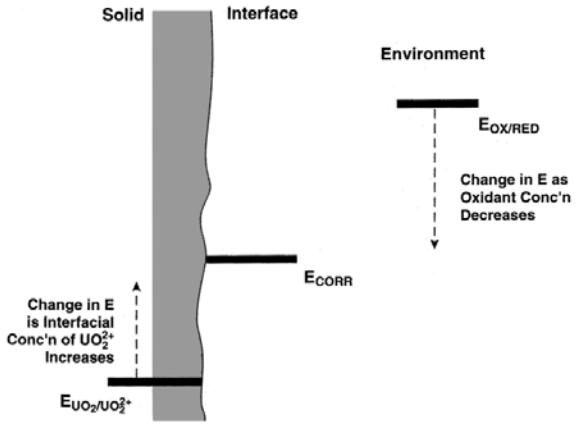

Figure 5. 3 Scheme of the potentials when the surface of the SNF is not in equilibrium with the environmental potential, hence a driving force is created and corrosion occurs. Image from Shoesmith(2000)

For instance, under sealed conditions, where the availability of oxygen is limited, the oxidizing species will be consumed and the potential of the system will decrease with time. In this case the equilibrium will be reached depending on the solubility of UO_2 in the electrolyte solution. In the case of unlimited source of oxidizing species, the potential of the environment will not decrease, hence the corrosion potential will increase. This mechanism will cause the corrosion of UO_2.

Since E_{CORR} partially depends on the solution, several studies have been performed either with UO_2, doped UO_2 or with SIMFUEL in order to determine these values, as it can be observed in Table 5. 1. The presence of oxidizing species such as H_2O_2 causes the increase of E_{CORR}.

The oxidized state of the surface after determining E_{CORR} can be deduced from the UO_2 evolution reported by Shoesmith (2008) as a function of the potential obtained.

Table 5. 1 Reported values of corrosion potential of similes of SNF in the literature

Ref	Sample	Electrolyte	E_{CORR} (mV)
(Shoesmith et al., 1989)	Unirradiated CANDU	$[NaClO_4]$ = 0.1 mol·dm^{-3} pH = 9.5 Anoxic conditions	Between -140 and 260 mV (vs. SCE)
(Sunder et al., 2004)*	UO_2 from CANDU	$[NaClO_4]$ = 0.1 mol·dm^{-3} $[H_2O_2]$ from 10^{-5} to 0.1 mol·dm^{-3} pH = 9.5	Function of the amount of H_2O_2 in the electrolyte
(Carbol et al., 2005)	10% ^{233}U doped UO_2	[NaCl] = 10 mmol·dm^{-3} Anoxic conditions	Between 70 and 80 mV (vs. SHE)
(Carbol et al., 2005)	10% ^{233}U doped UO_2	[NaCl] = 10 mmol·dm^{-3} N_2/H_2 (8%)	Between 70 and 80 mV (vs. SHE)
(Razdan et al., 2014)*	UO_2, UO_2-Y_2O_3, UO_2-Y_2O_3-Pd, UO_2-Pd and 1.5 at% SIMFUEL	[NaCl] = 0.1 mol·dm^{-3} $[NaHCO_3]$ = 0.01 mol·dm^{-3} pH = 9.0	Between -400 and -600 mV (vs. SCE)
(Razdan et al., 2014)*	UO_2, UO_2-Y_2O_3, UO_2-Y_2O_3-Pd, UO_2-Pd and 1.5 at% SIMFUEL	[NaCl] = 0.1 mol·dm^{-3} $[NaHCO_3]$ = 0.01 mol·dm^{-3} $[H_2O_2]$ = 2 mmol·dm^{-3} pH = 9.0	Between 0 and 100 mV (vs. SCE)

**Values obtained from figures published in the reference mentioned.*

Kinetics

What remains unknown is the rate at which the system evolves toward the equilibrium. Therefore, the knowledge of electrochemical reaction kinetics is of primary importance to improve corrosion control methods, to predict corrosion lifetime of any structure and to develop more resistant alloys.

Since the electrochemical reactions involve an electron exchange, an electrode is not at equilibrium when there is a net current passing through it. Two types of reactions are identified: anodic reactions (in the case of uranium it will involve uranium oxidation) that produce electrons and cathodic reactions that consume electrons. By measuring the rate of electron flow to or from an electrode, information about the reaction rate is obtained.

Faraday's Law

In order to determine the corrosion rate of a material, Faraday developed a mathematical expression that relates the rate (r) with the current density (5.5):

$$r\left({}^{g}/_{(cm^2 \cdot s)}\right) = \frac{j \cdot MW}{n \cdot F} \tag{5.5}$$

Where 'j' is the current density in (A·cm^{-2}), 'MW' is the molecular weight of the reacted material, 'n' is the number of electrons transferred and 'F' is Faraday's constant (96485 C·mol^{-1}).

As it can be observed in Eq. (5.5), the corrosion rate is proportional to the current density. This means that by studying the current density, which is easily measured, the corrosion rate is also studied.

Cyclic Voltammetry

This technique allows to obtain qualitative information about the system and the different electrochemical reactions involved – both thermodynamics and kinetics of the redox processes. Additionally, cyclic voltammetry provides rapid identification of the approximate redox potentials of the electroactive species.

To obtain cyclic voltammetric measurements, a scan of potential is applied at a specific rate – usually between 5 and 200 $mV \cdot s^{-1}$ between the reference electrode (RE) and the working electrode (WE), where the material studied is placed, – and the evolution current density is shown as a function of the applied potential.

In the case of the methodology used in this chapter, the starting potential of the measurements is -1.2 V and the typical ending potential is 0.4 V (vs. SCE). In this part of the scan, the WE is being oxidized. Then, the reverse scan is performed from 0.4 to -1.2 V. In this part of the scan, the previously oxidized phases are reduced. Figure 5. 4 shows a cyclic voltammetric curve (CV) obtained for a reversible system as well as the typical characteristic parameters of the curve.

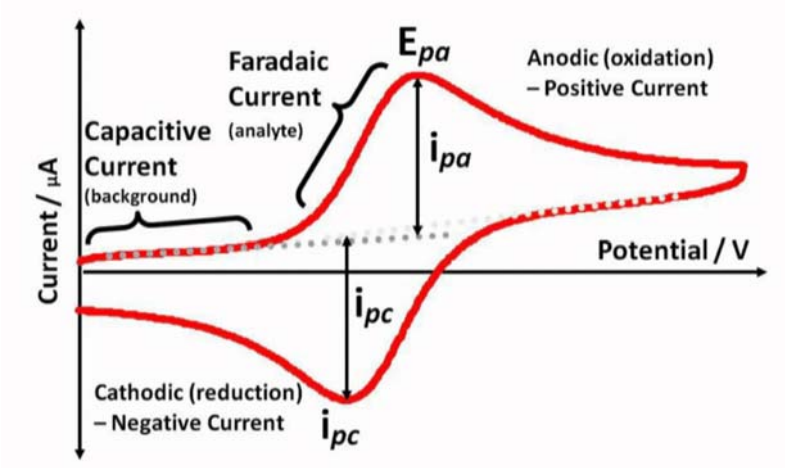

Figure 5. 4 Typical CV obtained for a reversible system with one electron-transfer process

If the system is reversible, some data interpretation can be done by using the diagnosis developed by Nicolson and Shair (1964) in order to analyze the cyclic voltammetric response of a system. One of the main characteristics for this type of systems is that the current density of both processes is the same since the same reaction is being carried out.

Specific Objectives

This study will be performed in order to determine the effect of cementitious water on the corrosion of the spent nuclear fuel.

In order to achieve this goal, a working electrode will be made by using a 3% at. simulated BU SIMFUEL as a analogue of SNF. To simulate cementitious water, an electrolyte solution containing calcium and silicate at pH 12 will be used in the experiments.

The corrosion study will be performed by using cyclic voltammetric experiments, potentiostatic experiments at 200 mV and corrosion potential experiments.

First, cyclic voltammetric measurements will be performed in order to determine the effect of the presence of silicate, the presence of calcium and silicate together and the effect of the silicate concentration on the SIMFUEL corrosion. All the electrolytes used in this study will be at pH 12 and 0.1 $mol \cdot dm^{-3}$ of NaCl.

Then, with the aim of determining the long term electrochemical evolution of the SIMFUEL in the presence of silicate and the presence of both calcium and silicate, potentiostatic and corrosion potential measurements will be performed. In order to study the oxidation state of the SIMFUEL electrode after the experiments, its surface will be analyzed by XPS after all the potentiostatic experiments and corrosion potential measurements.

Experimental Methodology

Electrode Preparation

The SIMFUEL electrode was prepared by using 3% at. simulated BU SIMFUEL pellets made by Atomic Energy of Canada Limited at Chalk River Laboratories. The amount of each non-radioactive element that can be found in the electrode is shown in Table 5. 2.

Table 5. 2 Composition of the 3% at. doped SIMFUEL used in this work

Element	U	Mo	Ru	Rh	Pd
Value ($\mu g/g_{SIMFUEL}$)	880000	180	50	13	260

Element	La	Ce	Nd	Ga	Sr	Zr	Ba
Value ($\mu g/g_{SIMFUEL}$)	900	2700	4500	29	1600	2200	1000

The procedure used in order to prepare the electrode from the bare pellet was the same as detailed by (Ofori et al., 2010). The pellet was cut to obtain a 3 mm thick disc and on one of the disc faces, a thin layer of copper was electrochemically deposited (see Figure 5. 5) in order to make it conductive (Santos et al., 2004). Afterwards, the copper layer was attached to stainless steel threaded post with a conductive epoxy resin containing silver (Hysol KS004, Wolcott-Park Inc.). In order to have a better control on the exposed area of the electrode, the pellet was introduced into a non-conductive canister and embedded with a non-conductive epoxy resin. Finally, before the resin was dry, the electrode was introduced into a vacuum chamber to remove all the air that was trapped and that could cause defects and malfunction of the electrode.

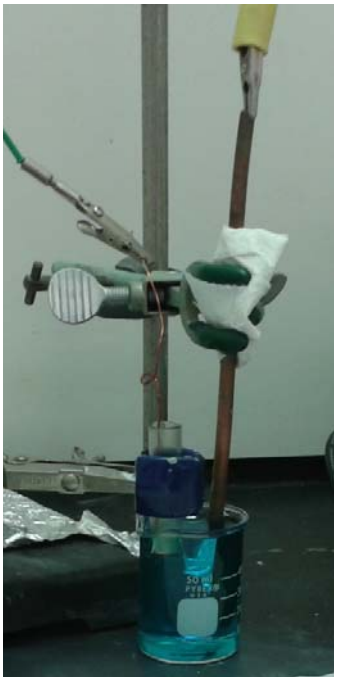

Figure 5. 5 Deposition of the Cu thin film on one of the electrode's faces

Once the preparation procedure was finished, and in order to uncover the SIMFUEL surface, the electrode was polished using 600 grit and 1200 grit SiC paper.

Before the start of any experiment, the electrode surface was again polished with the 1200 grit SiC paper at least three times to remove any oxidized phase.

Electrochemical Equipment

The Cell

A three separate compartment cell was used to perform all the experiments, which permitted the separation of all the electrodes. The counter electrode was a platinum net; its area was 1 cm^2; the reference electrode was a commercial saturated calomel electrode (SCE) (Fisher Scientific); the cell was placed into a Faraday cage to minimize any possible noise from the environment.

In order to remove any possible dissolved oxygen in the electrolyte solution and to perform the experiments under anoxic conditions, the system was purged for 1 hour with an argon stream before performing any experiment. The argon used was UHP Ar from BOC gases.

The Electrolyte

All the solutions were prepared using Milli-Q water (ρ=18.2 MΩ·cm) with 0.1 mol·dm^{-3} of NaCl (Caledon, 99.0%). The pH was adjusted at 12 in all cases with a pH meter from Orion, model 720A, and adding HCl or NaOH when necessary. An electrolyte containing 0.1 mol·dm^{-3} of NaCl at pH 12 (hereinafter named Na^+-OH^- electrolyte) was used to obtain cyclo-voltammetric curves, the corrosion potential and to perform potentiostatic measurements at 200 mV.

Na_2SiO_3 from Aldrich was used to prepare solutions 10^{-3}, $5\cdot10^{-3}$, 10^{-2}, $2\cdot10^{-2}$, $5\cdot10^{-2}$ and 0.1 mol·dm^{-3} of silicate in the electrolyte (see Table 5. 3). All of them were used to perform cyclo-voltammetric measurements and to determine whether the silicate concentration has an effect on the SIMFUEL corrosion process. Then, 10^{-2} mol·dm^{-3} of Na_2SiO_3 (hereinafter named SiO_3^{2-} electrolyte) was used to perform the potentiostatic measurements at 200 mV and the corrosion potential measurements.

Table 5. 3. Summary of electrolytes used in this study with their compositions

Electrolyte	pH	[NaCl] (mol·dm^{-3})	[Na_2SiO_3] (mol·dm^{-3})	[$CaCl_2$] (mol·dm^{-3})
Na^+-OH^-	***12***	***0.1***	**----**	**----**
SiO_3^{2-} (-3)	12	0.1	10^{-3}	----
SiO_3^{2-} (5-3)	12	0.1	$5\cdot10^{-3}$	----
SiO_3^{2-}	***12***	***0.1***	***10^{-2}***	**----**
SiO_3^{2-} (2-2)	12	0.1	$2\cdot10^{-2}$	----
SiO_3^{2-} (5-2)	12	0.1	$5\cdot10^{-2}$	----
SiO_3^{2-} (-1)	12	0.1	0.1	----
Ca^{2+}- SiO_3^{2-} (-3)	12	0.1	10^{-3}	10^{-3}
Ca^{2+}- SiO_3^{2-}	***12***	***0.1***	***10^{-2}***	***10^{-3}***

In bold and italic are the electrolytes used in the study

$CaCl_2$ from Fisher Scientific was used to introduce 10^{-3} mol·dm^{-3} of calcium in two different solutions: one of them with 10^{-2} mol·dm^{-3} and the other one with 10^{-3} mol·dm^{-3} of silicate (see Table 5. 3). These solutions were used to obtain the cyclo-voltammetric curves. Then, a solution with 10^{-3} mol·dm^{-3} of calcium and 10^{-2} mol·dm^{-3} of silicate (hereinafter named Ca^{2+}-SiO_3^{2-} electrolyte) was used to perform potentiostatic data at 200 mV and corrosion potential measurements.

The Potentiostat

All the data were recorded by using a Solatron Potentiostat that controlled the applied potential between the reference electrode (RE) and the SIMFUEL electrode or working electrode (WE). Three different kinds of experiments were carried out: cyclo-voltammetric, potentiostatic and corrosion potential. Before carrying out any of these experiments, the potential was checked for 1 minute and then a cathodic cleaning at -1400 mV was performed on the electrode to check that it was working and to reduce any oxidized surface layer.

Cyclo-voltammetric experiments were performed between -1200 mV and 400 mV (vs. SCE), the step rate was set at 10 mV·s^{-1} and the WE was stirred at 500 rpm. Additional cyclo-voltammograms were performed at different ranges, always starting at -1200 mV and ending either at -400, -200, 0 or 200 mV. This experimental methodology was performed using all the electrolytes shown in Table 5. 3.

To perform the potentiostatic experiments, the potential applied between the WE and the RE was 200 mV for 1 hour. Prior to the experiments, the electrolyte was purged with an Ar stream for 1 hour. In this case, the WE was not stirred during the experiment. This experimental methodology was performed using three electrolytes defined previously: Na^+-OH^-, SiO_3^{2-} and Ca^{2+}-SiO_3^{2-}.

The corrosion potential experiments, also called open circuit experiments, were performed by letting the system evolve as an open circuit. By doing this, the potential between the RE and the WE changed with time. As in the previous case, before performing the experiments, the electrolyte was purged with an Ar stream for 1 hour. The WE was not stirred while the experiments were performed. The corrosion potential measurements were obtained for the same electrolytes used in the potentiostatic experiments.

The data obtained were recorded using the Corrware and Corrview software (Scribner Associates).

Surface Analysis

After each potentiostatic experiment and each corrosion potential experiment, the WE surface was analyzed by XPS. In this case, the XPS analyses were carried out with a Kratos Axis Ultra spectrometer using a monochromatic Al K(alpha) source (15mA, 14kV) (see Figure 5. 6).

Figure 5. 6 XPS equipment at the Surface Science Center (Biesinger, 2015)

The spectra treatment was done following the same methodology detailed in Chapter 2.

Results and Discussion

The results obtained for the three electrolytes (Na^+-OH^-, SiO_3^{2-} and Ca^{2+}-SiO_3^{2-}) have been published in Espriu-Gascon et al. (2017).

Cyclic Voltammetric Experiments

Na^+-OH^- Electrolyte

First, in order to qualitatively determine the effect of silicate and calcium on the SIMFUEL surface under hyper-alkaline solutions, several cycle-voltammogram (CV) experiments were performed. This kind of experiment allowed to have a preliminary knowledge of the system behavior.

Figure 5. 7 shows the CV obtained by using the 3% at. SIMFUEL. Five different zones can be distinguished in the graph as identified by Shoesmith (2000).

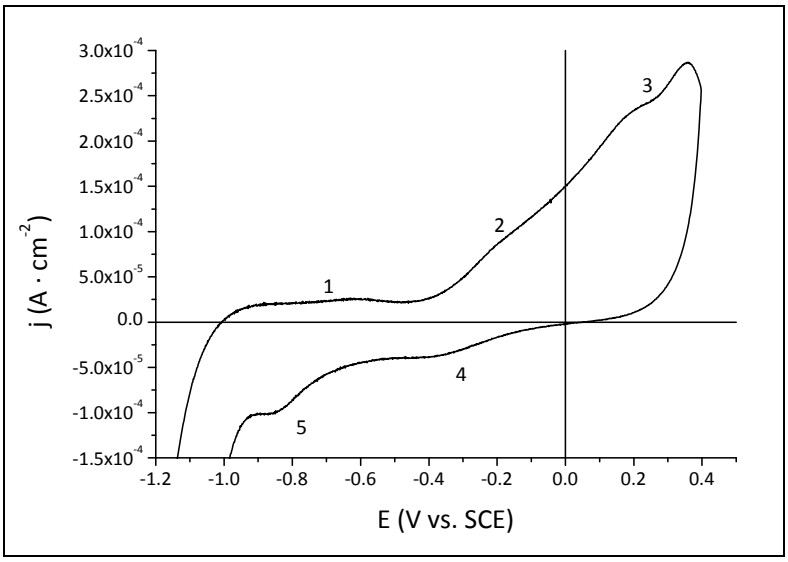

Figure 5. 7 Cyclo - voltammogram obtained at pH 12 with NaCl 0.1 mol·dm^{-3} in the dissolution and 3% at. doped SIMFUEL as electrode.

1. In the first one (1), the current density (j) remained constant from -900 mV to -400 mV, where the SIMFUEL started to oxidize at the surface, probably concentrated at the grain boundaries.
2. The starting point of the second region (2) obtained from the graph is shown in Table 5. 4 and is located between -400 mV and 300 mV. It can be observed in Figure 5. 7 that the current density increased almost following a linear tendency. This behavior is assumed to be caused by the irreversible oxidation of the UO_2 lattice to UO_{2+x} and the subsequent U(VI) dissolution.

3. In region (3), there was the maximum current density value followed by a decrease just before the reverse scan, which suggests that the oxidation reaction is being stopped. The exact potential of the peak is listed in Table 5. 4. This peak might be caused by the precipitation of a surface layer that could block the SIMFUEL corrosion or may decrease the diffusive mass transfer between the electrode surface and the bulk of the electrolyte. Considering the electrolyte used, the solid phase could be a uranyl oxide hydrate phase such as schoepite ($UO_3 \cdot 2H_2O$).
4. In region (4) the reduction peak that corresponds to region 3 is observed. This fact is deduced from Figure 5. 8 where the peak of region (4) appeared only when the full CV scan was performed. The potential value of the peak is reported in Table 5. 4.
5. Another peak can be observed in region (5). This peak first appeared when the anodic limiting potential used was -200 mV and region (2) appeared (see Figure 5. 8). Therefore, it can be concluded that the peak in region (5) is the reduction peak corresponding to the oxidation occurring in region (2).

Figure 5. 8 shows that the experimental methodology is highly reproducible, because the anodic current densities from all CVs obtained overlay with each other. The identified CV parameters are listed observed in Table 5. 4.

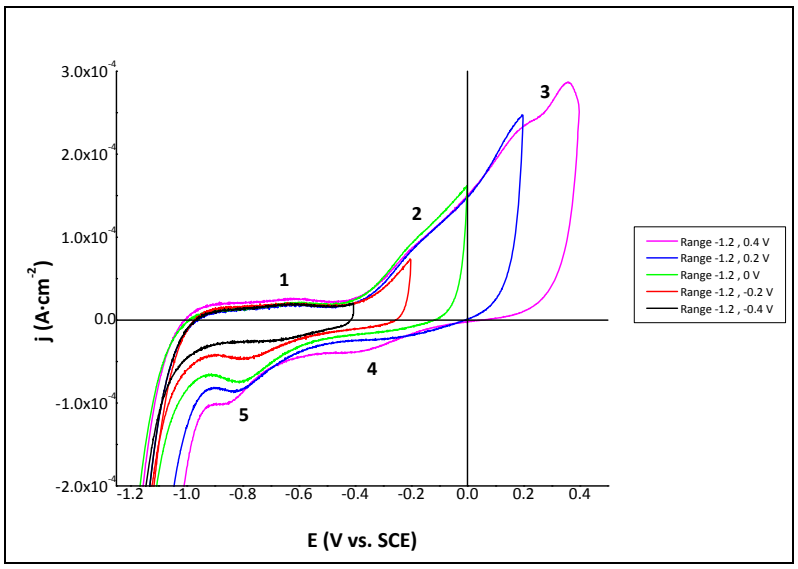

Figure 5. 8 CV series obtained by using the 3% at. SIMFUEL in contact with the Na^+-OH^- electrolyte . The CVs were obtained by using different anodic limiting potentials: -400, -200, 0.0, 200 and 400 mV vs. SCE

Table 5. 4 List of the CV characteristic values for each region identified in Figure 5. 7 and Figure 5. 8. The results are shown as function of the anodic limiting current for each curve

Anodic limit potential (V)	CV Parameters	Region 1*	Region 2**	Region 3	Region 4	Region 5
-0.4	E (V)	-0.9 & -0.4	--	--	--	No peak
	j (A·cm^{-2})	1.60 · 10^{-5}	--	--	--	No peak
-0.2	E (V)	-0.9 & -0.4	-0.37 ± 0.02	--	No peak	-0.80 ± 0.02
	j (A·cm^{-2})	1.73 · 10^{-5}	2.48 · 10^{-5}	--	No peak	-4.70 · 10^{-5}
0.0	E (V)	-0.9 & -0.4	-0.41 ± 0.02	--	No peak	-0.81 ± 0.02
	j (A·cm^{-2})	1.81 · 10^{-5}	2.30 · 10^{-5}	--	No peak	-7.45 · 10^{-5}
0.2	E (V)	-0.9 & -0.4	-0.39 ± 0.02	--	No peak	-0.83 ± 0.02
	j (A·cm^{-2})	1.60 · 10^{-5}	2.26 · 10^{-5}	--	No peak	-8.74 · 10^{-5}
0.4	E (V)	-0.9 & -0.4	-0.40 ± 0.02	0.36 ± 0.02	-0.43 ± 0.02	-0.86 ± 0.02
	j (A·cm^{-2})	2.28 · 10^{-5}	2.70· 10^{-5}	2.87 · 10^{-5}	-3.95 · 10^{-5}	10^{-4}

**Region 1 values correspond to the steady state observed between -0.90 and -0.40 V of the anodic current*
***Region 2 values show the starting point of the current increase due to a no clear peak is observed*

SiO_3^{2-} Electrolytes

The effect of silicate was studied by performing CV with 10^{-3}, 5·10^{-3}, 10^{-2}, 2·10^{-2}, 5·10^{-2} and 0.1 mol·dm^{-3} of silicate in the electrolyte at pH 12; the solutions also contained 0.1 mol·dm^{-3} of NaCl. The results showed that the silicate concentration had no significant effect on the system behavior since all the CVs obtained showed the same behavior, as it can be seen in Figure 5. 9.

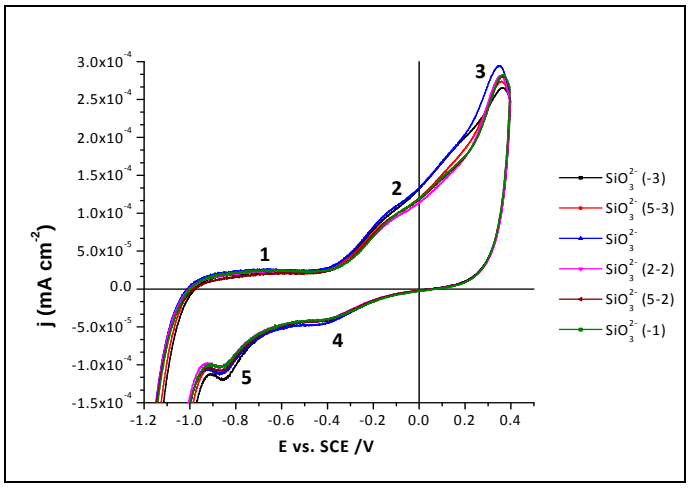

Figure 5. 9 Cyclo-voltammograms of the experiments performed with the 3% at. SIMFUEL to study the effect of the silicate concentration in the solution on the corrosion process

From all the silicate electrolytes used, the resulting CV obtained with the SiO_3^{2-} electrolyte was chosen to perform several CV scans using different potential ranges: all of them started at -1200 mV and they ended at -400, -200, 0, 200 and 400 mV in order to follow the stages of oxidation and reduction observed (Figure 5. 9). In addition, the evolution of anodic oxidation processes and

corresponding cathodic reduction processes can be observed as a function of the anodic limiting potential.

Five different regions can be observed in Figure 5. 9. As in the previous case, the behavior of the system can be defined as a function of the potential of the CV (Shoesmith, 2000).

1. In the first one (1), the current density (j) remained constant from -900 mV to -380 mV and corresponds to the SIMFUEL oxidation on the surface, probably concentrated at the grain boundaries.
2. The second region (2) was identified between -380 mV and 300 mV (see Table 5. 5). It can be observed in Figure 5. 9 that the current density increased almost following a linear tendency. This behavior is assumed to be caused by the irreversible oxidation of the UO_2 to UO_{2+x} and the subsequent U(VI) dissolution.
3. In region (3), there was a maximum current density followed by a decrease before the reverse scan at 350 mV (see Table 5. 5). As in the previous case, this may be caused by the precipitation of a surface layer blocking the SIMFUEL surface or decreasing the diffusive mass transfer between the electrode surface and the bulk of the electrolyte. Considering the electrolyte used, the solid phase might be a uranyl silicate phase.
4. In region (4) the reduction peak corresponding to oxidation in region 3 is observed. This is deduced from Figure 5. 10 where the peak of region (4) appeared only when the full CV scan was performed. The potential value of the reduction peak is -450 mV (see Table 5. 5).
5. In region (5), another peak can be observed. This peak first appeared when the anodic limiting potential used was -200 mV and region (2) appeared (see Figure 5. 10). Therefore, the peak in region (5) is a reduction peak corresponding to the oxidation occurring in region (2).

Figure 5. 10 also shows that each CV overlapped with the previous one in the anodic cycle, indicating the high reproducibility of the experimental system.

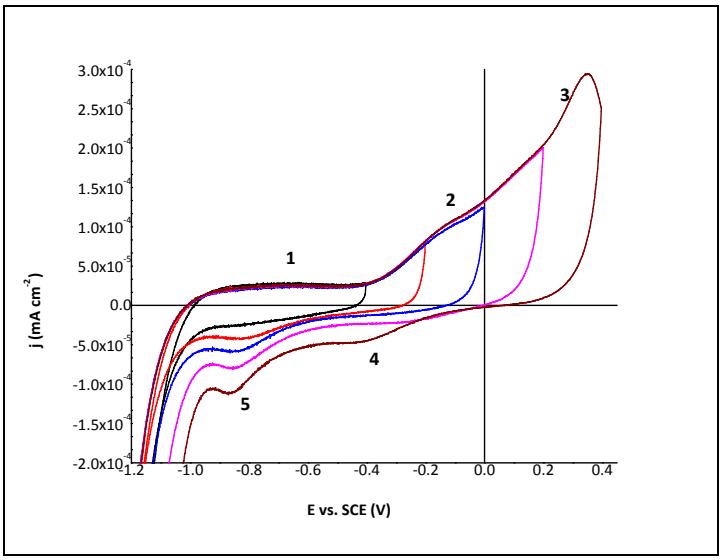

Figure 5. 10 CV scans obtained by using different scan potential ranges with the SiO_3^{2-} electrolyte.

Table 5. 5 List of the CV characteristic values for each region identified in presence of SiO_3^{2-} electrolyte (Figure 5. 10). The results are shown as function of the anodic limiting current for each curve

Anodic limit potential (V)	CV Parameters	Region 1*	Region 2**	Region 3	Region 4	Region 5
-0.4	E (V)	-0.9 & -0.4	--	--	--	No peak
	j ($A \cdot cm^{-2}$)	$2.66 \cdot 10^{-5}$	--	--	--	No peak
-0.2	E (V)	-0.9 & -0.4	-0.38 ± 0.02	--	No peak	-0.83 ± 0.02
	j ($A \cdot cm^{-2}$)	$2.45 \cdot 10^{-5}$	$3.00 \cdot 10^{-5}$	--	No peak	$-4.25 \cdot 10^{-5}$
0.0	E (V)	-0.9 & -0.4	-0.38 ± 0.02	--	No peak	-0.85 ± 0.02
	j ($A \cdot cm^{-2}$)	$2.23 \cdot 10^{-5}$	$2.85 \cdot 10^{-5}$	--	No peak	$-5.85 \cdot 10^{-5}$
0.2	E (V)	-0.9 & -0.4	-0.38 ± 0.02	--	No peak	-0.86 ± 0.02
	j ($A \cdot cm^{-2}$)	$2.37 \cdot 10^{-5}$	$3.09 \cdot 10^{-5}$	--	No peak	$-8.15 \cdot 10^{-5}$
0.4	E (V)	-0.9 & -0.4	-0.37 ± 0.02	0.35 ± 0.02	-0.45 ± 0.02	-0.87 ± 0.02
	j ($A \cdot cm^{-2}$)	$2.40 \cdot 10^{-5}$	$3.12 \cdot 10^{-5}$	$2.39 \cdot 10^{-4}$	$-4.70 \cdot 10^{-5}$	$-1.11 \cdot 10^{-4}$

**Region 1 values correspond to the steady state observed between -0.90 and -0.40 V of the anodic current*
***Region 2 values show the starting point of the current increase due since clear peak is observed*

Ca^{2+}-SiO_3^{2-} Electrolyte

Under the experimental conditions used in this study where two electrolytes were used (Ca^{2+}-SiO_3^{2-} and Ca^{2+}-SiO_3^{2-} (-3)) (see Table 5. 3), it was observed that the corrosion process was not affected by the silicate concentration. As it can be observed in Figure 5. 11, the two CVs overlapped each other and the five regions can be identified.

1. In the first one (1), the current density (j) remained constant from -900 mV to -300 mV and corresponds to the SIMFUEL oxidation on the surface, probably concentrated at the grain boundaries.

2. The second region (2) was identified between -300 mV and 300 mV (see Table 5. 6). It can be observed in Figure 5. 11 that the current density increased almost following a linear tendency. This behavior is assumed to be caused by the irreversible oxidation of the UO_2 to UO_{2+x} and the U(VI) dissolution.
3. In region (3), there was a maximum current density at 380 mV (see Table 5. 6). In this case, the suppression of the corrosion process was not clearly observed; further experiments might be needed to determine the effect of the Ca^{2+}-SiO_3^{2-} electrolyte under oxidizing conditions.
4. In region (4) the reduction corresponding to oxidation in region 3 is observed. This fact is deduced from Figure 5. 12 where the peak of region (4) appeared only when the full CV scan was performed. The potential value of the reduction peak is -380 mV (see Table 5. 6).
5. In region (5), another peak can be observed. This peak first appeared when the anodic limiting potential used was -200 mV and region (2) appeared (see Figure 5. 12). Therefore, the peak in region (5) is a reduction peak corresponding to the oxidation occurring in region (2).

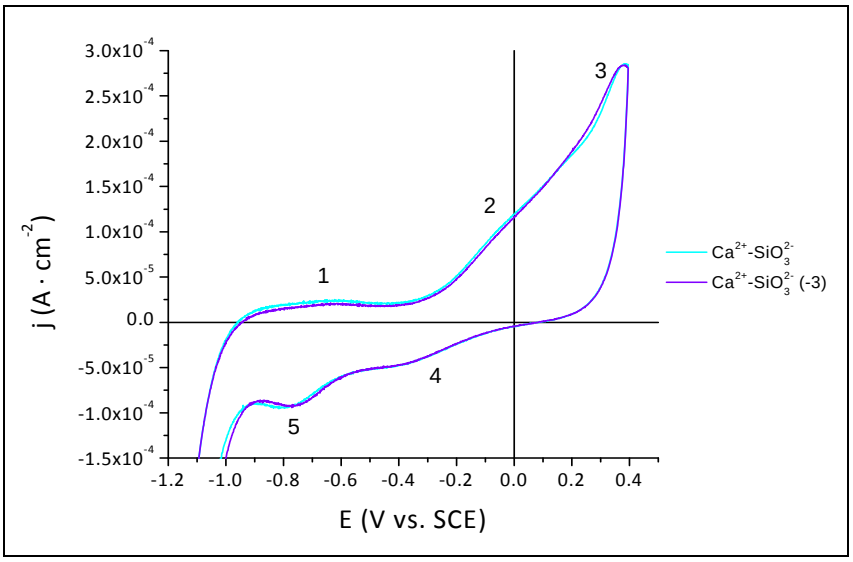

Figure 5. 11 CV curves obtained after performing the experiments with the Ca^{2+}-SiO_3^{2-} (-3) and the Ca^{2+}-SiO_3^{2-} electrolytes

Table 5. 6 List of the CV characteristic values for each region identified in presence of the Ca^{2+}-SiO_3^{2-} electrolyte (Figure 5. 11). The results are shown as function of the anodic limiting current for each curve

Anodic limit potential (V)	CV Parameters	Region 1*	Region 2**	Region 3	Region 4	Region 5
-0.2	E (V)	-0.9 & -0.4	--	--	--	No peak
	j ($A \cdot cm^{-2}$)	$2.20 \cdot 10^{-5}$	--	--	--	No peak
0.0	E (V)	-0.9 & -0.4	-0.29 ± 0.02	--	No peak	-0.81 ± 0.02
	j ($A \cdot cm^{-2}$)	$2.06 \cdot 10^{-5}$	$2.88 \cdot 10^{-5}$	--	No peak	$-4.85 \cdot 10^{-5}$
0.2	E (V)	-0.9 & -0.4	-0.30 ± 0.02	--	No peak	-0.81 ± 0.02
	j ($A \cdot cm^{-2}$)	$1.87 \cdot 10^{-5}$	$2.57 \cdot 10^{-5}$	--	No peak	$-5.59 \cdot 10^{-5}$
0.4	E (V)	-0.9 & -0.4	-0.30 ± 0.02	0.38 ± 0.02	-0.38 ± 0.02	-0.80 ± 0.02
	j ($A \cdot cm^{-2}$)	$2.21 \cdot 10^{-5}$	$2.96 \cdot 10^{-5}$	$2.86 \cdot 10^{-4}$	$-4.64 \cdot 10^{-5}$	$-9.41 \cdot 10^{-5}$

**Region 1 values correspond to the steady state observed between -0.90 and -0.40 V of the anodic current*
***Region 2 values show the starting point of the current increase due to a no clear peak is observed*

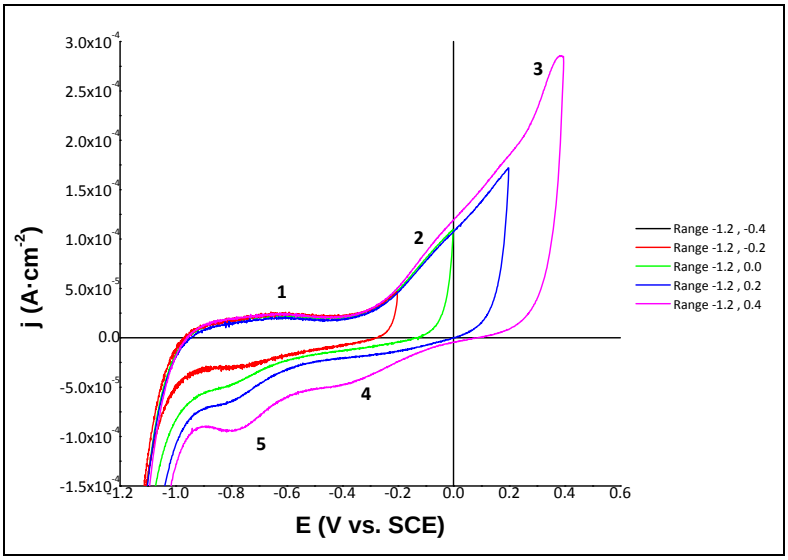

Figure 5. 12 CV scans obtained by using different scan potential ranges for the Ca^{2+}-SiO_3^{2-} electrolyte.

Effect of the electrolyte composition

In Figure 5. 13, the CV curves of the Na^+-OH^-, SiO_3^{2-} and Ca^{2+}-SiO_3^{2-} electrolytes are plotted together in order to better appreciate the effect of each ion added to the electrolyte solution. It can be observed that the presence of silicate produced a decrease of the corrosion of SIMFUEL between -100 mV and 300 mV. This is the main effect since the other regions of the CV curves for Na^+-OH^- and SiO_3^{2-} are overlapped to each other and present similar CV scans characteristics in Table 5. 7.

The cathodic region obtained is different in both curves, with a lower current density for the SiO_3^{2-} electrolyte. This means that the presence of silicate enhances the reduction of the oxidized phases

by facilitating the O^{2-} extraction from the crystal structure. The effect of the presence of silicate was studied by (Santos et al., 2006b) in contact with 1.5% at. SIMFUEL at pH 9.5. Under those conditions, the results showed that silicate suppressed the formation of $UO_3 \cdot yH_2O$ at potentials lower than 250 mV. At higher potentials, the SIMFUEL was covered by a hydrated surface layer containing silicate as the SEM images published in Shoesmith (2007) confirmed.

Similar results were obtained in the present study, where a first oxidation process starts at -400 mV and ends at -100 mV in region 2 for both systems, Na^+-OH^- and SiO_3^{2-} (Figure 5. 13). This first oxidizing step most likely corresponds to the oxidation of UO_2 to $U^{V}_{2x}U^{IV}_{1-2x}O_{2+x}$.

The second oxidizing step, that starts at -100 mV and ends at 300 mV in region 2, produces the uranyl ion that may be complexated in contact with anions in solution such as hydroxyl (Santos et al., 2006a) or silicate.

Table 5. 7 List of the main characteristic values of the full CV scan recorded as a function of the electrolyte composition

Electrolyte	CV Parameters	Region 1*	Region 2**	Region 3	Region 4	Region 5
Na^+-OH^-	E (V)	-0.9 & -0.4	-0.40 ± 0.02	0.36 ± 0.02	-0.43 ± 0.02	-0.86 ± 0.02
	j ($A \cdot cm^{-2}$)	$2.28 \cdot 10^{-5}$	$2.70 \cdot 10^{-5}$	$2.87 \cdot 10^{-5}$	$-3.95 \cdot 10^{-5}$	10^{-4}
SiO_3^{2-}	E (V)	-0.9 & -0.4	-0.37 ± 0.02	0.35 ± 0.02	-0.45 ± 0.02	-0.87 ± 0.02
	j ($A \cdot cm^{-2}$)	$2.40 \cdot 10^{-5}$	$3.12 \cdot 10^{-5}$	$2.39 \cdot 10^{-4}$	$-4.70 \cdot 10^{-5}$	$-1.11 \cdot 10^{-4}$
Ca^{2+}-SiO_3^{2-}	E (V)	-0.9 & -0.4	-0.30 ± 0.02	0.38 ± 0.02	-0.38 ± 0.02	-0.80 ± 0.02
	j ($A \cdot cm^{-2}$)	$2.21 \cdot 10^{-5}$	$2.96 \cdot 10^{-5}$	$2.86 \cdot 10^{-4}$	$-4.64 \cdot 10^{-5}$	$-9.41 \cdot 10^{-5}$

**Region 1 values correspond to the steady state observed between -0.90 and -0.40 V of the anodic current*
***Region 2 values show the starting point of the current increase due to a no clear peak is observed*

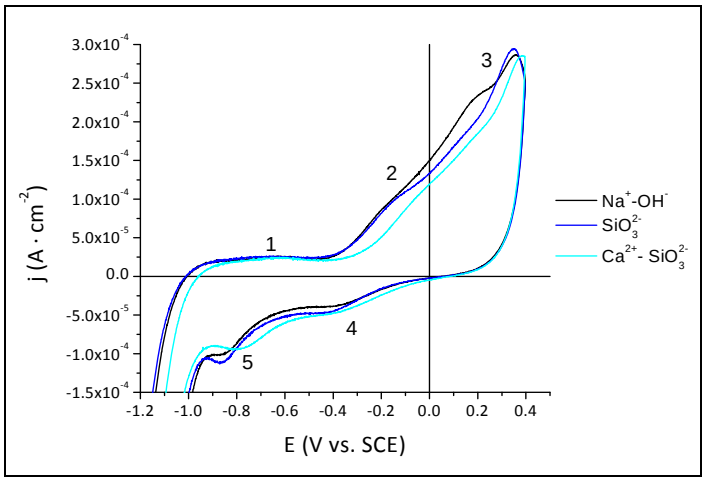

Figure 5. 13 CV curves obtained with the Na^+-OH^- electrolyte, the SiO_3^{2-} electrolyte and the Ca^{2+}-SiO_3^{2-} electrolyte

On the other hand, in the presence of calcium, the whole oxidation and reduction processes were shifted to higher potentials as it can be observed in Table 5. 7.

The effect of calcium was studied by (Santos et al., 2006c) and the results showed that calcium partially inhibited the corrosion process by means of two possible mechanisms:

- Inhibiting the $UO_2(OH)_2$(ads) stabilization on the electrode which will avoid further uranium oxidation to U(VI).
- Secondary phase precipitation on the surface electrode that will impede the corrosion process to continue.

Regarding the scans obtained, it can be concluded that the presence of silicate in solution may avoid the $U^{V}_{2x}U^{IV}_{1-2x}O_{2+x}$ oxidation to soluble U(VI). The presence of both calcium and silicate may help to stabilize the reduced solid phases or may enhance the reduction process.

Potentiostatic experiments

To determine the effect of the presence of each ion and the reactions involved in the corrosion process, potentiostatic experiments were performed. These experiments consisted on applying a constant potential, in this case 200 mV, and following the evolution of the current density as a function of time. They were performed for 1 hour with the 3% at. SIMFUEL in contact with the three different kind of electrolytes mentioned in the previous section.

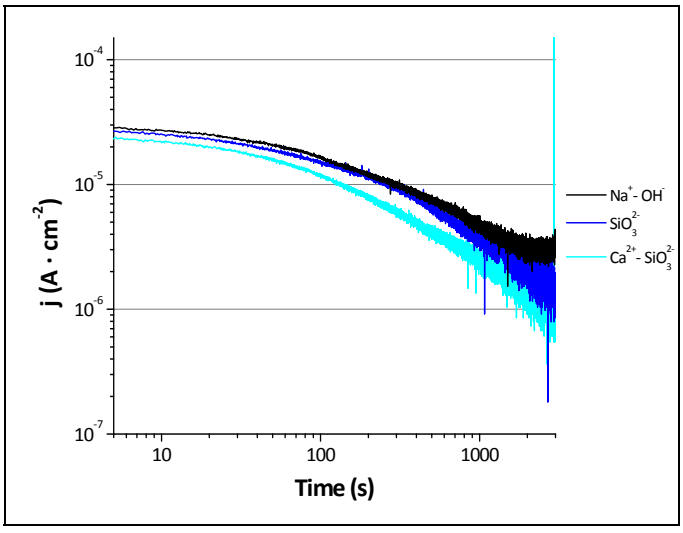

Figure 5. 14 Potentiostatic current-time curves of the 3% at. SIMFUEL in contact with the Na^+-OH^- electrolyte, the SiO_3^{2-} electrolyte and the Ca^{2+}-SiO_3^{2-} electrolyte.

In Figure 5. 14, the evolution of the current density as a function of time can be seen. The graph shows that the highest current density was obtained with the Na^{+}-OH^{-} electrolyte, and the lowest was obtained with the Ca^{2+}-SiO_3^{2-} electrolyte. These results are in agreement with the results obtained in the cyclo-voltammetry study, where the highest current density at 200 mV was obtained when the Na^{+}-OH^{-} was used and the lowest current density was obtained when the Ca^{2+}-SiO_3^{2-} electrolyte was used.

In order to appreciate better the electron exchange in each system, Figure 5. 15 shows the integration of the current density from Figure 5. 14 as a function of time for the three experiments (deriving from Faraday's law and the Eq. (5.5)). It can be observed that approximately within the first two minutes, the anodic charge density (Q_A) was the same independently of the presence of silicate and calcium. Afterwards, the exchange of electrons decreased with the Ca^{2+}-SiO_3^{2-} electrolyte and diverged from the results obtained with the Na^{+}-OH^{-} and the SiO_3^{2-} electrolytes. On the other side, the current density obtained with the SiO_3^{2-} electrolyte diverged from the results obtained with the Na^{+}-OH^{-} electrolyte after 5 minutes approximately.

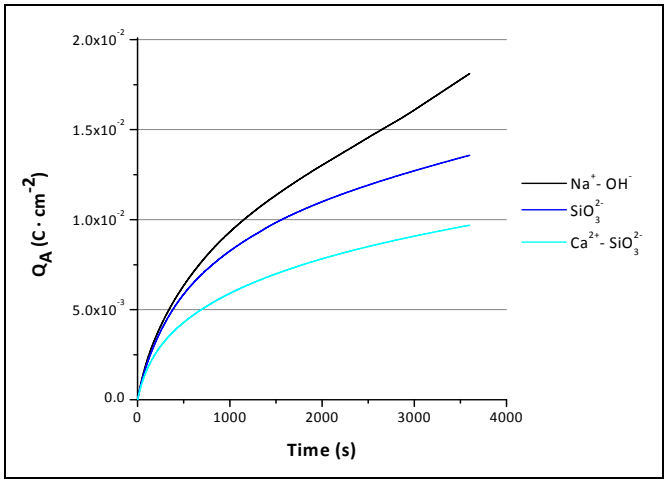

Figure 5. 15 Comparison of all the anodic charges obtained by the integration of the current densities in the Figure 5. 14.

The trend of the Q_A in Figure 5. 15 at the end of the SiO_3^{2-} and Ca^{2+}-SiO_3^{2-} curves indicates that the corrosion process was being suppressed since the electrons transferred from the WE reached a constant current density at the end of the experiment (Figure 5. 14). A possible explanation could be that the precipitation of secondary phases on the electrode surface could be preventing the electron transfer.

After performing the potentiostatic experiments, the SIMFUEL electrode was analyzed by XPS and the results obtained for the uranium band (U 4f) are shown in Figure 5. 16. It can be observed that with the Ca^{2+}-SiO_3^{2-} electrolyte the uranium oxidation state was lower than with Na^{+}-OH^{-}.

The results of the O 1s band deconvolution are shown in Figure 5. 17. The oxygen band was deconvoluted into O^{2-}, OH^{-}, O-Si and H_2O band when necessary. It can be observed that the Na^{+}-OH^{-} electrolyte presented a high proportion of oxygen as hydroxyl group and as water molecules on the electrode surface. On the other hand, the Ca^{2+}-SiO_3^{2-} electrolyte, oxygen was mainly present as oxygen-silicate and as O^{2-}, probably corresponding to either the UO_2 that was not oxidized during the experiment and to the $U^{V}_{2x}U^{IV}_{1-2x}O_{2+x}$ oxidized layer.

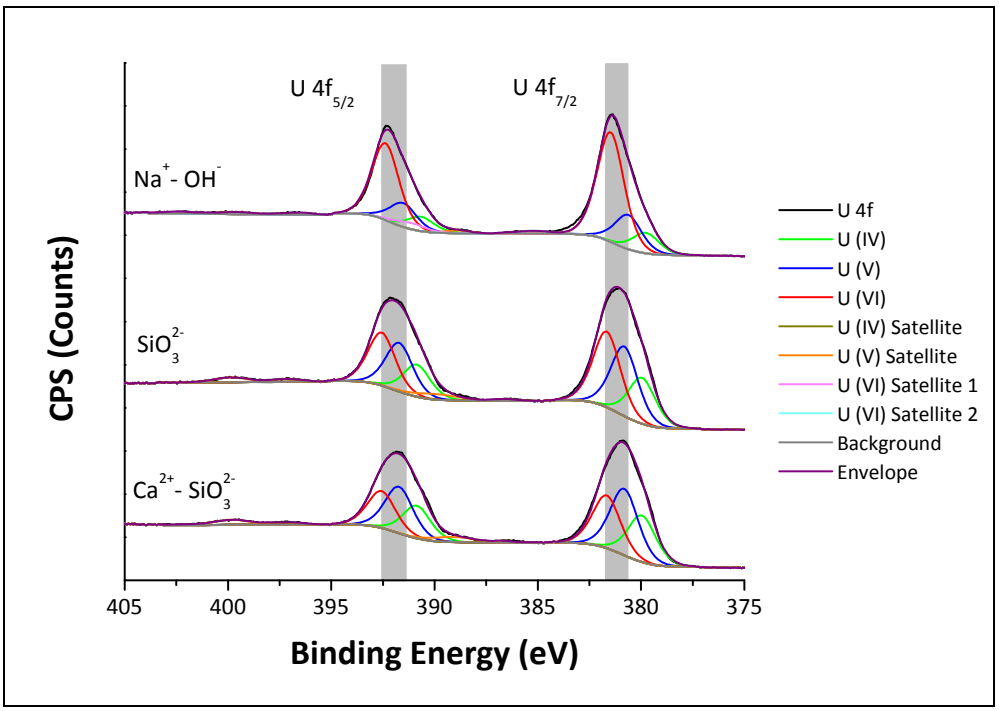

Figure 5. 16 XPS spectra and deconvolution of the U 4f band for the SIMFUEL electrode after performing each of the potentiostatic experiments.

Comparing the results with those obtained with Na^{+}-OH^{-} at 200 mV, it can be concluded that the presence of silicate partially avoided the oxidation of UO_2 under these experimental conditions (Figure 5. 16). Furthermore, when calcium was added to the electrolyte, the corrosion was even lower. Therefore, the addition of both ions, calcium and silicate, decreased the UO_2 corrosion at high oxidizing potentials.

XPS results (not shown here) seem to indicate that at the end of the experiment silicate and calcium were incorporated into the SIMFUEL structure once the process of oxidation started. The

incorporation of such species may have stopped the corrosion process by blocking the O^{2-} and the OH^- anions before entering in contact with the UO_2 surface.

Regarding the results obtained with the XPS, the precipitation of secondary phases on the electrode surface was not fully confirmed.

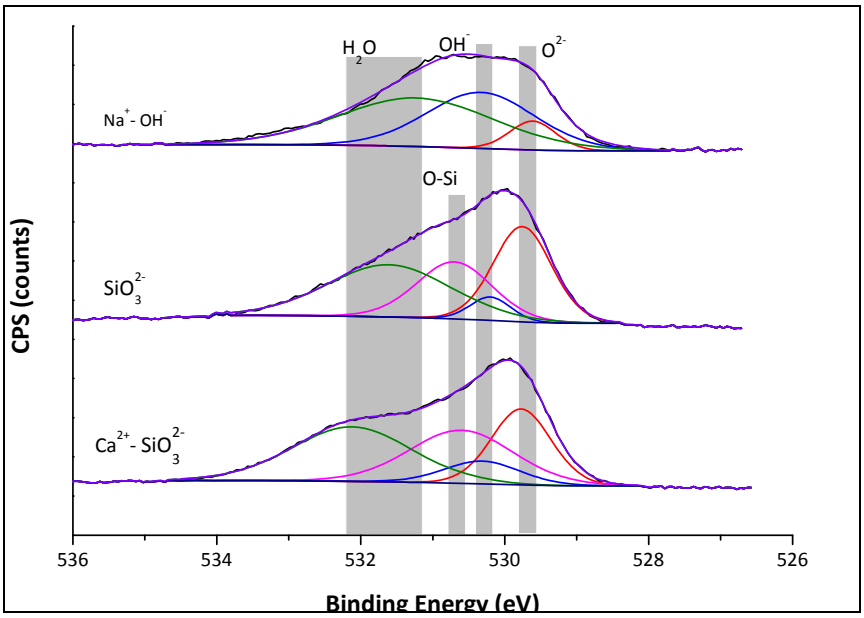

Figure 5. 17 XPS spectra and deconvolution of the O 1s band from the SIMFUEL electrode after performing each of the potentiostatic experiments.

E_{CORR} Experiments

To perform the corrosion potential experiments, the SIMFUEL electrode was in contact with the three different solutions for 24 hours, without applying any specific potential. The system evolved from the cathodic cleaning potential (-1400 mV) of the electrode to the steady state, as it can be observed in Figure 5. 18. The potential rapidly increased in all three cases until approximately -300 mV. From there, the behavior of the potential was different depending on the composition of the solution. The potential obtained with the Na^+-OH^- electrolyte increased until it reached the steady state in less than three hours at -80 mV at the end of the experiment. This result can be compared with the one obtained by (Broczkowski et al., 2007),who also studied a 3% at. SIMFUEL under argon atmosphere. They performed corrosion potential measurements at pH 9.5 and used 0.1 $mol{\cdot}dm^{-3}$ of KCl at 60^0C. Under these experimental conditions, the corrosion potential reached -220 mV which is lower than the value obtained in this section (-80 mV). Hence, and despite the difference in the temperature values, it is possible to assume that the increase of the pH enhanced the corrosion of the SIMFUEL (Santos et al., 2006a; Torrero et al., 1997).

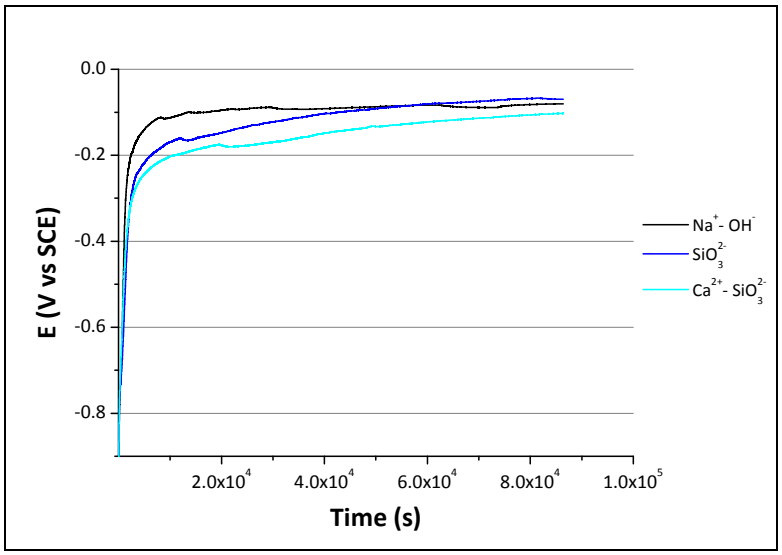

Figure 5. 18 E_{CORR} measurements on the 3% at. SIMFUEL in contact with Na^+-OH^- electrolyte (black line); SiO_3^{2-} electrolyte (navy blue line); Ca^{2+}-SiO_3^{2-} electrolyte (light blue line)

In presence of silicate, the corrosion potential increased until just before the end of the experiment to the value obtained with Na^+-OH^- electrolyte (about -70 mV). As it can be observed, this result is close to the E_{CORR} obtained with the Na^+-OH^-. This fact might be caused by the initial oxidation of the lattice UO_2 to UO_{2+x} at the potential values obtained (Shoesmith, 2000) that is not avoided by the presence of the silicate.

The corrosion potential in the case of the calcium electrolyte was always lower than in the other two curves obtained, as it can be seen in Figure 5. 18. The evolution of the potential as function of time would indicate that the UO_2 oxidation continued for 24 hours. In this case, the potential at the end of the experiment was lower than in the other experiments: -105 mV, which points to a lower final oxidized state of uranium than in the other two experiments. This result might be caused by the stabilization of the reduced species under the Ca^{2+}-SiO_3^{2-} electrolyte conditions.

This fact was corroborated by the XPS analysis of the surfaces performed at the end of the experiments (Figure 5. 19 and Figure 5. 20). The XPS results showed that in the experiments carried out with and without silicate in the electrolyte solution the final oxidation state of the uranium in the surface was very similar. These results are congruent with the potential values obtained in Figure 5. 18, where E_{CORR} measures for Na^+-OH^- and SiO_3^{2-} electrolytes were close to each other. The addition of calcium partially avoided the oxidation compared with the Na^+-OH^- and the SiO_3^{2-} electrolytes, since the main contribution was due to the U (IV) band (see Figure 5. 19).

These results are in good agreement with the ones deduced from the results described previously in this work.

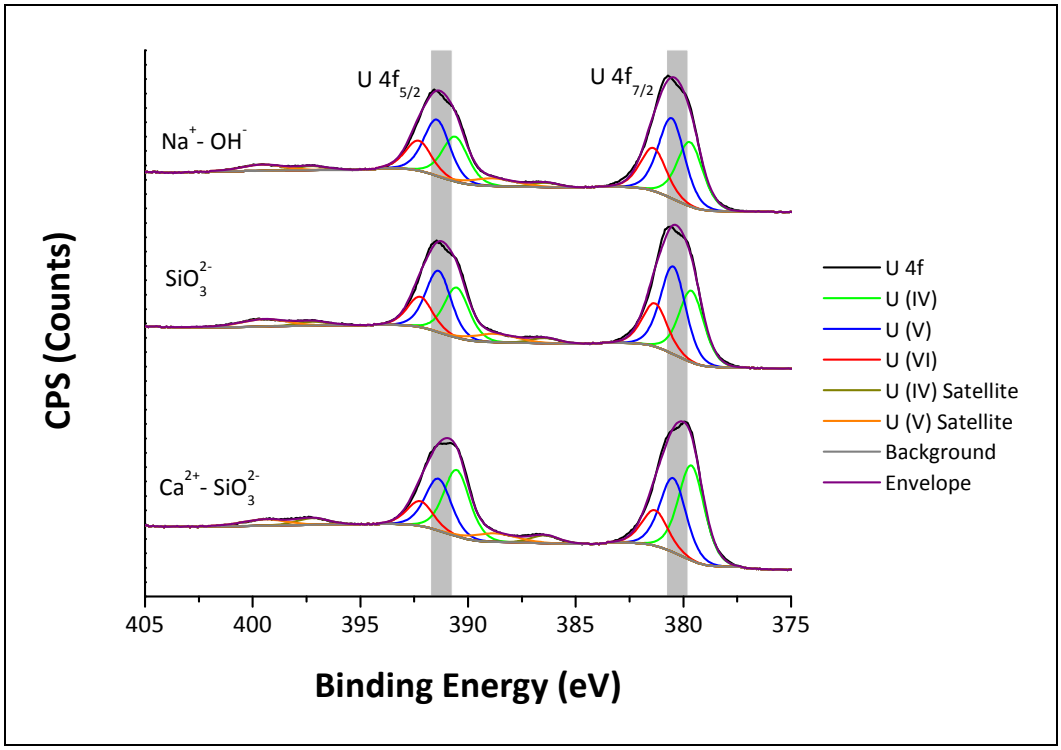

Figure 5. 19 XPS spectra and deconvolution of the U 4f band from the SIMFUEL electrodes after performing each of the corrosion potential experiments.

In order to obtain more information about the SIMFUEL surface composition, the oxygen band of the XPS spectra was also recorded (Figure 5. 20). It was observed that the main contribution to the oxygen was the O^{2-} band for all the results obtained. In addition the hydroxyl and the oxygen-silicate were observed in the O 1s band obtained after performing the experiments with silicate and both calcium and silicate. At the same time, the contribution of the OH^- band decreased with the addition of ions to the electrolyte. On the other side, the H_2O band contribution increased as the ions were added to the solution indicating that the precipitation of a hydrated phase on the electrode surface may have occurred.

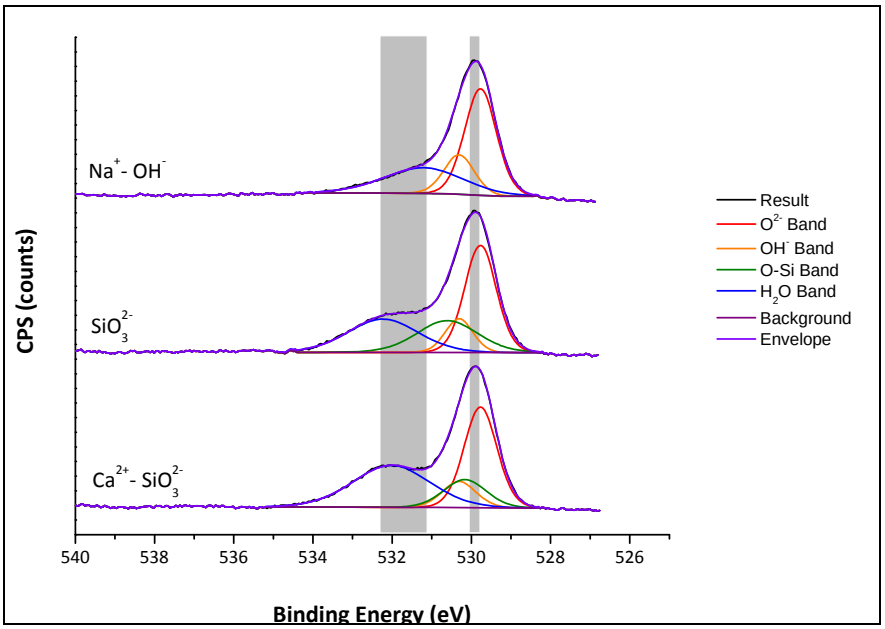

Figure 5. 20 XPS spectra of the O 1s band from the 3% at SIMFUEL electrodes after performing the corrosion potential experiments. Also the deconvolation of the band is shown.

Conclusions

A completely new electrode was built from a 3% at. SIMFUEL pellet and used to perform corrosion studies.

The results obtained showed the highest oxidation for the SIMFUEL electrode at high potential values in contact with the Na^{+}-OH^{-} electrolyte. The evolution of the current density obtained in the potentiostatic measurements suggests that the corrosion process was enhanced at pH 12. The resulting corrosion potential measured was -80 mV and the resulting surface composition showed that the amount of U (IV) obtained after performing experiment was 34%. At this potential values, the SIMFUEL surface is oxidized to UO_{2+x} (Shoesmith, 2007) as it was determined by XPS. Broczkowski et al. (2007), performed a similar study using the same ions in the electrolyte but at pH 9.5 and 60^{0}C. The E_{CORR} obtained was -220 mV; their XPS results showed that the U(IV) fraction on the electrode surface was approximately 50%. Therefore and despite the different temperatures used in both studies, it can be conclude that alkaline pH values enhance the corrosion process of the UO_2 with Ar purge and the same type of electrode.

The presence of silicate had no significant effect on the first oxidation step which is supposed to be the oxidation of UO_2 to a mixture of U (IV) and U (V). However, it decreased the oxidation step of $U^{V}_{2x}U^{IV}_{1-2x}O_{2+x}$, layer at potential values from -100 to 300 mV which has been associated to the U(IV) oxidation and U(VI) release to the electrolyte. At high oxidizing potential values, the CV measurements showed that the SIMFUEL corrosion is suppressed, probably by solid phase precipitation. It was also observed that the silicate concentration used did not cause any effect on the corrosion behavior of the system under the experimental conditions used in this work.

The addition of calcium to the silicate electrolyte under hyper-alkaline conditions caused a shift to approximately 0.06 V higher values in the CV curves. This can be caused by the stabilization of the reduced species and/or the blocking of O^{2-} incorporation into UO_2 by the Ca^{2+} adsorption on the surface. At the same oxidizing potential, the presence of both calcium and silicate in the dissolution partially avoided the SIMFUEL corrosion compared with the other electrolytes used in this study. The corrosion potential measured in presence of calcium and silicate was the lowest obtained in this work (-105 mV) and the resulting electrode surface was mainly U(IV).

These results suggest that the cement waters might reduce the corrosion of SNF.

Bibliography

Berner, U.R., 1992. Evolution of pore water chemistry during degradation of cement in a radioactive waste repository environment. Waste Manag. 12, 201–219. doi:10.1016/0956-053X(92)90049-O

Biesinger, M.C., 2015. X-ray Photoelectron Spectroscopy (XPS) Reference Pages [WWW Document]. XPS Descr. URL www.xpsfitting.com

Broczkowski, M.E., Noël, J.J., Shoesmith, D.W., 2007. The influence of dissolved hydrogen on the surface composition of doped uranium dioxide under aqueous corrosion conditions. J. Electroanal. Chem. 602, 8–16. doi:10.1016/j.jelechem.2006.11.021

Carbol, P., Cobos-Sabate, J., Glatz, J.-P., Ronchi, C.., Rondinella, V., Loida, A., Metz, V., Kienzler, B., Spahiu, K., Grambow, B., Quiñones, J., Martínez-Esparza, A., 2005. TR-05-09 on the dissolution of ^{233}U doped UO_2(s), high burn-up spent fuel and MOX fuel. Stockholm, Sweden.

Cerrato, J.M., Barrows, C.J., Blue, L.Y., Lezama-Pacheco, J.S., Bargar, J.R., Giammar, D.E., 2012. Effect of Ca^{2+} and Zn^{2+} on UO_2 Dissolution Rates. Environ. Sci. Technol. 46, 2731–2737. doi:10.1021/es203751t

Chung, D.-Y., Seo, H.-S., Lee, J.-W., Yang, H.-B., Lee, E.-H., Kim, K.-W., 2010. Oxidative leaching of uranium from SIMFUEL using Na_2CO_3–H_2O_2 solution. J. Radioanal. Nucl. Chem. 284, 123–129. doi:10.1007/s10967-009-0443-6

de Pablo, J., Casas, I., Giménez, J., Clarens, F., Duro, L., Bruno, J., 2004. The oxidative dissolution mechanism of uranium dioxide. The effect of pH and oxygen partial pressure, in: Materials Research Society Symposium Proceedings. pp. 83–88. doi:10.1557/PROC-807-83

Espriu-Gascon, A., Shoesmith, D.W., Giménez, J., Casas, I., de Pablo, J., 2017. Study of SIMFUEL corrosion under hyper-alkaline conditions in the presence of silicate and calcium. MRS Adv. 2, 543–548. doi:10.1557/adv.2016.619

Grenthe-Chairman, I., Fuger, J., Lemire, R.J., Canada, M., Muller, A.B., Wanner, H., Forest, I., 1992. Chemical Thermodynamics of Uranium, Digital. ed. Nuclear Energy Agency, Paris.

Harfouche, M., Wieland, E., Dähn, R., Fujita, T., Tits, J., Kunz, D., Tsukamoto, M., 2006. EXAFS study of U(VI) uptake by calcium silicate hydrates. J. Colloid Interface Sci. 303, 195–204. doi:10.1016/j.jcis.2006.07.019

Kienzler, B., Metz, V., Brendebach, B., Finck, N., Plaschke, M., Rabung, T., Rothe, J., Schild, D., 2010. Chemical status of U(VI) in cemented waste forms under saline conditions. Radiochim. Acta 98, 674–683. doi:10.1524/ract.2010.1768

Nicholson, R.S., Shain, I., 1964. Theory of Stationary Electrode Polarography. Single Scan and Cyclic Methods Applied to Reversible, Irreversible, and Kinetic Systems. Anal. Chem. 36, 706–723. doi:10.1021/ac60210a007

Ofori, D., Keech, P.G., Noël, J.J., Shoesmith, D.W., 2010. The influence of deposited films on the anodic dissolution of uranium dioxide. J. Nucl. Mater. 400, 84–93. doi:10.1016/j.jnucmat.2010.02.014

Puigdomènech, I., 2004. MEDUSA.

Razdan, M., Trummer, M., Zagidulin, D., Jonsson, M., Shoesmith, D.W., 2014. Electrochemical and Surface Characterization of Uranium Dioxide Containing Rare-Earth Oxide (Y_2O_3) and Metal (Pd) Particles. Electrochim. Acta 130, 29–39. doi:10.1016/j.electacta.2014.02.134

Rojo, I., Rovira, M., de Pablo, J., 2014. Selenate Diffusion Through Mortar and Concrete. Environ. Eng. Sci. 31, 469–473. doi:10.1089/ees.2014.0037

Santos, B.G., Nesbitt, H.W., Noël, J.J., Shoesmith, D.W., 2004. X-ray photoelectron spectroscopy study of anodically oxidized SIMFUEL surfaces. Electrochim. Acta 49, 1863–1873. doi:10.1016/j.electacta.2003.12.016

Santos, B.G., Noël, J.J., Shoesmith, D.W., 2006a. The effect of pH on the anodic dissolution of SIMFUEL (UO_2). J. Electroanal. Chem. 586, 1–11. doi:10.1016/j.jelechem.2005.09.021

Santos, B.G., Noël, J.J., Shoesmith, D.W., 2006b. The influence of silicate on the development of acidity in corrosion product deposits on SIMFUEL (UO_2). Corros. Sci. 48, 3852–3868. doi:10.1016/j.corsci.2006.02.012

Santos, B.G., Noël, J.J., Shoesmith, D.W., 2006c. The influence of calcium ions on the development of acidity in corrosion product deposits on SIMFUEL, UO_2. J. Nucl. Mater. 350, 320–331. doi:10.1016/j.jnucmat.2006.02.002

Shoesmith, D.W., 2008. The Role of Dissolved Hydrogen on the Corrosion / Dissolution of Spent Nuclear Fuel. NWMO TR-2008-19. Ontario, Canada.

Shoesmith, D.W., 2007. Used Fuel and Uranium Dioxide Dissolution Studies – A Review. MWMO TR-2007-03. Ontario, Canada.

Shoesmith, D.W., 2000. Fuel corrosion processes under waste disposal conditions. J. Nucl. Mater. 282, 1–31. doi:10.1016/S0022-3115(00)00392-5

Shoesmith, D.W., Sunder, S., Bailey, M.G., Wallace, G.J., 1989. The corrosion of nuclear fuel (UO2) in oxygenated solutions. Corros. Sci. 29, 1115–1128. doi:10.1016/0010-938X(89)90048-6

Sunder, S., Miller, N.H., Shoesmith, D.W., 2004. Corrosion of uranium dioxide in hydrogen peroxide solutions. Corros. Sci. 46, 1095–1111. doi:10.1016/j.corsci.2003.09.005

Torrero, M.E., Baraj, E., Pablo, J.D.E., Giménez, J., Casas, I., 1997. Kinetics of Corrosion and Dissolution of Uranium Dioxide as a Function of pH. Int. J. Chem. Kinet. 29, 261–267.

Wu, L., Shoesmith, D.W., 2014. An Electrochemical Study of H_2O_2 Oxidation and Decomposition on Simulated Nuclear Fuel (SIMFUEL). Electrochim. Acta 137, 83–90. doi:10.1016/j.electacta.2014.06.002

Chapter 6:
Cesium and Strontium retention onto uranophane and soddyite

Introduction

Regarding the processes involved in the SNF dissolution studied in this thesis, once the nuclear waste starts to dissolve, the uranium concentration might reach saturation and solid phases might precipitate. The solid phase composition depends on water composition (Finch and Ewing, 1992); for instance, soddyite ($(UO_2)_2(SiO_4)\cdot 2H_2O$) and uranophane ($Ca(UO_2)_2(SiO_3OH)_2\cdot 5H_2O$) are two of the uranyl secondary solid phases precipitating in waters containing silica and calcium (Gorman-Lewis et al., 2008; Kienzler et al., 2010). As it has been seen in previous chapters, these species are present in cement water.

The combined processes of RN release and solid phase precipitation in the SNF near field might reduce the RN release via ion re-immobilization in or on the solid phases precipitated.

Insights of ion retention by sorption mechanisms

The sorption process can be defined as the retention of a specific ion in the aqueous phase on the solid. The interaction mechanisms between the ion and the solid phase can be superficial, structural, associated with ion precipitation on the solid phase, polymerization or others (Stumm, 1992). However, most of the studies performed only refer to the process as sorption process due to the difficult differentiation among the mechanisms mentioned.

Sorption kinetic mechanisms

The study of the time dependence on the adsorption and desorption process is important to understand the mechanisms involved in the process and to determine its equilibrium. Thus, several kinetic models were designed based on the interaction mechanisms.

The transport and adsorption process of the ion on the adsorbent can be divided into 5 stages (Boyd et al., 1947):

1. The ion diffuses from the bulk of the solution to the near field of the adsorbent.
2. The ion diffuses into the adsorbent. This diffusion process could be a bi or three – dimensional process on the surface of the solid – phase.

3. The adsorption of the ion on the active sites. This process might involve a chemical reaction or substitution.
4. The desorbed ion must diffuse from its original position to the outer part of the adsorbent. This is the reverse mechanism of the second step.
5. The desorbed ion must diffuse into the bulk of the solution, away from the adsorbent. This is the reverse mechanism of the first step.

The amount of radionuclide adsorbed by the solid is determined using the Eq. (6.1). Where '$\{RN\}_{ads}$' refers to the amount of radionuclide adsorbed on the solid; '*V*' is the sample volume, which is 20 ml; '$[RN]_{ini}$' and '$[RN]_{final}$' are the initial and final concentrations of the radionuclide, respectively; '$g_{solid\ phase}$' is the weight of solid introduced in each sample and '*SA*' is the surface area of the solid phase.

$$\{RN\}_{ads} = \frac{V \cdot \left([RN]_{initial} - [RN]_{final}\right)}{g_{solid\ phase} \cdot SA} \tag{6.1}$$

Pseudo – first – order kinetic model

This model is based on the mathematical expression in Eq. (6.3), developed in previous studies (Boyd et al., 1947; Lagergren, 1898) and reported by Azizian (2004). The expressions based on reaction (6.2) and applied to the sorption of radionuclides are shown below.

$$A^+ + (B - S) \leftrightarrow (A - S) + B^+ \tag{6.2}$$

$$\frac{d\{RN\}}{dt} = k_1(\{RN\}_e - \{RN\}_t) \tag{6.3}$$

Where '$\{RN\}$' is the amount of radionuclide adsorbed on the solid phase, '$\{RN\}_t$' is the amount of radionuclide sorbed on the solid phase ($mol \cdot m^{-2}$) at a certain time, '$\{RN\}_e$' is the amount of radionuclide sorbed on the solid phase at equilibrium and 'k_1' is the rate constant. Boyd et al. (1947) extended the model based on the limiting step. In case that the kinetic process is limited by the diffusion through a thin liquid film (step 1) the resulting expression is shown in Eq. (6.3).

If the rate is controlled by the diffusion through the adsorbent (step 2), the resulting expression is function of the surface of the adsorbent, considered to be spherical (Eq. (6.4)).

$$\frac{\{RN\}_t}{\{RN\}_e} = 1 - \frac{6}{\pi^2}\sum_{n=1}^{\infty}\frac{1}{n^2} \cdot exp\left(-\frac{D^i \pi^2 n^2 t}{r^2}\right) \tag{6.4}$$

Where 'D^i' is the internal diffusion coefficient, 'r' is the radius of the solid particle.

In the case that the adsorption of the ion on the surface (stage 3) is the governing step, both reactions (adsorption and desorption) must be taken into account. Considering the mass balance, the resulting equation is as follows (Eq. (6.5)):

$$\{RN\}_e - \{RN\} = \{RN\}_e e^{-(k_{ads}[A^+]+k_{des}[B^+])t} \tag{6.5}$$

Where 'k_{ads}' and 'k_{des}' are the equilibrium constant for the adsorption and for the desorption processes respectively. '$[A^+]$' and '$[B^+]$' are the ion concentration in the bulk of the solution for the adsorbed and the desorbed species, respectively.

Pseudo – second – order kinetic model

This model is based on the reaction mechanism (6.6). The 'S^-' represents the polar sites on the surface where the adsorption is taking place. The rate law for the process described is expressed in Eq. (6.7).

$$2\,S^- + A^{2+} \leftrightarrow A - S_2 \tag{6.6}$$

$$\frac{d\{RN\}}{dt} = k(\{RN\}_e - \{RN\}_t)^2 \tag{6.7}$$

The integration of Eq. (6.7) defining the evolution of the amount of adsorbed ion as a function of time is described by the Eq. (6.8)(Ho, 2006) taking into account that at t = 0, there is no ion adsorbed on the solid – phase ($\{RN\}_{initial} = 0$).

$$\frac{t}{\{RN\}_t} = \frac{1}{k_s\{RN\}_e^2} + \frac{1}{\{RN\}_e}t \tag{6.8}$$

Where 't' is the time and 'k' is the kinetic constant of the whole process. This kinetic model is based on the chemisorption of the ion on the solid phase as the rate limiting step (stage 3), hence there is an exchange or sharing of electrons between the ion and the solid phase that involve valency forces.

Modeling of adsorption isotherm systems

The isotherm curves are widely used in sorption studies to characterize the governing retention mechanisms, release or mobility of a substance from the aqueous to the solid – phase (Foo and Hameed, 2010). Their adjustment to the different empirical mathematical models provides information about adsorption mechanisms, solid surface properties and affinity degree of the adsorbents.

Two parameters models

Langmuir isotherm

This isotherm model was developed by I. Langmuir and it was described in Langmuir (1916). It assumes that the adsorbed specie creates a one molecule thick layer on a finite number of sites (adsorption sites). These sites are all identical and equal among themselves which means that there is no lateral interaction between the adsorbed molecules. Essentially, the adsorption process is a homogeneous process with the same enthalpies and sorption activation energy on all the active sites (Foo and Hameed, 2010; Limousin et al., 2007). As a consequence, there is a maximum of adsorbed species on the solid – phase. This is described graphically as a plateau when the {RN} is plotted as a function of the ion concentration at equilibrium. The results are fitted by using Eq. (6.9).

$$\frac{1}{\{RN\}} = \frac{1}{\{RN\}_{max} \cdot [RN] \cdot K_L} + \frac{1}{\{RN\}_{max}} \tag{6.9}$$

Where '$\{RN\}_{max}$' is the maximum retention capacity of the solid – phase, 'K_L' is the Langmuir constant and '*[RN]*' is the ion concentration of the solution after performing the experiment.

Freundlich isotherm

The Freundlich model is based on a heterogeneous, non – ideal and reversible sorption process. In this case, the sorption is not restricted to only mono – layer. Actually, it takes into account the possibility of more than one sorption layer with heterogeneous distribution of adsorption enthalpies and affinities (Foo and Hameed, 2010; Limousin et al., 2007). Therefore, the amount of ion adsorbed is the sum of the ions adsorbed on all active sites. Those sites with higher binding energy will be the first being occupied. Then, more ions will be retained and the sorption layer will grow thicker until the adsorption energy decreases to zero.

The equation used to describe the system is Eq. (6.10):

$$\{RN\} = K_F \cdot [RN]^{\frac{1}{f}} \tag{6.10}$$

Where 'K_F' is the Freundlich constant and '*f*' is the Freundlich exponent that provides information about whether the process is favored or not. These are the parameters that must be determined in order to characterize the system by using the Freundlich isotherm.

Effect of the surface properties

As it was mentioned, some sorption processes are due to the interactions between the ion in the aqueous phase and the surface of the solid phase. Thus, the sorption can be influenced by certain properties of the surface.

Chemical Interactions with the hydroxyl group

Under aqueous conditions, a primary interest is the surface hydroxyl group that can form different types of bonds with the ions in the aqueous phase. These interactions are all short range because they are chemical interactions that require contact between adsorbent and adsorbate.

The acid – base reactions on the surface are shown in reaction (6.11) and reaction (6.12). The resulting deprotonated surface has a Lewis base behavior.

K_{a1}^{S} $$S - OH_2^+ \leftrightarrow S - OH + H^+ \quad (6.11)$$

K_{a2}^{S} $$S - OH \leftrightarrow S - O^- + H^+ \quad (6.12)$$

Hence, it is assumed that the adsorption process is a competitive complex formation that involves one or two surface hydroxyls as shown in reaction (6.13) and reaction (6.14).

${}^{*}K_1^{S}$ $$S - OH + M^{2+} \leftrightarrow S - OM^+ + H^+ \quad (6.13)$$

${}^{*}\beta_2^{S}$ $$2(S - OH) + M^{2+} \leftrightarrow M(S - O)_2 + 2H^+ \quad (6.14)$$

Another type of reaction is caused by the ligand exchange between the aqueous species and the hydroxyl group on the surface (see reaction (6.15)).

$$S - OH + M^{2+} + L \leftrightarrow S - OML^+ + H^+ \quad (6.15)$$

Another type of surface complex has the ligand between the surface and the metal and, in this case, a hydroxyl anion is released from the surface, as reaction (6.16) shows:

$$S - OH + M^{2+} + L \leftrightarrow S - L - M^{3+} + OH^- \quad (6.16)$$

As it can be observed in the chemical reactions above, some sorption process are pH-dependent due to the properties of the ion, its speciation and the surface charge of the solid – phase.

Surface charge

The surface charge of the solid – phase can be affected by ionizable functional groups in the solution, such as H^+ or OH^-. The total superficial charge value can be determined by using Eq. (6.17) (Sposito, 1984).

$$\sigma_T \equiv \sigma_0 + \sigma_H + \sigma_{IS} + \sigma_{OS} = F(z_+\Gamma_+ + z_-\Gamma_-) \quad (6.17)$$

Where 'σ_T' is the total superficial charge density, 'σ_0' is the structural and permanent charge density, 'σ_H' is the charge density caused by both H^+ groups and OH^- groups, 'σ_{IS}' is the charge from the formation of inner – sphere complexes and 'σ_{OS}' is the charge density caused by the outer – sphere complexes or species localized in the diffuse layer. 'F' is the Faraday constant (96485 C·mol^{-1}), 'z_+' and 'z_-' are the valences of the different species on the surface, including their charge sign, and 'Γ_+' and 'Γ_-' are the adsorption densities of the determining ionic species. Thus, the surface charge is function of the pH, the aqueous concentration (ionic strength) and the composition of the electrolyte (Parks and Bruyn, 1962; Sprycha, 1989, 1984), hence the sorption process can be electrostatically favored or impeded. Additionally, the adsorption of charged species has an effect on the solid surface charge and, in case of high ion concentration, the resulting surface charge can even be reversed (Stumm, 1992).

One of the most important parameters that allows to characterize the charge of the surface layer is the zero point of surface charge (pzc) where $\sigma_T = 0$. This state is reached at a determined value of activity of the ions in the solution. In aqueous systems, the charged layer is influenced by the presence of both OH^- and H^+ (σ_H). Hence, the pzc can be determined by the pH value at which the adsorption densities of protons and hydroxyl ions are equal in Eq. (6.17) (Parks and Bruyn, 1962). This exposure must be numerically equal for both charge signs. The pH value which shows $\Gamma_+ - \Gamma_- = 0$ is known as pH of the zero point of surface charge (pH_{pzc}). It can be determined by the difference between the total added acid or base and the equilibrium pH.

Depending on the value of the pH_{pzc}, it can be concluded how strongly the protons or the hydroxyl ions are bonded to the solid surface. Additionally, the equilibrium constant of the following surface reaction (K_{sa}) can be determined (Parks and Bruyn, 1962).

$$K_{sa} \qquad > S - OH_3^+ \leftrightarrow > S - OH^- + 2H^+ \quad (6.18)$$

Where '$>S - OH_3^+$' are the adsorption sites occupied with protons ions, '$>S$' are the surface sites unoccupied and the '$>S - OH^-$' are the adsorption sites occupied with hydroxyls ions. Therefore, taking

into account reaction (6.18), if each ion activity is approximated to their concentration, the equilibrium constant can be expressed as:

$$K_{sa} = \frac{[> S - OH^-] \cdot [H^+]^2}{[> S - OH_3^+]} \quad (6.19)$$

Since at equilibrium the adsorption site density of proton and hydroxyl ions is the same, the equilibrium constant can be approximated to (Parks and Bruyn, 1962):

$$K_{sa} = [H^+]^2 \quad (6.20)$$

The surface charge creates an electrostatic field where complexation reactions can take place. This allows to study the sorption equilibrium in a similar way to the solution steady state: by using acidity constants (see reactions (6.11) and (6.12) with K_{a1}^S and K_{a2}^S) or adsorption constants involving metal ions (see reactions (6.13) and (6.14) with ${}^*K_1^S$ and $*\beta_2^S$). Obtaining the values of the constants mentioned is experimentally possible; thus, an effort is made in order to determine their values (Rovira et al., 2008).

Two factors where suggested to be happening simultaneously when a decrease of the surface stability constants is observed with the increase of the surface coverage with charged species (Stumm, 1992):

- The fact that there is a surface potential due to the adsorption of charged species
- The increase of the activity of the adsorbed species caused by lateral interactions among them

Retention of RN by uranyl secondary phases

The interaction of different RN has been studied by using uranyl secondary phases that are likely to precipitate under relevant conditions for the DGR. The results obtained are presented as a function of the ion studied. A brief summary of the reported results of RN retention in contact with uranyl solid phases is shown in Table 6. 1.

Retention of Actinides and Lanthanides by secondary phases

Burns et al. (1997) studied the possible incorporation of some actinides into the structure of uranyl secondary phases. Bond lengths and angles were discussed and compared with other structures containing actinides (Np, Pu, Th, Am and/or Cm) in order to suggest possible substitution and incorporation mechanisms. This study led to the following conclusions:

- The actinides with valence state 6+ (Pu^{6+}) and 5+ (Np^{5+} and Pu^{5+}) are likely to be incorporated into most of the uranyl structures.

- The actinides with valence state 4+ (Th^{4+}, Np^{4+} and Pu^{4+}) will easily be incorporated and substitute U(VI) in the schoepite, ianthinite, becquerelite, compreignacite, α-uranophane and botlwoodite.
- The actinides with valence state 3+ (Pu^{3+}, Am^{3+} and Cm^{3+}) might be incorporated and substitute U(VI) in α-uranophane and botlwoodite. On the other hand, they are unlikely to be incorporated in schoepite.

Kim et al. (2006, 2002) published a study regarding the incorporation of Nd^{3+} and Ce^{4+} as a analogues for Am^{3+} and Pu^{4+}, due to their atomic similarities (ionic radii and electronic configuration), into dehydrated schoepite, ianthinite and becquerelite.

Kim et al. observed that Nd(III) could not replace U(VI) in the dehydrated shoepite structure; this is in good agreement with the observation of Burns et al. (1997). In fact, Nd precipitated forming a segregated phase. In the case of ianthinite and bequerelite, the incorporation of Nd(III) requires a charge balancing substitution due to the replacement of U(IV) (ianthinite) or the replacement of Ca^{2+} (bequerelite) by Nd(III). This can be done by the substitution of O^{2-} by OH^{-} in the crystal structure.

The retention of Ce(IV) was observed for all the solids studied by Kim et al. Ianthinite showed U(IV) direct substitution due to the same valence charge of both ions and similar ionic radii. In the case of the other uranyl solid phases, Ce(IV) was observed to be retained by replacing the UO_2^{2+} ion of the polyhedral sheet in the crystal structure. In this case, the replacement might also involve a local charge compensating substitution.

Neptunium is one of the actinides of interest due to the long – lived isotope ^{237}Np and the mobility of Np (V) in groundwater. As a consequence, the retention of Np by its incorporation into uranyl secondary phases has been widely studied (Alessi et al., 2013; Burns et al., 2004; Douglas et al., 2005; Friese et al., 2004; Murphy and Grambow, 2008). The results showed an important effect of the pH value on the Np incorporation into solid phase. At acidic pH values, the Np remained in the leachant solution while at alkaline pH, Np was retained by the uranyl solid - phase. Friese et al. (2004) observed different solid structures when Np was incorporated into the uranyl phase and the resulting solid phase had less crystallinity than the pure uranyl phases. The authors suggested the disruption of the crystal growth of the mineral due to the presence of Np as a hypothesis to explain their results.

Retention of Selenium and Technetium

Se and Tc have long lived isotopes (^{79}Se with half-life of $1.1 \cdot 10^6$ years and ^{99}Tc with half life time of $2.1 \cdot 10^5$ years) so their retention in contact with uranyl secondary phases has been of interest.

Selenite and selenate are the two main forms of selenium under oxidizing conditions. The study performed by Chen et al. (1999) was focused on these species. Since they have negative charge, they are likely to substitute negative functional groups such as SiO_3OH^- of uranophane and boltwoodite or CO_3^{2-} of rutherfodine. However, the substitution of SiO_4 group of soddyite and PO_4 group of phosphuranylite was considered improbable since it might disturb the structure of the solid phases.

Martínez-Torrents et al. (2015) studied the sorption process of Se (IV) and Se (VI) onto studtite. The results showed higher sorption of Se at acidic pH values which is congruent with the selenium speciation and the solid surface charge at low pH values. The authors suggested that the sorption process occurs by a two-step mechanism through macropore and micropore diffusion. The coverage of the solid phase by Se consists of a monolayer and the maximum capacities are $3.6 \cdot 10^{-6}$ mol·m^{-2} for Se(IV) and $2.3 \cdot 10^{-6}$ mol·m^{-2}.

Under the conditions of the oxidative alteration of the SNF, Tc could be found as TcO_4^-, which is highly soluble. As for the case of selenium, TcO_4^- could be incorporated in solid phases by replacing the functional groups with similar characteristics like SiO_4^- of uranyl silicates solid phases, but Chen et al. (2000) suggested that this might cause the destabilization of the uranyl phase; therefore, large TcO_4^- substitution might be unlikely.

Retention of Cesium and Strontium

As it was observed in a previous chapter, Cs is one of the most mobile RN inside the SNF and it is expected to be partially segregated in the gap and GB. As it was mentioned before, ^{135}Cs (half-life: $3 \cdot 10^6$ years) and ^{137}Cs (half-life: 30 years) are long lived isotopes and therefore, a special effort has been done to determine possible retention of this specific element (Douglas et al., 2002; Gimenez et al., 2009; Rovira et al., 2004).

Table 6. 1 Retention of RN on different uranyl secondary phases

Reference	RN	Solid Phase	Retention
(Chen et al., 1999)	Se	Schoepite $(UO_2)_8O_2(OH)_{12} \cdot 12H_2O$	Unlikely
		Soddyite $[(UO_2)_2SiO_4] \cdot 2H_2O$	Unlikely
		Uranophane $Ca(UO_2)_2(SiO_3OH)_2 \cdot 5H_2O$	Likely

		Botlwoodite [Na,K][$(UO_2)(HSiO_4)$]·0.5H_2O	Likely
(Burns, 1999)	Cs	Botlwoodite [Na,K][$(UO_2)(HSiO_4)$]·0.5H_2O	Yes
(Chen et al., 2000)	Tc	Uranyl phases	Unlikely
(Burns and Li, 2002)	Sr	Bequerelite Ca[$(UO_2)_6O_4(OH)_8$]·8H_2O	Yes
(Douglas et al., 2002)	Cs	Uranophane Ca$(UO_2)_2(SiO_3OH)_2$·5H_2O	Yes
	Sr	Uranophane Ca$(UO_2)_2(SiO_3OH)_2$·5H_2O	Yes
(Hoskin and Burns, 2003)	Cs	Compreignacite $K_2[(UO_2)_6O_4(OH)_6]$·7H_2O	Yes
(Kim et al., 2002)	Ce	Uranyl hydroxide $UO_2(OH)_2$	Yes
	Nd	Uranyl hydroxide $UO_2(OH)_2$	Yes
(Burns et al., 2004)	Np	Uranophane Ca$(UO_2)_2(SiO_3OH)_2$·5H_2O	Yes
		Meta-schoepite	No
(Friese et al., 2004)	Np	Meta-schoepite	No
		Uranophane Ca$(UO_2)_2(SiO_3OH)_2$·5H_2O	Yes
		Na-Botlwoodite Na[$(UO_2)(HSiO_4)$]·0.5H_2O	Yes
(Douglas et al., 2005)	Np	Meta-schoepite	No
		Studtite UO_2O_2·4H_2O	Yes
(McNamara et al., 2005)	Tc	Metastudtite UO_2O_2·2H_2O	Likely
(Kim et al., 2006)	Ce	ianthinite [$U^{IV}(UO_2)_5O_7$]·10H_2O	Yes
		becquerelite Ca$(UO_2)_6O_4(OH)_6$·8H_2O	Yes
	Nd	ianthinite [$U^{IV}(UO_2)_5O_7$]·10H_2O	Yes
		becquerelite Ca$(UO_2)_6O_4(OH)_6$·8H_2O	Yes
(Giménez et al., 2010)	Cs	Studtite UO_2O_2·4H_2O	Yes
(Sureda et al., 2010)	Sr	Studtite UO_2O_2·4H_2O	Yes
(Alessi et al., 2013)	Np	Soddyite [$(UO_2)_2SiO_4$]·2H_2O	Yes
		Botlwoodite [Na,K][$(UO_2)(HSiO_4)$]·0.5H_2O	No
(Baker, 2014)	Sr	Schoepite $(UO_2)_8O_2(OH)_{12}$·12H_2O	Likely
(Martínez-Torrents et al., 2015)	Se (IV) and (VI)	Studtite UO_2O_2·4H_2O	Yes

Burns et al (1999) studied the possible incorporation of Cs into boltwoodite due to the similarities between K^+ and Na^+ with Cs^+. The Cs incorporation was suggested to proceed by ion exchange due to the high stability of the structures of the other functional groups (UO_2^{2+} and $HSiO_4^-$) and it was suggested similar retention mechanisms for other uranyl silicate phases. In this sense, Douglas et al (2002) studied the incorporation of Cs into uranophane and Hoskin and Burns (2003) into compreignacite. The results showed that both solid phases were able to incorporate Cs in their structure: in the case of uranophane, Cs^+ replaced Ca^{2+}; in the case of compreignacite, Cs^+ replaced K^+ in the interlayer positions.

The influence of studtite on cesium concentration was studied by Giménez et al (2010). The results showed that cesium concentration decreased rapidly in contact with studtite at pH 5. The authors also observed that the sorption process might proceed via multilayer sorption on the uranyl solid phase. This result agrees with previous sorption studies of Cs onto other mineral phases that did not contain

uranium in their structure (Rovira et al., 2003). The sorption process was observed to be enhanced at high pH values, which means that cesium is likely to be retained on studtite in contact with ground water.

Sr might also be segregated to the GB as it was observed in this manuscript. Even though ^{90}Sr isotope is short-lived (half-life: 28.8 years), it is of interest due to the substitution of Ca^{2+} by Sr^{2+} in some structures such as human bone structure. As a consequence, the retention of Sr under relevant conditions for the DGR has been also studied (Douglas et al., 2002; Gimenez et al., 2009; Sureda et al., 2010).

Strontium incorporation has been studied in contact with uranyl phases containing Ca^{2+} in their structure due to the high possibility of substitution between these ions. Burns and Li (2002) observed the calcium substitution in bequerelite in the interlayer of the solid structure. In the case of uranophane, Douglas et al. (2002) observed a full substitution of Ca and the resulting solid phase containing Sr presented XRD spectra similar to results than uranophane. In this work, the authors did not suggest a specific location for the Sr atoms to be located in the uranyl – silicate structure.

The sorption process of Sr in contact with studtite was studied by Sureda et al. (2010). They observed a relatively fast sorption process. It proceeds via monolayer coverage process; there was a maximum capacity of Sr sorbed on the surface of $2.5 \cdot 10^{-5}$ mol·m^{-2} at 0.01 mol·dm^{-3} of ionic strength, and of $7.28 \cdot 10^{-6}$ mol·m^{-2} at 0.1 mol·dm^{-3}. As in the previous case, the sorption process was enhanced at high pH values, which indicates that under repository conditions strontium is likely to be retained by studtite.

Specific Objectives

This chapter is focused on the sorption process as a possible way to retain cesium and strontium onto the surface of two uranyl silicates phases – soddyite and uranophane – that may precipitate when the SNF gets in contact with cement waters.

In order to achieve this goal, first the two solid phases are synthesized in the laboratory and characterized by XRD and Raman spectroscopy. In addition, the surface area of the solid phases and their point of zero charge are determined by using the immersion methodology.

In order to perform the study of the sorption process for each one of the systems, the kinetics, the isotherms and the pH effect are studied. To elucidate the mechanism of sorption for each system, the experimental results are explained considering different theoretical models. Additionally, the effect of the ionic strength is studied.

Experimental Methodology

Reagents

The solutions were prepared by using $CsClO_4$ and $Sr(NO_3)_2$ from Acros Organics with 99% of purity. The ionic medium was prepared by using $NaClO_4 \cdot H_2O$ from Merck. The pH was measured by using a Crison pH – meter and adjusted by using $HClO_4$ and NaOH from Merck in order to determine the influence of the pH on the sorption process.

Kinetic Experiments

20 ml of a solution containing 10^{-5} mol·dm^{-3} of the cation, either Cs^+ or Sr^{2+}, was put in contact with 50 mg of the solid, either uranophane or soddyite.

To study the kinetics of the system, several aliquots of the leachant solution were put in contact with the solid phase, each one with a different contact time: 5, 10, 30, 60, 300, 1440 and 2880 minutes. Afterwards, the resulting solution was filtered through 0.20 μm filters and the concentration of the cation was analyzed by ICP-MS.

The results of this study allowed to establish the time necessary to achieve the steady state of the sorption system in view of the next experiments that were performed to characterize the system.

Sorption isotherms

20 cm^3 of radionuclide solution were put in contact with 50 mg of solid phase. To perform this study, each dissolution had different initial concentration of the cation from 10^{-7} to $5 \cdot 10^{-3}$ mol·dm^{-3}. The contact time was set to ensure the equilibrium of the sorption process. Afterwards, the solution was filtered through a 0.20 μm filter and the concentration of each radionuclide in the aqueous phase was analyzed by ICP-MS.

The results obtained from this study provided experimental information on the sorption mechanism; they were combined with mathematical models in order to correlate the sorption isotherms to the sorption mechanism as recently reported by Limousin et al. (2007). Among them, Langmuir isothermal model and Freundlich isothermal model are the most adequate to model the sorption of metals and semimetals.

Effect of the pH

The influence of the pH on the sorption process was determined by varying the initial pH of the solution in contact with 50 mg of solid phase. The initial cation concentration and the contact time were set at 10^{-5} mol·dm^{-3} and 24 hours, respectively. Afterwards, the solution was filtered using a 0.20 µm filter and the liquid phase was separated from the solid phase. Finally, the final pH was measured again and the solution concentration was determined by ICP-MS.

Point of zero charge, pH_{pzc}

Each solid phase was characterized and, in particular, its point of zero charge (pH_{pzc}) was determined. The immersion method used to obtain the pH_{pzc} is described in previous reports and studies (Bourikas et al., 2003; Fiol and Villaescusa, 2008; Giménez et al., 2014). Several samples with 50 mg of solid phase were put in contact with a solution containing 0.1 mol·dm^{-3} of $NaClO_4$ at different initial pH for 24 hours. The pH values were adjusted by using $HClO_4$ 0.1 mol·dm^{-3} or NaOH 0.1 mol·dm^{-3} and the pH was measured.

Afterwards, the solution was filtered through a 0.2 µm filter and the final pH of the solution was measured. The pH variation as a function of the initial pH is determined which usually leads to a graph with a 'V' shape. Each side of the graph can be fitted by a linear tendency line, and the crossing of the lines gives the pH that suffered no change during the process, which is the point of zero charge.

Synthesis and Characterization of Secondary Phases

Both solid phases were prepared in the laboratory following the methodology described elsewhere (Nguyen et al., 1992; Pérez et al., 2000, 1997; Sureda, 2011; Sureda et al., 2011). The solids obtained were characterized by X-ray diffraction (XRD) and Raman spectroscopy.

Synthesis of Solid Phases

Soddyite

150 ml of a solution containing 0.045 mol·dm^{-3} of $UO_2(NO_3)_2{\cdot}6H_2O$ and 50 ml of another solution containing 0.025 mol·dm^{-3} of $Na_2SiO_3{\cdot}5H_2O$ were mixed and heated at 80 ^{0}C for 24 hours. The solid obtained was filtered using a 0.20 μm filter, washed with hot ultra-pure MILLI-Q water and stored for 24 hours in a vacuum drier. Later, it was introduced into a Parr-bomb with MILLI-Q water and heated up to 120 ^{0}C for two weeks, in order to increase its crystallinity. Finally, the solid was again filtered using the same methodology explained before, washed and stored in the vacuum drier.

Uranophane

Three different solutions were prepared: 44 ml of one dissolution containing 0.08 mol·dm^{-3} of $UO_2(NO_3)_2{\cdot}6H_2O$; 35 ml of another solution containing 0.05 mol·dm^{-3} of $(CH_3COO)_2Ca{\cdot}XH_2O$ and 42.5 ml of a third solution containing 0.085 mol·dm^{-3} of $Na_2SiO_3{\cdot}5H_2O$ were mixed and heated up to 80 ^{0}C for 24 hours. The solid obtained was filtered by using a 0.20 μm filter, washed with hot MILLI-Q water and stored in the vacuum drier for 24 hours. Later, the solid was put into a Parr-bomb with MILLI-Q water and heated up to 120^{0}C for 4 weeks, in order to increase it crystallinity. Afterwards, the solid was filtered and washed again.

Solid Phase Characterization

The solids synthesized were grinded and sieved to obtain a particle diameter between 75 and 50 μm and were characterized by XRD and Raman.

The XRD spectra were obtained in "*Centros Científicos y Tecnológicos*" (CCiT) from Universitat de Barcelona (UB) by using a PANalytical X'Pert PRO MPS θ/θ powder diffractometer that works with 240 mm radius and a copper anode. The device was set in a configuration of convergent beam with a focalizing mirror and transmission geometry. The sample was placed between two polyester films with 3.6 μm of thickness that have no XRD signal, hence they do not interfere in the XRD analysis. The

resulting patterns were obtained measuring from 2 to 88 º2θ with a step size of 0.013 º2θ and 200 seconds per stem to reduce the noise.

The samples were also analyzed by means of Raman Spectroscopy. A 735 nm laser wavelength was used to obtain all the Raman spectra showed in this chapter. The spectra were recorded by using an i-Raman from MicroBeam with 5000 ms of integration time, 10 ms time to obtain the average signal and the power of the laser was set at the 45 mW of the laser power. Since the samples were not stirred during the analysis and the measurement is punctual, several spectra were obtained from different points of the sample in order to confirm the homogeneity of the sample.

Soddyite

X-Ray Diffraction

The solid phase was characterized by XRD and the spectrum is shown in Figure 6. 1 with the crystalline parameters determined by the pattern identified.

The sample was successfully identified as Soddyite R060361 from the RRUFF public Database (Lafuente B., Downs R. T., Yang H., 2015). The solid phase showed an orthorhombic crystal structure with preferential crystal orientation.

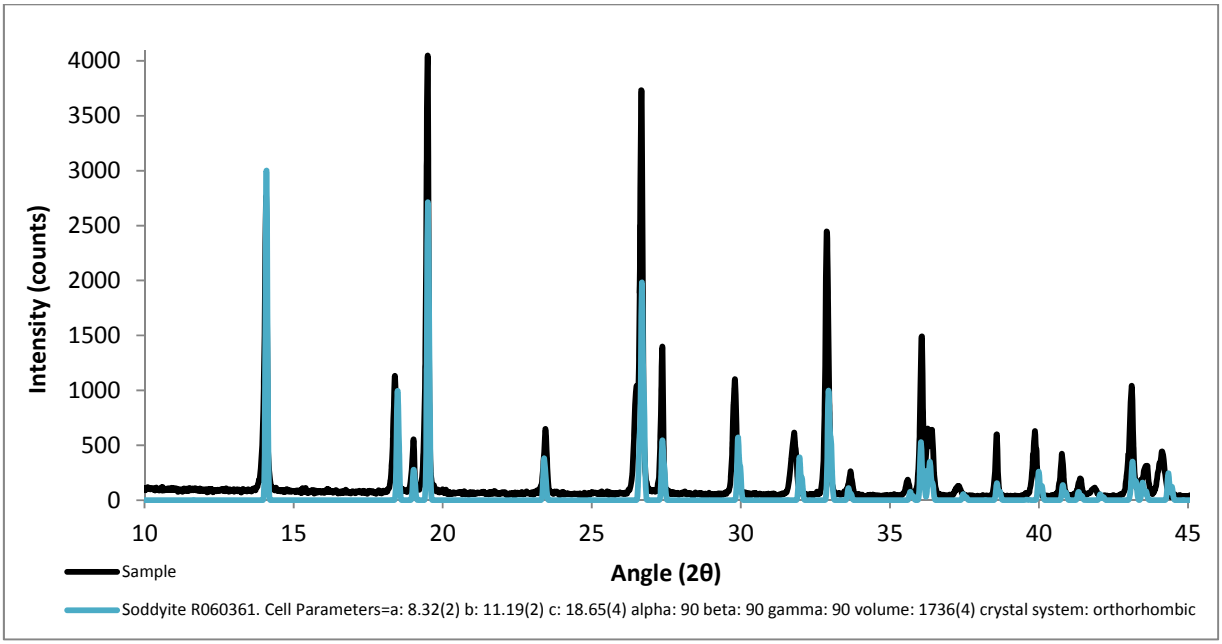

Figure 6. 1 XRD spectrum and pattern for Soddyite from RRUFF database (Lafuente B., Downs R. T., Yang H., 2015)**.**

Raman

The Raman spectrum of the sample is shown in Figure 6. 2 along with the matching Raman pattern. The spectrum matches the Raman spectrum from Soddyite R060361 in RRUFF database. Taking into account the chemical groups of the solid phase and the previous works from Frost et al. (2006) and Bonales et al (2015), the spectrum obtained matched the reported peak positions of the functional groups of UO_2^{2+} and SiO_4^{4-} corresponding to Soddyite

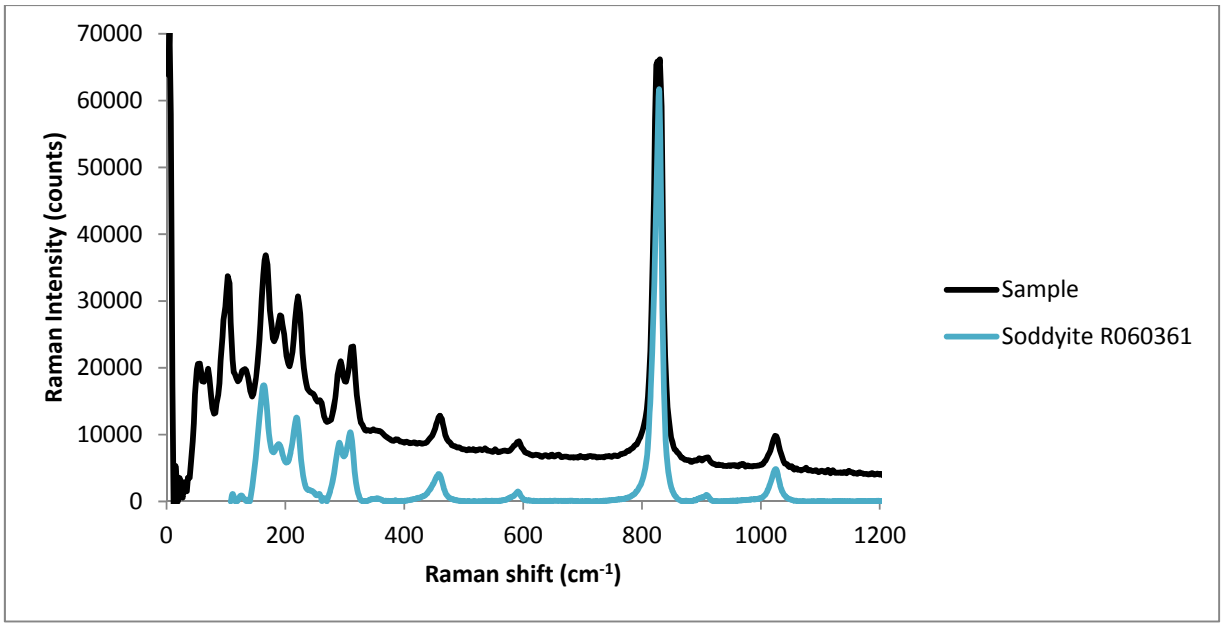

Figure 6. 2 Raman spectrum obtained for soddyite by using a 735 nm laser. Also, the pattern corresponding to soddyite R06036 from RRUFF Data base is shown.

Table 6. 2 Results of the Raman spectrum of soddyite as well as the reported peak positions for each chemical group

Group	Frequency in this work (cm^{-1})	(Bonales et al., 2015) (cm^{-1})	(Ray L. Frost et al., 2006) (cm^{-1})
UO_2^{2+}	193	195	190
	221	225	229
	293	293	290
	314	312	310
	826	832	828
SiO_4^{4-}	460	463	459
	593	---	591
	1023	---	1025

Surface Properties

The variation of the pH as a function of initial pH is shown in Figure 6. 3, where two regions can be observed. The first one goes from initial pH 5 to 6.48. In this region, the final pH was higher than the initial pH so the solid surface adsorbed the protons. The second region goes from initial pH 6.48 to 8.40. In this region, the final pH was lower than the initial pH which means that the solid surface had adsorbed the hydroxyl anions.

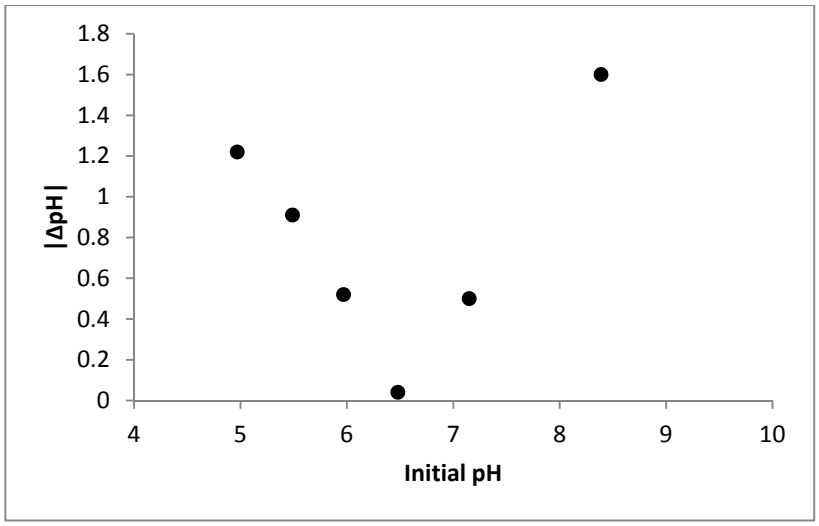

Figure 6. 3 Variation of the pH as a function of the initial pH in contact with 0.05 grams of soddyite

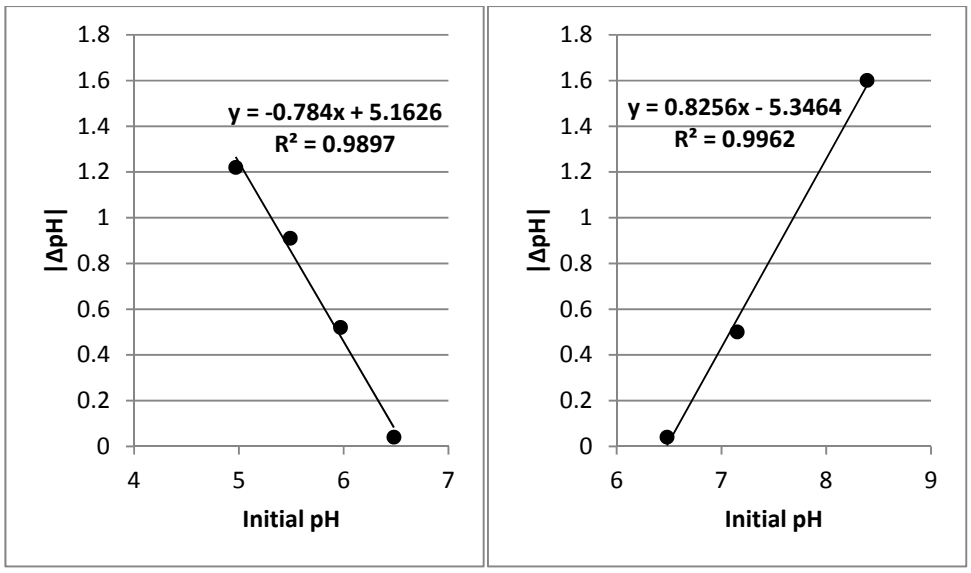

Figure 6. 4 Variation of the pH as a function of the initial pH with its line fitting for each region identified

In order to determine the pH_{pzc} of soddyite, Figure 6. 3 has been separated into two graphs and each region has been fitted by using its linear trend in Figure 6. 4. The resulting value of pH_{pzc} was 6.53 ± 0.05.

By using Eq. (6.20), the K_{sa} of soddyite is $8.7 \cdot 10^{-14}$. The pH_{pzc} obtained is close to neutral conditions; it can be concluded that the bond strength for hydroxyl ions is slightly stronger than for proton ions in the solution.

As a consequence, the sorption process of anions onto soddyite is expected to be enhanced at pH lower than 6.5 when the surface charge will be determined by the protons. At the same time, the sorption process of cations is expected to be favored at pH values higher than 6.5 when the surface charge will be due to the hydroxyl ions in the solution.

In addition, the surface area was determined by using the Brunauer – Emmett – Teller (BET) technique for the particle size between 0.074 and 0.050 mm and the result obtained was 7.89 ± 0.09 $m^2 \cdot g^{-1}$.

Uranophane

X-ray Diffraction

The XRD results of the synthesized solid and its characterization are shown in Figure 6. 5. The XRD pattern obtained matched uranophane patterns from RUFF public Database. The solid phase obtained was α-uranophane with a monoclinic crystal system.

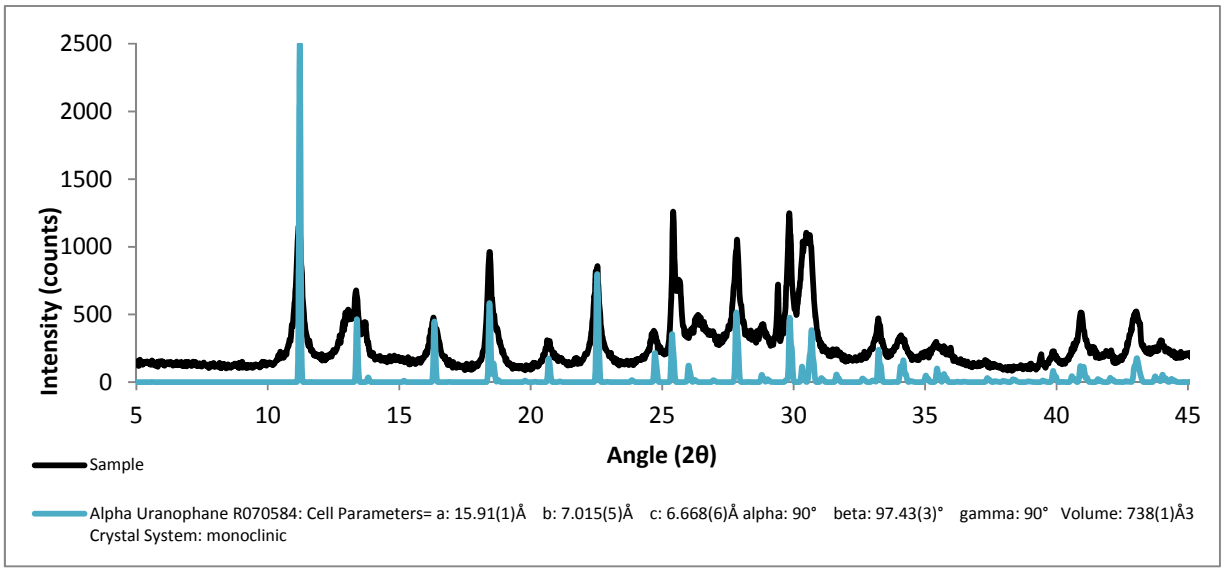

Figure 6. 5 XRD spectrum obtained for the sample that has been determined to be alpha-uranophane from the RRUFF Database (Lafuente B., Downs R. T., Yang H., 2015).

Raman

The Raman spectrum obtained matched the uranophane Raman patterns provided by RRUFF Raman database. Not only patterns are in good agreement with the spectrum, but also the main peak positions observed in Figure 6. 6 are in good agreement with the ones reported in the literature, as it is shown in Table 6. 3.

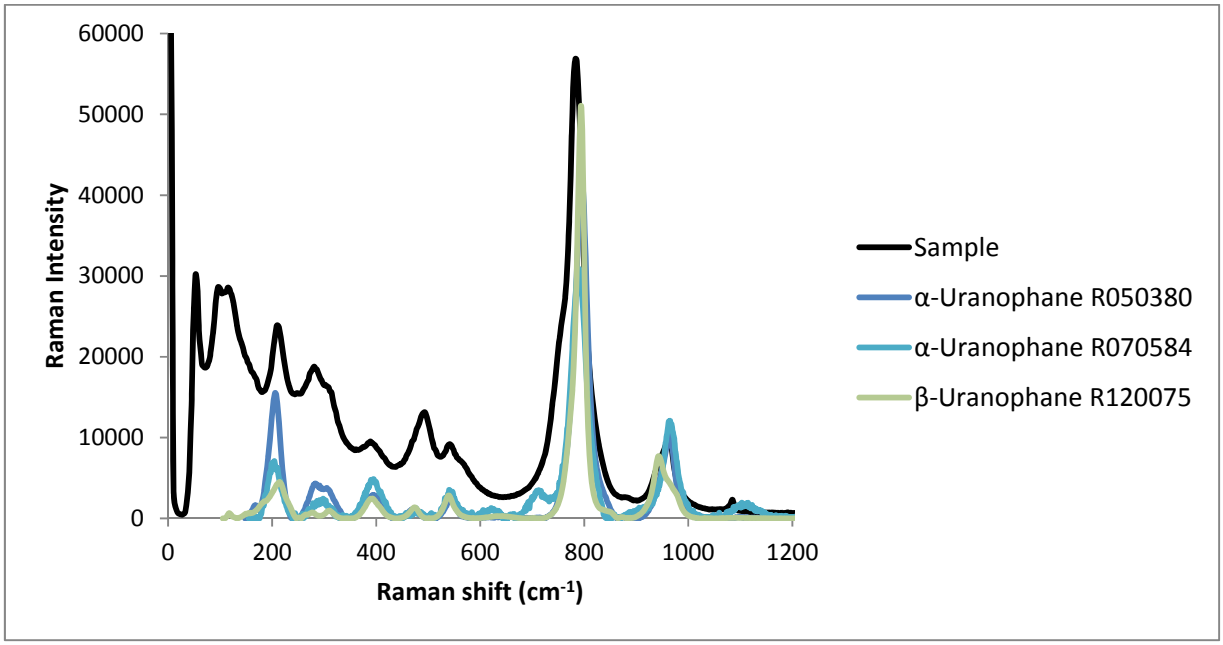

Figure 6. 6 Raman spectrum obtained for the sample determined to be a mixture of alpha and beta - uranophane from the RRUFF database

Table 6. 3 List of the main frequency peaks obtained in the Raman spectrum together with the previously reported peaks for uranophane

Group	Frequency in this work (cm^{-1})	(Bonales et al., 2015) (cm^{-1})	(Ray L. Frost et al., 2006) (cm^{-1})
UO_2^{2+}	212	209	213.7
	281 ; 315	300	306.5
	783	798	796.9
	962	967	963.9
SiO_4^{4-}	389	403	398.9
	542	547	544.6

Surface properties

The same methodology previously explained for the determination of the point of zero charge of soddyite was used to determine the pH_{pzc} of uranophane. The initial pH range used was from 5.88 to 9.93 to avoid the dissolution of the solid phase at lower pHs.

Figure 6. 7 was divided into two different graphs in Figure 6. 8, where the pH_{pzc} obtained was 7.37 ± 0.2. This result is close to the neutral pH value, and means that protons bond to the solid surface is slightly stronger than the hydroxyl surface bond. The value of the equilibrium constants can be determined by using the equation (6.20) and the result obtained was $2.3 \cdot 10^{-15}$.

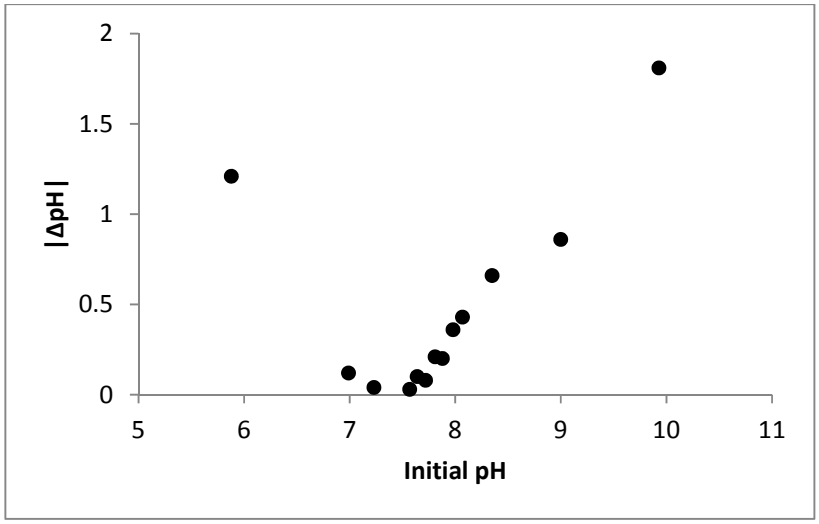

Figure 6. 7 Variation of the pH as a function of the initial pH after the addition of 0.05 grams of uranophane

The surface area of the same powder has been determined by BET analysis and the value obtained was 22.69 ± 0.06 $m^2 \cdot g^{-1}$ for a particle size between 0.074 and 0.050 mm of diameter.

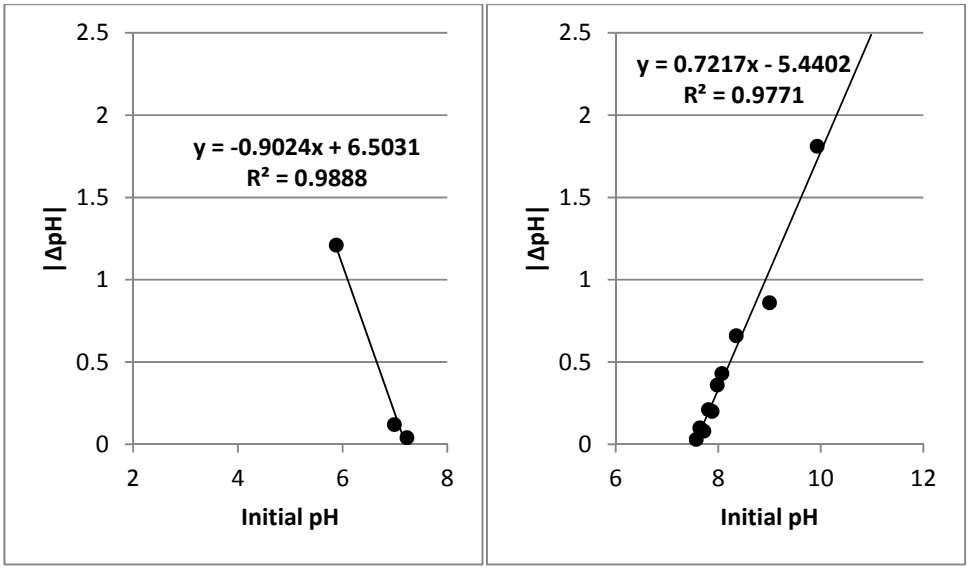

Figure 6. 8 Variation of the pH as a function of the initial pH and the linear fitting for each region identified previously

Results and Discussion

Cs Sorption onto Soddyite

Kinetic Study

The results of the kinetic study of cesium sorption process onto soddyite are shown in Figure 6. 9. The amount of cesium adsorbed on the solid surface was determined by using Eq. (6.1) applied to Cs concentration and the amount of solid phase introduced

The results show that the sorption process reached a steady state after 12 hours. A fast adsorption occurred during the first moments, followed by a desorption process. This is likely governed by the equilibrium between the solution and the solid phase. As a consequence, the experimental time to perform the sorption experiments for the cesium-soddyite system was set to 24 hours in order to ensure reaching the equilibrium of the system.

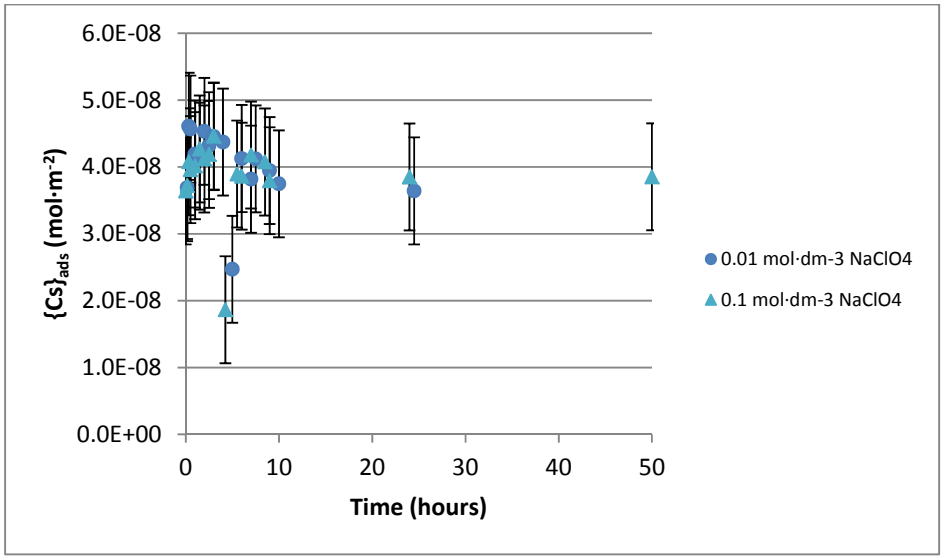

Figure 6. 9 Experimental results of the cesium sorption process onto soddyite in 0.01 mol·dm^{-3} and 0.1 mol·dm^{-3} of $NaClO_4$ and with initial cesium concentration of 10^{-5} mol·dm^{-3}

As can be seen in Figure 6. 9, the ionic medium showed no significant effect under the experimental conditions used in this study, since the data points both series overlapped.

Effect of Cesium Concentration. Isotherm

The following experiments were performed in order to study the effect of cesium concentration on the sorption process. The results can be observed in Figure 6. 10 together with the modeling results. It can

be observed that there is a maximum sorption capacity of the solid phase. The Langmuir model was used and fitted to the experimental data by using Eq. (6.9).

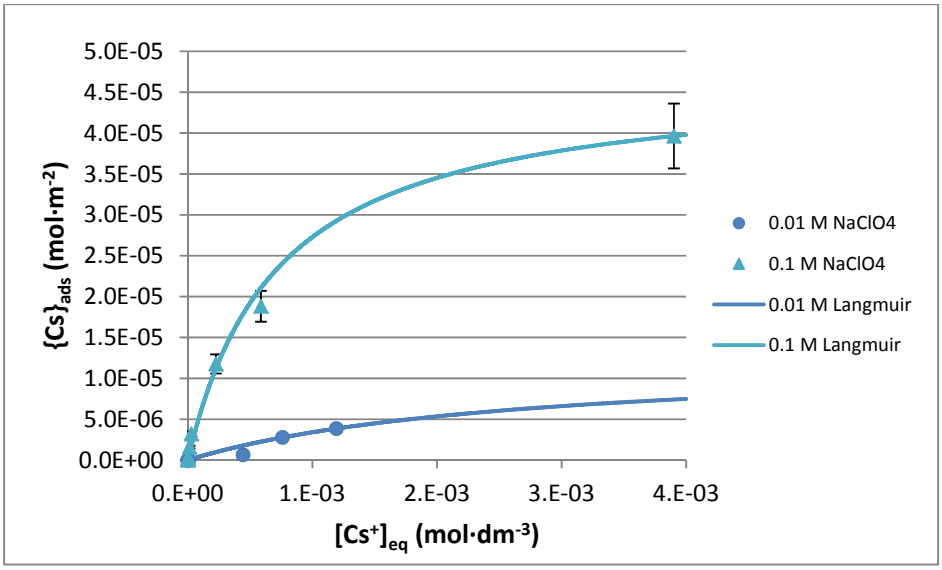

Figure 6. 10 Amount of cesium adsorbed on soddyite surface as a function of the cesium concentration in the dissolution

The model constants that fitted with the experimental data are shown in Table 6. 4. The model was fitted by using the Matlab® software and the least squares routine.

Table 6. 4 Values of the main Langmuir parameters obtained by fitting the Langmuir model with the experimental results obtained for the system Cs-soddyite

Parameter	Experimental series	
	0.1 mol·dm^{-3} $NaClO_4$	0.01 mol·dm^{-3} $NaClO_4$
K_L	1385	375
$\{Cs\}_{max}$	$4.70 \cdot 10^{-5}$	$1.25 \cdot 10^{-5}$
R^2	0.9946	0.9877

Considering the results in Table 6. 4, and also the experimental results in Figure 6. 10, the sorption process was favored at high ionic strengths as the maximum cesium adsorbed was obtained when the perchlorate concentration was higher.

A similar behavior was observed by Giménez et al. (2010) who studied the sorption of cesium onto studtite. Their results also showed higher cesium sorption when the ionic strength was higher. The authors suggested that these results might be caused by electrostatic factors governing the sorption process. However, the isotherms used to fit the experimental data in their study were from the Freundlich model (see Eq. (6.10)), which is in disagreement with the results obtained in Figure 6. 10 where the best fitting was obtained with Langmuir isotherms.

Effect of the pH on the Sorption Process

Due to the change of the surface charge with the pH, the retention capacity of the solid phase might change as well. Therefore it is necessary to study the effect of the pH on the sorption process in the Cs-soddyite system. Regarding Figure 6. 11, where the experimental sorption results are shown as a function of the pH in the dissolution, it can be seen that there was no sorption at pH lower than 5. This fact might be caused by the surface charge which was likely positive due to the adsorption of H^+ ions on all the possible adsorption sites. The presence of protons on the surface could also avoid the Cs^+ adsorption due to electrostatic repulsion. This fact can be observed at pH values below the pH_{pzc} (6.53 in the case of soddyite).

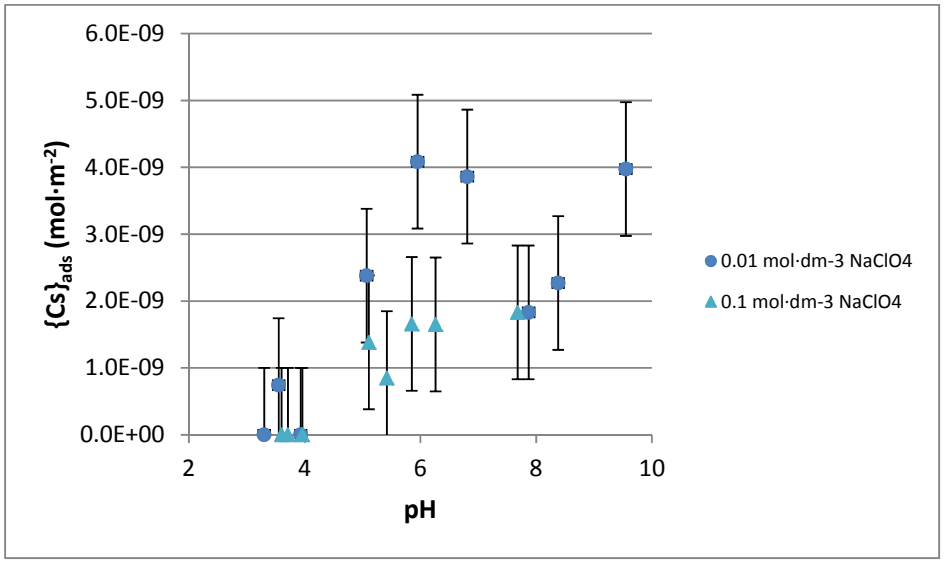

Figure 6. 11 Amount of cesium adsorbed on soddyite surface as a function of the pH at equilibrium

Once the pH increased to higher values than the pH_{pzc} of soddyite, the evolution of the amount of Cs^+ sorbed depended on the medium. Under high ionic strength conditions, the Cs sorbed was constant at pH values between 6 and 8.

On the other hand, at low ionic conditions, the amount of Cs retained decreased from pH 6 to pH 8. This fact might be caused by the change of the surface charge before and after the pH_{pzc} at 6.53 which might avoid the sorption of charged species on soddyite. When the pH increased from 8 to 10, the amount of cesium sorbed increased probably due to the negative charge of the surface of the solid phase that might enhance the sorption of cations.

Cs Sorption onto Uranophane

Kinetic Study of Cs-uranophane sorption process

As observed before in the Cs-soddyite system, there was a first stage where the sorption process was highly favored, and after 5 hours desorption process started until the steady state was reached after 10 hour of contact time. Given the results in Figure 6. 12, the contact time chosen to perform the following studies was 24 hours to ensure reaching equilibrium of the system.

The experiments were performed under two different ionic strengths and the results obtained in Figure 6. 12 show that the adsorption was similar in both cases during the first 10 hours of test.

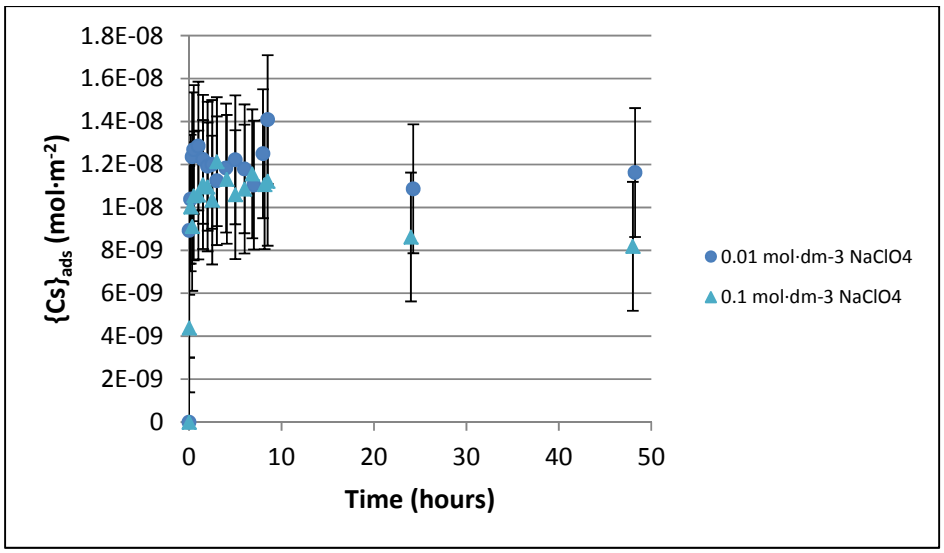

Figure 6. 12 Experimental results of cesium sorption onto uranophane as a function of time for 48 hours

Effect of Cesium Concentration. Isotherm

The study of the isotherms of the Cs-uranophane system was performed using the same methodology explained previously. In order to calculate the amount of adsorbed cesium on uranophane with Eq. (6.1), cesium concentration was analyzed. The results are shown in Figure 6. 13 as well as the modeling obtained by fitting the experimental results with the Langmuir model (Eq. (6.9)).

The fitting routine was performed by using the same methodology as in the previous case: Matlab software was used to adjust all the parameters with the least square routine. The Langmuir parameters obtained are shown in Table 6. 5.

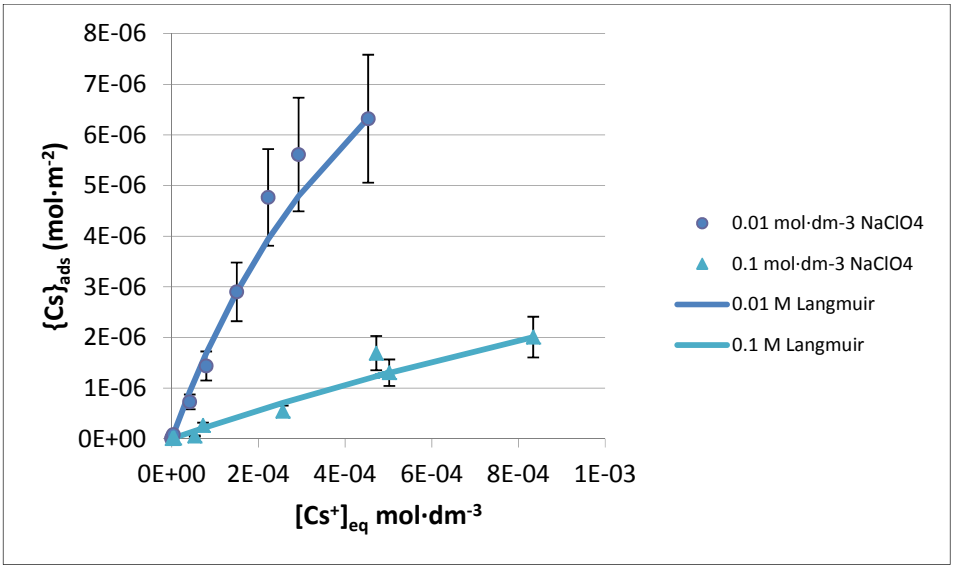

Figure 6. 13 Amount of cesium adsorbed onto uranophane as a function of the cesium concentration in the solution

In this case, the maximum cesium retained on the solid surface under the studied conditions was reached when the ionic strength was 0.01.

It can be observed that there was an effect of the ionic strength on the sorption process since the higher $\{Cs\}_{ads}$ was reached when $NaClO_4$ concentration was lower, in contrast to what can be observed in the Cs – soddyite system and in Giménez et al. (2010). This strong effect of the ionic strength might be due to electrostatic interactions between complexes.

Table 6. 5 Values of Langmuir parameters obtained by fitting the Langmuir model with the experimental results obtained for the system Cs-uranophane

Parameter	Experimental series	
	0.1 mol·dm^{-3} $NaClO_4$	0.01 mol·dm^{-3} $NaClO_4$
K_L	276	1561
$\{Cs\}_{max}$	$1.07 \cdot 10^{-5}$	$1.53 \cdot 10^{-5}$
R^2	0.9886	0.9952

Effect of the pH on the sorption process

In Figure 6. 14 the amount of cesium adsorbed on the uranophane is shown as a function of the pH at equilibrium. It can be observed that there is no clear correlation between the final pH and the $\{Cs\}_{ads}$. It was observed that the final pH remained almost constant in all the samples although the initial pH was varied from 5 to 11. This fact might be caused by the sorption and desorption process of proton and hydroxyl from the solution to the solid surface or vice versa and hence, the Cs-uranophane-$NaClO_4$ system might exhibit a buffer behavior.

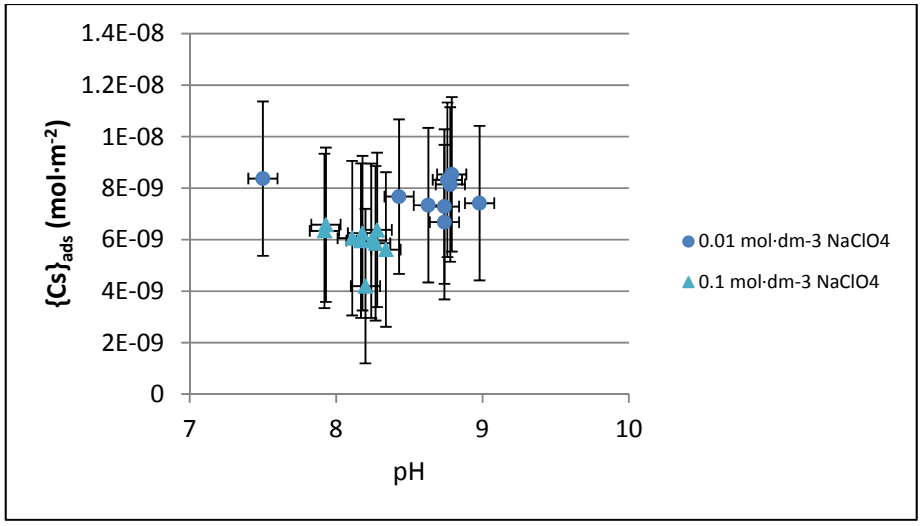

Figure 6. 14 Cesium adsorbed onto uranophane as a function of the pH at equilibrium

It can be observed that the final pH of all the sorption processes was higher than the pH_{pzc} of uranophane (7.32) previously determined. Therefore, under these conditions, the solid surface is negatively charged which might enhance the Cs sorption due to electrostatic forces.

Another factor that should be taken into account is the sorption selectivity towards each one of the ions. Since there are Cs^+, Na^+ and H^+ ions with the same charge, they might compete for the same active sites of the solid. This can be observed in Figure 6. 14 where the high concentration of sodium cations might have partially avoided the retention of Cs.

Sr Sorption onto Soddyite

Kinetic study

The kinetics of the sorption process was studied by using samples of 20 ml of a solution with 10^{-5} mol·dm^{-3} in contact with 50 mg of soddyite for different contact time. The strontium concentration of the resulting solution as a function of time is shown in Figure 6. 15. It can be observed that the system needed one hour at least to reach the equilibrium.

The effect of the ionic medium is also observed in the same graph. The results obtained at lower ionic strength showed ten times more strontium retention on the solid phase.

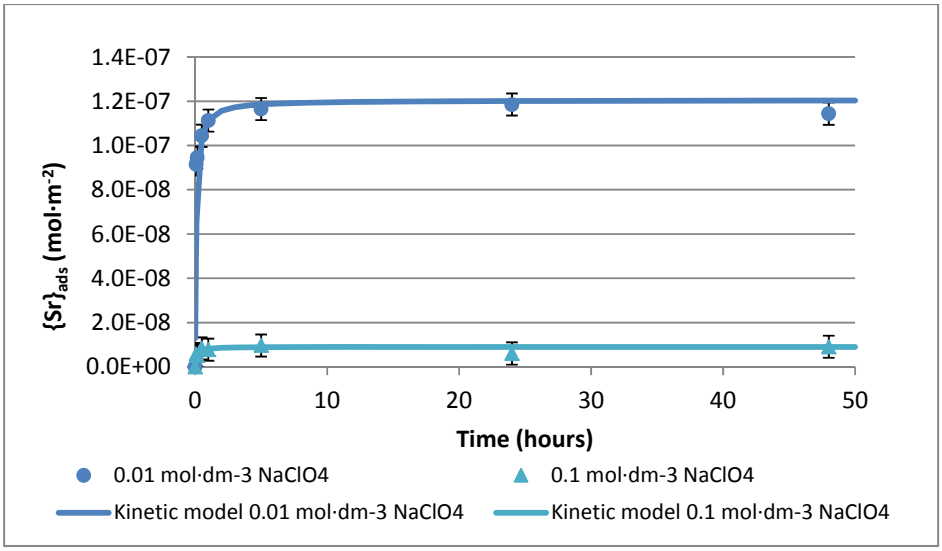

Figure 6. 15 Kinetic experimental results of the sorption process of strontium onto soddyite; the kinetic model used is also shown

A theoretical kinetic model was used to fit the experimental data shown in Figure 6. 15. The pseudo-second order kinetic model was the suitable model that fitted the data. The results are shown in Table 6. 6 along with the R-square values obtained. The analysis was performed using the Matlab® software with the least square routine using Eq. (6.8).

Since the pseudo-second kinetic model was suitable for the Sr-soddyite system, it can be concluded that the rate-limiting step may be chemisorption involving valency forces (Ho and Mckay, 1999). This may be due to the exchange or sharing electrons between strontium and the soddyite and more precisely between Sr^{2+} and the SiO_4^{4-} group from the solid phase.

Table 6. 6 Results obtained when the data was fitted to the pseudo-second kinetic model for the Sr-soddyite sorption system.

Parameter	Experimental series	
	0.1 mol·dm^{-3} $NaClO_4$	0.01 mol·dm^{-3} $NaClO_4$
K_c ($m^2 \cdot mol^{-1} \cdot h^{-1}$)	10^9	10^8
$\{Sr\}_{eq}$	$9.06 \cdot 10^{-9}$	$1.21 \cdot 10^{-7}$
R^2	0.924	0.9664

An influence of the ionic strength can also be observed on the sorption process in Table 6. 6. Also, the $\{Sr\}_{eq}$ values obtained by the fitting show that the sorption decreases more than one order of magnitude from low ionic strength to high ionic strength. Similar results were obtained by Small et al. (2001) who studied the Sr^{2+} sorption onto different bacteria and observed a strong dependency of Sr sorption on the media. The authors suggested that the sorption process proceeds through outer – sphere complexes

since they are affected by changes in ionic strength (Stumm and Morgan, 1996). This type of interaction leads to a system governed by electrostatic interactions between the active sites of the solid phase which are presumably charged negatively, and the metal cation.

Another possible cause for obtaining this result is the selectivity towards other cations in the leachant (Na^+). The sodium might be adsorbed on the active sites thus preventing the strontium cations to be bonded to the solid surface. This might suggest that the sorption process on soddyite is favored for monovalent species.

Effect of Strontium Concentration. Isotherms

The experiments were performed using different initial concentrations from 10^{-7} to $5{\cdot}10^{-3}$ mol·dm^{-3} of strontium. $\{Sr\}_{ads}$ on soddyite was determined by using Eq. (6.1) and the results are shown in Figure 6. 16 as a function of the strontium concentration at equilibrium.

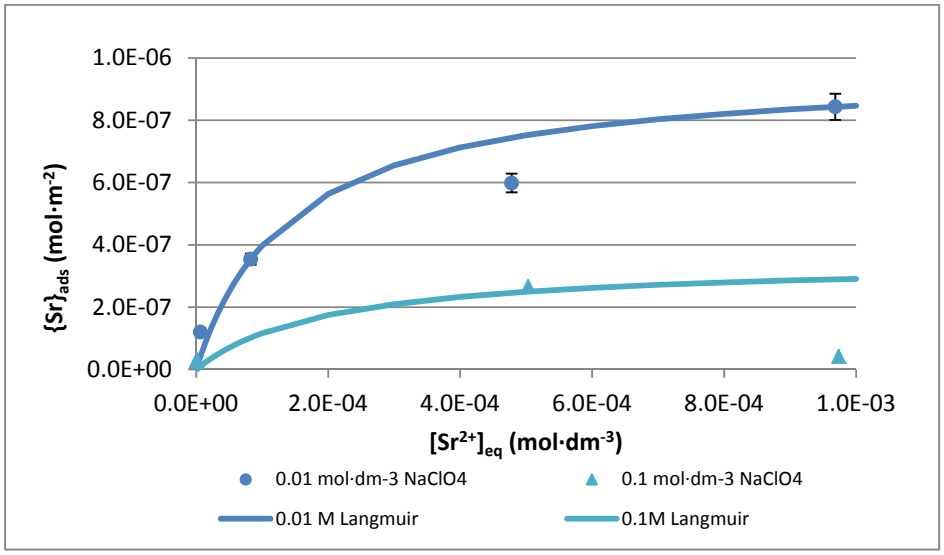

Figure 6. 16 Isotherms of strontium sorption onto 50 mg of soddyite where circles are for low ionic strength media and triangles are for high ionic strength media. The fitting obtained with Langmuir Isotherms model is also shown for each group of data.

The results were fitted by using the Langmuir mode in Eq. (6.9) because there was a maximum strontium retained on the surface, as it can be observed in Figure 6. 16. The fitting routine was the same as in the previous cases. The results obtained are shown in Table 6. 7.

Table 6. 7 Values of Langmuir parameters obtained by fitting the Langmuir model with the experimental results obtained for the system Sr-soddyite

Parameter	Experimental series	
	0.1 mol·dm^{-3} $NaClO_4$	0.01 mol·dm^{-3} $NaClO_4$
K_L	5010	6980
$\{Sr\}_{max}$	$3.49 \cdot 10^{-7}$	$9.68 \cdot 10^{-7}$
R^2	0.9762	0.9299

Sureda et al. (2010) observed a maximum strontium capacity in contact with studtite of $2.5 \cdot 10^{-5}$ mol·m^{-2} under low ionic strength, which is much higher than the maximum capacity with soddyite under the same experimental condition ($9.68 \cdot 10^{-7}$ mol·m^{-2}). The system was well fitted by the Langmuir model, as it has been observed previously for studtite, which means that the sorption process proceeds towards one layer coverage onto specific active sites of the solid.

Effect of the pH on the Sorption Process

The results are shown in Figure 6. 17 as function of the final pH and the ionic strength. It can be observed that there was a decrease of the sorption as the pH increased from 5.5 to 7. The results obtained in this range decreased as the final pH approaches to the pH_{pzc}. This might be caused by the decrease of the surface charge density and the weakening of the electrostatic forces of the system. At pH higher than the pH_{pzc} the soddyite surface was negatively charged by OH^- ions that were likely to adsorb cations such as Sr^{2+}. As a consequence, the strontium concentrations decreases and the Sr is retained on the solid surface.

Compared with studtite (Sureda et al., 2010), the solid phase used does not retain so much strontium.

Additionally, the result obtained with the different media is coherent with the behavior observed in the kinetic and the isotherm studies.

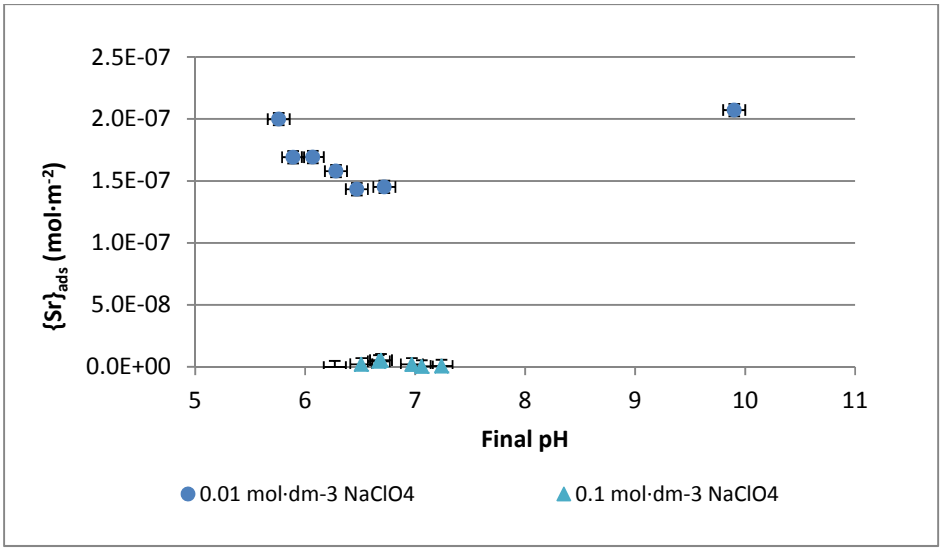

Figure 6. 17 Amount of strontium adsorbed onto soddyite as a function of the equilibrium pH with an initial strontium concentration of 10^{-5} mol·dm^{-3}.

Sr Sorption onto Uranophane

Kinetic study

The sorption process of strontium onto uranophane has been studied starting by the kinetics of the sorption process.

The results are shown in Figure 6. 18 where the amount of strontium adsorbed onto the solid phase is shown as a function of time. It can be observed that the sorption process was highly favored since the steady state was reached within the first hour of contact time.

The experimental results were fitted by using a pseudo-second order kinetic model (Eq. (6.8)). The fitting routine has been performed using the Matlab software with the least square routine and the results of the fitting routine are shown in Table 6. 8. As in the previous system, the interaction between strontium and uranophane may be due to the chemisorption of the cation on the solid phase that involved electron sharing or exchange through valency forces.

Table 6. 8 Kinetic parameters values obtained by fitting the experimental amount of strontium adsorbed onto uranophane as a function of the contact time

Parameter	Experimental series	
	0.1 mol·dm^{-3} $NaClO_4$	0.01 mol·dm^{-3} $NaClO_4$
K (m^2·mol^{-1}·h^{-1})	$1.01 \cdot 10^6$	$2.72 \cdot 10^5$
$\{Sr\}_{eq}$	$5.10 \cdot 10^{-5}$	$1.25 \cdot 10^{-4}$
R^2	0.8225	0.9767

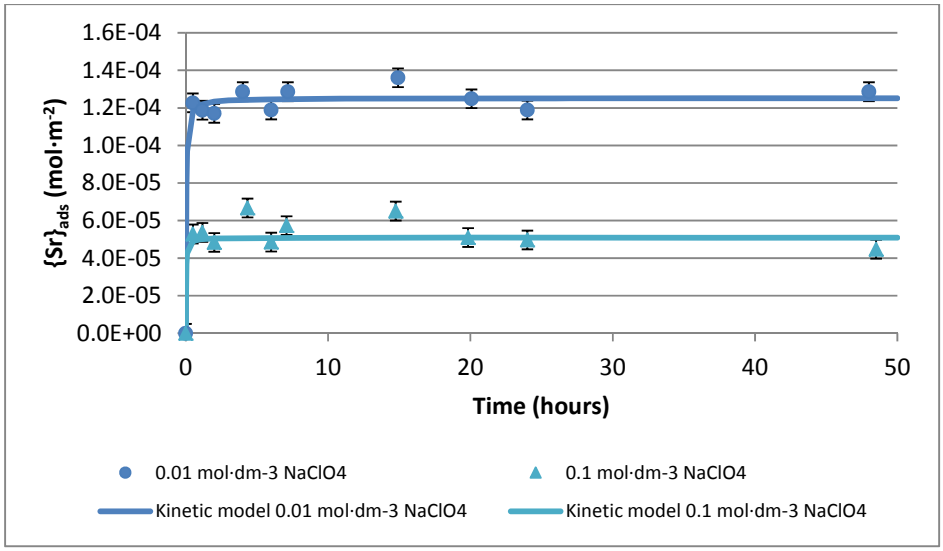

Figure 6. 18 Experimental results of the strontium adsorbed on the uranophane surface as a function of the experimental time.

Effect of Strontium Concentration. Isotherm

Figure 6. 19 shows the amount of strontium adsorbed onto the uranophane surface as a function of the strontium concentration at equilibrium. It can be observed that there is a maximum of the sorption capacity of the solid phase. Taking into account this phenomenon, the experimental results have been modeled by using the Langmuir model described in Eq. (6.9).

The results were obtained by using the same methodology explained in the previous cases. The Matlab software was used to determine the main Langmuir parameters and the results are shown in Table 6. 9.

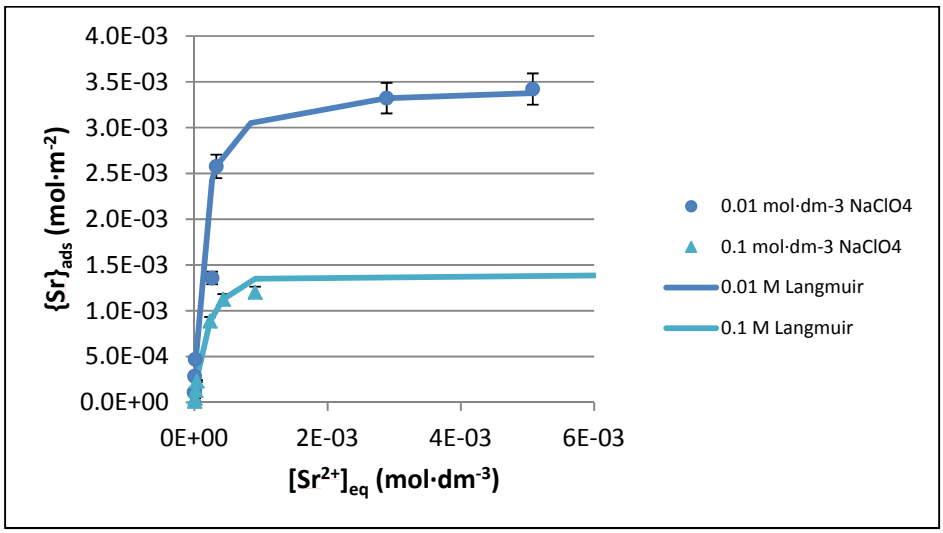

Figure 6. 19 Amount of strontium adsorbed on the uranophane surface as a function of the strontium concentration in the solution. Langmuir model is also shown in the graph as well as the parameters obtained.

Table 6. 9 Values of the Langmuir parameters obtained for the Sr-uranophane system

Parameter	Experimental series	
	0.1 mol·dm^{-3} $NaClO_4$	0.01 mol·dm^{-3} $NaClO_4$
K_L	4979	8933
$\{Sr\}_{max}$	$1.647 \cdot 10^{-3}$	$3.451 \cdot 10^{-3}$
R^2	0.9857	0.9851

As it can be observed in Figure 6. 19 and in Table 6. 9, the sorption of strontium is influenced by the ionic strength. This is most likely due to the ion competition between strontium and sodium for the localized adsorption sites on the solid surface. These results indicate that the presence of sodium in the solution could inhibit the sorption of strontium on uranophane.

Effect of the pH on the Sorption Process

Finally, the effect of the pH was studied by following the same methodology explained before. Several dissolutions with 10^{-3} mol·dm^{-3} were put in contact with the solid phase and the initial pH was adjusted to different values from 5 to 12.

In Figure 6. 20 the amount of strontium adsorbed onto uranophane surface is shown as a function of the final pH. At pH lower than 9, the final pH value remained constant (7.70 ± 0.5) and showed no significant correlation between the Sr sorption and the pH. At pH values higher than 10 the sorption process may be favored since the strontium concentration in the solution decreased.

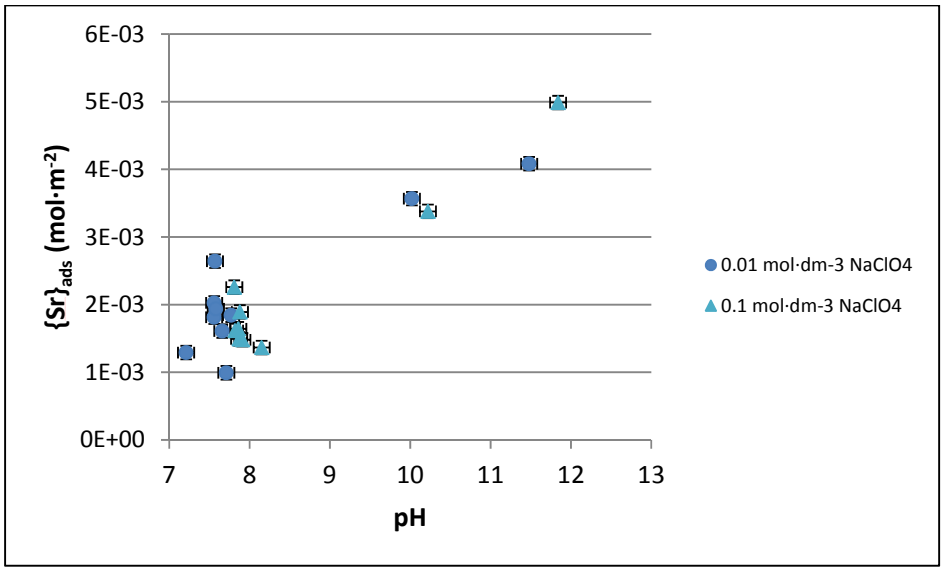

Figure 6. 20 Amount of strontium adsorbed on uranophane as a function of the pH in the equilibrium

The results obtained at pH lower than 9 might be caused by their proximity to the pHpzc (7.32) where the surface charge is neutralized. In this state, the electrostatic forces are weak which hinders the sorption of strontium. On the other hand, at pH higher than 10, the solid surface is negatively charged and this enhances the sorption of Sr^{2+} due to electrostatic forces. Under these conditions, the sorption process might proceed via the adsorption on active sites of uranophane surface or via the chemisorption on surface hydroxyl ions.

Conclusions

The different solid phases were successfully synthesized and were characterized by means of XRD and Raman spectroscopy. The results obtained were in good agreement with the reported spectra for soddyite and uranophane. In addition, the pH_{pzc} was determined for each solid phase. Soddyite has its pH_{pzc} at 6.53 ± 0.05 and hence, the bond between hydroxyl ions and soddyite is slightly stronger than between protons and soddyite. The acidity constant determined for soddyite was $K_{sa} = 8.7 \cdot 10^{-14}$. Uranophane has its pH_{pzc} at 7.3 ± 0.2; therefore, proton bond to the surface is slightly more favored than hydroxyl bond. The acidity constant determined for uranophane was $K_{sa} = 2.3 \cdot 10^{-15}$.

From the kinetic study of all the sorption processes, the evolution of the sorbed radionuclides as a function of time depended on the radionuclide used. In case of the cesium sorption process, there was a first adsorption stage which was kinetically favored, but then a desorption process occurred just before reaching the final steady state within 12 hours of contact time. On the other hand, strontium showed no intermediate adsorption stages and the experimental results could be modeled by using the pseudo-second order kinetic model in Eq. (6.8). Since this kinetic model is based on chemisorption as a sorption mechanism, it can be conclude that the interaction between strontium and the two solid phases studied is due to either sharing or exchanging electrons.

The sorption isotherms obtained for both radionuclides were modeled by the Langmuir equation which is based on a monolayer sorption. Thus, all the sorption processes occurred on a specific amount of localized sites with equal affinity to the cation which leaded to a homogeneous sorption along the solid surface. Taking into account the results obtained from the isotherm fitting, the solid phase that has higher adsorption capacity of Cs is soddyite at high ionic strength ($4.70 \cdot 10^{-5}$ mol·m^{-2}). For strontium, uranophane showed the maximum sorption capacity at low ionic strength values ($3.5 \cdot 10^{-3}$ mol·m^{-2}).

The effect of the pH on the sorption processes strongly depended on the solid phase used. In case of the soddyite no adsorption was observed at pH values lower than 5. On the other side, when the effect of the pH on the sorption process onto uranophane was studied the results showed no specific trend. In fact, it was observed that the final pH of the experiments reached similar values although the initial pH values were set from 5 to 12; therefore, uranophane may act as a solid buffer for the final dissolution.

Bibliography

Alessi, D.S., Szymanowski, J.E.S., Forbes, T.Z., Quicksall, A.N., Sigmon, G.E., Burns, P.C., Fein, J.B., 2013. Mineralogic controls on aqueous neptunium(V) concentrations in silicate systems. J. Nucl. Mater. 433, 233–239. doi:10.1016/j.jnucmat.2012.09.013

Azizian, S., 2004. Kinetic models of sorption: A theoretical analysis. J. Colloid Interface Sci. 276, 47–52. doi:10.1016/j.jcis.2004.03.048

Baker, R.J., 2014. Uranium minerals and their relevance to long term storage of nuclear fuels. Coord. Chem. Rev. 266–267, 123–136. doi:10.1016/j.ccr.2013.10.004

Bonales, L.J., Menor-Salván, C., Cobos, J., 2015. Study of the alteration products of a natural uraninite by Raman spectroscopy. J. Nucl. Mater. 462, 296–303. doi:10.1016/j.jnucmat.2015.04.017

Bourikas, K., Vakros, J., Kordulis, C., Lycourghiotis, A., 2003. Potentiometric mass titrations: Experimental and theoretical establishment of a new technique for determining the point of zero charge (PZC) of metal (hydr)oxides. J. Phys. Chem. B 107, 9441–9451. doi:10.1021/jp035123v

Boyd, G.E., Adamson, A.W., Myers Jr, L.S., 1947. The Exchange Adsorption of Ions from Aqueous Solutions by Organic Zeolites. II. Kinetics. J. Am. Chem. Soc. 69, 2836–2848. doi:10.1021/ja01203a066

Burns, P.C., 1999. Cs boltwoodite obtained by ion exchange from single crystals: Implications for radionuclide release in a nuclear repository. J. Nucl. Mater. 265, 218–223. doi:10.1016/S0022-3115(98)00646-1

Burns, P.C., Deely, K.M., Skanthakumar, S., 2004. Neptunium incorporation into uranyl compounds that form as alteration products of spent nuclear fuel: Implications for geologic repository performance. Radiochim. Acta 92, 151–160. doi:10.1524/ract.92.3.151.30491

Burns, P.C., Ewing, R.C., Miller, M.L., 1997. Incorporation mechanisms of actinide elements into the structures of U6+ phases formed during the oxidation of spent nuclear fuel. J. Nucl. Mater. 245, 1–9. doi:10.1016/S0022-3115(97)00006-8

Burns, P.C., Li, Y., 2002. The structures of becquerelite and Sr-exchanged becquerelite. Am. Mineral. 87, 550–557. doi:10.2138/am-2002-0418

Chen, F., Burns, P.C., Ewing, R.C., 2000. Near-field behavior of 99Tc during the oxidative alteration of spent nuclear fuel. J. Nucl. Mater. 278, 225–232. doi:10.1016/S0022-3115(99)00264-0

Chen, F., Burns, P.C., Ewing, R.C., 1999. ^{79}Se: geochemical and crystallo-chemical retardation mechanisms. J. Nucl. Mater. 275, 81–94. doi:10.1016/S0022-3115(99)00105-1

Douglas, M., Clark, S.B., Friese, J.I., Arey, B.W., Buck, E.C., Hanson, B.D., 2005. Neptunium(V) partitioning to uranium(VI) oxide and peroxide solids. Environ. Sci. Technol. 39, 4117–24. doi:10.1021/es0405169

Douglas, M., Clark, S.B., Utsunomiya, S., Ewing, R.C., 2002. Cesium and strontium incorporation into uranophane. J. Nucl. Mater. 504–507. doi:10.1080/00223131.2002.10875517

Finch, R.J., Ewing, R.C., 1992. The corrosion of uraninite under oxidizing conditions. J. Nucl. Mater. 190, 133–156. doi:10.1016/0022-3115(92)90083-W

Fiol, N., Villaescusa, I., 2008. Determination of sorbent point zero charge: usefulness in sorption studies. Environ. Chem. Lett. 7, 79–84. doi:10.1007/s10311-008-0139-0

Foo, K.Y., Hameed, B.H., 2010. Insights into the modeling of adsorption isotherm systems. Chem. Eng. J.

156, 2–10. doi:10.1016/j.cej.2009.09.013

Friese, J.I., Douglas, M., Mcnamara, B.K., Clark, S.B., Hanson, B.D., 2004. Np Behavior in Synthesized Uranyl Phases : Results of Initial Tests, PNNL-14856. Richland, Washington, USA.

Frost, R.L., Čejka, J., Weier, M.L., Martens, W., 2006. Molecular structure of the uranyl silicates—a Raman spectroscopic study. J. Raman Spectrosc. 37, 538–551. doi:10.1002/jrs.1430

Frost, R.L., Cejka, J., Weier, M.L., Martens, W., Kloprogge, J.T., 2006. A Raman and infrared spectroscopic study of the uranyl silicates--weeksite, soddyite and haiweeite. Spectrochim. Acta. A. Mol. Biomol. Spectrosc. 64, 308–15. doi:10.1016/j.saa.2005.07.028

Giménez, J., de Pablo, J., Casas, I., Martínez-Lladó, X., Rovira, M., Martínez Torrents, A., 2014. Solubility study and point of zero charge of studtite ($UO_2O_2{\cdot}4H_2O$). Appl. Geochemistry 49, 42–45. doi:10.1016/j.apgeochem.2014.07.004

Giménez, J., Martínez-Lladó, X., Rovira, M., De Pablo, J., Casas, I., Sureda, R., Martínez-Esparza, A., 2010. Cesium sorption on studtite (UO2O2 · 4H2O). Radiochim. Acta 98, 479–483. doi:10.1524/ract.2010.1742

Gimenez, J., Sureda, R., De Pablo, J., Casas, I., Martinez-Llado, X., Rovira, M., Martinez-Esparza, A., 2009. The role of uranium peroxide studtite on the retention of Cs, Sr and Se(VI), in: Materials Research Society Symposium Proceedings. pp. 621–626. doi:10.1557/PROC-1193-621

Gorman-Lewis, D., Burns, P.C., Fein, J.B., 2008. Review of uranyl mineral solubility measurements. J. Chem. Thermodyn. 40, 335–352. doi:10.1016/j.jct.2007.12.004

Ho, Y.-S., 2006. Second-order kinetic model for the sorption of cadmium onto tree fern: a comparison of linear and non-linear methods. Water Res. 40, 119–25. doi:10.1016/j.watres.2005.10.040

Ho, Y.S., Mckay, G., 1999. Pseudo-Second Order Model for Sorption Process. Process Biochem. 34, 451–465. doi:10.1016/S0032-9592(98)00112-5

Hoskin, P.W.O., Burns, P.C., 2003. Ion exchange between aqueous fluid and spent nuclear fuel alteration products: Implications for the mobility of Cs in the probable repository at Yucca Mountain. Mineral. Mag. 67, 689–696. doi:10.1180/0026461036740127

Kienzler, B., Metz, V., Brendebach, B., Finck, N., Plaschke, M., Rabung, T., Rothe, J., Schild, D., 2010. Chemical status of U(VI) in cemented waste forms under saline conditions. Radiochim. Acta 98, 674–683. doi:10.1524/ract.2010.1768

Kim, C.-W., Wronkiewicz, D.J., Finch, R.J., Buck, E.C., 2006. Incorporation of cerium and neodymium in uranyl phases. J. Nucl. Mater. 353, 147–157. doi:10.1016/j.jnucmat.2006.02.087

Kim, C.W., Wronkiewicz, D.J., Finch, R.J., Buck, E.C., Wronkiewicz, D.J., Bates, J.K., Wolf, S.F., Buck, E.C., Wronkiewicz, D.J., Bates, J.K., Gerding, T.J., Veleckis, E., Tani, B.S., Finn, P.A., Hoh, J.C., Wolf, S.F., Slater, S.A., Bates, J.K., Burns, P.C., Ewing, R.C., Miller, M.L., Buck, E.C., Wronkiewicz, D.J., Finn, P.A., Bates, J.K., Urbanec, Z., Čejka, J., HARRIS, L.A., TAYLOR, A.J., Bosze, S., Rakovan, J., 2002. Incorporation of Cerium and Neodymium in a Uranyl Hydroxide Solid. MRS Proc. 713, JJ11.66. doi:10.1557/PROC-713-JJ11.66

Lafuente B., Downs R. T., Yang H., S.N., 2015. RRUFF Database [WWW Document]. URL ruff.info (accessed 2.28.16).

Lagergren, S., 1898. About the theory of so-called adsorption of soluble substances. K. Sven. Vetenskapsakademiens Handl. 24, 1–39.

Langmuir, I., 1916. The constitution and fundamental properties of solids and liquids. Part I. Solids. J.

Am. Chem. Soc. 38, 2221–2295. doi:10.1021/ja02268a002

Limousin, G., Gaudet, J.-P., Charlet, L., Szenknect, S., Barthès, V., Krimissa, M., 2007. Sorption isotherms: A review on physical bases, modeling and measurement. Appl. Geochemistry 22, 249–275. doi:10.1016/j.apgeochem.2006.09.010

Martínez-Torrents, A., Giménez, J., Martínez-Lladó, X., de Pablo, J., Casas, I., 2015. Incorporation of selenium(IV) and selenium(VI) on uranyl peroxide. J. Radioanal. Nucl. Chem. 303, 153–159. doi:10.1007/s10967-014-3323-7

McNamara, B., Hanson, B., Buck, E., Soderquist, C., 2005. Corrosion of commercial spent nuclear fuel. 2. Formation of studtite and metastudtite. Radiochim. Acta 93, 169–175. doi:10.1524/ract.93.3.159.61613

Murphy, W.M., Grambow, B., 2008. Thermodynamic interpretation of neptunium coprecipitation in uranophane for application to the Yucca Mountain repository. Radiochim. Acta 96, 563–567. doi:10.1524/ract.2008.1537

Nguyen, S.N., Silva, R.J., Weed, H.C., Andrews, J.E., 1992. Standard Gibbs free energies of formation at the temperature 303.15 K of four uranyl silicates: soddyite, uranophane, sodium boltwoodite, and sodium weeksite. J. Chem. Thermodyn. 24, 359–376. doi:10.1016/S0021-9614(05)80155-7

Parks, G.A., Bruyn, P.L., 1962. The zero point of charge of oxides. J. Phys. Chem. 66, 967–973. doi:10.1021/j100812a002

Pérez, I., Casas, I., Martín, M., Bruno, J., 2000. The thermodynamics and kinetics of uranophane dissolution in bicarbonate test solutions. Geochim. Cosmochim. Acta 64, 603–608. doi:10.1016/S0016-7037(99)00337-3

Pérez, I., Casas, I., Torrero, M.E., Cera, E., Duro, L., Bruno, J., 1997. Dissolution studies of soddyite as a long-term analogue of the oxidative alteration of the spent nuclear fuel matrix, in: Materials Research Society Symposium - Proceedings. Materials Research Society, pp. 565–572. doi:10.1557/PROC-465-565

Rovira, M., De Pablo, J., Casas, I., Giménez, J., Clarens, F., 2004. Sorption of caesium on commercial magnetite with low silica content: Experimental and modelling, in: MRS Proceedings. pp. 677–682. doi:10.1557/PROC-807-677

Rovira, M., Giménez, J., Martínez, M., Martínez-Lladó, X., de Pablo, J., Martí, V., Duro, L., 2008. Sorption of selenium(IV) and selenium(VI) onto natural iron oxides: goethite and hematite. J. Hazard. Mater. 150, 279–84. doi:10.1016/j.jhazmat.2007.04.098

Rovira, M., Pablo, J. de, Casas, I., Giménez, J., Clarens, F., Venkataramani, B., Venkateswarlu, K.., Shankar, J., Todorović, M., Milonjić, S.K., Čomor, J.J., Gal, I.J., Catalette, H., Dumonceau, J., Ollar, P., Marmier, N., Delisée, A., Fromage, F., Ebner, A.D., Ritter, J.A., Navratil, J.D., Marmier, N., Fromage, F., Lützenkirchen, J., Marmier, N., 2003. Sorption of Caesium on Commercial Magnetite with low Silica Content: Experimental and Modelling. MRS Proc. 807, 677. doi:10.1557/PROC-807-677

Small, T.D., Warren, L.A., Ferris, F.G., 2001. Influence of ionic strength on strontium sorption to bacteria , Fe (III) oxide and composite bacteria-Fe (III) oxide surfaces . Appl Geochem Fe (III) oxide , and composite bacteria-Fe (III) oxide surfaces. Appl. Geochemistry 16, 939–946. doi:10.1016/S0883-2927(00)00065-2

Sposito, G., 1984. The Surface Chemistry of Soils. Oxford University Press, New York, NY, USA.

Sprycha, R., 1989. Electrical double layer at alumina/electrolyte interface. I. Surface charge and zeta potential 127, 1–11. doi:10.1016/0021-9797(89)90002-7

Sprycha, R., 1984. Surface charge and adsorption of background electrolyte ions at anatase/electrolyte interface. J. Colloid Interface Sci. 102, 173–185. doi:10.1016/0021-9797(84)90211-X

Stumm, W., 1992. Aquatic Surface Chemistry. Chemical processes at the particle-water interface, First Edit. ed. John Wiley and Sons, Inc., Zurich, Switzerland.

Stumm, W., Morgan, J.J., 1996. Aquatic Chemistry, 3rd ed. Wiley, New York, NY, USA.

Sureda, R., 2011. Disolución del combustible nuclear gastado en un almacenamiento geologico profundo. Efecto de los productos radiolíticos y de formación de fases secundarias. Ph.D. Dissertation. Universitat Politècnica de Catalunya.

Sureda, R., Casas, I., Giménez, J., De Pablo, J., Quinones, J., Zhang, J., Ewing, R.C., 2011. Effects of ionizing radiation and temperature on uranyl silicates: Soddyite $(UO_2)_2(SiO_4)(H_2O)_2$ and uranophane $Ca(UO_2)_2(SiO_3OH)_2 \cdot 3.5H_2O$. Environ. Sci. Technol. 45, 2510–2515. doi:10.1021/es1041496

Sureda, R., Martínez-Lladó, X., Rovira, M., de Pablo, J., Casas, I., Giménez, J., 2010. Sorption of strontium on uranyl peroxide: implications for a high-level nuclear waste repository. J. Hazard. Mater. 181, 881–5. doi:10.1016/j.jhazmat.2010.05.095

Chapter 7:
General Conclusions

The results obtained in this thesis provided with new and useful information regarding some of the possible alteration mechanisms of the SNF and radionuclides release under relevant conditions of the DGR. The work was performed by using different analogues of the SNF, such as UO_2 and SIMFUEL, and the techniques used allowed to focus the study on specific processes involving the matrix oxidation and the RN release.

The main conclusions from the four scenarios proposed in this thesis are:

1. Regarding the study of UO_2 in contact with water vapor, the evolution of the oxidation state of the uranium on the surface has been determined as a function of the gas stream used and as a function of the temperature.

XPS proved to be suitable to study the evolution of UO_2 surface in contact with water vapor as function of the temperature. Additionally, the facility used allowed to perform the study *in situ* avoiding any contact with the atmosphere.

It was observed that the oxidation caused by water vapor was enhanced with the increase of temperature from 100 to 350 ^{0}C under anoxic conditions. This result is in good agreement with the bibliography, which reports an increase of the oxidation rate with the increase of temperature. When hydrogen was used as gas stream, the oxidation was partially avoided at high temperatures (350 ^{0}C) compared with the results obtained under argon atmosphere. This result suggests that hydrogen was preventing the oxidation.

When Pd-NPs were used, the oxidation under anoxic conditions occurred at temperatures higher than 100 ^{0}C. Taking into account the complete dissociation of the water molecule reported in the bibliography, the hydrogen produced could be preventing the oxidation in contact with the Pd-NPs at low temperatures. At high temperatures uranium was oxidized by the water vapor. Under reducing environment, no uranium oxidation was observed at any of the temperatures used in the study in presence of Pd particles. In addition, no significant effect of the amount of Pd introduced to the UO_2 was observed on the system in contact with hydrogen.

2. The mathematical model (SERNIM) and a specific algorithm were designed in order to predict the release of RN under aqueous conditions.

The general mathematic expression is as follows and the algorithm is detailed in Chapter 4.

$$m_{RN}(t) = \sum_{c=1}^{N} m(c)_{RN,\infty} \cdot \left(1 - e^{-k_c t}\right)$$

SERNIM was applied to experimental release data from a 42 MWd/kg_U SNF powder sample from the core of the pellet. The model was fitted to the uranium release data in order to determine the main parameters of the model and predict the rest of the radionuclides release. The results obtained of uranium dissolution rate ((2.75 ± 0.30) · 10^{-11} $mol_U \cdot m^{-2} \cdot s^{-1}$) is in good agreement with the previously reported values of matrix dissolution ((4.60 ± 1.80) · 10^{-11} $mol_U \cdot m^{-2} \cdot s^{-1}$ and (3.20 ± 0.20) · 10^{-11} $mol_U \cdot m^{-2} \cdot s^{-1}$), which gives confidence in the model, the results obtained and the algorithm used.

The elements that were well predicted by using the SERNIM parameters from the uranium release were assumed to be dissolved in the SNF matrix. The results of using the 42 MWd/kg_U SNF powder sample showed that Mo, Am, Pu, Ce, La and Tc were well predicted, hence are dissolved in the uranium matrix.

Other RN were over predicted by using the matrix parameters, which means that they had a slower dissolution than the matrix. These elements were Ru and Rh. This result is assumed to be caused by metallic precipitates segregated in the SNF.

Finally, Cs, Rb, Nd and Sr were identified as RN segregated from uranium with higher dissolution rate than the matrix because the SERNIM prediction under estimated the release of these RN. Hence, they were considered to contribute to the IRF from the GB. The amount of RN segregated: 2.06% of Cs, 1.00% of Nd, 0.91% of Rb and 0.65% of Sr.

3. The corrosion study of a 3% at. simulated BU SIMFUEL was studied under hyper alkaline conditions in the presence of calcium and silicate.

The study of the oxidation of SIMFUEL in presence of Si and Ca under hyper-alkaline has been studied by using corrosion experiments under anoxic conditions. Additionally, the resulting oxidation state of the SIMFUEL surface was obtained by using XPS. This methodology allowed to

observe a inhibiting effect of the SIMFUEL corrosion when Ca and Si were dissolved in the electrolyte.

The presence of silicate at pH 12 in the electrolyte was observed to influence the corrosion behavior at potential values between -100 and 300 mV (vs. SCE) compared with the system under alkaline conditions. The effect of the silicate concentration was also studied by cyclic voltammetry from 10^{-3} to 0.1 mol·dm^{-3} and the results showed no clear influence of the conditions used.

When calcium was added to the electrolyte, the corrosion was partially avoided. This fact suggests the stabilization of the reduced species or precipitation of protecting solid phases on the electrode surface.

The corrosion potential measurements showed that the E_{CORR} obtained in the presence of calcium and silicate under hyper alkaline conditions was the lowest (-105 mV) compared with the electrolyte containing silicate at pH 12 (-70 mV) and with the electrolyte at pH 12 (-80 mV). The surface composition of the electrode showed that less oxidized surface was obtained when the electrolyte used contained both calcium and silicate at pH 12. At the same time, the surface composition obtained was similar for the other two electrolytes used in the study.

4. Remediation of Cs and Sr by soddyite and uranophane was studied and characterized as function of the ionic strength.

First, the two solid phases were synthesized and analyzed by XRD and Raman spectroscopy that provide information about crystalline structure and information of the functional groups present in the solid phase. The results showed that the solids obtained were soddyite and uranophane. Additionally, the pH value of their point of zero charge was determined: for soddyite, the pH_{pzc} is 6.53 ± 0.05 and for uranophane, the pH_{pzc} is 7.3 ± 0.2.

The sorption kinetics were determined to be mainly influenced by the ion used. The sorption kinetics obtained in the case of cesium suggested an intermediate state in the first stage of the sorption process; the equilibrium was reached after 12 hours. In the case of the sorption of strontium, the kinetics was well modeled by using the pseudo-second order kinetic model which indicates a possible chemisorption of strontium on the two solid phases used. In this case, the steady state was reached in 1 hour.

The study of the isotherms of each system determined that the results were well modeled by using the Langmuir isotherms. This means that the sorption processes proceeded through a monolayer on the sorption active sites of the solid phase. The maximum sorption capacity for the Cs – soddyite system was obtained at high ionic strength ($4.70 \cdot 10^{-5}$ $mol_{Cs} \cdot m^{-2}$) and the maximum sorption capacity for Sr was obtained in contact with uranophane at low ionic strength ($3.46 \cdot 10^{-3}$ $mol_{Sr} \cdot m^{-2}$).

The effect of the pH was studied for all four systems. In this case, the solid phase determined the trend of the sorption process. When soddyite was used, the results showed that there was an effect of the pH on the sorption of either Cs or Sr. At low pH there was no ion sorption and at pH higher than the pH_{pzc}, the sorption was enhanced. When uranophane was used, the resulting pH of the sorption process remained constant, which suggests that the system was buffered by the solid phase. In this case, no specific correlation between the pH and the ion sorption was observed.

Except for the Cs-soddyite system, the rest of the RN-solid phase sorption systems showed higher sorption capacity when the ionic strength was lower. This might be caused by the ion competition for the sorption active sites on the solid phases.

Acronyms

AES	Auger Electron Spectroscopy
AGP	Almacenamiento Geológico Profundo
BE	Binging Energy (eV)
BET	Brunauer – Emmett – Teller analysis technique to measure surface area
BSM	Basic Stern Model
BU	Burn - up (MWd/kgU)
C	Coulomb
c	Contribution to the IRF of the dissolution model
C_1	Capacitance of the system in the CCM
CCiT	Centros Científicos y Tecnológicos
CCM	Constant Capacity Model
CNG	Combustible nuclear gastado
CRnE	Center for Research in nanoEngineering
CTDS	Centralized Temporary Dry Storage
DGR	Deep Geological Repository
DLM	Doble - Layer Model
E	Potential (V)
E_{CORR}	Corrosion Potential (V)
EDS	Energy Dispersive X-Ray Spectroscopy
EIL	Electron Induced Luminiscence
ENUSA	Empresa Nacional de Uranio S.A.
E^o	Standard Potential of a reaction (V)
F	Faraday number (96485 $C \cdot mol^{-1}$)
f	Freundlich exponent
FGR	Fission gas release (%)
FIAP	Cumulative fraction of inventory in aqueous phase
FNU	Fractional radionuclide release normalized to uranium
FP	Fission products

FWHM	Full Width at Half Maximum
GB	Grain boundaries
HBS	High burn-up structure
HR-TEM	High Resolution Transmission Electron Microscopy
H_{Tc}	Technetium Inventory
H_U	Uranium inventory
hυ	Energy of a photon (eV)
i_{CORR}	corrosion current
ICP-MS	Inductively Coupled Plasma Mass Spectrometry
i_{pa}	anodic peak current
i_{pc}	cathodic peak current
IRF	Instant Release Fraction
j	current density ($A \cdot cm^{-2}$)
k	rate constant
k_{ox}	Dissolution constant of the oxidized contribution to the leaching experiments
k_{ma}	Dissolution constant of the matrix contribution to the leaching experiments
k_c	Kinetic dissolution constant of a certain contribution to the IRF ((time units)$^{-1}$)
KE	Kinetic Energy (eV)
K_L	Langmuir constant
LPR	Linear Power Rate (W/cm)
M	Reduced metal
$m(c)_{RN,\infty}$	The total amount of radionuclide released from a certain IRF contribution (moles)
$m(ma)_{U,\infty}$	Total amount of uranium for the matrix release contribution to the leaching experiments (moles)
$m(ox)_{U,\infty}$	Total amount of uranium for the oxidized release contribution to the leaching experiments (moles)
M^+	Oxidized metal
$m_{RN}(t)$	Amount of radionuclide leached in the dissolution (moles)
M_{sample}	Sample weight
$m_{U,TOTAL}$	Total amount of uranium in the sample (moles)
MW	Molecular weight
n	Number of electrons exchanged in the reaction

N	Total amount of contributions to the IRF considered in the dissolution model
NF-PRO	Near Field Processes European Project
NPP	Nuclear Power Plants
Pd-NPs	Palladium nanoparticles
pH_{pzc}	Point of zero charge
P_{O2}	partial pressure of oxygen
pzc	zero charge point
Q_A	Anodic charge density ($C \cdot cm^{-2}$)
R	Gas constant 8.314 ($C \cdot V \cdot mol^{-1} \cdot K^{-1}$)
RE	Reference electrode
RN	Radionuclide
RRF	Rapid release fraction
S/TEM	Scanning Transmission Microscopy
SA	Specific surface area of the solid phase
SCE	Saturated Calomel Electrode
SEM	Scanning Electron Microscopy
SFS	Spent Fuel Stability European Project
SHE	Standard Hydrogen Electrode
SIMS	Seconday Ion Mass Spectroscopy
SNF	Spent Nuclear Fuel
t	Time
T	Temperature (K)
TDS	Thermal Desorption Spectroscopy
TLM	Triple - Layer Model
U4f	Uranium main band obtained by X-Ray Photoelectron Spectroscopy
$U4f_{7/2}$	Uranium band obtained by X-Ray Photoelectron Spectroscopy from 384 to 377 eV
UB	Universitat de Barcelona
UHV	Ultra High Vacuum
WE	Working electrode
XPS	X-Ray Photoelectron Spectroscopy
XRD	X-ray diffraction
z_-	the valence of the different ionic species on the solid surface with negative charge sign

z_+	the valence of the different ionic species on the solid surface with positive charge sign
(S)	Amount of sorption sites occupied
(S)e	Amount of sorption sites occupied in the equilibrium
[ion]	Concentration of an ion ($mol \cdot dm^{-3}$)
$[ion]_0$	ion concentration before performing the experiment ($mol \cdot dm^{-3}$)
$[ion]_e$	ion concentration at the equilibrium ($mol \cdot dm^{-3}$)
$\{ion\}_{ads}$	Amount of ion sorbed on the solid phase ($mol \cdot m^{-2}$)
$\{ion\}_e$	Amount of ion sorbed on the solid phase ($mol \cdot m^{-2}$) in the equilibrium
$\{ion\}_{max}$	Maximum amount of ion sorbed on the solid phase ($mol \cdot m^{-2}$)
$\{ion\}_t$	Amount of ion sorbed on the solid phase ($mol \cdot m^{-2}$) at a certain time
Γ_-	Adsorption density of the determining ionic species on the solid surface with negative charge
Γ_+	Adsorption density of the determining ionic species on the solid surface with positive charge
$\Delta G_{adsorption}$	Variation of the Gibbs free of the adsorption process
$\Delta G_{coulombic}$	energy necessary to transport the ion from the bulk of the solution to the solid surface site at potential ψ_0
$\Delta G_{intrinsic}$	Variation of the Gibbs free of chemical bond in the adsorption process
$\Delta\overline{G}$	Surface charge density from outer - sphere complexes ($C \cdot m^{-2}$)
Δz	Variation of the charge
σ_0	Permanent surface charge density ($C \cdot m^{-2}$)
σ_H	Surface charge density from H^+ and OH^- ($C \cdot m^{-2}$)
σ_{IS}	Surface charge density from inner - sphere complexes ($C \cdot m^{-2}$)
σ_T	Total surface charge density ($C \cdot m^{-2}$)
Φ_S	Work function of the spectrometer in the XPS technique
ψ_0	Potential of the charged surface of the solid - phase in the adsorption process

Annex A

Numerical results

In this section, the results obtained from the U4$f_{7/2}$ peak deconvolution are shown following the order of the figures in the chapter. Even though the same results will be shown several times, each table corresponds to one figure to facilitate the reading.

UO_2 Sample

T-Ar-H_2O treatments

Table A. 1 Results obtained from the U 4$f_{7/2}$ de-convolution shown in Figure 3. 10

Temperature	U(IV) (%)	U(V) (%)	U(VI) (%)
100	56.9	14.2	28.9
200	41.2	18.9	39.9
350	7.1	57.1	35.8

T-H_2-H_2O treatments

Table A. 2 Results obtained from the U 4$f_{7/2}$ de-convolution shown in Figure 3. 11

Temperature	U(IV) (%)	U(V) (%)	U(VI) (%)
60	59.1	19.7	21.2
120	34.6	30.4	35.0
200	37.7	25.4	36.9
350	64.2	20.4	15.4

UO_2 doped with Pd-NPs samples

T-Ar-H_2O treatments

Table A. 3 Results obtained from the U 4$f_{7/2}$ de-convolution shown in Figure 3. 16(A)

Temperature	U(IV) (%)	U(V) (%)	U(VI) (%)
100	100	0	0
200	42.6	39.3	18.1
350	2.4	48.2	31.4

Table A. 4 Results obtained from the U $4f_{7/2}$ de-convolution shown in Figure 3. 16(B)

Temperature	U(IV) (%)	U(V) (%)	U(VI) (%)
100	100	0	0
200	49.8	23.2	27.0
350	5.3	38.6	56.1

T-H_2-H_2O treatments

Table A. 5 Results obtained from the U $4f_{7/2}$ de-convolution shown in Figure 3. 17 for the sample with 0.5% wt. of Pd

Temperature	U(IV) (%)	U(V) (%)	U(VI) (%)
60	100	0	0
100	100	0	0
200	100	0	0
350	100	0	0

Table A. 6 Results obtained from the U $4f_{7/2}$ de-convolution shown in Figure 3. 17 for the sample with 1.5% wt. of Pd

Temperature	U(IV) (%)	U(V) (%)	U(VI) (%)
60	100	0	0
100	100	0	0
200	100	0	0
350	100	0	0

Effect of the ε-particles and metallic particles

T-Ar-H_2O treatments

Table A. 7 Percentage of U(IV) in the U$4f_{7/2}$ band after performing the experiments under argon atmosphere as a function of sample and temperature. The graph is shown in Figure 3. 19(A).

Sample	Temperature		
	100	**200**	**350**
UO_2	56.9	14.2	28.9
UO_2 + 0.5% wt. Pd	100	42.6	2.4
UO_2 + 1.5% wt. Pd	100	49.8	5.3

Table A. 8 Percentage of U(V) in the U4f$_{7/2}$ band after performing the experiments under argon atmosphere as a function of sample and temperature. The graph is shown in Figure 3. 19 (B).

Sample	Temperature		
	100	200	350
UO_2	14.2	18.9	57.1
UO_2 + 0.5% wt. Pd	0	39.3	58.2
UO_2 + 1.5% wt. Pd	0	23.2	38.6

Table A. 9 Percentage of U(VI) in the U4f$_{7/2}$ band after performing the experiments under argon atmosphere as a function of sample and temperature. The graph is shown in Figure 3. 19 (C).

Sample	Temperature		
	100	200	350
UO_2	28.9	39.9	35.8
UO_2 + 0.5% wt. Pd	0	18.0	31.4
UO_2 + 1.5% wt. Pd	0	27.0	56.1

Table A. 10 BE of the U4f$_{7/2}$ band after performing the experiments under argon atmosphere as a function of sample and temperature. The graph is shown in Figure 3. 19(D).

Sample	Temperature		
	100	200	350
UO_2	379.8	380.0	380.5
UO_2 + 0.5% wt. Pd	379.6	379.8	380.3
UO_2 + 1.5% wt. Pd	379.6	380.1	380.6

T-H_2-H_2O treatments

Table A. 11 Percentage of U(IV) in the U4f$_{7/2}$ band after performing the experiments under hydrogen atmosphere as a function of sample and temperature. The graph is shown in Figure 3. 20(A).

Sample	Temperature			
	60	120	200	350
UO_2	59.1	34.6	37.7	64.2
UO_2 + 0.5% wt. Pd	100	100	100	100
UO_2 + 1.5% wt. Pd	100	100	100	100

Table A. 12 Percentage of U(V) in the $U4f_{7/2}$ band after performing the experiments under hydrogen atmosphere as a function of sample and temperature. The graph is shown in Figure 3. 20(B).

Sample	Temperature			
	60	120	200	350
UO_2	19.7	30.4	25.4	20.4
UO_2 + 0.5% wt. Pd	0	0	0	0
UO_2 + 1.5% wt. Pd	0	0	0	0

Table A. 13 Percentage of U(VI) in the $U4f_{7/2}$ band after performing the experiments under hydrogen atmosphere as a function of sample and temperature. The graph is shown in Figure 3. 20(C)

Sample	Temperature			
	60	120	200	350
UO_2	21.2	35.0	36.9	15.4
UO_2 + 0.5% wt. Pd	0	0	0	0
UO_2 + 1.5% wt. Pd	0	0	0	0

Table A. 14 BE of the $U4f_{7/2}$ band after performing the experiments under argon atmosphere as a function of sample and temperature. The graph is shown in Figure 3. 20 (D)

Sample	Temperature			
	60	120	200	350
UO_2	379.9	380.3	380.1	379.8
UO_2 + 0.5% wt. Pd	379.55	379.55	379.55	379.55
UO_2 + 1.5% wt. Pd	379.60	379.60	379.60	379.60

Annex B

Spectrum Characteristics

In this appendix the main characteristics of each spectrum obtained are shown. These characteristics were compared with the bibliographic values shown in Table 3. 3 in order to identify the treatments that oxidized the UO_2 surface. Additionally, the satellite position is shown as their relative distance to the U $4f_{5/2}$ XPS band. All the measures are given in eV.

As in the previous appendix, each table corresponds to one graph shown in the chapter.

UO_2 Sample

T-Ar-H_2O treatments

Table B. 1 XPS spectrum characteristics of the results obtained after putting in contact the UO_2 sample with an argon stream saturated with water vapor as function of the temperature. They correspond to the results shown in Figure 3. 10.

Temperature	U$4f_{7/2}$ BE (eV)	FWHM (eV)	ΔBE Satellite 1	ΔBE Satellite 2
100	379.8	2.4	6.5	8.3
200	380.0	2.6	6.1	8.0
350	380.5	2.6	5.5	8.2

T-H_2-H_2O treatments

Table B. 2 XPS spectrum characteristics of the results obtained after putting in contact the UO_2 sample with a hydrogen stream saturated with water vapor as function of the temperature. They correspond to the results shown in Figure 3. 11.

Temperature	U$4f_{7/2}$ BE (eV)	FWHM (eV)	ΔBE Satellite 1	ΔBE Satellite 2
60	379.9	2.5	6.5	9.0
120	380.3	2.6	5.8	8.5
200	380.1	2.6	5.9	8.5
350	379.8	2.4	6.4	9.1

UO_2 doped with Pd-NPs samples

T-Ar-H_2O treatments

Table B. 3 XPS spectrum characteristics of the results obtained after putting in contact the UO_2 doped sample with an argon stream saturated with water vapor as function of the temperature. They correspond to the results shown in Figure 3. 16(A)

Temperature	U$4f_{7/2}$ BE (eV)	FWHM (eV)	ΔBE Satellite 1	ΔBE Satellite 2
100	379.6	2.1	6.7	---

200	379.8	2.4	6.5	8.5
350	380.3	2.5	6.3	8.1

Table B. 4 XPS spectrum characteristics of the results obtained after putting in contact the UO_2 doped sample with an argon stream saturated with water vapor as function of the temperature. They correspond to the results shown Figure 3. 16(B)

Temperature	$U4f_{7/2}$ BE (eV)	FWHM (eV)	ΔBE Satellite 1	ΔBE Satellite 2
100	379.6	2.1	6.7	---
200	380.1	2.5	6.1	8.1
350	380.6	2.4	---	7.7

T-H_2-H_2O treatments

Table B. 5 XPS spectrum characteristics of the results obtained after putting in contact the 0.5% UO_2 doped sample with a hydrogen stream saturated with water vapor as function of the temperature. They correspond to the results shown in Figure 3. 17

Temperature	$U4f_{7/2}$ BE (eV)	FWHM (eV)	ΔBE Satellite 1	ΔBE Satellite 2
60	379.55	2.0	6.7	---
120	380.55	2.0	6.7	---
200	380.55	2.0	6.7	---
350	379.6	2.0	6.7	---

Table B. 6 XPS spectrum characteristics of the results obtained after putting in contact the 1.5% UO_2 doped sample with a hydrogen stream saturated with water vapor as function of the temperature. They correspond to the results shown in Figure 3. 17

Temperature	$U4f_{7/2}$ BE (eV)	FWHM (eV)	ΔBE Satellite 1	ΔBE Satellite 2
60	379.6	2.0	6.7	---
120	380.6	2.0	6.7	---
200	380.6	2.0	6.7	---
350	379.6	2.0	6.7	---

Annex C

Here the graphs obtained by the model for each radionuclide are shown. Also, the experimental error and the error range obtained from the uranium fitting are considered in the graphs. These considerations will allow to identify those elements that are segregated.

Uranium fitting

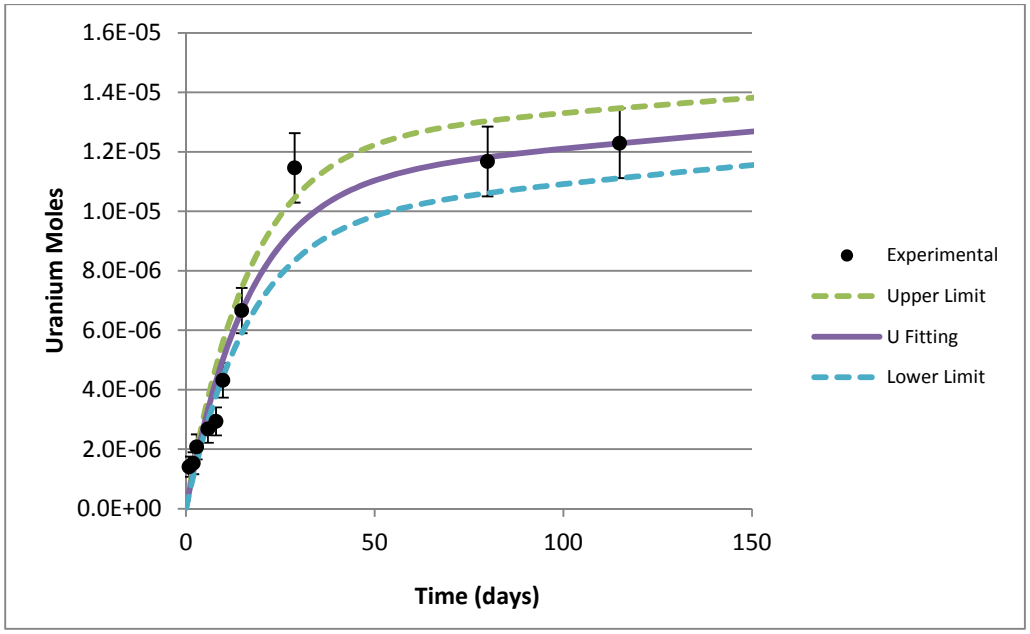

Figure C. 1 SERNIM fitted to the Uranium release data taking into account the experimental error reported

Table C. 1 Values of the SERNIM parameters for the Uranium release with the boundary values reported by Matlab®

Parameter	Nominal Value	Upper Boundary	Lower Boundary	Range
$m(ox)_{U,\infty}$	$1.1 \cdot 10^{-5}$	$2.0 \cdot 10^{-5}$	$0.2 \cdot 10^{-5}$	$\pm 0.9 \cdot 10^{-5}$
k_{ox}	$6.0 \cdot 10^{-2}$	$12.3 \cdot 10^{-2}$	$-0.3 \cdot 10^{-2}$	$\pm 6.3 \cdot 10^{-2}$
k_{ma}	$0.3 \cdot 10^{-4}$	$2.7 \cdot 10^{-4}$	$-2.1 \cdot 10^{-4}$	$\pm 2.4 \cdot 10^{-4}$
R^2	**0.9535**			

Cesium fitting

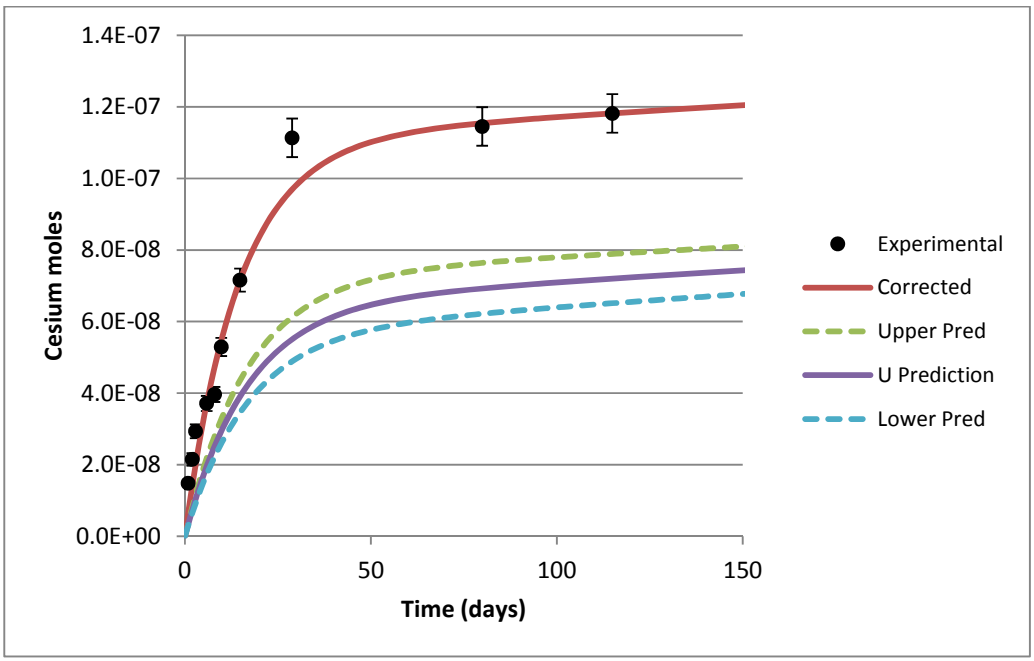

Figure C. 2 SERNIM fitted to the Cesium release data taking into account the experimental error reported

Table C. 2 Values of the SERNIM parameters for the Cesium release with the boundary values reported by Matlab®

Parameter	Nominal Value	Upper Boundary	Lower Boundary	Range
$m(seg)_{Cs,\infty}$	$4.6 \cdot 10^{-8}$	$5.9 \cdot 10^{-8}$	$3.4 \cdot 10^{-8}$	$\pm 1.2 \cdot 10^{-8}$
k_{seg}	0.08	0.14	0.02	± 0.06
$m(ox,U)_{Cs,\infty}$	$6.5 \cdot 10^{-8}$	$7.2 \cdot 10^{-8}$	$5.7 \cdot 10^{-8}$	$\pm 0.7 \cdot 10^{-8}$
k_{ox}	$6.0 \cdot 10^{-2}$	$12.3 \cdot 10^{-2}$	$-0.3 \cdot 10^{-2}$	$\pm 6.3 \cdot 10^{-2}$
k_{ma}	$0.3 \cdot 10^{-4}$	$2.7 \cdot 10^{-4}$	$-2.1 \cdot 10^{-4}$	$\pm 2.4 \cdot 10^{-4}$
R^2	**0.9647**			

Strontium fitting

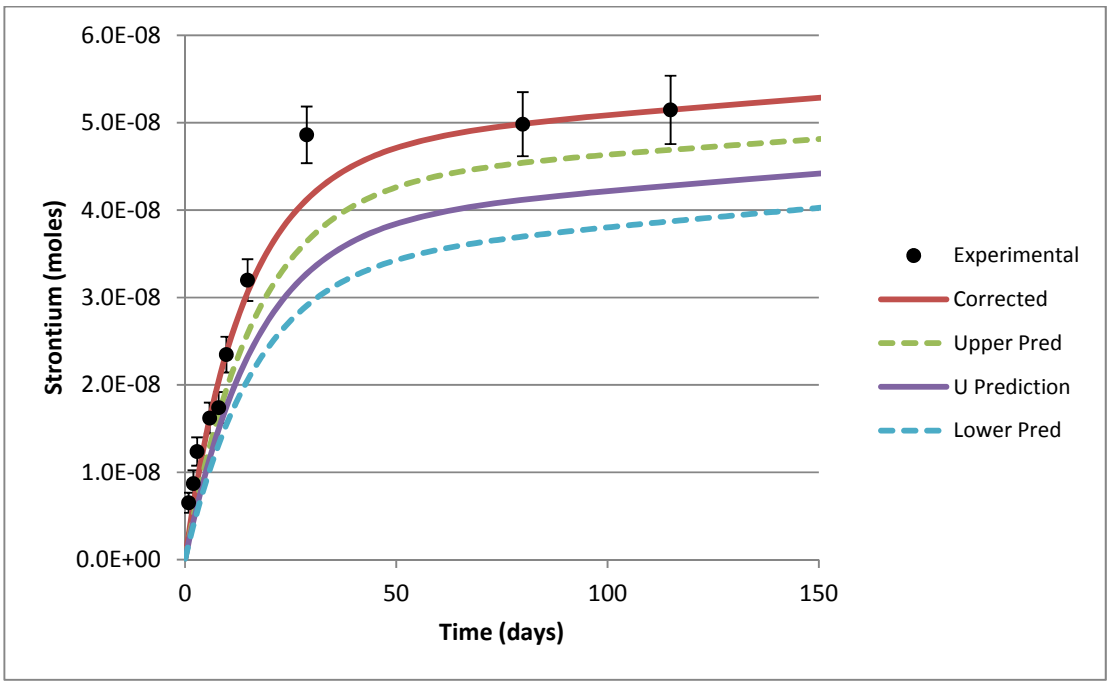

Figure C. 3 SERNIM fitted to the Strontium release data taking into account the experimental error reported

Table C. 3 Values of the SERNIM parameters for the Strontium release with the boundary values reported by Matlab®

Parameter	Nominal Value	Upper Boundary	Lower Boundary	Range
$m(seg)_{Sr,\infty}$	$8.7 \cdot 10^{-9}$	$8.8 \cdot 10^{-9}$	$8.6 \cdot 10^{-9}$	$\pm 0.1 \cdot 10^{-9}$
ks_{eg}	0.13	0.27	-0.02	± 0.14
$m(ox,U)_{Sr,\infty}$	$3.8 \cdot 10^{-8}$	$4.3 \cdot 10^{-8}$	$3.4 \cdot 10^{-8}$	$\pm 0.4 \cdot 10^{-9}$
k_{ox}	$6.0 \cdot 10^{-2}$	$12.3 \cdot 10^{-2}$	$-0.3 \cdot 10^{-2}$	$\pm 6.3 \cdot 10^{-2}$
k_{ma}	$0.3 \cdot 10^{-4}$	$2.7 \cdot 10^{-4}$	$-2.1 \cdot 10^{-4}$	$\pm 2.4 \cdot 10^{-4}$
R^2	**0.9625**			

Technetium fitting

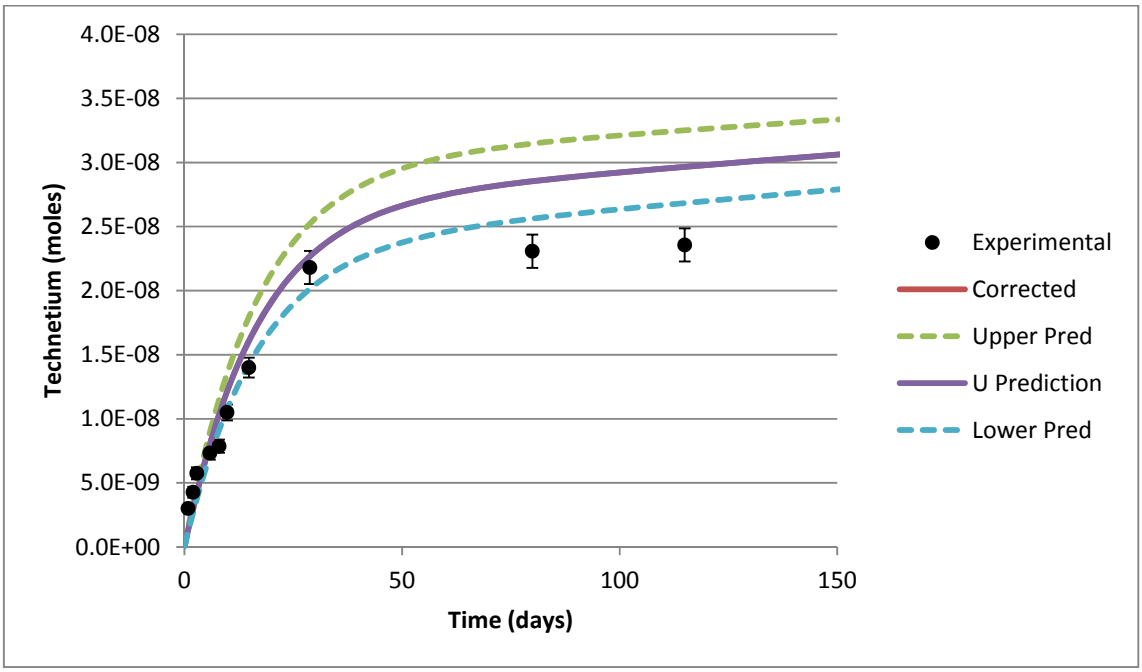

Figure C. 4 SERNIM fitted to the Technetium release data taking into account the experimental error reported

Table C. 4 Values of the SERNIM parameters for the Technetium release with the boundary values reported by Matlab®

Parameter	Nominal Value	Upper Boundary	Lower Boundary	Range
$m(ox,U)_{Tc,\infty}$	$2.7 \cdot 10^{-8}$	$3.0 \cdot 10^{-8}$	$2.3 \cdot 10^{-8}$	$\pm 0.3 \cdot 10^{-8}$
k_{ox}	$6.0 \cdot 10^{-2}$	$12.3 \cdot 10^{-2}$	$-0.3 \cdot 10^{-2}$	$\pm 6.3 \cdot 10^{-2}$
k_{ma}	$0.3 \cdot 10^{-4}$	$2.7 \cdot 10^{-4}$	$-2.1 \cdot 10^{-4}$	$\pm 2.4 \cdot 10^{-4}$
R^2	**0.94**			

Molybdenum fitting

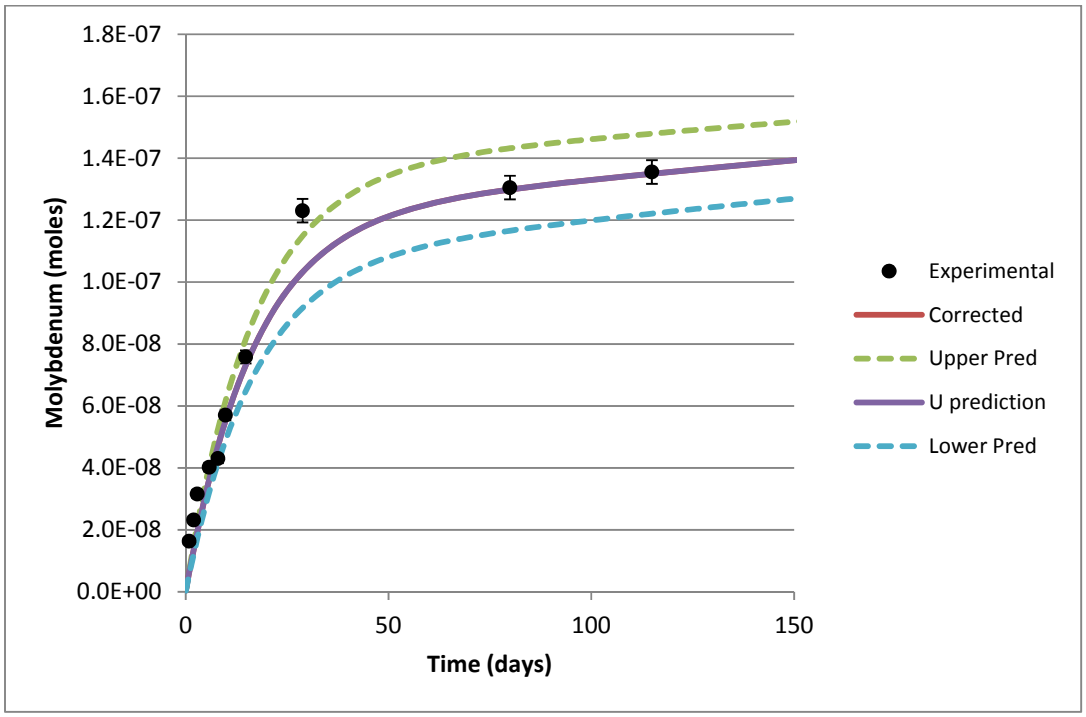

Figure C. 5 SERNIM fitted to the Molybdenum release data taking into account the experimental error reported

Table C. 5 Values of the SERNIM parameters for the Molybdenum release with the boundary values reported by Matlab®

Parameter	Nominal Value	Upper Boundary	Lower Boundary	Range
$m(ox,U)_{Mo,\infty}$	$1.2 \cdot 10^{-7}$	$1.4 \cdot 10^{-7}$	$1.1 \cdot 10^{-7}$	$\pm 0.2 \cdot 10^{-7}$
k_{ox}	$6.0 \cdot 10^{-2}$	$12.3 \cdot 10^{-2}$	$-0.3 \cdot 10^{-2}$	$\pm 6.3 \cdot 10^{-2}$
k_{ma}	$0.3 \cdot 10^{-4}$	$2.7 \cdot 10^{-4}$	$-2.1 \cdot 10^{-4}$	$\pm 2.4 \cdot 10^{-4}$
R^2	**0.9535**			

Rubidium fitting

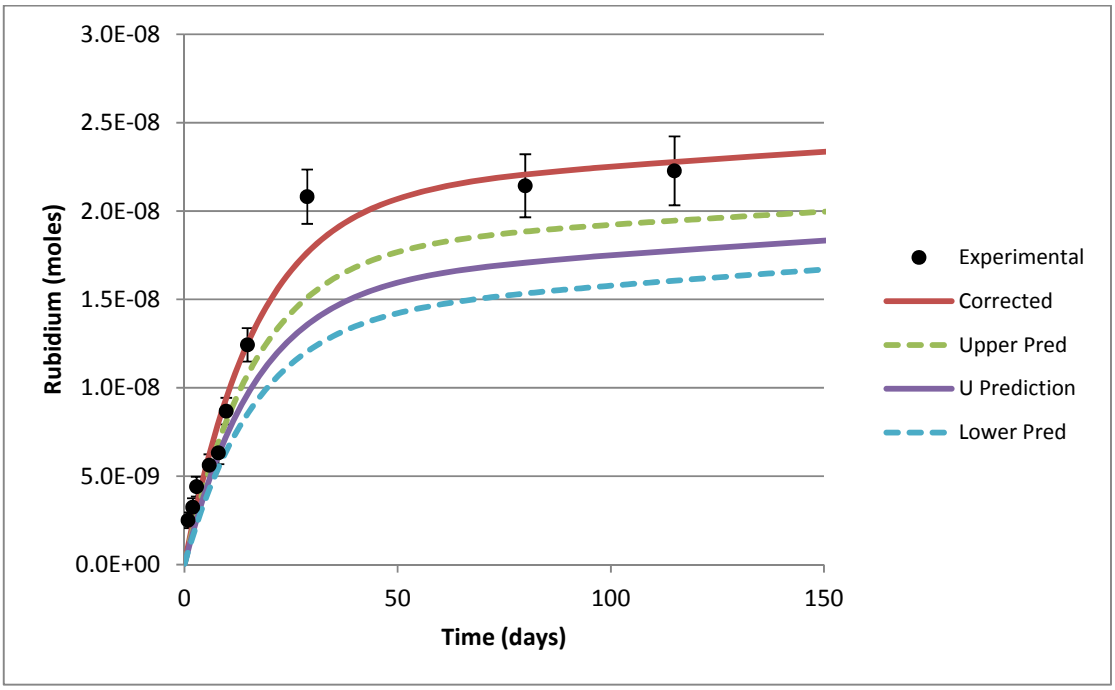

Figure C. 6 SERNIM fitted to the Rubidium release data taking into account the experimental error reported

Table C. 6 Values of the SERNIM parameters for the Rubidium release with the boundary values reported by Matlab®

Parameter	Nominal Value	Upper Boundary	Lower Boundary	Range
$m(seg)_{Rb,\infty}$	$5.0 \cdot 10^{-9}$	$5.1 \cdot 10^{-9}$	$4.9 \cdot 10^{-9}$	$\pm 0.1 \cdot 10^{-9}$
k_{seg}	$5.7 \cdot 10^{-2}$	$12.2 \cdot 10^{-2}$	$-0.8 \cdot 10^{-2}$	$\pm 6.5 \cdot 10^{-2}$
$m(ox,U)_{Rb,\infty}$	$1.6 \cdot 10^{-8}$	$1.8 \cdot 10^{-8}$	$1.4 \cdot 10^{-8}$	$\pm 0.2 \cdot 10^{-8}$
k_{ox}	$6.0 \cdot 10^{-2}$	$12.3 \cdot 10^{-2}$	$-0.3 \cdot 10^{-2}$	$\pm 6.3 \cdot 10^{-2}$
k_{ma}	$0.3 \cdot 10^{-4}$	$2.7 \cdot 10^{-4}$	$-2.1 \cdot 10^{-4}$	$\pm 2.4 \cdot 10^{-4}$
R^2	**0.9474**			

Americium fitting

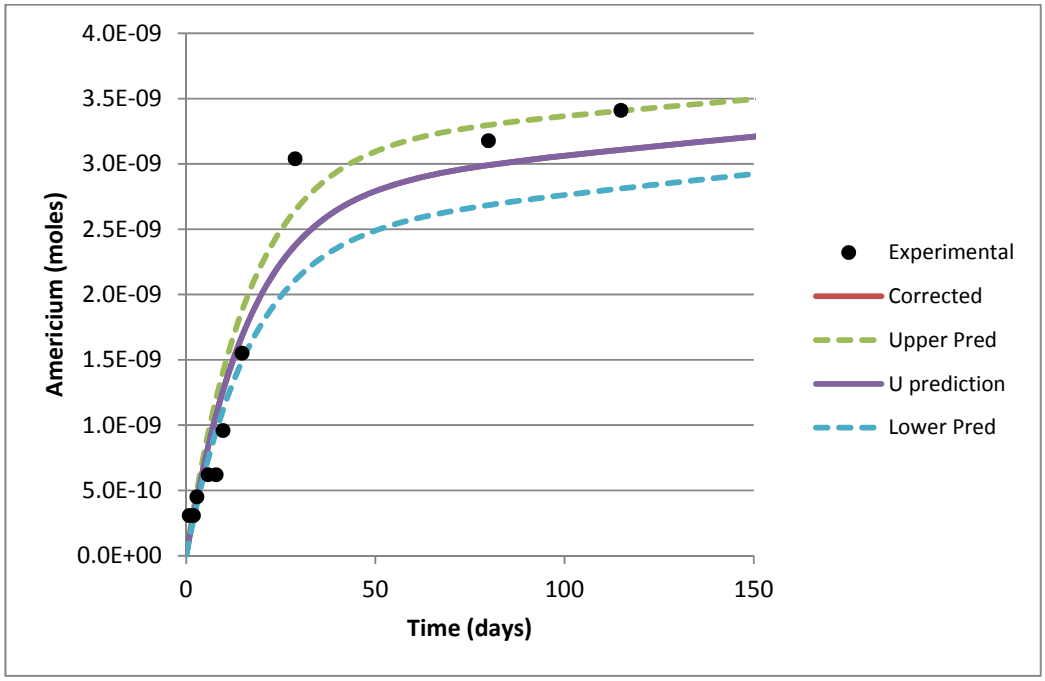

Figure C. 7 SERNIM fitted to the Americium release data taking into account the experimental error reported

Table C. 7 Values of the SERNIM parameters for the Americium release with the boundary values reported by Matlab®

Parameter	Nominal Value	Upper Boundary	Lower Boundary	Range
$m(ox)_{Am,\infty}$	$2.8 \cdot 10^{-9}$	$3.1 \cdot 10^{-9}$	$2.6 \cdot 10^{-9}$	$\pm 0.3 \cdot 10^{-9}$
k_{ox}	$6.0 \cdot 10^{-2}$	$12.3 \cdot 10^{-2}$	$-0.3 \cdot 10^{-2}$	$\pm 6.3 \cdot 10^{-2}$
k_{ma}	$0.3 \cdot 10^{-4}$	$2.7 \cdot 10^{-4}$	$-2.1 \cdot 10^{-4}$	$\pm 2.4 \cdot 10^{-4}$
R^2	**0.9535**			

Rhodium fitting

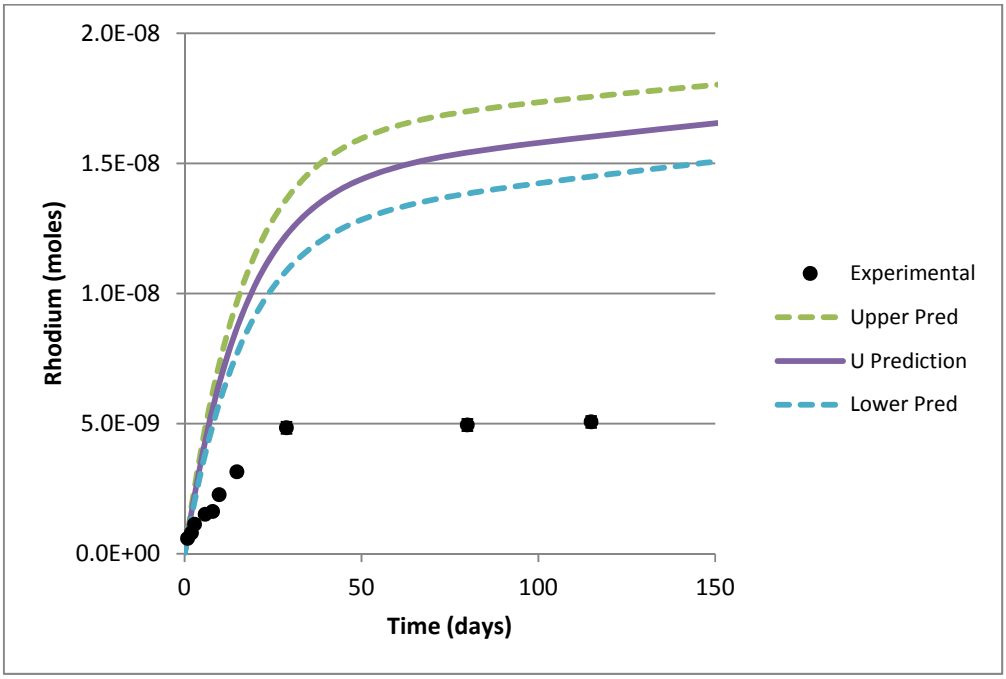

Figure C. 8 SERNIM fitted to the Rhodium release data taking into account the experimental error reported

Table C. 8 Values of the SERNIM parameters for the Rhodium release with the boundary values reported by Matlab®

Parameter	Nominal Value	Upper Boundary	Lower Boundary	Range
$m(ox)_{Rh,\infty}$	$1.4 \cdot 10^{-8}$	$1.6 \cdot 10^{-8}$	$1.3 \cdot 10^{-8}$	$\pm 0.2 \cdot 10^{-8}$
k_{ox}	$6.0 \cdot 10^{-2}$	$12.3 \cdot 10^{-2}$	$-0.3 \cdot 10^{-2}$	$\pm 6.3 \cdot 10^{-2}$
k_{ma}	$0.3 \cdot 10^{-4}$	$2.7 \cdot 10^{-4}$	$-2.1 \cdot 10^{-4}$	$\pm 2.4 \cdot 10^{-4}$
R^2	**0.0**			

Ruthenium fitting

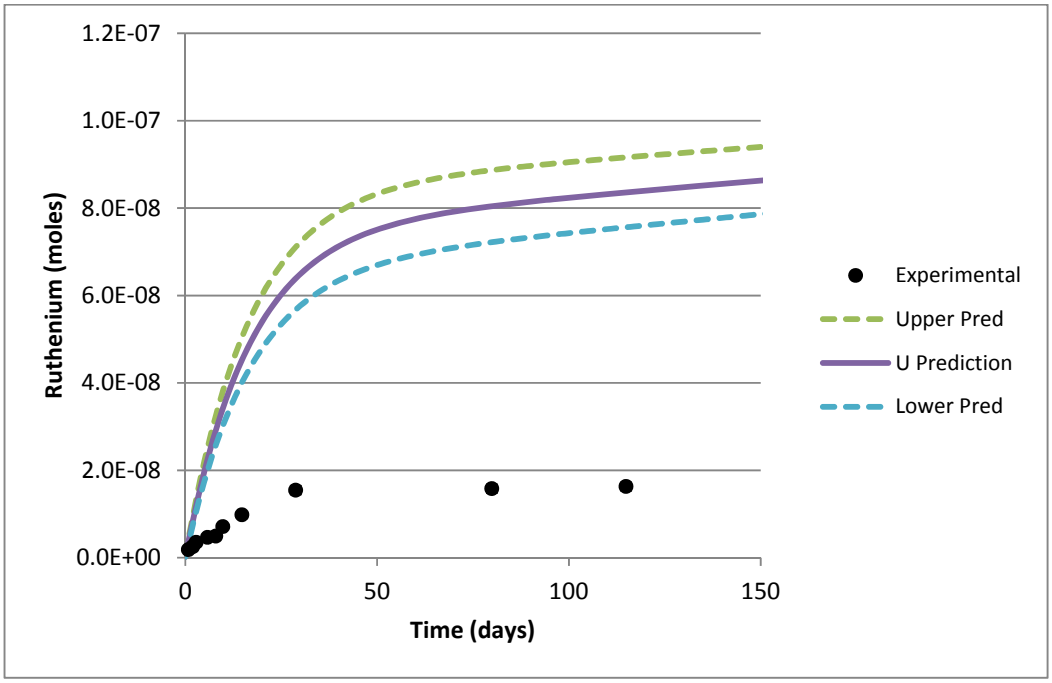

Figure C. 9 SERNIM fitted to the Ruthenium release data taking into account the experimental error reported

Table C. 9 Values of the SERNIM parameters for the Ruthenium release with the boundary values reported by Matlab®

Parameter	Nominal Value	Upper Boundary	Lower Boundary	Range
$m(ox)_{Ru,\infty}$	$7.5 \cdot 10^{-8}$	$8.4 \cdot 10^{-8}$	$6.6 \cdot 10^{-8}$	$\pm 10^{-8}$
k_{ox}	$6.0 \cdot 10^{-2}$	$12.3 \cdot 10^{-2}$	$-0.3 \cdot 10^{-2}$	$\pm 6.3 \cdot 10^{-2}$
k_{ma}	$0.3 \cdot 10^{-4}$	$2.7 \cdot 10^{-4}$	$-2.1 \cdot 10^{-4}$	$\pm 2.4 \cdot 10^{-4}$
R^2	**0.0**			

Plutonium fitting

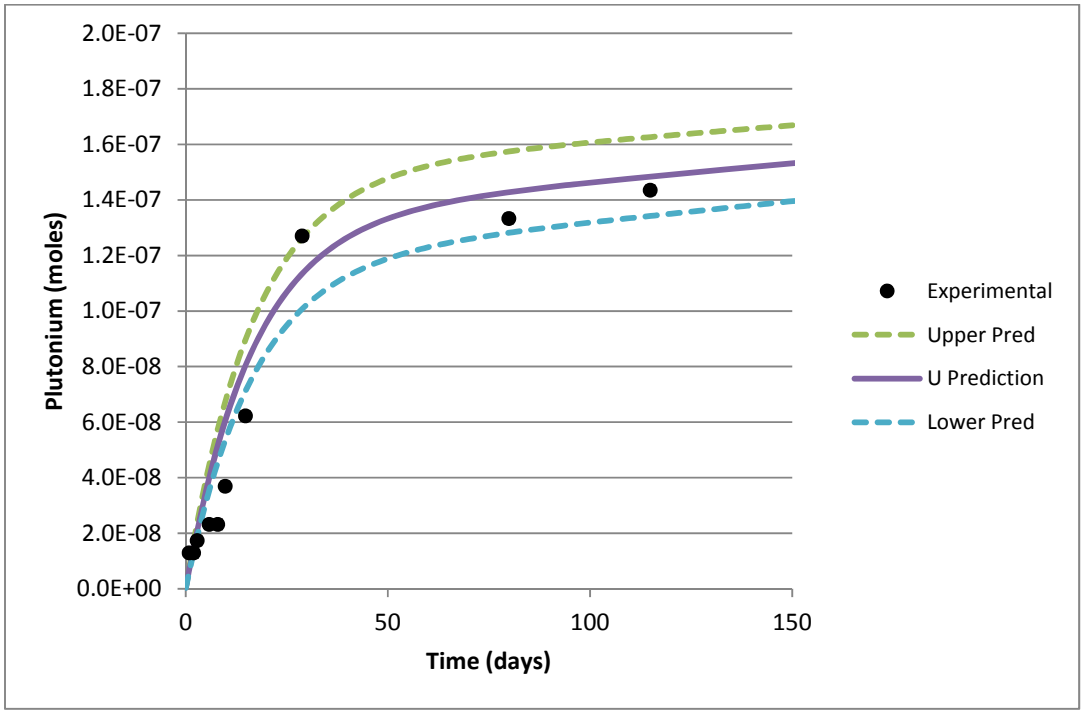

Figure C. 10 SERNIM fitted to the Plutonium release data taking into account the experimental error reported

Table C. 10 Values of the SERNIM parameters for the Plutonium release with the boundary values reported by Matlab®

Parameter	Nominal Value	Upper Boundary	Lower Boundary	Range
$m(ox)_{Pu,\infty}$	$1.3 \cdot 10^{-7}$	$1.5 \cdot 10^{-7}$	$1.2 \cdot 10^{-7}$	$\pm 0.2 \cdot 10^{-7}$
k_{ox}	$6.0 \cdot 10^{-2}$	$12.3 \cdot 10^{-2}$	$-0.3 \cdot 10^{-2}$	$\pm 6.3 \cdot 10^{-2}$
k_{ma}	$0.3 \cdot 10^{-4}$	$2.7 \cdot 10^{-4}$	$-2.1 \cdot 10^{-4}$	$\pm 2.4 \cdot 10^{-4}$
R^2	**0.9535**			

Cerium fitting

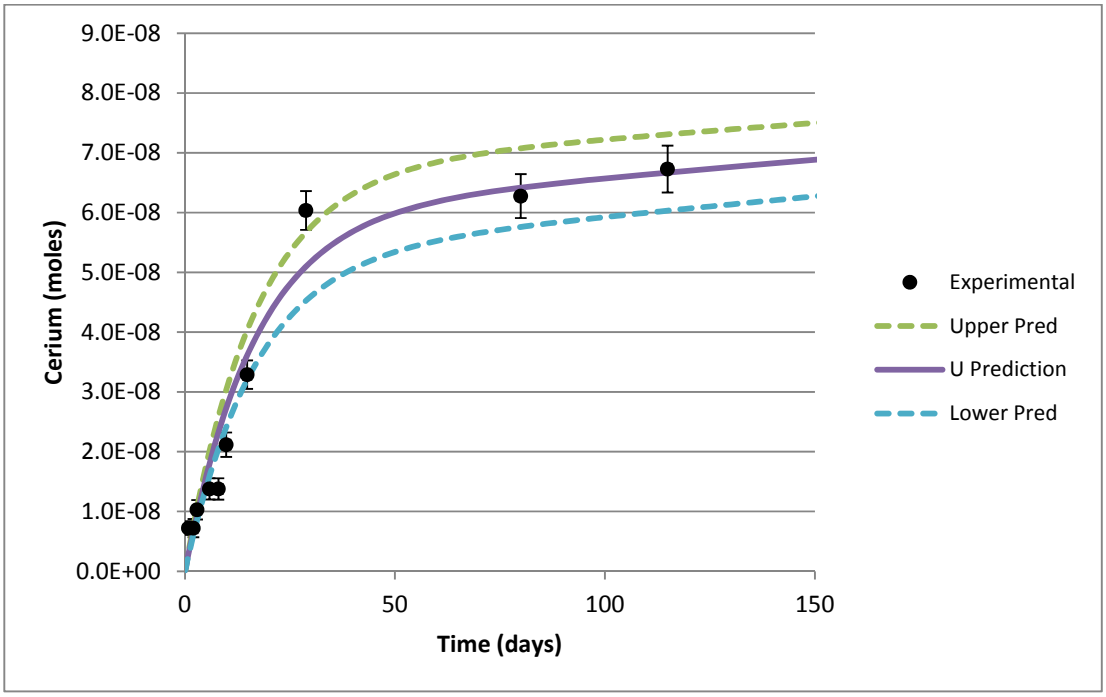

Figure C. 11 SERNIM fitted to the Cerium release data taking into account the experimental error reported

Table C. 11 Values of the SERNIM parameters for the Cerium release with the boundary values reported by Matlab®

Parameter	Nominal Value	Upper Boundary	Lower Boundary	Range
$m(ox)_{Ce,\infty}$	$6.0 \cdot 10^{-8}$	$6.7 \cdot 10^{-8}$	$5.3 \cdot 10^{-8}$	$\pm 0.7 \cdot 10^{-8}$
k_{ox}	$6.0 \cdot 10^{-2}$	$12.3 \cdot 10^{-2}$	$-0.3 \cdot 10^{-2}$	$\pm 6.3 \cdot 10^{-2}$
k_{ma}	$0.3 \cdot 10^{-4}$	$2.7 \cdot 10^{-4}$	$-2.1 \cdot 10^{-4}$	$\pm 2.4 \cdot 10^{-4}$
R^2	**0.9535**			

Lanthanum fitting

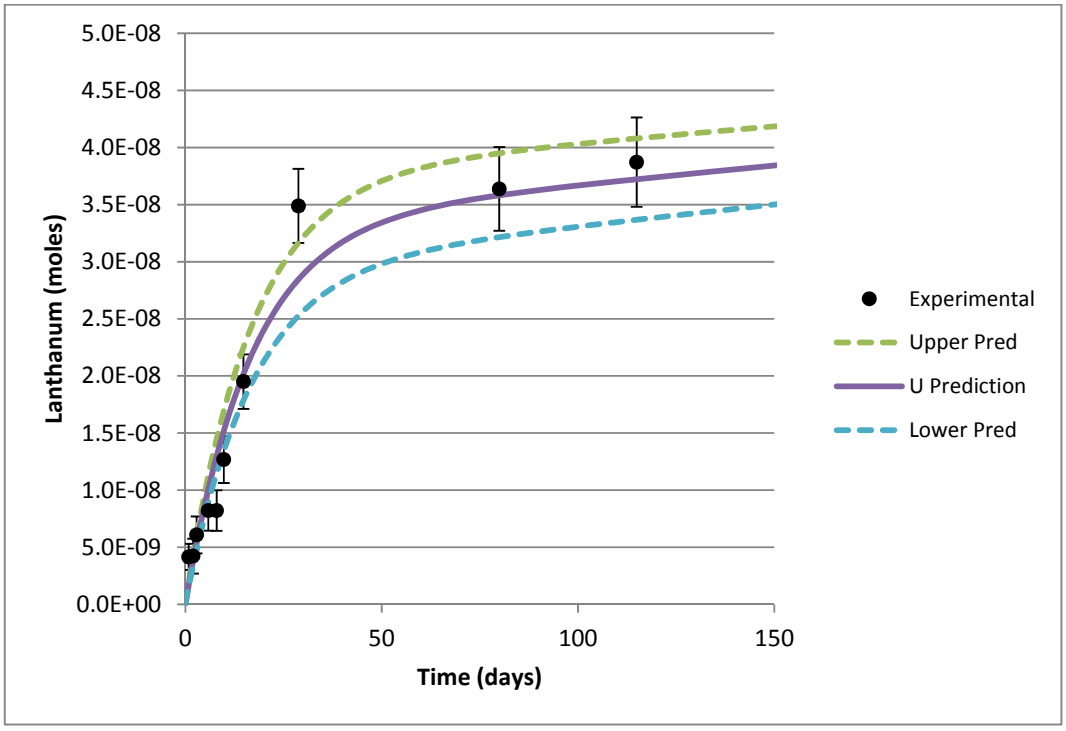

Figure C. 12 SERNIM fitted to the Lanthanum release data taking into account the experimental error reported

Table C. 12 Values of the SERNIM parameters for the Lanthanum release with the boundary values reported by Matlab®

Parameter	Nominal Value	Upper Boundary	Lower Boundary	Range
$m(ox,U)_{La,\infty}$	$3.3 \cdot 10^{-8}$	$3.7 \cdot 10^{-8}$	$2.9 \cdot 10^{-8}$	$\pm 0.4 \cdot 10^{-8}$
k_{ox}	$6.0 \cdot 10^{-2}$	$12.3 \cdot 10^{-2}$	$-0.3 \cdot 10^{-2}$	$\pm 6.3 \cdot 10^{-2}$
k_{ma}	$0.3 \cdot 10^{-4}$	$2.7 \cdot 10^{-4}$	$-2.1 \cdot 10^{-4}$	$\pm 2.4 \cdot 10^{-4}$
R^2	**0.9535**			

Annex D

This section is included in this chapter in order to provide with all the information available about Cs, Sr and Rb in Valls et al. (2014). The amount of RN segregated shown in the graphs was obtained from Valls et al. (2014) and it was calculated by using the Eq. (4.3) from the FIAP data. As a consequence, the results need to be corrected by the specific surface area of the sample in order to be able to compare samples among them. These results are shown in the Discussion section. In this Annex the bare results from Valls et al. (2014) are shown.

Cs segregated from the matrix

Data of Cs segregation as a function of the BU is shown in the following graphs.

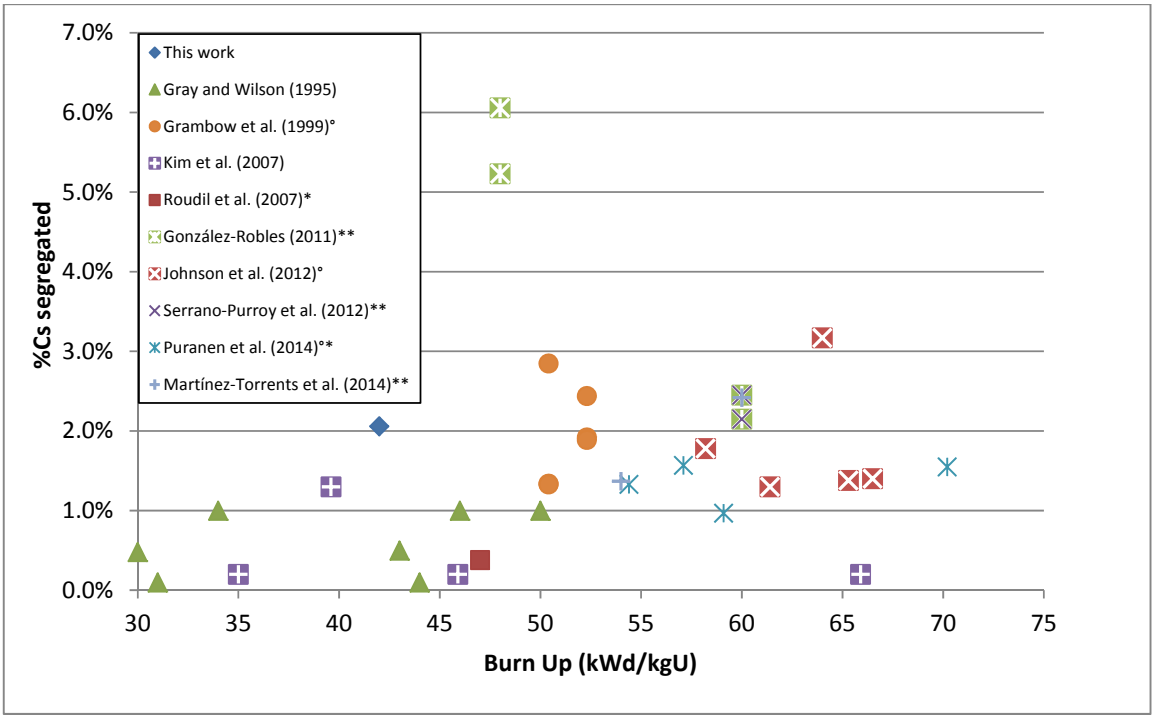

Figure D. 1 Amount of Cs segregated from the matrix in powder and fragmented as a function of the BU.

[0] Fragment samples
** FIAP data*
*** IRF determined by using the Eq. (4.3)*

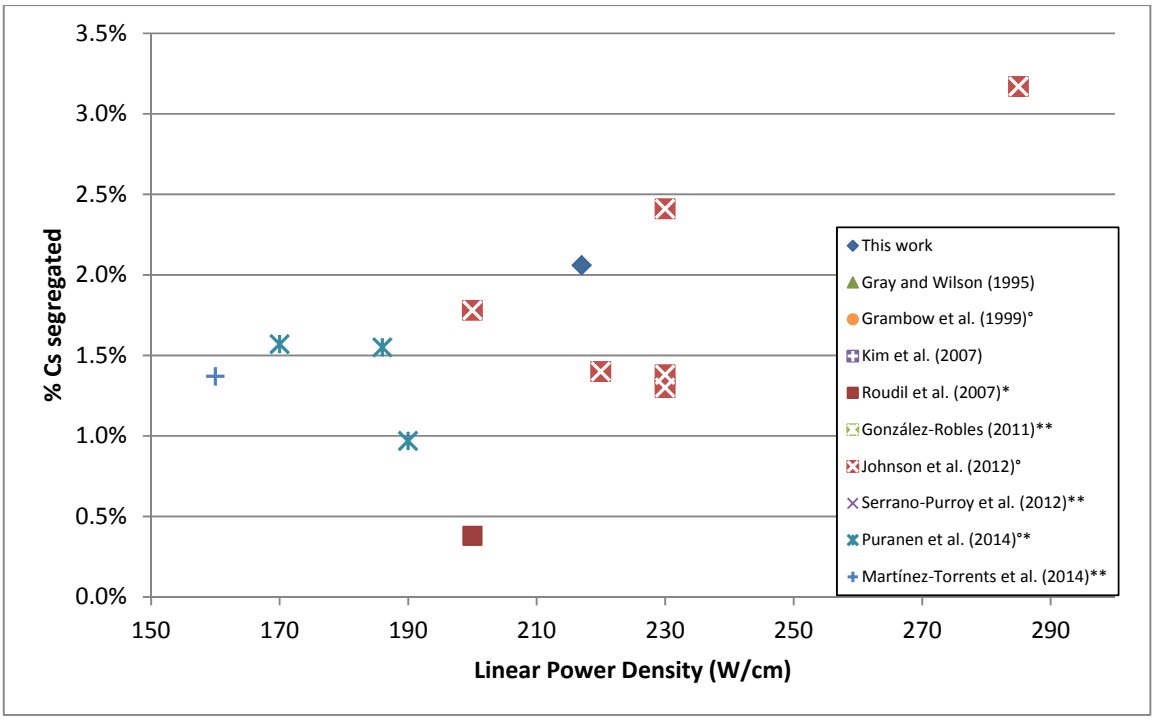

Figure D. 2 Cs segregated from the matrix in powder and fragmented samples from as a function of the average linear power density

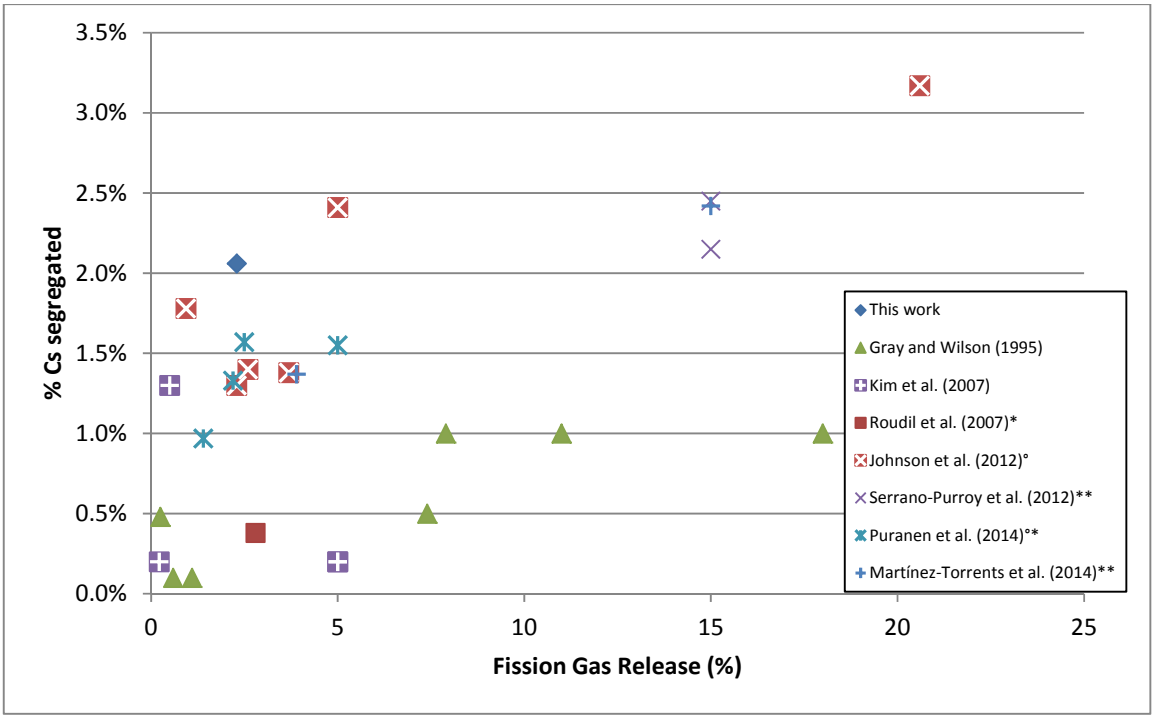

Figure D. 3 Cs segregated from the matrix in powder and fragmented samples from as a function of the Fission Gas Release

Sr segregated from the matrix

Data of the amount of Sr segregated from the matrix is shown in the following graphs.

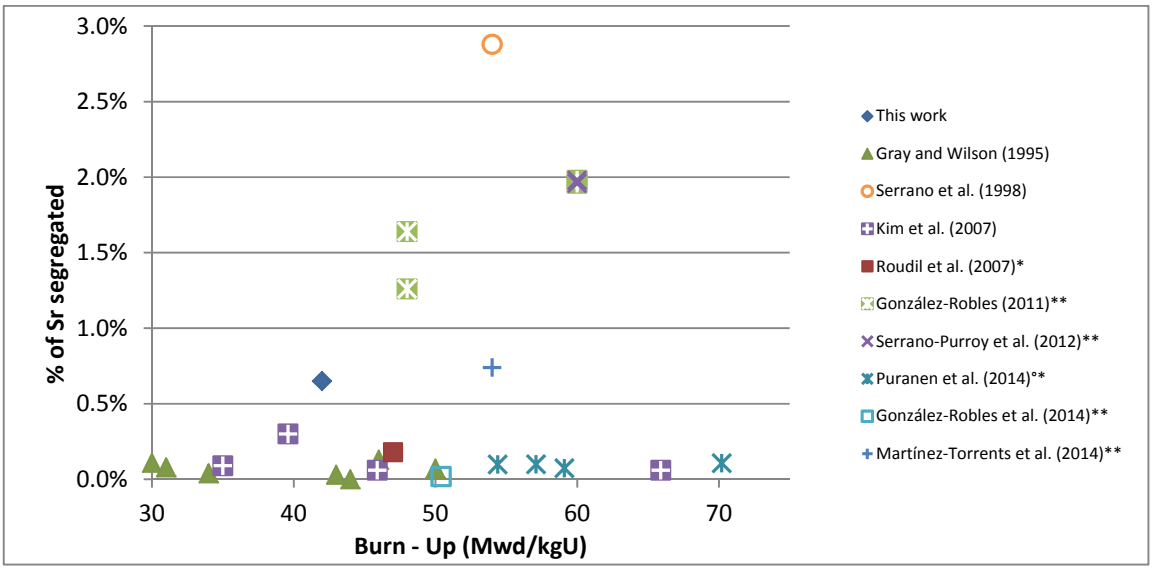

Figure D. 4 Evolution of the Sr segregated from the matrix determined for powder and fragmented samples as a function of the sample BU.

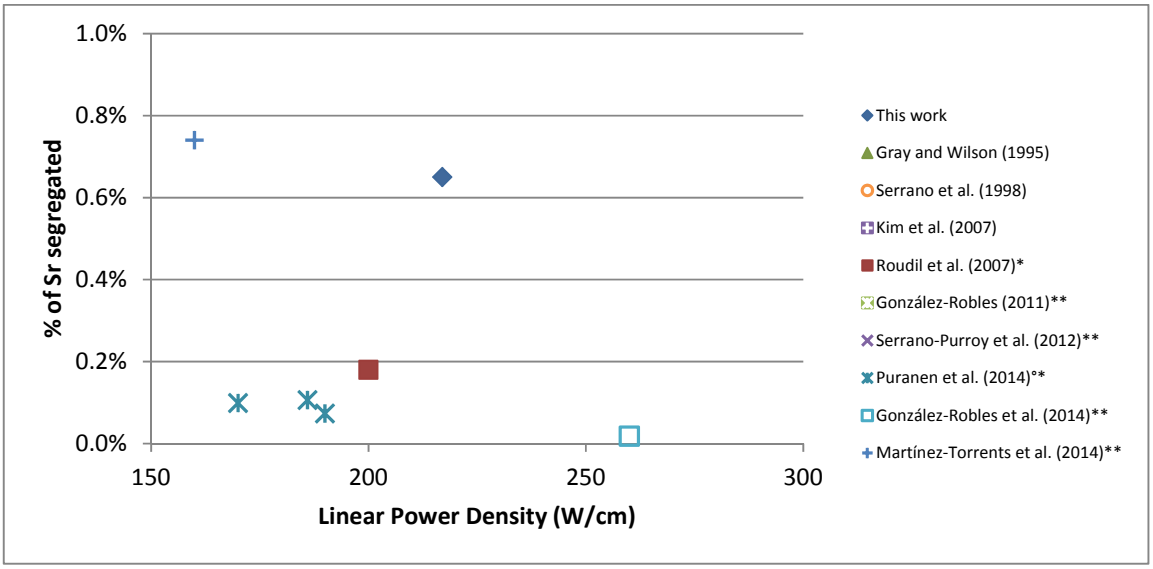

Figure D. 5 Evolution of the Sr segregated from the matrix determined for powder and fragmented samples as a function of the sample LPD.

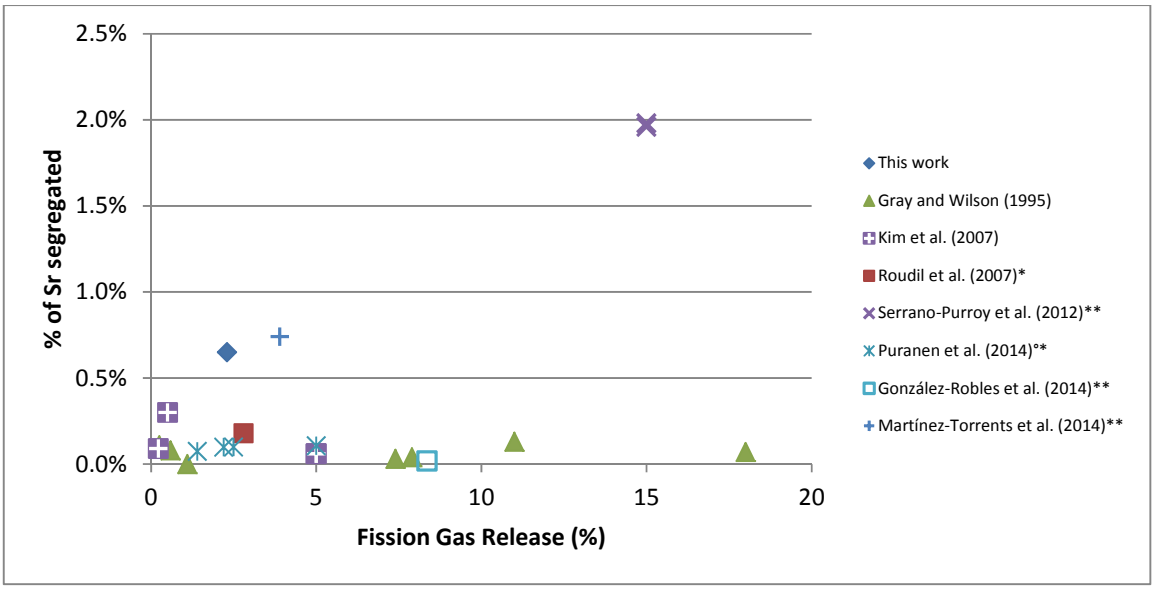

Figure D. 6 Evolution of the Sr segregated from the matrix determined for powder and fragmented samples as a function of the SNF FGR.

Rb segregated from the matrix

Data of the amount of Rb segregated from the matrix is shown in the following graphs.

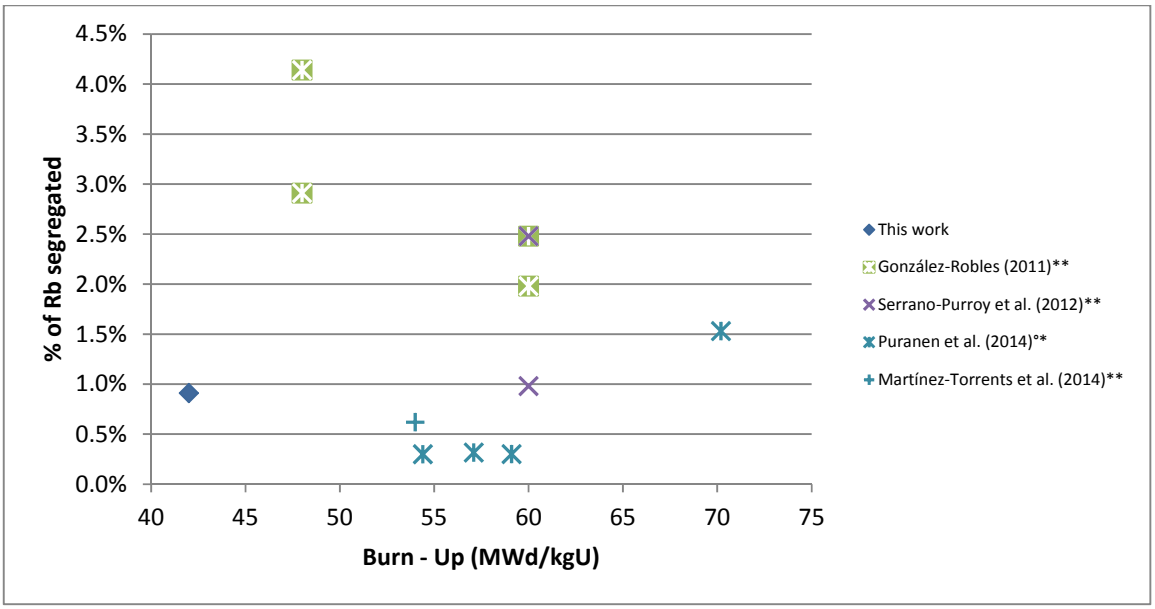

Figure D. 7 IRF of Rb as a function of the sample BU

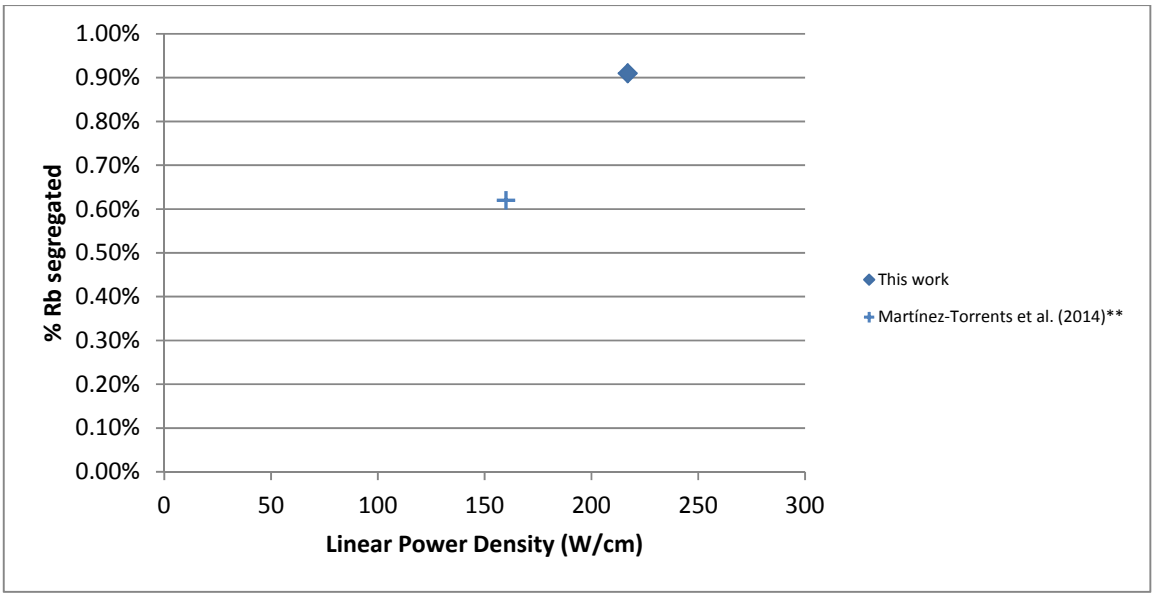

Figure D. 8 IRF of Rb as a function of the LPD

As it can be observed in Figure D. 8, the result obtained with the SERNIM can also be compared with one experimental value , hence no conclusions can be obtained from this graph. In order to determine a possible tendency, more data should be available regarding the LPD of the fuel samples. Unfortunately, some studies did not provide this information for publication and their results cannot be introduced in the graph.

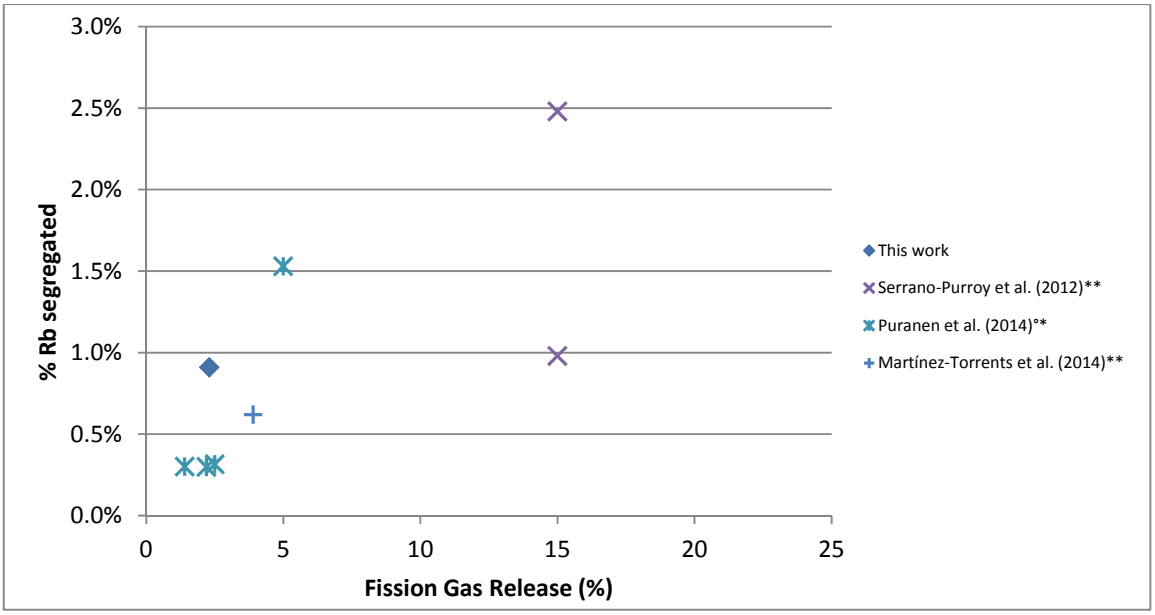

Figure D. 9 IRF of Rb as a function of the SNF FGR